Study of interfacial water at the nanoscale at ambient conditions with SPM

Mar Cardellach i Redon

September 25, 2012

Contents

Acknowledgements

Després de quatre anys de feina cal que doni les gràcies a tota aquella gent que n'ha format part d'una manera o altra. Primer de tot vull agrair a l'Albert Verdaguer i a en Jordi Fraxedas la dedicació, l'ajuda, i la paciència (tot sovint molta paciència) que han abocat en mi i el projecte. Gràcies per motivar-me i encoratjar-me, la vostra ajuda ha estat indispensable. Així mateix vull agrair a la resta de membres del grup SPM que en un moment o altre han dedicat el seu temps en poder fer més fàcil i amena la meva feina. Gràcies a tots vosaltres he après molt tant científicament com a nivell personal.

Gràcies a l'ICN per recolzar-me en tots els sentits, moral i econòmic, i vull agrair especialment a la Rosa i a la Cristina el seu recolzament. Gràcies també a en Xavier Borrisé que m'ha ensenyat i guiat dins la Sala Blanca, al Dr. Jos Santiso per les mesures de X-ray, i al Dr. Dani Ruiz i al seu equip.

Aquesta tesi no ha estat un camí de roses, tot sovint m'he sentit acorralada i en volia escapar com fos, però la persistència i estima de les persones més properes m'han ajudat a tirar endavant tot sovint. Per aquest motiu avui us dedico aquesta tesi (ja ho sé, és un regal una mica estrany) a tots vosaltres: Eva (condemnades a estimar-nos, passi el que passi, all t'hi trobo), Anna, Esther, Gemma, al grup AFM (Alguna Fefa Més? Marc, Princesita, Helloy's, Albapú, etc.), a la Carme Bonastre (sempre m'has guiat, encoratjat i animat), a la Meritxell (l'esperit més lliure que conec) i al Grup d'Esplai Vidrerenc, per tot el que ens hem donat mútuament. A en cucano i en pedete (també a

en pirriaki) i al grup de les Fefes. A tots vosaltres us dic una vegada més que m'he sentit molt estimada i us en dono les gràcies.

Als dos mestres més grans de la història de l'humanitat: l'Ivan i l'Artur. Gràcies per deixar-me compartir pis, converses, riures, truites de patates, grinyolades de porta, inquietuds i pel suport incondicional. I arran d'aquesta amistat també puc dir: gràcies a Déu.

En especial aquesta tesi va dedicada a vosaltres: Iana, Manel i Remei. En tot aquest procés heu estat el pilar bàsic, m'heu animat i recolzat fins al final, heu tingut una paciència enorme i m'heu fet entendre que si volia podia arribar on fos. A vosaltres no us hauria de dedicar aquesta tesi, us hauria de dedicar la meva biografia!!!

Us estimo.

Preface

As Paracelsus said in the 16th century: *water is the matrix of the world and of all its creatures.* Water has some unusual and important physical and chemical properties (its potency as a solvent, its ability to form hydrogen bonds, its amphoteric nature, etc.) that makes it unique. But water is not only essential for life on Earth, water is present on any surface exposed to air, everywhere is possible to find it. Even so, water does not interact in the same way with each surface, for this reason it is essential the knowledge about how water interacts with surfaces at the macroscale and the sub-micrometer level.

In order to do studies at dimensions as small as micrometers or nanometers, it is absolutely necessary suitable tools to perform much studies. During the last decades, Scanning Probe Microscopy (SPM) has opened a new instrumental door in terms of sub-micrometer measurements, and has allowed following processes at the nanoscale in real time. Atomic Force Microscopy (AFM) is one of these tools, probably the most versatile tool of the SPM group, which allows following processes as complex and amazing as water adsorption on surfaces, or detect properties like hydrophilicity or hydrophobicity.

The present Thesis work presents the study of water adsorption on different surfaces using nanoscale techniques . Liquids on surfaces is a current issue in nanoscience and I performed my work in the *Small Molecules on Surfaces in Ambient and Pristine Condition* group, . This research group be-

longs to the *Centre d'Investigació en Nanociència i Nanotecnologia* (CIN2) (a mixed Center between *Consejo Superior de Investigaciones Científicas* and the *Fundació Privada Institut Català de Nanotecnologia*) and focuses its scientific goals towards the physics and chemistry of interfaces involving small molecules within the nanoscale perspective. The molecules to be studied in this group are: (*a*) water and (*b*) those forming molecular organic materials. Altough water has been and continues to be exhaustively studied, many fundamental questions remain unanswered becoming accepted that water is still an enduring mystery. The group is particulary interesed in water interacting with surfaces, searching for the formation of structured water at ambient conditions. The approach of my group consists on exploring such interfaces in real (ambient) conditions with surface science techniques (explained in the chapter 2).

It is known, as explained in chapter 1, that ice formation is enhanced in the presence of external agents. Based on this, and using the appropriate tools, the present Thesis work presents a nanoscale study of different substrates that can help the nucleation of ice. BaF_2 and CaF_2 were chosen for this study, and later, aliphatic alcohol chains arranged as a monolayer on graphite for the same reason. The study of wettability of graphene is presented as well in order to understand how water interacts with a hydrophobic surface.

Objectives

- Study and characterization of defects on BaF_2 surface, and the role of its in the ice nucleation.

- Study of lattice constant in order to know the importance in the ice nucleation processes.

- Study of water role on hydrophobic substrates.

- Formation and characterization of Langmuir-Blodgett films of aliphatic alcohols on graphite.

- Study of water adsorption on these Langmuir-Blodgett films.

Chapter 1

Introduction

Water, as the most abundant molecule on the Earth and in our own bodies, is ubiquitous in terrestrial chemical processes. These processes range from conventional solution reactions to critical atmospheric reactions. As a result of the prevalence for water to be involved in natural chemistry, there have been a great many studies of water, as a molecule, as a liquid, solid, or vapor, as a medium for reactions, and as a reactant. But, what's water? Why is water important? And how water is involved in our lives? In order to answer these questions, first of all there is the need to analize the water molecule, and then, how it interacts with the environment.

1.1 Isolated water molecule

The water molecule, H_2O, is formed by hydrogen and oxygen, with electronic configurations $1s^1 2s^2 2p^4$, respectively. Orbital hybrideze is sp^3-like orbitals leaving the lone pairs (Fig. 1.1), but there is not yet consensus about the real hybridization. Ab initio calculations on isolated molecules, however, do not confirm the presence of significant directed electron density where lone pairs are expected. The negative charge is more evenly smeared out along the line

between where these lone pairs would have been expected, and lies closer to the center of the O-atom than the centers of positive charge on the hydrogen atoms (*Martin, RB; 1998* and *Laing, M; 1987*)

In a perfect tetrahedral arrangement the bond-bond, bond-lone pair and lone pair-lone pair angles would all be 109.47° (*Pauling, L; 1931*). The water molecule belongs to the C_{2v} point group , having two mirror planes of symmetry (σ_v and σ'_v) and a 2-fold rotation axis (C_2) (see Fig. 1.2). The experimental values for water monomers are O-H length of 0.95718 Å and H-O-H angle of 104.474° (*Hasted, JB; 1972*). The charge distribution depends significantly on the atomic geometry and the method for its calculation but is likely to be about -0.7e on the O-atom (with the equal but opposite positive charge equally divided between the H-atoms) for the isolated molecule (*Martin, F; and Zipse, H; 2005*).
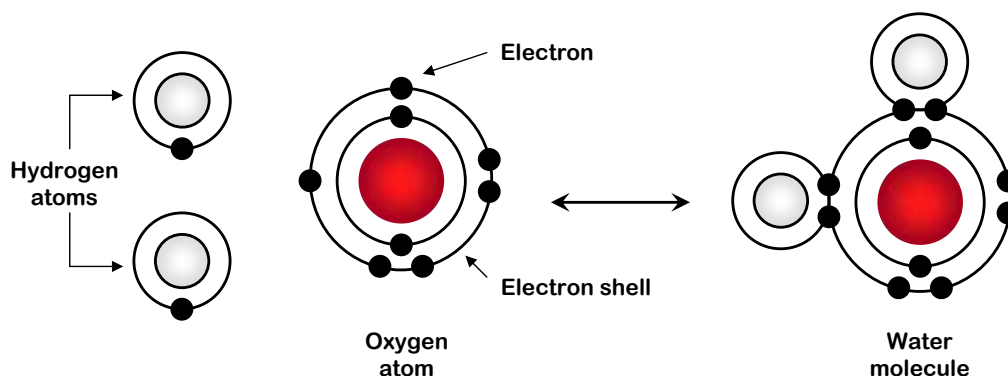
Figure 1.1: Reversible process of water molecule formation. Sharing the lone electrons of both atoms, they complete the electron shell forming the water molecule.

The isolated water molecule exhibits the parameters shown in Fig. 1.3 and vibrations and rotations, which are represented in figure 1.4. Fig. 1.4 a, b and c represent how hydrogen atoms can move with respect to oxygen atom, and Fig. 1.4 d shows different rotation movements through the x, y and z axis, respectively.
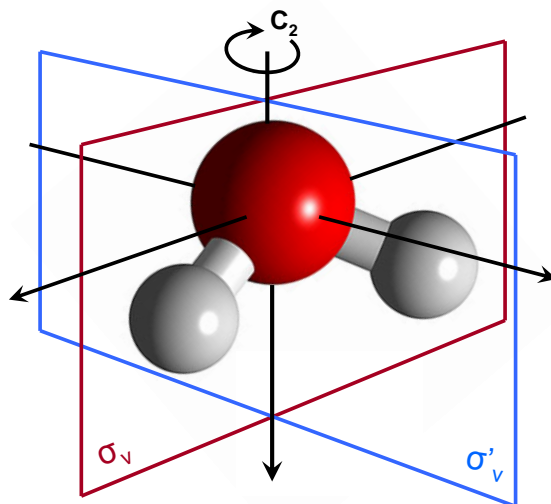
Figure 1.2: Water molecule symmetry. It has two symmetry planes (σ_v and σ'_v) and one rotation axis (C_2).

Figure 1.3: Left: H-O-H angle and the diameter of a water molecule. Right: water molecule geometry indicating the polarization.

Figure 1.4: Different movements of the atoms in water molecule due to temperature and vibrations. Taken from: M. Chaplin web, http://www.lsbu.ac.uk/water/

1.1.1 Hydrogen bonding

Each water molecule can interact with other water molecules due to the larger electronegativity of the oxygen atoms with respect to that of the hydrogen atoms, causing a dipole moment. The resulting dipole causes the attraction 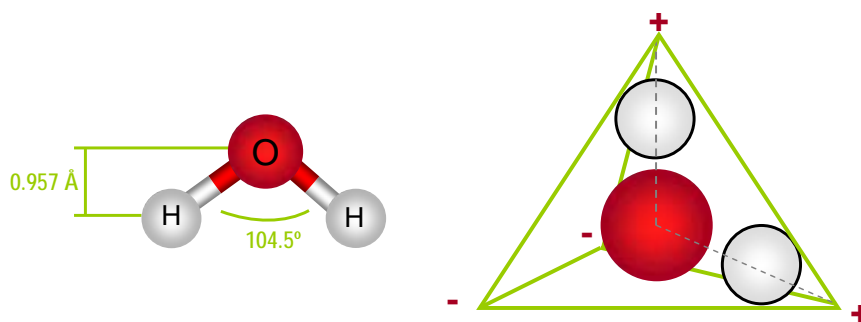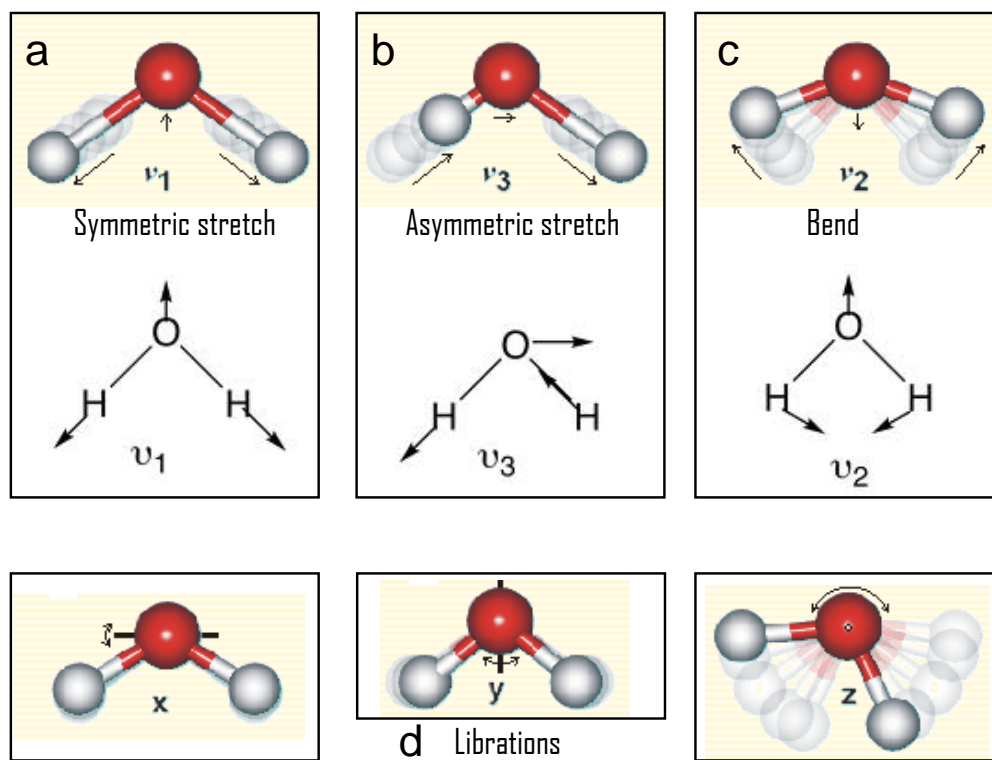of hydrogen atoms of water molecules to the oxygen atoms of a nearby water molecules, the so-called hydrogen bonding (H-bonding), as shown in figure 1.5 (*Maksyutenko, P; 2006*). H-bonding of water molecules has an electrostatic part (about 90%) and a covalent part (about 10%) (*Isaacs, ED; 2000*). The force is the strongest when the three atoms are in line (O-H···O), and when the O atoms are separated by about 2.82 Å indicating the directionality of the H-bonding. Hydrogen bonding is much weaker than covalent bond (∼20 kJ/mol vs ∼460 kJ/mol) but it is strong enough to remain at ambient conditions. Due to the hydrogen bond formed between two water molecules, it causes an excess of negative charge in one of the molecule acting as a donor, and a defiency of negative charge in the other molecule acting as a acceptor. The result is the stimulation to create new hydrogen bonds with other water molecules with the opposite role, the so-called cooperativity effect.

1.2 Solid water

Water has many solid phases (ices). There are sixteen crystalline phases, where the oxygen atoms are in fixed positions relative to each other but the hydrogen atoms may or may not be disordered but obeying the Bernal-Fowler rules or ice rules (the set of rules describing the arrangement of hydrogen atoms in an ideal ice crystal) (*Knight, C; 2006*) and three amorphous (non-crystalline) phases. All the crystalline phases of ice involve the water molecules being hydrogen bonded to four neighboring water molecules (*Zheligovskaya, EA; 2006*). The H-O-H angle in the ice phases is expected to be
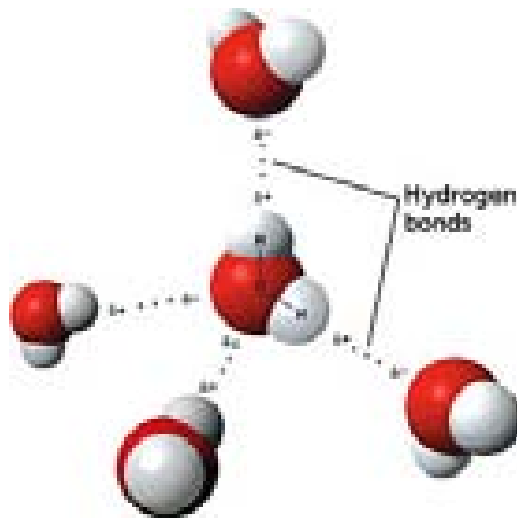
Figure 1.5: Through weak interactions, the water molecule can interact with other four water molecules. Hydrogen bond is more stable when the atoms involved are linear. The water molecule that offers the hydrogen in order to create the hydrogen bond is called the donor molecule, while the other water molecule is named acceptor. Taken from: M. Chaplin web, http://www.lsbu.ac.uk/water.

a little less than the tetrahedral angle (109.5°), at about 106.6° (greater than the liquid water angle) (*Petrenko and Whitworth; 2002*).

Hexagonal ice, known as ice I_h (space group $P6_3/mmc$), is the most abundant of the varying solid phases on the Earth. In the following chapters, I will give relevance to I_h ice because of its involvement in environmental processes. I_h has a six-fold symmetry and only hexagonal I_h ice, ice III, ice V, ice VI, ice VII and perhaps ice X can be in equilibrium with liquid water, whereas the other ice phases are not stable (figure 1.9). As hydrogen bonding is predicted to be more ordered in the surface with respect to the bulk (Pan *et.al.*; 2008), ice nucleation occurs greatly enhanced, by a factor of $\sim 10^{10}$, at the air-water surface (interface) rather than within bulk water (*Shaw, RA; 2005*).

Forms and symmetries

Snowflakes or snow crystals show a great variability of forms and symmetries that have created a scientific interest for hundred of years (*Frank, FC; 1982, and Nakaya, U; 1954*).

Johannes Kepler was the pioneer in this area, when in 1611 presented a work where he described and classified thoroughly the snow crystals and their symmetries. Few years later, René Descartes extended the Kepler's work with a detailed description of the snow crystals forms in his work "Les Météores" (*Descartes, R; 1637*).

Centuries later, in 1931, the photography revolution gave the opportunity to Wilson Bentley to take pictures of the snow crystals and could make a wider and more realistic classification. From the work done, Bentley's images became a winter icon and were used to numerous works and papers.

The snowflakes are formed when vapour water molecules are adsorbed on suspended particles into the clouds (dust particles, for example), through heterogeneous nucleation (explained in detail in section 1.5.1). Since some particles promote the nucleation better than others, droplets do not all freeze simultaneously. When the particles fall and leave the cloud, during the course, its experience temperature and relative humidity changes. For this reason, depending to the relative humidity and temperature conditions of the way the particles suffer different growth behaviour. The growth of snow crystals is not a simple process because there are many parameters involved (*Libbrecht, KG; 2007*).

Natural snow crystals have been categorized into morphological types by several different authors, acquiring names like stellar dendrites, spatial dendrites, sectored plates, hollow columns, bullet rosettes, capped columns and many others (see Fig. 1.6).

The physicist Ukichiro Nakaya was the first to perform in-depth labora-

Figure 1.6: Natural snow crystals from: http://www.snowcrystals.net/gallery1sm/index.htm - Kenneth Libbrecht gallery.

tory studies of snow crystal growth in the 1930's (*Nakaya, U; 1954*). Nakaya not only categorized natural snow crystals under different meteorical conditions, he was also the first to grow synthetic snow crystals in the laboratory in a controlled environment. He observed the different growth morphologies that appeared at different temperatures and supersaturations and combined these observations into what is called the snow crystal morphology diagram (see Fig. 1.7) which refers to snow crystals growing in air at a pressure near 1 atmosphere, thus applying to natural snow crystals.

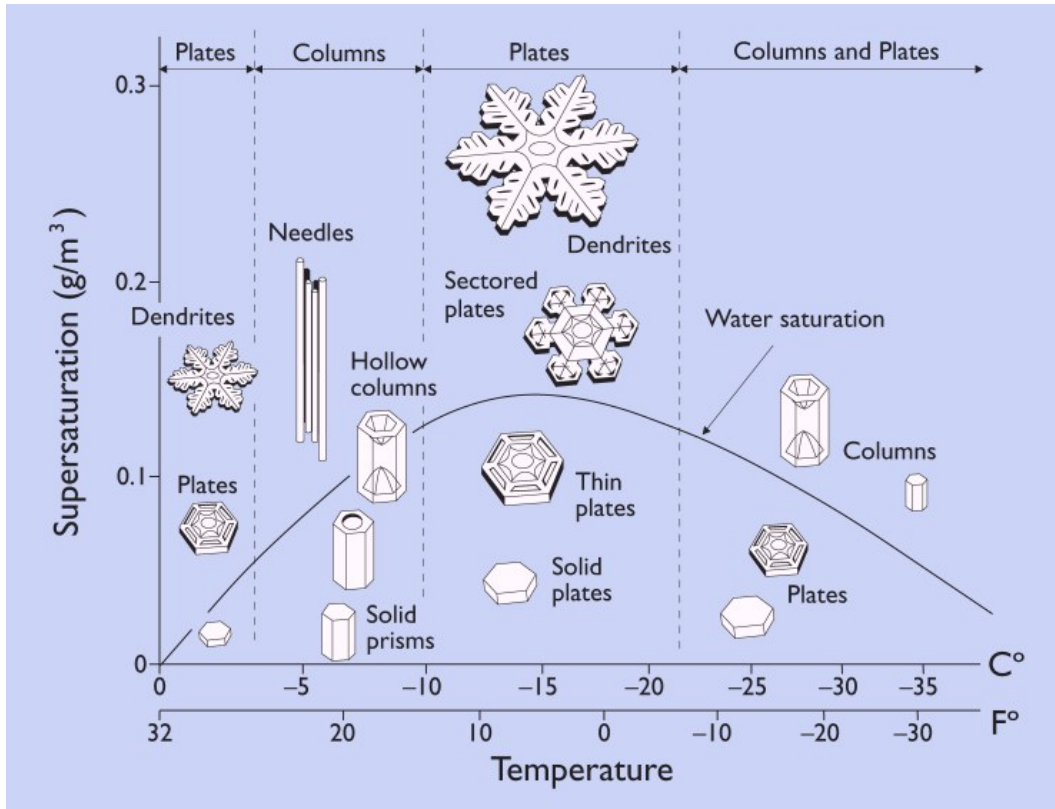Figure 1.7: Nakaya's diagram shows the different growth morphologies depending on temperature. Taken from: http://physicstoday.org/journals/doc/PHTOAD-ft/vol_60/iss_12/captions/70_1cap2.shtml

Just below freezing, at temperatures near to T=-2°C, the growth is in plate-like shape, with thick plates at lower supersaturations, thinner plates at intermediate supersaturations, and plate-like dendritic structures at high

supersaturations (see figure 1.7). For temperatures near to T=-5°C, the ice growth is columnar, with stout columns at a lower supersaturations, more slender, often hollow columns at intermediate supersaturations, and clusters of thin, needle-like crystals at higher supersaturations. Temperatures near to T=-15°C, the growth becomes again in plate-like shapes, and again one see the increase if dendrites at high saturations. Finally, at very low temperatures the growth becomes a mixture of thick plates at low supersaturations and columns at higher supersaturations.

1.3   Liquid water

In the liquid state, about 80% of electrons of water molecule are involved with bonding. The three atoms of the water molecule are not always linked, but the hydrogen atoms are constantly transferred between water molecules due to protonation and deprotonation processes, and the average time for the atoms in a water molecule is about one millisecond (*Loparo, et.al.; 2004*), longer than hydrogen bonding duration (few ps) (*Fecko, et.al.; 2005*). Regarding to liquid water values ab initio (O-H length 0.991 Å, H-O-H angle 105.5° (*Silvestrelli, PL. and Parrinello, M; 1999*)) and diffraction studies (O-H length 1.01Å (*Soper, AK. and Benmore, CJ; 2008*)) suggest slightly greater values mainly due to the hydrogen bonds, that weaken the covalent bonds and the repulsion between the electron orbitals is reduced. Molecular models commonly use O-H lengths between 0.957 Å and 1.00 Å and H-O-H angles from 104.52° to 109.5°. The most common molecular models are represented in figure 1.8 where the table shows the parameters used, being l_1 the length of the covalent bond, q_1 the hydrogen charge density, q_2 the oxygen charge density, ϕ the angle formed by the three atoms of water molecule and σ and ϵ are the Lennard-Jones parameters (the separation and depth of

the potential energy minimum between two similar molecules (equivalent to diameter)).

Model	Type	σ (Å)	ε (kJ/mol)	l_1 (Å)	q_1 (e)	q_1 (e)	φ
SPC	planar	3.166	0.650	1.0000	+0.410	-0.8200	109.47
SPC/E	planar	3.166	0.650	1.0000	+0.4238	-0.8476	109.47
TIP3P	planar	3.15061	0.6364	0.9572	+0.4170	-0.8340	104.52
TIP3P/Fw	planar	3.1506	0.6368	0.9600	+0.4170	-0.8340	104.5
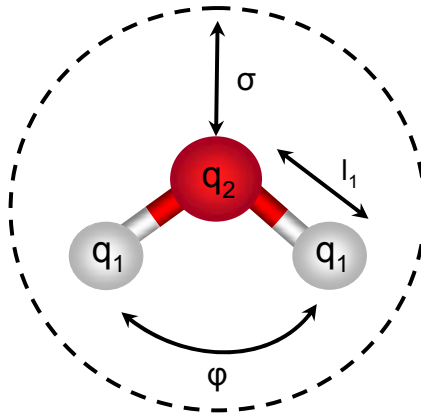
Figure 1.8: Planar molecular model of water and parameters for some of these models.

As explained for solid water, there are also some structural differences between bulk and surface water that affect to its behavior. The structure of the surface is not completely understood but some information has been determined. Hydrogen bonding in the surface is stronger than in the bulk (*Gan, W. et.al.; 2006*) but some hydrogen bonding is lost, giving a more reactive environment (*Kuo, W and Mundy, CJ; 2004*) and greater ice nucleation (*Shaw, RA; Durant, AJ; and Mi, Y; 2004*). The increased strength in the water hydrogen bonds of surface, is partially due to the reduced competition from neighboring water molecules, and this stronger bonding is due to lower anticooperativity (the formation of two simultaneous donor or acceptor hydrogen bond) and compensation for the increase chemical potential on the

loss of some bonding. The O$\cdots$O distance, between surface water molecules, within 2-3 nm from the surface is about 6% larger than that bulk water at 25°C. Analysis of simple thermodynamics shows that the surface probably has considerable structuring, having it identical in density to that of bulk water at just under 4°C. In addition, the structure of surface water molecules varies less with temperature than into the bulk (*Greef, R; and Frey, JG; 2008*).

Water molecules vary according to the environmental conditions. Consequently, it is necessary to discuss about the different states of water.

The phase diagram is the graphic representation of the boundaries between different states of a compound in function of temperature and pressure. At normal Earth temperature and pressure, water is liquid, but it changes and solidifies if temperature is decreased below 273 K (0°C, through a heterogeneous nucleation process, explained in section 1.5.1), and it changes to vapour state if temperature is increased to 373 K (pressure invariable). Each line represents a phase limit and gives us information about the conditions where two phases coexist. A triple point is done when three phases are found in one point. The water phase diagram is complex because there are a great number of triple points as shown in figure 1.9.

1.4   Water cycle

Water is everywhere. Water is surrounding us and it forms the most important Earth's natural cycle: the water cycle. In figure 1.10 the scheme of the cycle is shown, where one can observe the main parts of this phenomenon:

1. **Evaporation**: 90% of water evaporation in the planet comes from the evaporation of seas, oceans and continental water (i.e. lakes). When the Earth receives Sun rays, a volume of water from seas, oceans and lakes is evaporated (evaporation is most important in seas and oceans than
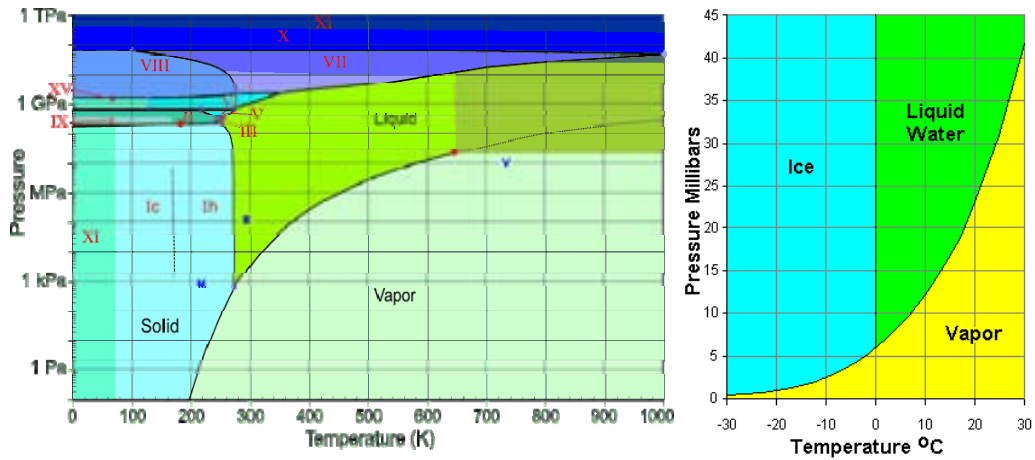
Figure 1.9: Left: complete phase diagram of water with all different ices types depending of T° and pressure. Right: simplified phase diagram of the three basic states of water. Taken from: M. Chaplin web, http://www.lsbu.ac.uk/water/

in the lithosphere). Evaporation is a state change from liquid to gas of water molecules, and in this process, salts dissolved into the water volume are not evaporated with water, therefore the evaporated water is pure. The other 10% of water evaporation, called evapotranspiration, comes from living beings and soil.

2. **Condensation**: As water vapour amounts through the troposphere, it is slowly cooled and is condensed forming clouds. Clouds are formed by liquid water, atmospheric gases, suspended particles and other substances from dissolution of atmospheric gases. Then, condensation represents the state change from gas to liquid.

3. **Transport**: Clouds move because of the wind.

4. **Nucleation**: Water droplets slowly begin to condense. When nucleation takes place (see section 1.5.1) solid nuclei is formed, and the force of gravity finishes the work causing water (snow or hail) precipitation.

5. **Drain**: Water is drained through the soil and filtered, coming back
   again to lakes, seas and oceans.

The cycle of water is easy to understand and often one can observe it.
But in fact, it includes a large number of extraordinary chemical and physical
processes, although the state change has the main role in this phenomenon. In
order to understand the objectives of this thesis, it is necessary to emphasise
one of this processes: water nucleation and water condensation.

Once water is evaporated (gaseous state), it remains into the clouds in
liquid state (reaching temperatures as low as -40°C without freezing). Pure
water is frozen at temperatures of -40°C and this process is called homoge-
neous nucleation. But when the water droplets find suspended particles into
the cloud, these can help increasing the temperature of nucleation and the
change of state (liquid to solid) is carried out at higher temperatures. This
process is called heterogeneous nucleation (both explained in detail in sec-
tion 1.5.1). This phenomenon that takes place every day in troposphere is
reproducible into the laboratory when one wants to study the different types
of particles and surfaces that allow the water nucleation. And this is the
starting point of the research presented here.

1.5   Overview on ice nucleation and thin wa-
ter films

In spite of the fact that only a small percentage of the total condensed wa-
ter in the troposphere (it contains approximately 80% of the atmosphere's
mass and 99% of its water vapor and aerosols) is in the form of ice, this con-
densed form of water exerts a critical influence on important meteorological
processes such as precipitation and cloud electrification (*Langmuir, I; 1950*).
It has been known from decades that the presence of foreign bodies facilitates
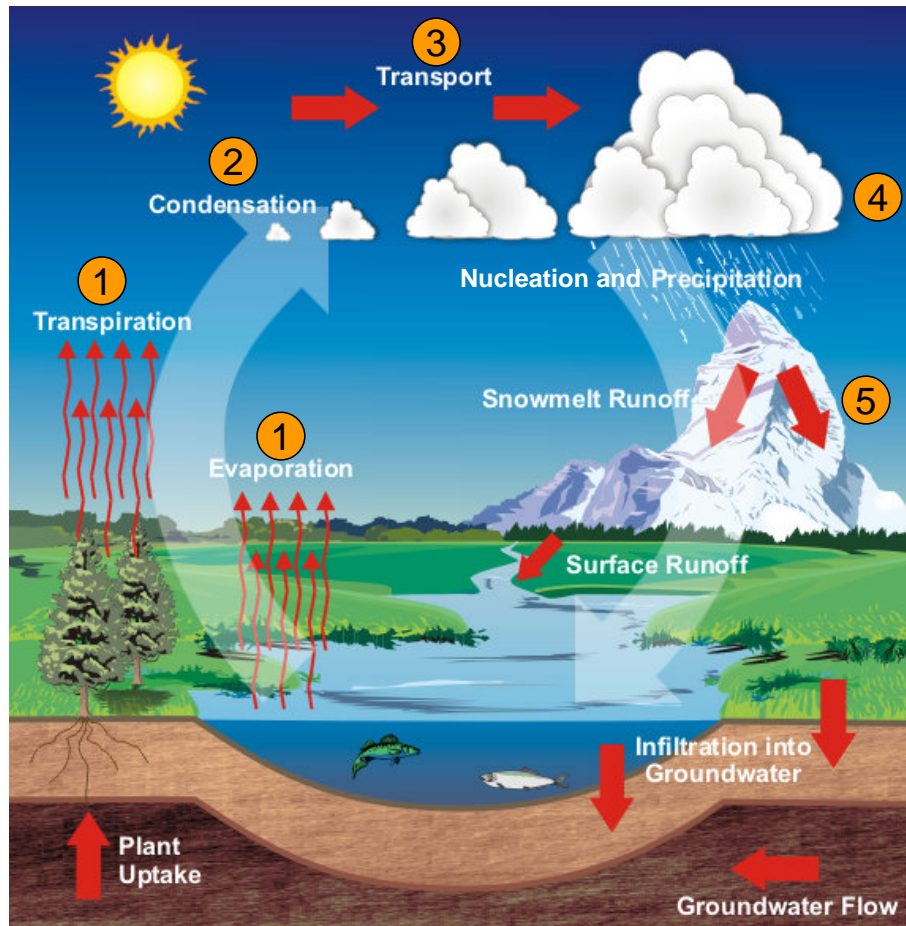
Figure 1.10: Water cycle describes the continuous movement of water on, above and below the surface of the Earth. Water can change states among liquid, vapor, and solid at various places in the water cycle. The sun, which drives the water cycle, heats water in oceans and seas. Water evaporates as water vapor into the air. Then, the principal parts of this cycle are: evaporation, condensation, transport, nucleation and drain. One can observe that during the nucleation clouds are formed. Their color is white, and the reason for this is simple. Light in its natural state is white light. None of the colors are separated. However, when white light hits an object four things happen depending on the object's properties. Light can be adsorbed, reflected, refrected, or scattered. If light is refracted, it separates into its seven main colors and scatter. This is how the color of clouds is determined. Clouds are made up of water droplets and ice crystals. These droplets and crystals are larger enough to scatter light uniformly. Since the light is not separated it remains white light and that is why clouds look white. Image taken from http://www.education.noaa.gov

the freezing of water and even in high purified water remaining small dust particles or impurities that can induce ice nucleation, as explained Dorsey (*Dorsey, NE; 1948*). The ice formation in the troposphere at temperatures above -33°C is mainly induced by a foreign body. Nucleation induced by a foreing body is called heterogeneous nucleation (explained in section 1.5.1). Nowadays, the physical and chemical mechanisms involved in efficient heterogeneous nucleating surfaces are still uncertain (*Cantrell, W; 2005*).

Once the great potential of these suspended particles is accepted, its have been used to artificially induce water condensation in clouds using nucleation agents with uncertain success (*Pruppacher, HR; 1997*). It is the old dream of controlling rain, which would alleviate regions suffering from prolonged shortage of water (drought), but also avoid phenomena of disastrous consequences such as hail, flooding, tornados, etc.

To understand and control these macroscopic phenomena we need a better knowledge of the mechanisms involved at the nanoscale. The next section aims to give a brief explanation about how water adsorbs and interacts with surfaces, and which mechanisms are involved in water freezing phenomena.

1.5.1   Ice Nucleation

Nucleation is a physical process that occurs when water molecules start to precipitate out, forming nuclei which would then attract more precipitate. In general, nucleation is the beginning of a change in state of a condensed phase localized in a small but stable region.

This process begins with the formation of small "embryos or clusters" of the new phase inside the large volume of the parent phase. The sizes of these clusters undergo continuous fluctuations due to the incorporation of more molecules or the detachment of other. New clusters appear while others disapear in a dynamical process. When the cluster of the new phase is large

enough, it becomes stable and does not decay anymore. This is what is called the critical size, and it is the starting point of the growing of the new phase (*Hohenberg, PC; 1977*).

The parent phase becomes metastable, which explains why it can transform into the new phase after an external action. Its metastability is understood by considering the free energy changes associated with the formation of the small clusters (*Kashchiev, D; 1998*). Because the surface molecules are less well bound to their neighbors than are those in the bulk, their contribution to the free energy of the new phase is greater. The difference between the free energy per molecule of the bulk and that of the surface is referred to as the interfacial free energy. The interfacial free energy is always a positive term and acts to destabilize the nucleus. As a consequence, at very small size when many of the molecules reside at the surface, the nucleus is unstable. Adding even one more molecule just increases the free energy of the system. But once the nucleus gets large enough (critical size), the drop in free energy associated with the formation of the bulk phase becomes sufficiently high that the surface free energy becomes less important, and every addition of a molecule to the lattice lowers the free energy of the system (*Yoreo, JJ; 2003*). During phase transformations, like precipitation or solidification, processes such as nucleation, growth and coarsening depend strongly on interfacial effects, named Gibbs-Thomson effects (modifies the solubility limits given by equilibrium thermodynamics) (*Perez, M; 2005*). For an isolated spherical solid particle of diameter x in its own liquid, the Gibbs-Thomson equation for the structural melting point depression (reduction of the melting point of a material with reduction of its size) can be written as:

$$\Delta T_m(x) = T_{mB} - T_m(x) = T_{mB} \frac{4\sigma_{sl}}{H_f \rho_s x} \qquad (1.1)$$

Where, T_{mB} = bulk Melting temperature, T_x = particle x Melting tem-

perature, σ_{sl} = solid-liquid interface energy (per unit area), H_f = bulk enthalpy of fusion (per gram of material), ρ_s = density of solid. The "4" in the above equation comes from the spherical geometry of the solid-liquid interface. Then, when the particle size is small, the melting temperature is higher than when the particle is big.

Once known how the embryos grow, it is important to explain the different types of nucleation. Nucleation can be classified as *homogeneous* and *heterogeneous*. In homogeneous nucleation a new solid phase forms homogeneously from the parent liquid phase. It occurs spontaneously and the process requires supercooling of the medium. In heterogeneous nucleation, a new solid phase forms on a pre-existing particle or surface which catalyzes the nucleation of different materials. The energy required for a heterogeneous process is lower than a homogeneous nucleation. Heterogeneous nucleation is the most likely in most natural nucleation processes. In addition, a smaller number of atoms is required to catch the critical radius core in heterogeneous nucleation.

Homogeneous Nucleation

Consider the homogeneous nucleation of an α phase from a β phase. If we consider a spherical particle of radius r with an isotropic interfacial energy (the cost associated to the creation of a new phase) $\sigma_{\alpha\beta}$, the change in free energy as a function of the embryo's radius is:

$$\Delta G = \frac{4}{3}\pi r^3 \Delta G_v + 4\pi r^2 \sigma_{\alpha\beta} \tag{1.2}$$

Where the first term $\Delta G_v = G_v^\alpha$ - G_v^β, and G_v is the Gibbs free energy per unit volume (the energy gain of creating a new volume). The second term corresponds to the energy loss due to surface tension (σ) of the new interface.

Figure 1.11 shows the variation in the free energy ΔG of nucleation with increasing size of the embryo. The maximum in the curve is found by differ-
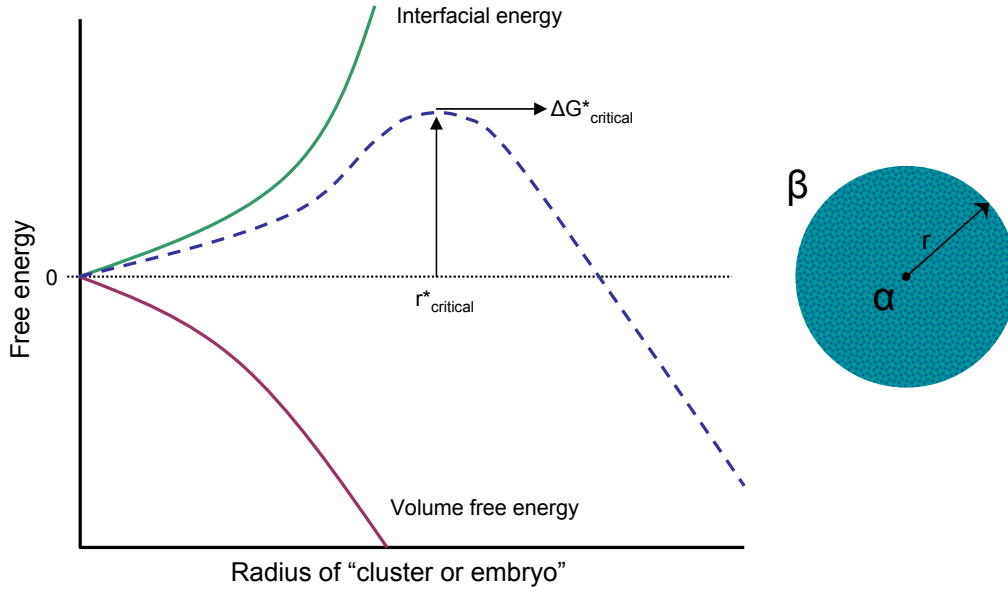
Figure 1.11: The activation energy barrier G^* and critical nucleus size r^* according to classical nucleation theory.

entiating Eq. 1.2 with respect to r:

$$\frac{\partial(\Delta G)}{\partial r} = 4\pi r^2 \Delta G_v + 8\pi r \sigma_{\alpha\beta} \tag{1.3}$$

And r^* is obtained by setting this result to zero:

$$r^* = \frac{2\sigma_{\alpha\beta}}{\Delta G_v}, \tag{1.4}$$

where r^* is the critical radius, which means that it is the minimum radius for which the embryo will be stable and it can grow. When the value of r^* is substituted into Eq. 1.2, the activation energy is obtained:

$$G^* = \frac{16\pi\sigma_{\alpha\beta}^3}{3(\Delta G_v)^2} \tag{1.5}$$

This is the barrier that determines the kinetics of nucleation. The nucleation rate per unit volume, J_n is proportional to the exponential of the barrier height divided by $k_B T$ (where k_B is defined as Boltzmann constant,

and is the physical constant relating energy at the individual particle level with temperature). Thus, the nucleation rate is given by:

$$J_n = A exp(-G^*/k_B T), \qquad (1.6)$$

where A is a factor that depends on many parameters such as the shape of the atoms, the area to which atoms can join, and the vibrational frequency of the particles (*Jackson, CL and McKenna, GB; 1990*).

Heterogeneous Nucleation

When a foreign surface is present, the interfacial energy between an embryos and a solid substrate is lower than that of the crystal in contact with the solution (*Abraham, FF; 1974*). This is because the molecules in the crystal can form bonds with those in the substrate that are stronger than the bonds of solvation (*Yoreo, J.J; 2003*). Stronger bonds lead to a smaller interfacial free energy. Obviously, the strength of the bonds at the interface will depend on the structure and chemistry of the substrate surface. When the atomic structure of the substrate surface closely matches with a particular plane of the nucleating phase, the lattice strain is minimized, and the enthalpic contribution to the interfacial free energy becomes small, and then nucleation occurs preferentially on the crystal plane.

One can perform the same analysis of homogeneous nucleation to heterogeneous nucleation. There are now two interfacial energies to consider, one between the embryo and the solution and the other between the embryo and the substrate as shown in figure 1.12. If we assume that the embryo is a hemisphere of radius r, we have:

$$\Delta G = \frac{2}{3}\pi r^3 \Delta G_v + \pi r^2 (2\sigma_{\alpha\beta} + \sigma_{\alpha\gamma} - \sigma_{\beta\gamma}) \qquad (1.7)$$

Where the subscripts $\alpha\beta$, $\alpha\gamma$, $\beta\gamma$ refer to embryo-liquid, embryo-substrate
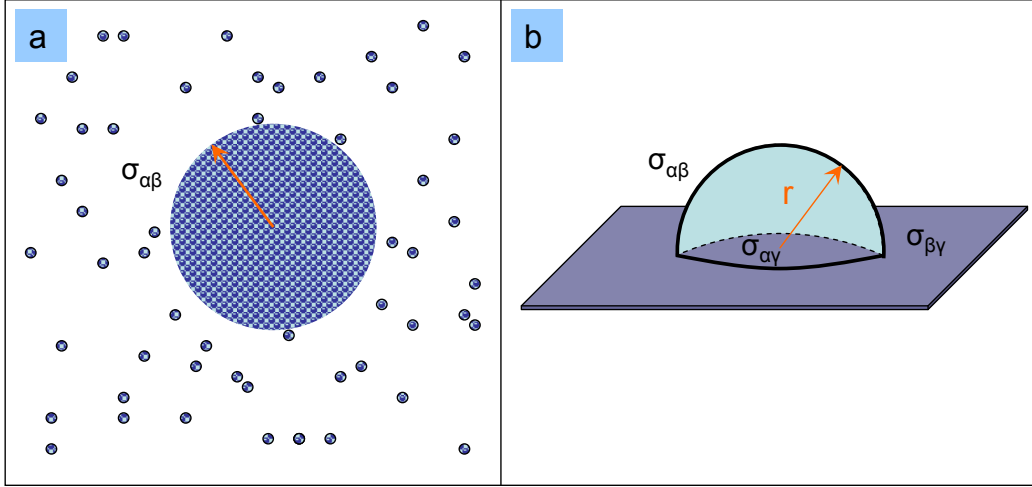
Figure 1.12: a) Formation of a spherical nucleus of radius r from a solution leads to the free energy changes. b) Heterogeneous formation of a hemispherical nucleus at a foreign substrate. Taken from *Yoreo, JJ; 2003*.

and liquid-substrate respectively. The new expression of r^* becomes: (*Fletcher, NH; 1958*)

$$r^* = \frac{2\sigma'}{\Delta G_v},$$ (1.8)

where

$$\sigma' = \sigma_{\alpha\beta}[1 - \frac{(\sigma_{\beta\gamma} - \sigma_{\alpha\gamma})}{2\sigma_{\alpha\beta}}].$$ (1.9)

The expression $[1 - \frac{(\sigma_{\beta\gamma} - \sigma_{\alpha\gamma})}{2\sigma_{\alpha\beta}}]$ is always less than one, providing a decrease in free energy of the embryo-substrate respect to that of the liquid-substrate interface. Then, the value of r^* is slightly reduced as compared to nucleation in free solution.

The mechanisms of heterogeneous nucleation of water are still uncertain. B. Vonnegut reasoned that inorganic substrates whose structure has lattice parameters similar to the basal prism face of hexagonal ice should be good nucleating agents (*Vonnegut, B; 1947*). Fletcher considered defects such as

steps, corners and edges as a favoured nucleation sites (*Fletcher, NH; 1958*).
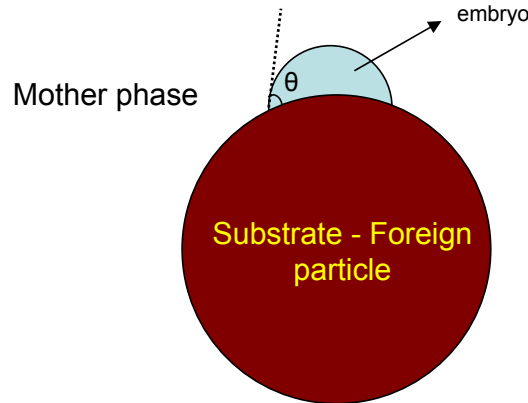

Figure 1.13: Schematic illustration of heterogeneous three-dimensional nucleation on a foreign particle.

The reason why impurities and foreign bodies like dust in contact with water reduce the required energy to reach the critical radius is because the effective surface energy is lowered, then the free energy barrier is diminished facilitating the nucleation as shown in Fig.1.14.

Thin water films

At the troposphere, water interacts with all the surfaces exposed forming thin water films that cover them from a fraction of a monolayer to a macroscopic layer depending on the water interaction with the exposed surfaces. In most conditions these layers are imperceptible to the human eye, but the presence of thin film has a profound effect on the physical and chemical properties of the surface (*Ewing, GE; 2004*).

Thin film water on surfaces has been studied for centuries, this phenomena is known as wetting. It was in the beginning of 20th century when Irving Langmuir measured and quantified the thickness of water films on insulator surfaces such as mica and glass (*Langmuir, I; 1918*). As explained in the previous section, this is originated from the existence of a surface energy or
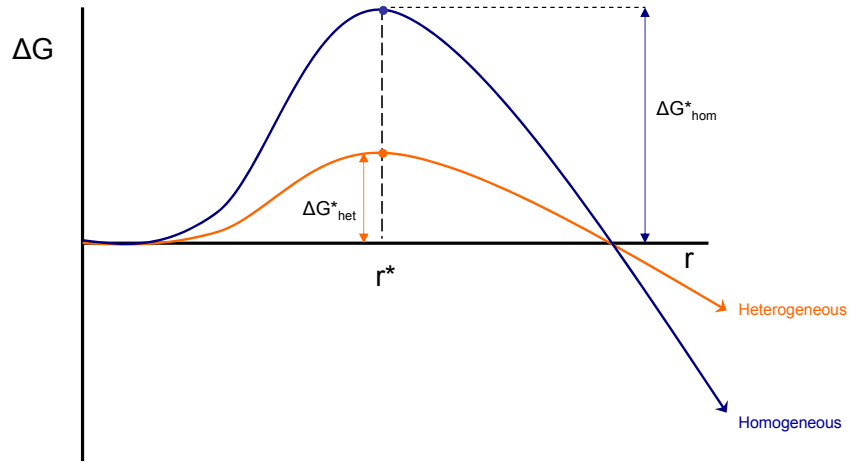
Figure 1.14: Difference in energy barriers between homogeneous and heterogeneous nucleation

surface tension. Actually, the surface tension is not the same for very thin liquid films and its bulk counterparts. It is known that when liquid droplets form on a flat substrate, they adopt spherical cap shapes with a contact angle θ. This angle depends solely on the interfacial energies as described by the Young's equation:

$$\gamma_{LS}cos\theta = \gamma_{SV} - \gamma_{SL}, \qquad (1.10)$$

where L=liquid, S=solid and V=vapor.

From the first works of Langmuir, thin water films on surfaces have been studied at very different conditions. Many efforts have been dedicated to study this phenomena in Ultra High Vacuum conditions and cryogenic temperatures (*Henderson, MA; 2002. Bruch, LW; 1995*) including metallic and non-metallic surfaces. Experiments under much conditions can provide information about the ordered structure of water or the stability of the adlayers dictated by the strength of the bonds between water molecules and water molecules and the substrate, but the water adlayers in vacuum and cryogenic

temperatures can create metastable structures that are unstable at ambient conditions. So it is difficult to know how much we can rely on the information obtained in these conditions to explain phenomena at ambient conditions.

The study of water films on surfaces at ambient conditions is much less controlled, and different techniques with submicrometer resolution have been developed. Some techniques directed to this way are, for example, SFA (Surface Forces Apparatus) (*Israelachvili, JN; 1992*) which can measure the interaction forces between two surfaces through a liquid; IR spectroscopy and ellipsometry which can measure the thickness of thin films with Å resolution, high resolution X-ray diffraction has a powerful method for studying layered structures, films and surfaces.

Depending on the technique used, the films are described by coverage, Θ, or by thickness, h. Both can be connected by the equation:

$$h = \frac{\Theta S_R}{\rho_w},\qquad\qquad(1.11)$$

where ρ_w is the density of bulk water at ambient conditions and S_R is the surface site density. Neither Θ nor h can give a satisfactory measure of thin film water (*Ewing, GE; 2006*) because no lateral distribution of the films is included in those parameters.

All these spectroscopic techniques provide a good vertical resolution (*Bardon, S; 1999*) but poor or negligible lateral resolution.

In order to understand wetting at smaller lateral scales, a lateral resolution improvement was required. The need to know how the molecules are arranged on the surface, had led to the creation of new techniques that allow the study of liquid droplets or water films with nanometer resolution. Examples of these techniques are: SPM (Scanning Probe Microscopy), and in particular, AFM (Atomic Force Microscopy) and related non-contact methods (such as SPFM (*Hu, J; 1995*)) developed to avoid the AFM's tip perturbation due to direct

contact with the liquid film in conventional methods.

But let me stop for a moment and come back. As I said previously, water is in contact with everything, and this gives rise a vast array of phenomena known as hydrophilicity and hydrophobicity, which describe the interaction between objects in aqueous media. These phenomena are crucial in biology and in material science, well known as wettability.

1.6 Wetting

The structure of water in bulk is slightly different than in a boundary or interface with other materials. Its structure in these boundaries determine their wetting properties. Now, the question that spontaneously arises is: *what is an interface?* An interface is a surface forming a common boundary among two different phases, two immiscible liquids, liquid-solid, gas-liquid, gas-solid, or solid-solid. At the interface surface, the molecules have diffenent orientations, from that in the bulk phase (*Chang, TM; 1996*).

1.6.1 The importance of wetting.

Wetting is the ability of a liquid to maintain contact with a solid surface, resulting from intermolecular interactions when both are brought together. The degree of wetting (called wettability) is determined by a force balance between adhesive force (the tendency of two different particles or surfaces to cling together) and cohesive force (tendency of similar or identical particles/surfaces to cling to one another). The phenomenon is pertinent to numerous industrial areas such as: chemical industry, glass, food, etc. But it also plays a role in life sciences: rise of sap in plants, surface tension (for example: locomotion of insects on the surface of water), wetting of the eye, etc (*Gennes, PG; 2002*).

Wetting parameters

Before starting with wetting features, one should briefly define some commonly used terms and useful thermodynamic relations.

- *Work of adhesion and cohesion in a vacuum*: the free energy changes or reversible work done to separate unit areas of two surfaces or media from contact to infinite in a vacuum (see Fig. 1.15). For two different media (media 1$\neq$ media 2), this energy is referred to the work of adhesion W_{12}, while for two identical media (media 1= media 2), is W_{11}. If 1 is a solid and 2 is a liquid, W_{12} i often denoted by W_{SL}.

- *Surface energy, surface tension*: the free energy change when the surface area of a medium is increased by unit area (γ). Now, the process of creating a unit area of surface is equivalent to separating two half-unit areas from contact (see Fig. 1.15), so that we may write:

$$\sigma_1 = \frac{1}{2}W_{11} \qquad (1.12)$$

  Is used σ_S for solids and σ_L for liquids.

- *Interfacial energy*: the minimum amount of work required to create a unit area of the interface. The magnitude of this energy is often measured through interfacial tension, and there are several techniques to measure it (such as Du Noy Ring method, Wilhelmy plate method, or Spinning drop method (*Girifalco, LA; 1957*). This tension apparently reflects the difference between the two phases. For example, the surface tension of water is 72.5 mN/m, and that of carbon tetrachloride (CCl_4) is 27 mN/m (at 298 K). The interfacial tension between water and CCl_4 is 45 mN/m, which is very close to the difference between the two surface tensions. But, on the other hand, the interfacial tension

between water and cyclohexanol is 4 mN/m, whereas the surface tension of cyclohexanol is 32 mN/m. This data indicates that the physical properties of the two liquids in the former case are quite different, but water and cyclohexanol have significant affinity for each other (*Gennes, PG; 2002*). When two immiscible liquids 1 and 2 are in contact, the free energy change in expanding their interfacial area by unit area is known as σ_{12}. The total free energy change σ_{12} is:

$$\sigma_{12} = \frac{1}{2}W_{11} + \frac{1}{2}W_{22} - W_{12} = \sigma_1 + \sigma_2 - W_{12} \qquad (1.13)$$

which is often referred to as the Dupré equation (*Israelachili, JN; 1992*). For a solid-liquid interface: $\sigma_{SL} = \sigma_S + \sigma_L - W_{SL}$.
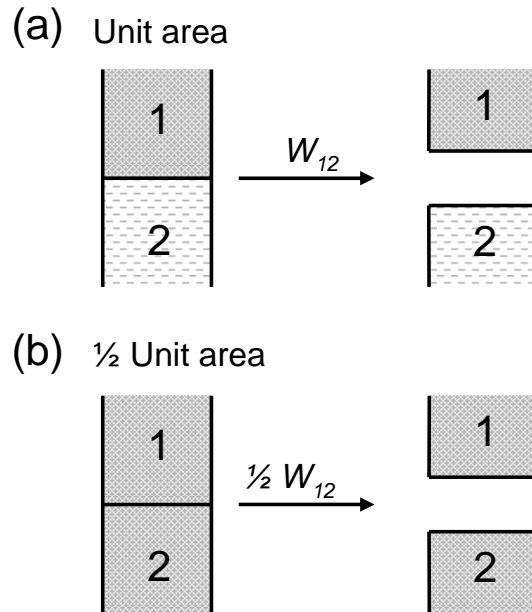

Figure 1.15: Work of adhesion (a) and cohesion (b).

1.6.2   How is wetting determined? Contact angles.

When a water drop is placed down on very clean glass, it easily spreads. By contrast, the same drop deposited on a sheet of plastic remains stuck in place. The conclusion is that there exist two regimes of wetting. The parameter that distinguishes them is the so-called *spreading parameter "S"*, which measures the difference between the *surface energy* (per unit area) of the sustrate when is dry or wet:

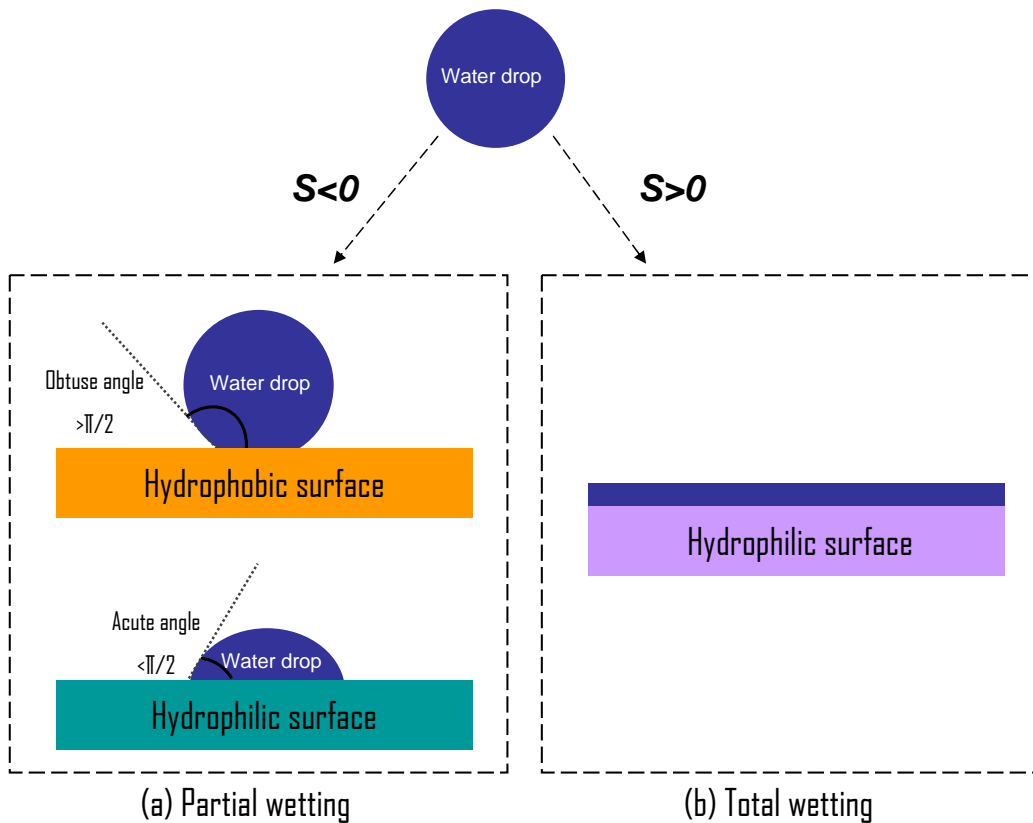$$S = \sigma_{SV} - (\sigma_{SL} + \sigma_{LV}) \tag{1.14}$$

Figure 1.16: The principal wetting regimes for drops. Partial wetting (a) shows how droplets cover partially the surface showing an obtuse angle ($>90°$) for hydrophobic surfaces and an acute angle ($<90°$) for hydrophobic surfaces. The total wetting regime (b) shows how droplets spread completely on the surface.

- When $S>0$: there is a *total wetting*. The liquid easily spreads in order to lower its surface energy, and $\theta=0$ (the angle at which the liquid-vapor interface meets the solid-liquid interface). The final outcome is a film of nanoscopic thickness.

- When $S<0$: there is a *partial wetting*. The drop does not spread but, instead, forms at equilibrium a spherical cap resting on the substrate with a contact angle θ.

A liquid is said to be "mostly wetting" when $\theta \leq \pi/2$ (90°), indicating that wetting of the surface is very favourable, and the fluid will spread over a large area of the surface. It is said that a liquid is "mostly non-wetting" when $\theta > \pi/2$. High contact angle generally means that wetting of the surface is unfavourable, so the fluid will minimize contact with the surface and form a compact liquid droplet. Thus, the contact angle provides an inverse measure of wettability (*Shafrin, EG; 1960*).

There are several methods for measuring the θ. For relatively large angles, it is possible to take a side-view photograph of the profile and use the snapshot to determine the angle. For better precision and for angles less than $\pi/4$ (45°), an optical reflection technique is often used. In Fig. 1.17 one can see a simple experimental setup to calculate the contact angle and a specific contact angle of a liquid sample onto a solid substrate. A brief contact angle and wettability summary is shown in Fig. 1.18.

For water, a wettable surface may also be termed **hydrophilic** and a non-wettable surface **hydrophobic**. Superhydrophobic surfaces have contact angles greater than 150°, showing almost no contact between the liquid drop and the surface. This is sometimes referred to as the "lotus effect". Figure 1.18 describes varying contact angles and the corresponding solid/liquid and liquid/liquid interactions (*Eustathopoulos, N; 1999*). For non-water liquids, the term lyophilic is used for low contact angle conditions and lyophobic is
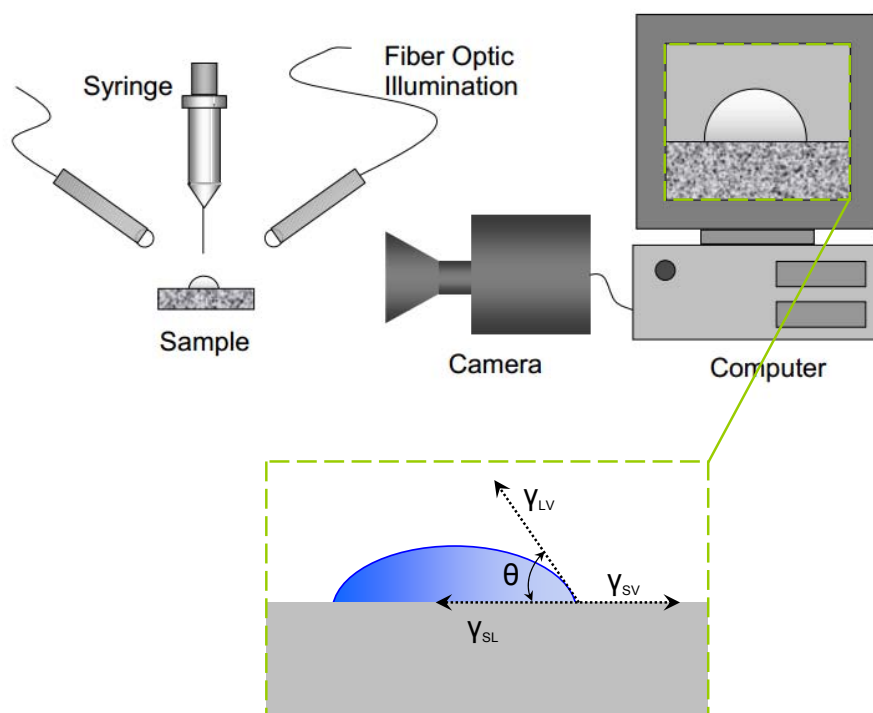
Figure 1.17: Experimental setup for a contact angle measurement.

used for higher contact angles.

Contact angle	Degree of wetting	Strength of:	
		Solid/liquid interactions	Liquid/liquid interactions
Θ=0	Perfect wetting	Strong	Weak
0<Θ<90º	High wettability	Strong	Strong
		Weak	Weak
90º≤Θ<180º	Low wettability	Weak	Strong
Θ=180º	Perfectly non-wetting	Weak	Strong

Figure 1.18: Table of different wettabilities depending of its contact angles.

There are a lot of different surfaces: ideal solid surfaces (flat, rigid, perfectly smooth, and chemically homogeneous), but there are also non-ideal rough solid surfaces (do not have perfect smoothness, rigidity or chemical homogeneity). One interesting example of a non-ideal surface is the lotus petal, an excellent superhydrophobic surface.

The lotus petal has a randomly rough surface and high contact angle, which means that the water droplet is not able to wet the microstructure spaces between the spikes. This allows air to remain inside the texture, causing a heterogeneous surface composed of both air and solid. As a result, the adhesive force between the water and the solid surface is extremely low, allowing the water to roll off easily (*Marmur, A; 2004*). On the other hand, the rose petal is another special example, that its micro and nanostructures are larger in scale than the lotus leaf, which allows the liquid film to impregnate the texture. Since the liquid can wet the larger scale grooves, the adhesive force between water and solid is very high.

1.7   From words to action

After the brief introduction about the water molecule, I can proceed introducing the subjects developed in this thesis.

The first part of this thesis is focused in the study of water adsorption on two types of inorganic surfaces: BaF_2 and CaF_2. The interest of BaF_2 relies on its hexagonal geometry as in ice I_h, and the surface interactomic distances, which is really similar to the distance between water molecules in the basal plane of ice I_h. By contrast, although CaF_2 is isostructural to BaF_2, the interatomic distances are shorter compared to ice I_h.

In order to visualise the water adsorption on BaF_2 and CaF_2 an Atomic Force Microscopy (explained in detail in section 2.1) has been used, because it allows to follow the process in detail with a good resolution. From this study three articles have been published.

In the second part of this thesis graphene occupies our attention. Few years ago, this carbon compound created a great expectative because of its exceptional electronic properties. From an earlier publication, was demonstrated that water adsorbes on graphene surface, and this is especially relevant because graphene is a hydrophobic surface. Our goal with graphene was to visualise the adsorbed water and how it spread through the surface. To perform this work the use of the AFM and the non-contact mode SPFM is needed. Two additional publications have been published.

The last part of this thesis and currently in progress, our attention is foccused on creating a home-made surface. Many workers have investigated a wide number of natural surfaces and particles, trying to find an ideal surface capable of nucleate water molecules on its surfaces. After our studies with BaF_2 and CaF_2, we decided to create a surface capable to adsorbe freezing water on its surface. Therefore, we looked forward a surface with its atoms placed geometrically as the basal plane of hexagonal ice I_h with a lattice

constant similar to the ice I$_h$.

To address this issue, self-assembly monolayers of aliphatic alcohols onto graphite surfaces are selected. Graphite is a hydrophobic surface and this means that aliphatic alcohols will tend to organize with the alcohols pointing upward. This is the first time that Langmuir-Blodgett film with a hydrophobic surface are attempted. The preparation of these surfaces carries certain challenges and problems such as the complication to form the film onto a hydrophobic surface, because of the weak interactions involed, explained in chapter 5.

Chapter 2

Experimental

In this chapter the main instrumental techniques used in the present thesis will be described. First of all, the general characteristics of the *Atomic Force Microscopy* technique are summarized, and a description of the different elements of the systems and modes are explained. The last section (2.2) of this chapter is denoted to the Langmuir-Blodgett technique, used to prepare thin films on a specific substrate.

2.1 Atomic Force Microscopy

2.1.1 A versatile tool

The term Scanning Probe Microscopy (SPM) covers a broad group of instruments used to image, modify and measure different surface properties of different material. The two primary forms of SPM are Scanning Tunneling Microscopy (STM) and Atomic Force Microscopy (AFM). STM was first developed at IBM in Zurich by Binnig, *et. al.* (*Binnig, G; 1982*) which had revolutionized the world of microscopes. Its working principle is based on the tunneling current between two very close conductive samples. This current is used to create a topography image because it depends exponentially

on the distace between electrodes. STM is limited only for good electrical conductors. In 1986 Binnig, Quate and Gerber developed the AFM which opened the door to imaging atomic scale features on a wide range of insulating surfaces as ceramic materials, biological samples and polymers (*Binnig, G; 1986*). For its qualities AFM is perhaps the most versatile member of the SPM family, which can be applied to various environments (air, liquid and vacuum) and provides a number of advantages over conventional microscopy techniques. AFM makes measurements in three dimensions, x, y and z with a good x-y resolutions (from 0,1 to 1,0 nm) and in z direction (0,01 nm) as well.

2.1.2   How it works?

As the name of AFM suggests, this type of microscope detects the interactive forces of van der Waals, electrostatic and capillary nature between the sample and a sharp tip.

The tip is attached to the free end of a cantilever and is brought manually close to the sample surface, and then the scanner makes a final adjustment in tip-sample distance based on a setpoint determined by the user. Attractive or repulsive forces resulting from interactions between the tip and the surface causing a positive or negative bending of the cantilever.

When the tip is in contact with the sample surface, and the laser beam is aimed at the back of the cantilever, the sample is scanned across under the action of a piezoelectric, either by moving the sample or the tip relative to the other. The photodiode detects the small cantilever deflections coming from the deviations of this laser. A feedback loop maintains constant tip-sample separation by moving the scanner in the z direction to maintain the setpoint deflection. Without this feedback loop, the tip would crash into a sample with even small topographic features. If we maintain the tip-sample sepa-

ration constant, we can calculate the force between the tip and the sample. Then, the scanner movement in z direction is used to generate a topographic image of the sample surface.
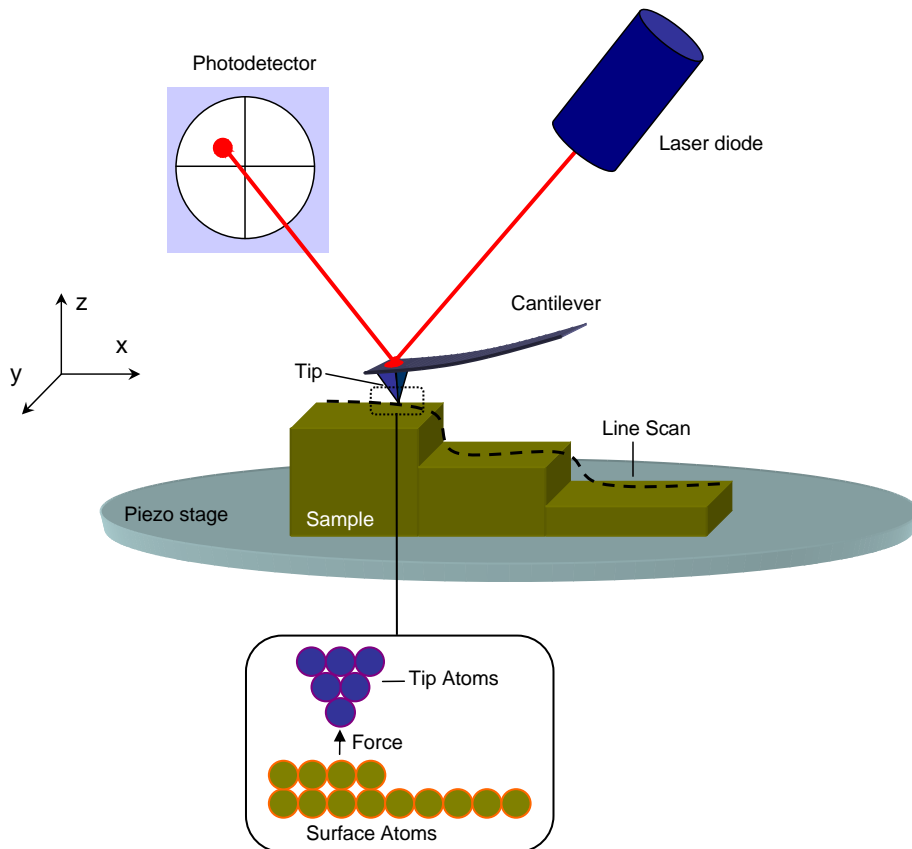

Figure 2.1: Schematics of an AFM. The probe scans the sample surface, which is generally mounted on the piezo stage, in the X and Y directions. The laser beam impacts to the end back of the cantilever and reflects then on the photodetector. The deflection of cantilever is maintained constant, and the piezo stage moves up and down so as to keep track of the sample roughness.

The main difference between the other types of microscopies and the AFM is, as mentioned above, interactive forces between the sample and the tip. The interactions most commonly associated with AFM are van der Waals, elec-

trostatic and capillarity forces. To understand the different AFM operation
modes, it is useful to analyze a *cantilever deflection vs. piezo displacement*
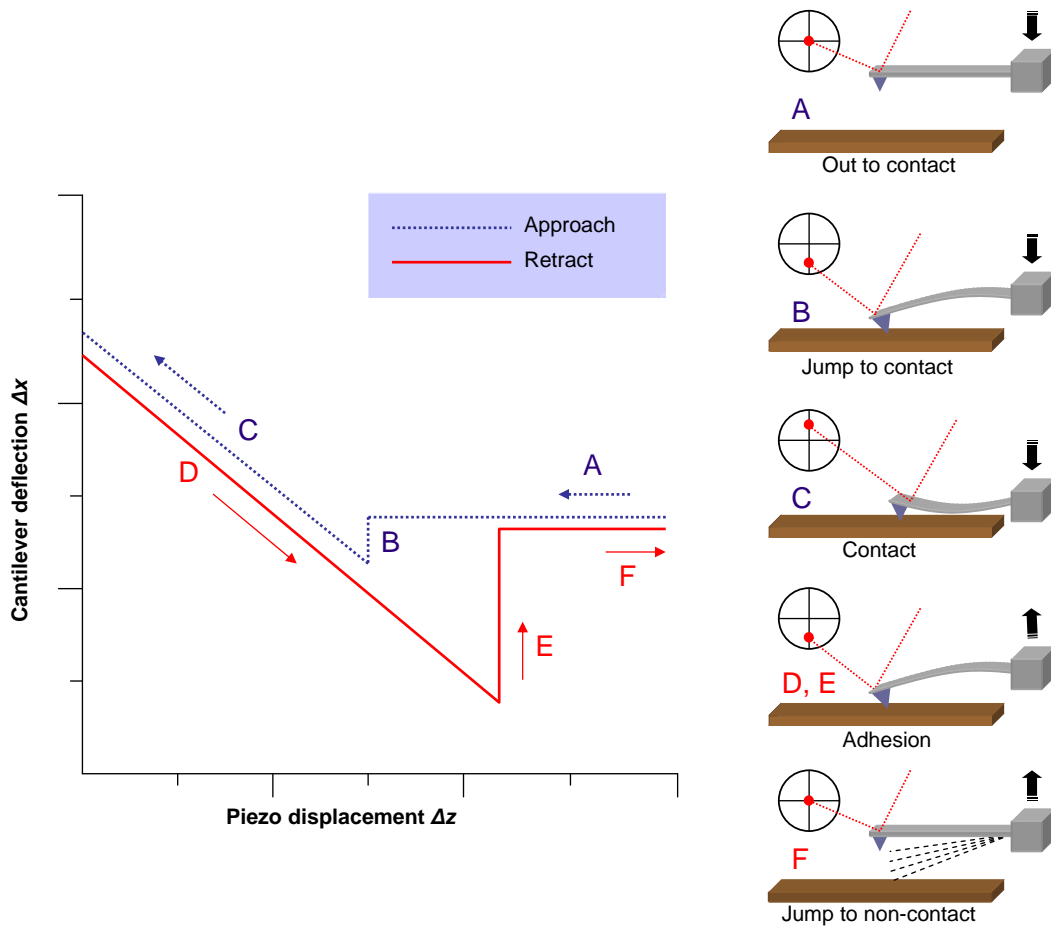(Δx *vs.* Δz) curve.

Figure 2.2: Experimental force vs. distance curve performed with an AFM that shows the different
contact regimes that the tip experienced when the distance between the tip and the sample changes.

As shown in figure 2.2 when the tip and the sample are so far from each
other, no interaction exists between the cantilever and the sample, and the
cantilever deflection (Δx) is nonexistent (2.2, A). As the distance between
the two bodies decreases (of the order of tens to hundreds of angstroms),
van der Waals, electrostatic and capillarity forces appear, and the cantilever,

attracted by the sample, bends down causing a $\Delta x \neq 0$ (2.2, B). As the tip goes down (less than a few angstroms (10^{-10} m), the repulsive interaction between the atoms of the tip and the sample becomes dominant and the cantilever bends upwards. It is considered real contact (2.2, C).

2.1.3 The main parts of AFM

The probe

The probe is a micro-fabricated cantilever with a sharp tip placed on the end, which "gently" touches the surface and records the small force between the probe and the surface. Cantilevers typically range from 50-200 μm in length, 10 to 40 μm in width and has an initial radius *(R)* that ranges from 5 to 30 nm (*Albrecht, TR; 1988*).

Each probe has different specifications and shape. There are two main cantilever shapes (see figure 2.3):

- *Triangular geometry (or V-shaped)*: this type of geometry provides a low mechanical resistance to vertical deflection, and high resistance to lateral torsion. Usually are made by silicon nitride (Si_3N_4) and its wide platform allow focusing the laser easily. Due to the transparency of silicon nitride to visible light, the cantilevers are usually covered with an Au layer to improve the amount of laser light reflected on the end of the cantilever. The adherence of the reflective layer can be improved depositing a Cr layer before the Au layer. These cantilevers are normally used for Lateral Force Microscopy (LFM) and for liquid operation.

- *Rectangular geometry*: easier to fabricate respect to the V-shaped probes. These type of cantilevers are usually made of silicon, and are available

with different coatings like Platinum, Platinum-Iridium ($PtIr_5$), Magnetic, Diamond or Gold depending on the surface of work. They are suitable for Lateral Force Microscopy (LFM) in air as well.
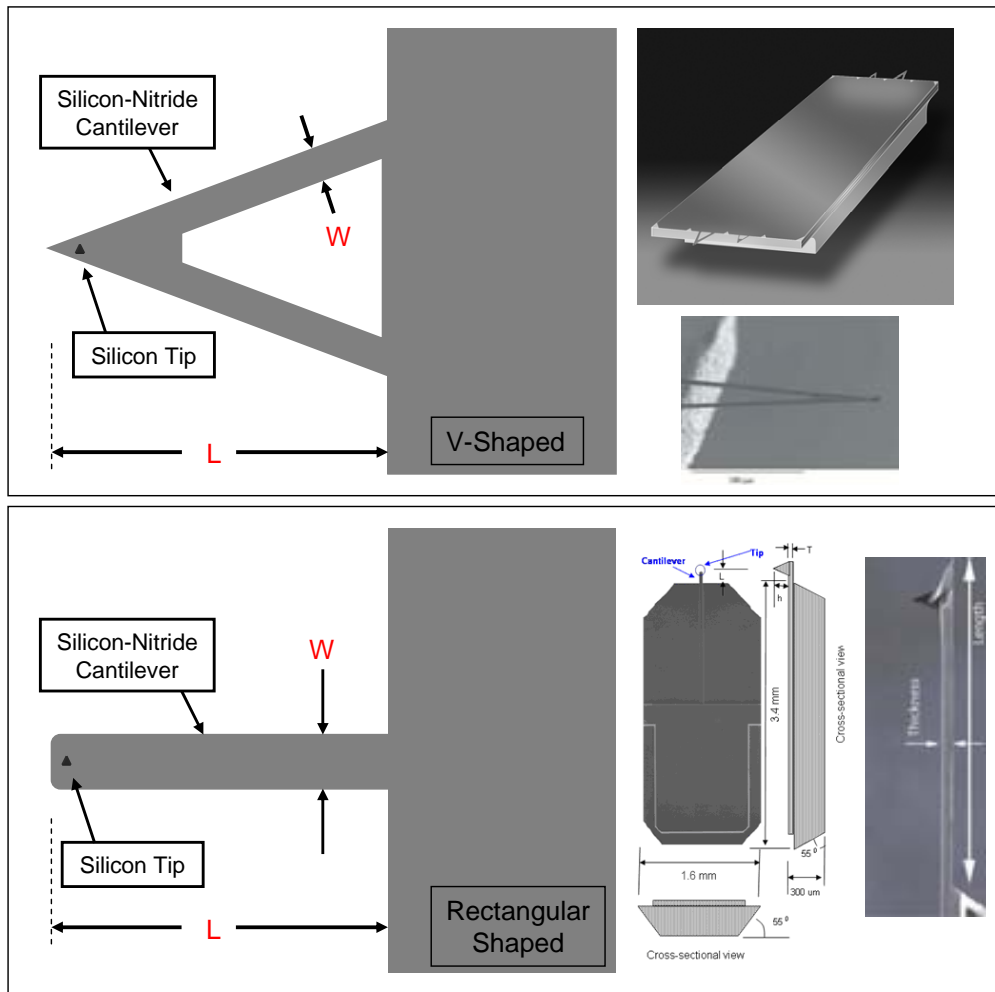

Figure 2.3: Scheme of a triangular and rectangular cantilevers and tips shape indicating their sizes.

Depending on the sample topography, however there are limitations in achieving atomic resolution. The physical probe used in AFM imaging has not an ideally sharp. As a consequence, an AFM image does not reflect exactly the true sample topography. Because of this, the ratio between the

total tip length and its central width is an important parameter. For an accurate measure of topography is necessary the use of high aspect ratio tip, but if we have a flat surface with a low aspect ratio tip is enough. Depending on the application a lot of specific tip shapes can be fabricated.
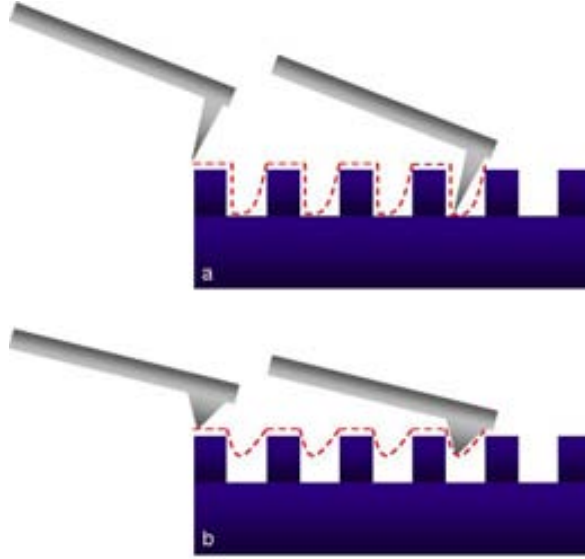

Figure 2.4: a) Scheme of a thin tip which can profile better the topography of this sample. b)Scheme of a thick tip which scans with low resolution the topography of this sample.

The cantilever is modeled as a spring in order to calculate the value of F_v exerted by the tip on the sample. If we think the cantilever as a spring, then the cantilever has an Elastic Vertical Constant (κ_v) which depends on the geometry and composition of the probe. The amount of force between the probe and sample is dependant on the spring constant of the cantilever and the distance between the probe and the sample surface. This force can be described using the *Hooke's Law* (*Ugural, AC; 2003*):

$$F_v = -\kappa_v \chi \tag{2.1}$$

where, F_v= Force, κ_v = spring constant, and χ = cantilever deflection.
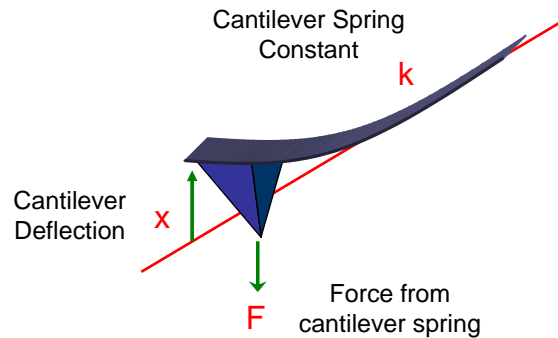
Figure 2.5: Schematic image of a tip acting as a spring and the forces involved.

Detectors

In order to detect the cantilever deflection, is normally used a laser beam. To detect the displacement of the cantilever, the laser must be positioned in the back-plated surface of the cantilever, and the laser reflection caused is collected by a photodiode. When the scan is running, the tip deflects due to the topography of the sample and this movement is detected as a displacement of the laser spot by the photodiode, and it is converted into an electric signal (*McClelland, GM; 1987*). There are different photodiodes. The simplest one has only two segments, and it can detect vertical information about the tip deflection. If the diode is divided into four parts, as seen in figure 2.6, lateral deflection can also be sensed, and LFM measurements are allowed. The signal received by the detector is sent to the feedback electronics, which maintains a constant deflection (*Meyer, G; 1990*).

Piezoelectric scanners

The piezoelectric scanner, also called piezo or piezodrive is made form piezo-electric materials, which expands and contracts proportionally to an applied
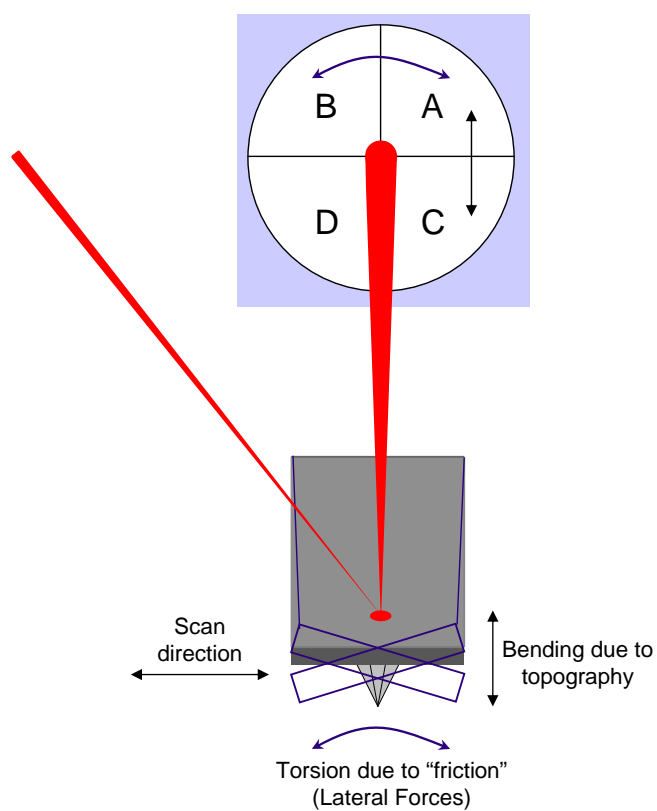
Figure 2.6: The scanned cantilever/tip system.

voltage. Whether they elongate or contract depends upon the polarity of the voltage applied.
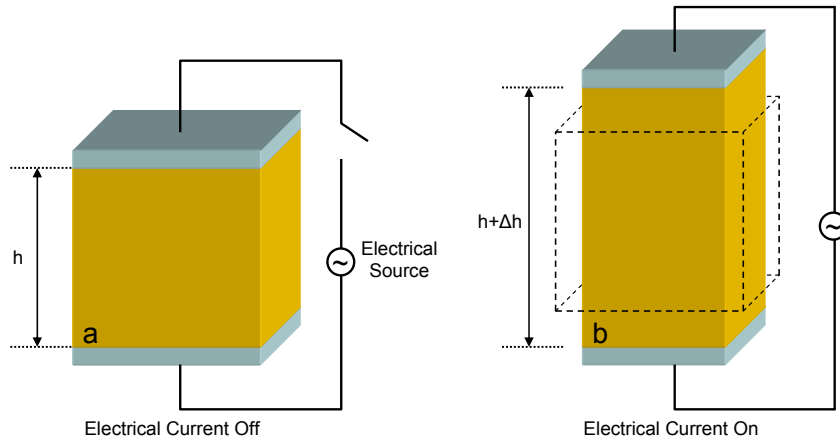

Figure 2.7: Elementary piezoelectric cube model. a) Null electric field,no mechanical deformation is produced; b) after polarized, the cube stretches by a small amount due to the piezoelectric effect and the total height is increased (h+Δh).

The piezoelectric effect was discovered by Pierre Curie and Jacques Curie in 1880, about 100 years before the invention of the STM. They observed that by applying a weight to generate vertical tension, an electrical charge was detected by an electrometer. A few months later, Lippman (*Lippman; 1881*) predicted the existence of the inverse piezoelectric effect: by applying a voltage on the quartz plate, a deformation should be observed. This effect was soon confirmed by the Curie brothers (*Curie and Curie; 1882*), who designed a clever experiment to measure the tiny displacement.

The deformation explained by Curie and Curie occurs in the three directions (x, y and z), and in the standard convention, the directions x, y, and z are labeled as 1, 2, and 3, respectively. As a result, a strain is generated. The measurement of the strain in a given direction (for x direction, S would be S_1) is defined as the ratio between the elongation or contraction (δx) when applaying a given voltage, and the initial length (x) in absence of this external

voltage:

$$S_1 = \frac{\delta x}{x} \tag{2.2}$$

,

and the zz strain component is:

$$S_3 = \frac{\delta z}{z} \tag{2.3}$$

The piezoelectric coefficients d_{ij} are defined as the ratios of the strain components over a component of the applied electrical field intensity, for example,

$$d_{31} = \frac{S_1}{E_3} \tag{2.4}$$

,

and

$$d_{33} = \frac{S_3}{E_3} \tag{2.5}$$

,

where E is the electrical field intensity.

Because strain is a dimensionless quantity, the piezoelectric coefficients have dimensions of m/V in SI units. Their values are extremely small. In the literature, the unit 10^{-12}m/V is commonly used. For applications in STM and AFM, a natural unit is Å/V or 10^{-10} m/V. Typical SPMs scanners can scan laterally from tens of angstroms to over 100 microns. In the vertical direction, SPM scanners can distinguish height variations from the sub-angstrom range to about 10 microns. Their compactness, and their high-speed response made them a critical elements in SPM techniques.

2.1.4   AFM Operation Modes

Contact Mode

One of the most exciting results from AFM has been the discovery that atomic resolution can be achieved when the tip is scanning a surface (*Binnig, G; 1987*).

In contact AFM, the tip and the sample are in perpetual contact. At the right side of the curve in figure 2.8, the tip and sample are separated. When the tip and the sample are gradually brought together, its atoms begin to weakly attract each other. This attraction increases until the atoms are so close together, where the electron clouds begin to repel each other. This electrostatic repulsion progressively inceases while the attractive force decreases because of the tip-sample separation. Contact AFM offers the best topographic resolution because the tip is truly tracking the surface profile (Fig. 2.9). This mode is adequate to scan hard materials because it can cause damages to soft samples due to the high perturbation of the tip with the sample.

In addition to the repulsive force, the capillary force exerted by the thin liquid layer is generally present during contact AFM imaging. This attractive force tends to hold the tip in contact with the surface.

Amplitude Modulation (AM-AFM) Mode

In this mode the cantilever is oscillated in its own resonance frequency through a small piezoelectric mounted on the cantilever holder. When the distance between the tip and the sample decreases, the vibration amplitude is reduced due the interactions between tip-surface. In this case, the feedback loop uses the vibration amplitude as the reference signal to maintain a constant distance from the surface (*García,R and Pérez, R; 2002*). It is necessary to point that AM-AFM mode is not a real non-contact because the probe lightly taps on
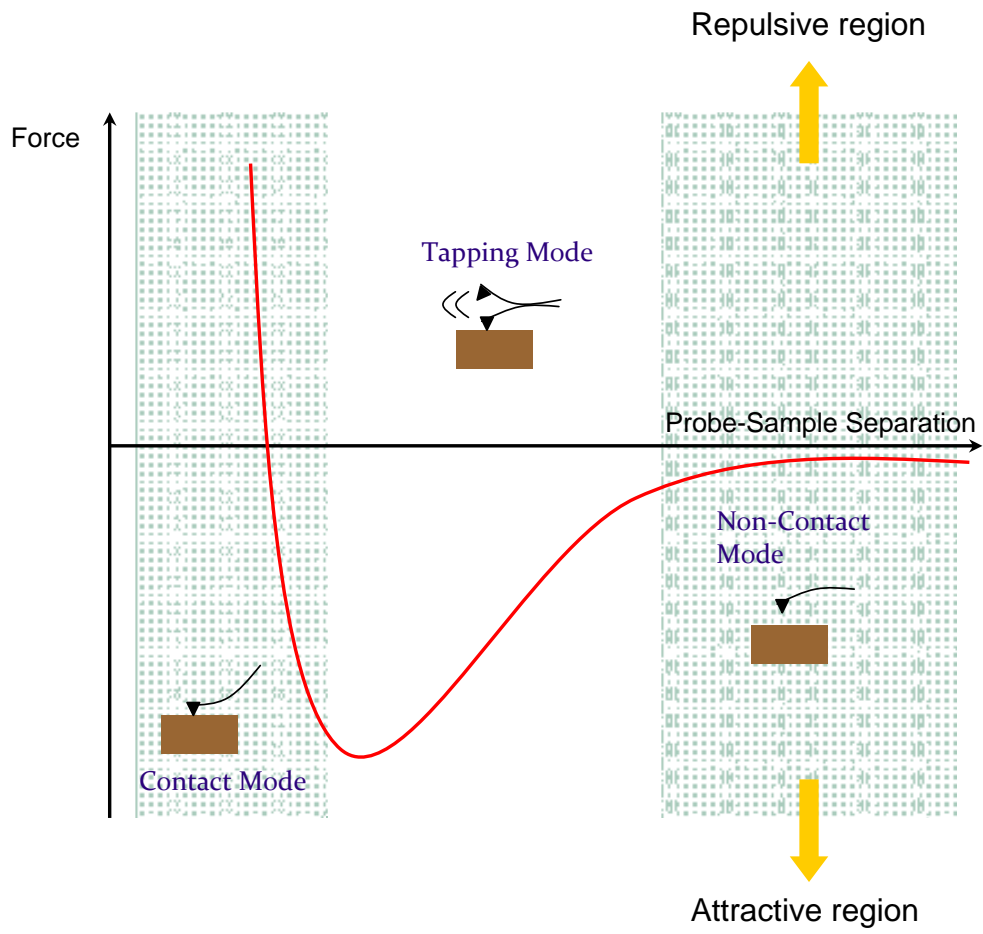
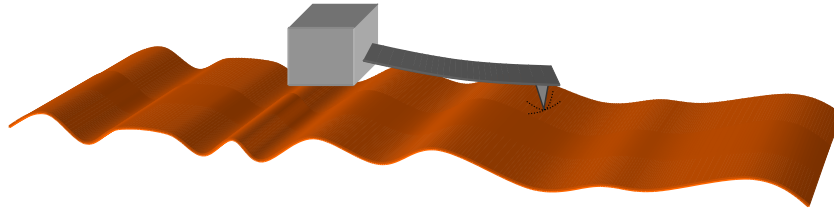Figure 2.8: Potential energy diagram of a probe and sample.

Figure 2.9: Contact mode AFM. The tip and the sample are always in contact, allowing scanning hard samples with very high resolution. The main features of the contact tips used are: cantilevers available as a long (450 μm) or short (225 μm). Length: Typically 225 - 450 μm . Width: Typically 28-40 μm. Thickness: 1- 2 μm. Resonant Freq: 12 - 28 KHz. Spring Constant: 0.1 - 0.2 N/m.

the sample surface during scanning, and jumps from non-contact to contact regimes (see figure 2.10).

Due the distance between the tip and the sample and the weaker interaction, this mode has a poorer resolution than the contact mode. Nevertheless, it allows a high resolution of samples that are easily damaged and/or loosely held to a surface. Is an ideal mode for biological and soft samples. Also, AM-AFM shows almost no lateral forces.

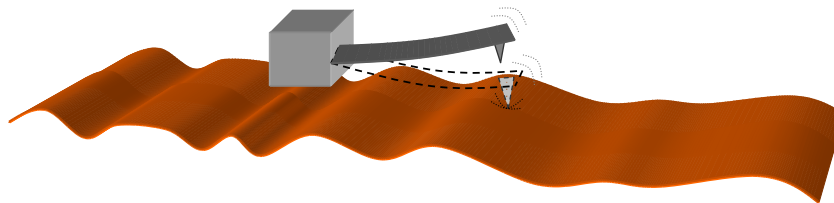Figure 2.10: AM-AFM mode or so-called dynamic mode or tapping mode AFM. The tip is intermittently in contact with the sample, allowing a lower damage in soft samples. Some features of AM-AFM tips are: Available cantilevers as a long (225 μm) or short (125 μm). Length: Typically 125 - 225 μm. Width: Typically 40 μm. Thickness: 4 - 8 μm. Resonant Freq: 190 - 300 KHz. Spring Constant: 40 - 48 N/m

Kelvin Probe Force Microscopy

Kelvin Probe Force Microscopy (KPFM) or Surface Potential Microscopy, was introduced as a tool to measure the local contact difference between a conducting atomic force microscopy (AFM) tip and the sample, in other words, measuring the potential difference between two materials (the probe and the sample) obtaining information about charges and dipoles distribution at the surface. Since its first introduction by Nonnenmacher *et al.* in 1991 (*Nonnenmacher, M; O'Boyle, MP; and Wickramasinghe, HK; 1991*), KPFM has been used extensively as a unique method to characterize the nano-scale electronic/electrical properties of metal/semiconductor surfaces and semiconductor devides. Recently, KPFM has also been used to study the electrical properties of organic materials/devices and biological materials (*Melitz, W; et al.; 2011*).

The band gap between the vacuum and the Fermi level, namely the work function ϕ, differs from one material to another. The difference between the work function of the tip and the work function of the sample is what we call the CPD:

$$CPD = \phi_{sample} - \phi_{tip} \tag{2.6}$$

Kelvin mode is based on a two-steps technique. In the first step the topography is acquired using standard AM-AFM mode (mechanical excitation of the cantilever). In the second step this topography is retraced at a set lift height from the sample surface to detect the electric surface potential ϕ. During this second pass the cantilever is no longer excited mechanically but electrically by applying to the tip the voltage V_{tip} containing dc and ac components:

$$V_{tip} = V_{dc} + V_{ac}sin(\omega t) \tag{2.7}$$

Where V_{dc} and V_{ac} correspond to the *dc* and *ac* voltages respectively and ω is the *oscillation frequency*. Assuming parallel-plate capacitor geometry for the tip-sample system the force sensed by the tip can be expressed by:

$$F = -\frac{1}{2}\frac{\partial C}{\partial z}(V_{tip} - \phi)^2 \tag{2.8}$$

Where C and F stand for the *system capacitance* and *local contact potential difference* between the tip and the surface, respectively, and z corresponds the *direction perpendicular to the surface*. Expanding equation 3.4 using equation 2.7, the following expressions for the *w* and *2w* components are obtained:

$$F_\omega = -\frac{\partial C}{\partial z}[(V_{dc} - \phi)V_{ac}\sin(\omega t)] \tag{2.9}$$

$$F_{2\omega} = \frac{1}{4}\frac{\partial C}{\partial z}[(V_{ac}^2\cos(2\omega t)] \tag{2.10}$$

Eq. 3.5 is called the ω component signal and is the key function to understand KPFM. If V_{dc} is equal to $\phi_{sample} - \phi_{tip}$, the value of ω component signal becomes zero. Therefore, we can obtain the intended potential by adjusting dc offset bias V_{dc} to null the ω component signal. If dc/dz is kept constant by keeping constant the tip-sample separation, the ω component is only sensitive to static charges and static dipoles.

In Fig. 2.11 is shown a schematic example of KPFM imaging, where topography and kelvin profiles are given.

A variation mode of KPFM used in this work is Scanning Polarization Force Microscopy (SPFM), which allow us scan in real non contact will be explained in detail in the next section 2.1.4.

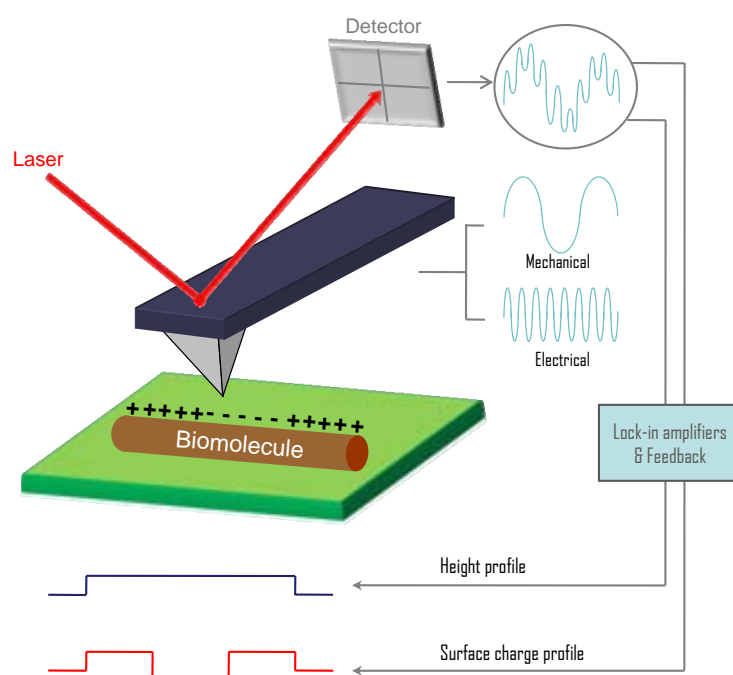Figure 2.11: KPFM can measure surface charges by contactless recording of the electrostatic force between a conductive AFM tip and a biomolecule on a support. If topography and kelvin profiles are compared, one can note that topography profile follows the relief of the molecule giving us information about the size of the molecue, while kelvin provides us information about the location of charges on the molecule surface.

Scanning Polarization Force Microscopy

Different noncontact AFM methods have been used to study liquid films and droplets in order to avoid the perturbations due the tip-sample contact with contact and amplitude modulation (AM-AFM) modes, explained before (2.1.4).

While AM-AFM eliminates the friction and dragging effects that occurs in contact mode, the brief interaction between tip and liquid surface can still result in perturbations that need to be considered. Scanning Polarization Force Microscopy (SPFM), developed in 1994 in Salmeron's group from *Lawrence Berkley National Laboratory* (*Hu, J; 1995*), overcomes many of these problems and provides, in addition to surface topography, information of other surface properties, such as local variations in the surface potential and ionic mobility (*Salmeron, M; 2000*).

SPFM uses the same technology as the AFM, which is based on sensing the force between sharp tips and the surface, the use of piezoelectric scanners and feedback control electronics as well. SPFM is based on electrostatic forces between the tip and the surface and can be applied to both conductive and nonconductive substrates. A bias voltage (*DC*, direct current, or *AC*, alternating current) is applied to the cantilever on the order of few volts (Si_3N_4 levers and other insulating levers can be made conductive by coating them with a thin metal film as Platinum (100 Å)). The opposite charges generated at the tip and surface cause their mutual attraction and this bends the lever toward the surface. Because electrostatic forces have a long range, they provide a means of imaging at distances of several nanometers. The large distance between the tip and the sample results in a lower spatial resolution and this represents a disadvantage. But in the other side, the large tip to sample distance makes possible to reduce the perturbation of the liquid surface to a negligible value. The resolution is on the same order as the tip-surface sepa-

ration, a few hundred Ångstroms when the applied bias is on the order of a few volts; this produces an attractive force in the nanometer range. This is much better than the typical optical resolution of several micrometers. The principle of operation is shown in figure 2.12 (*Salmeron, M; 1997*).
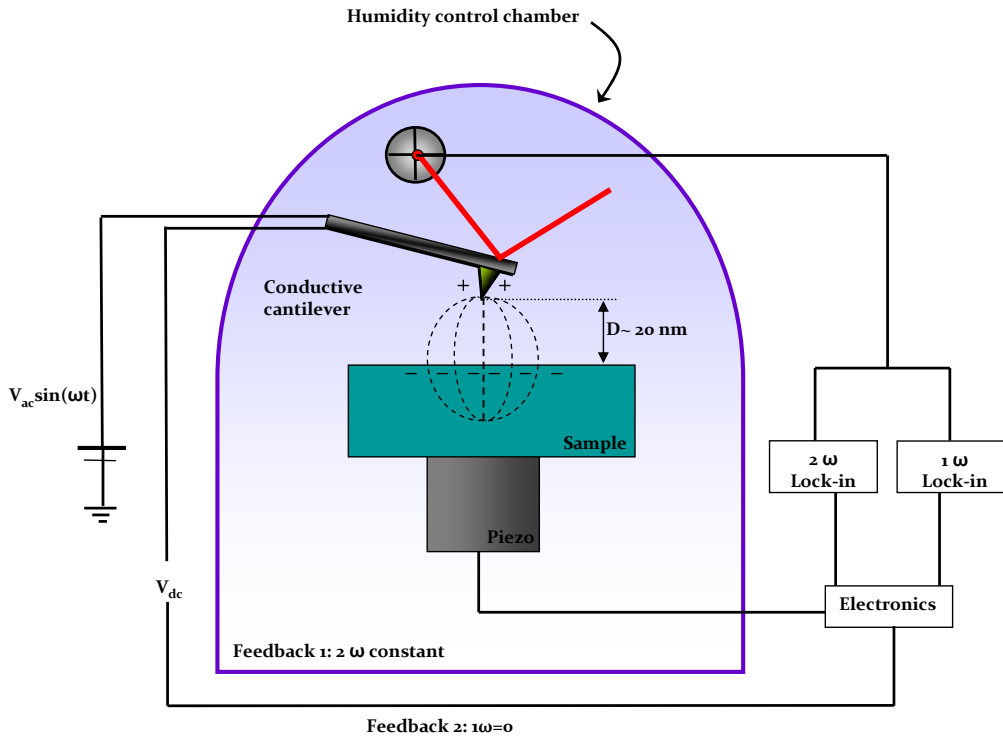

Figure 2.12: Scheme of the principle of operation of SPFM. A voltage of a few volts is applied to a conductive cantilever and the tip of the atomic force microscope. Induced charges at the tip and surface create attractive electrostatic forces that bend the tip toward the surface. An ac voltage, $V = V_{dc} + V_{ac}sin(\omega t)$, is applied to the metallic tip. Using a lock-in amplifiers, the second and first harmonics of the modulation frequency are measured separately in the electrostatic force. To separate the contributions of topography and the contact potential distribution at the surface, two feedback loops are used. The first one maintains the contact amplitude of $F(2\omega)$ by adjusting the tip-sample distance. The second adjusts the applied V_{dc} bias so that $F(\omega)$ is zero, as in the Kelvin Probe method.

SPFM is a very useful to study liquid droplets and films because it allows us to study the surface without no direct contact between the tip and the sample. A tip is brought about 10-20 nm above the sample surface and is then electrically biased, leading attractive electrostatic forces between the

two bodies (tip and polarisable surface). The external voltage applied to the tip is of the form shown in Eq.

During imaging, the attractive force (lever deflection) is kept constant by the feedback control electronics, and a constant force image is obtained. Two lock-in amplifiers are used to measure the $F(\omega)$ and $F(2\omega)$ forces experienced by the tip at the first and second harmonics, respectively.

The second harmonic term is used for feed back control. Controlling the z piezo displacement, a feedback loop maintains the amplitude of the 2ω component of the lever oscillation constant. In DC mode images, $F(2\omega)$ term, contains information on the polarizability (dielectric constant) and topography. If the polarizability of the sample increases, this change in the surface is shown in the SPFM images as a change in apparent height due to the piezo retraction to compensate the increase of the electrostatic interaction between the tip and the surface (*Schönenberger, C; 1990*).

On the other hand, the contact potential contribution to the electrostatic force can be determined from the first harmonic of the lever oscillation ($F(\omega)$). In other words, the first harmonic term is proportional to the tip-sample contact potential difference. A second feedback loop adjusts V_{dc} to null the $F(\omega)$ component, which providing a direct measurement of the tip-surface contact potential difference as for the KPFM technique.

The tip and the lever can be approximated by a sphere of radius R (the tip apex) separated by a distance z from the surface, and a flat parallel condenser plate at a distance $z+D$, representing the lever, as schemically represented in figure 2.14 (*Frantz, P; 1996*).

Wetting at small scales is important in many applications, which gives rise at localized regions of the surface. For this reason there is a need for techniques that allow the study of liquid droplets or films with nanometer resolution.
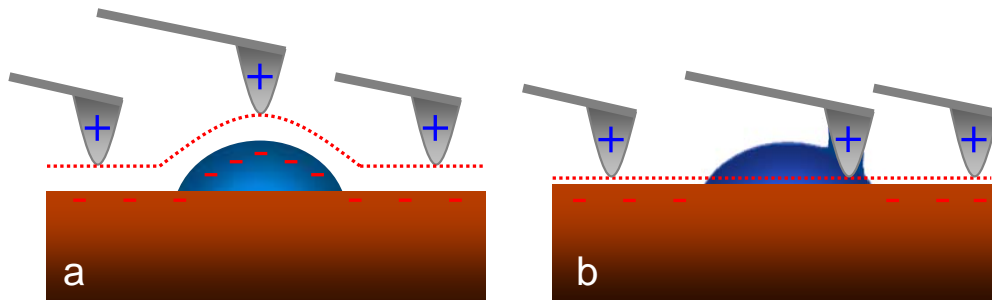
Figure 2.13: Scheme of the behavior of the tip on a covered surface by water droplets. a) SPFM mode. b) Contact or Tapping mode.
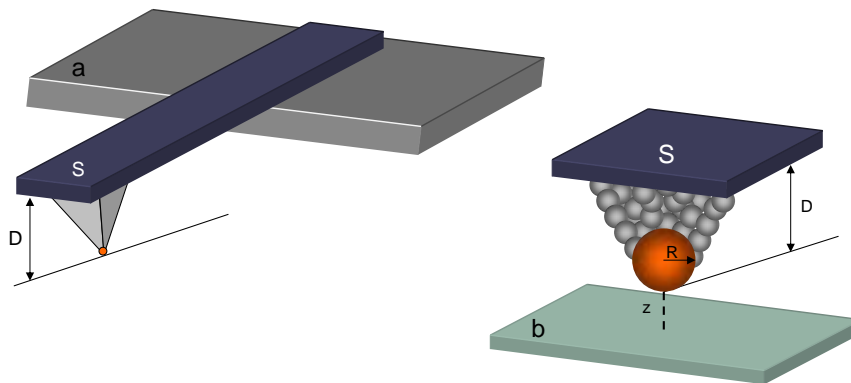

Figure 2.14: Model for the calculation of electrostatic forces. (a) the tip-lever system (b) the tip is approximated by a sphere of radius equal to the apex tip radius R and flat plate of area S equal to that of the support lever.

Many experimental methods have been developed to study wetting phenomena. It is possible to measure the spreading and the contact angle of the droplets deposited on the surface at micrometer level with an optical microscopy. But the study of disjoining pressure effects needs sub-micrometer level techniques, for this reason, this is a need of nanometric resolution instruments.

Other Operation Modes

Exist a large number of AFM modes that allow measure a wide range of properties. Some of them are: Torsional Resonance Mode (TRmode) AFM, Lateral Force Microscopy, Phase Imaging, Magnetic Force Microscopy, Conductive AFM, Tunneling AFM, Electric Force Microscopy, Surface Potential Imaging, Force Modulation Imaging, Scanning Capacitance Microscopy, Scanning Spreading Resistance Microscopy (SSRM), Scanning Thermal Microscopy, etc.

2.2   Langmuir-Blodgett Technique

A Langmuir-Blodgett film consists of a monolayer of an organic material created at the liquid-gas interface and transferred onto a solid substrat. Monolayers are composed by amphiphilic molecules with a hydrophilic head and a hydrophobic tail, and are assembled vertically (see figure 2.15).

2.2.1   Brief History

The whole issue began at 1770 with *Benjamin Franklin*, who was one of the first scientists to describe and attempt to quantify the spreading of monolayer films on a liquid surface, when he threw a spoontea of oil onto a small lake to form a surface of defined area approximately half an acre. He didn't think
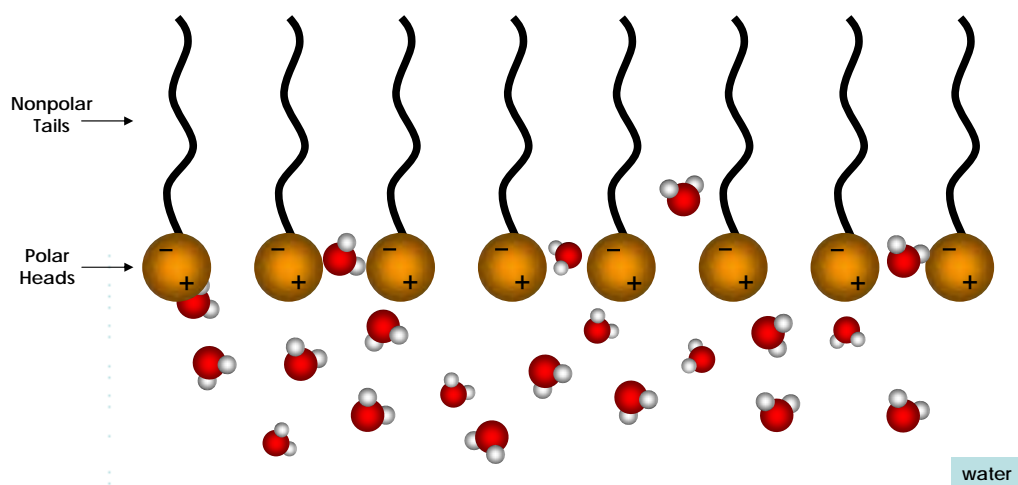
Figure 2.15: Amphiphilic molecules arranged on an air-water interface.

that the oil formed on the lake surface was a monolayer . Franklin suggested that the spreading was based in the repulsive forces between oil molecules (*Franklin, B; 1773*). It was not until a century later, when *Lord Rayleigh* quantified what *Benjamin Franklin* had seen at a pond and suggested that the spreading of oil on water resulted in a monolayer of oil molecules (*Rayleigh, FRS; 1890*), and quantified it as 1,6 nm thick, knowing the oil volume and the area of coverage of that oil. With the help of *Agnes Pockels*, a German woman and independent scientist, who described an apparatus designed to measure the surface tension of monolayers of hydrophobic and amphiphilic substances. They showed that the area of films can be controlled with barriers (*Pockels, A; 1891* and *Pockels, A; 1892*). She added that surface tension varies with contamination of water. With this new device Langmuir showed that amphiphilic films are truly monolayers, and these monolayers are oriented on the surface such that the "active or most hydrophilic portion of the surface molecules are in contact with the liquid below whereas the hydrophobic portions of the molecules are pointing up toward the air" (*Pockels, A;*

1891). Using this idea, *Irving Langmuir* continued the *Pockels'* work and he confirmed the previous results.

However, the real progress of Langmuir was not until he hired *Katherine B. Blodgett* as his assistant. Working together in *General Electric*, Langmuir and Blodgett discovered that when a solid surface is inserted into an aqueous solution that contains a monolayer of organic compound, the monolayer is homogeneously transferred onto the surface. This process allow create the named Langmuir-Blodgett Films (*Blodgett, KB; 1935*). Through this work in surface chemistry, Langmuir was awarded the Nobel Prize in 1932 (*Chechel, OV; 1991*).

2.2.2   Physical View

Langmuir-Blodgett Films are formed when amphiphilic molecules like surfactants interact with air at an gas-liquid interface. Surfactants are molecules with a hydrophilic part (heads), and a hydrophobic part (tails). As shown in figure 2.15, the surfactant molecules arrange themselves when surfactant concentration is less than *Critical Micellar Concentration* (CMC; defined as the concentration of surfactants above which micelles form and almost all additional surfactants added to the system go to micelles). The behavior of this type of molecules can be explained by surface-energy considerations. Because the tails are hydrophobic, the tendency of these will be their exposure to air over that to water. Because the heads are hydrophilic, the head-water interaction is more favorable than air-water interaction, and the tendency of these will be their orientation to water over that the air. The overall effect is reduction in the surface energy (or the surface tension of water).

When the concentration of the molecules on water surface is very small, far less than CMC, the surfactant molecules execute a random motion on the water-air interface. This motion can be thought to be similar to the motion

of ideal gas molecules enclosed in a container. The corresponding thermodynamic variables for the surfactant system are: *surface pressure* (p), *surface area* (A) and *number of surfactant molecules* (N). This system, therefore, is similarly to a gas in a container, and the density of surfactant molecules as well as the surface pressure increase upon reducing the surface area A (gas compression). The compression of the surfactant molecules shows a behavior similar to a phase transitions. The "gas" gets compressed into "liquid" and ultimately into a perfectly closed packed array of the surfactant molecules on the surface corresponding to a "solid" state.

Pressure-Area Characteristics

Adding a monolayer onto the liquid surface reduces the surface tension and the surface pressure (p). Then surface pressure is given by the following equation:

$$\Pi = \gamma_0 - \gamma \tag{2.11}$$

Where, γ_0 is the *surface tension* of the water and γ is the *surface tension* due to the monolayer. But the concentration-dependence of surface tension is as follows:

$$\gamma_0 - \gamma = RTK_HC = -RT\Gamma \tag{2.12}$$

Thus,

$$\Pi = -RT\Gamma \tag{2.13}$$

or,

$$\Pi A = RT \tag{2.14}$$

In the last equation is shown the relationship between this system and the ideal gas law ($PV=nRT$). However only when the solutions are dilute

and concentrations are low, then the concentration-dependence of surface tension is valid, as mentioned above.

Experimentally, the surface pressure is usually measured using the Wilhelmy Plate. A Wilhelmy plate is a thin plate that is used to measure equilibrium surface or interfacial tension at an air-liquid or liquid-liquid interface. The plate is oriented perpendicular to the interface, and the force exerted on it is measured. Based on the work of *Ludwig Wilhelmy*, this method finds wide uses in the preparation and monitoring of Langmuir-Blodgett films.

The Wilhelmy plate is in the order of a few centimeters square. The plate is often made from glass or platinum which may be roughened to ensure complete wetting. The plate is cleaned throughly and attached to a scale or balance via a thin metal wire. The force on the plate due to wetting is measured via a tensiometer or microbalance and used to calculate the surface tension (σ) using the Wilhelmy equation:

$$\gamma_0 = \frac{F}{l cos\theta} \tag{2.15}$$

Where, l is the *wetted perimeter* ($2w_F + 2h$) of the Wilhelmy plate and θ is the *contact angle* between the liquid phase and the plate (see figure 2.16). In practice the contact angle is rarely measured, instead either literature values are used, or complete wetting ($\theta = 0$) is assumed.

The Wilhelmy plate measurements give *pressure-area isotherms* that show phase transition-like behavior of the LB films. At the bottom and right part in figure 2.17, is shown the gaseous phase where the minimal pressure is done. When the pressure is increased, and the area decreases, the first transition takes place to a liquid phase. At high pressures, the film achieves the solid phase, where the maximum compactation is done. At this point, if more pressure is applied, the monolayer become unstable and it is broken (explained in detail in Chapter 5).
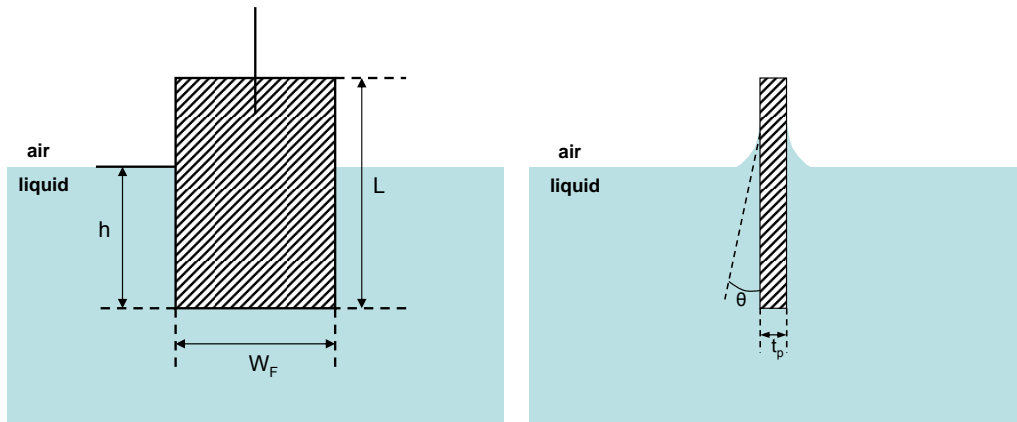
Figure 2.16: A Wilhelmy plate.

After the film formation, it is ready to transfer onto solid substrates in a controlled environment. Langmuir-Blodgett (LB) deposition allows a vertically film deposition (see Fig.2.18) while with the Langmuir-Schaefer (LS) method horizontal depositions are obtained (Fig.2.19).

Applications

LB films have different optical, electrical and biological properties which make them interesting in many possible applications. For example, LB films can be used as passive layers in metal-insulator-semiconductor, as biological membranes, etc (*Chechel, OV; 1991*).

2.2.3 Langmuir-Blodgett Trough

a) Trough: Nowadays, the most used trough is the Teflon (polytetrafluoroethylene) trough because it is hydrophobic and chemically inert. Occasionally metal or glass troughs coated with a thin layer of Teflon are used (*Chechel, OV; 1991*).

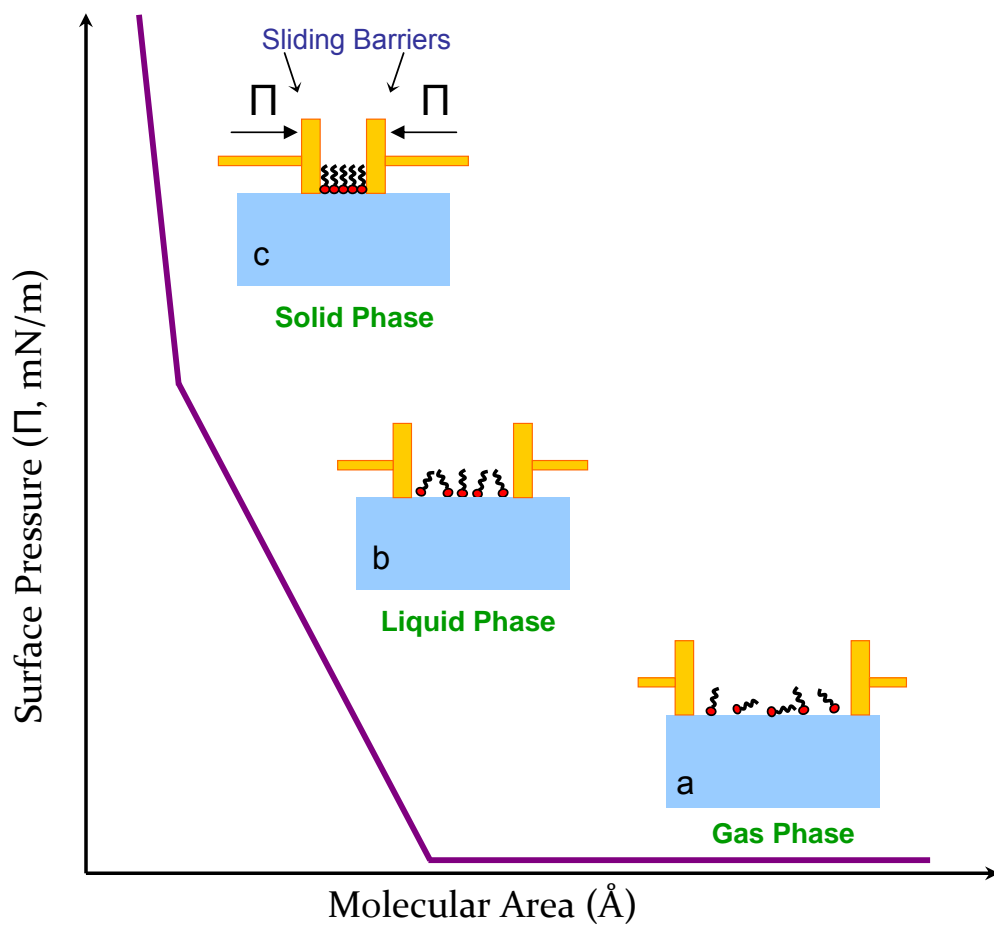b) Barriers: Different mechanisms have been used to compress or ex-

Figure 2.17: Surface pressure-Area isotherms. a) Molecular configuration in the gaseous phase. b) Molecular configuration in the liquid-expanded phase. c) Molecular configuration in the condensed of solid phase.
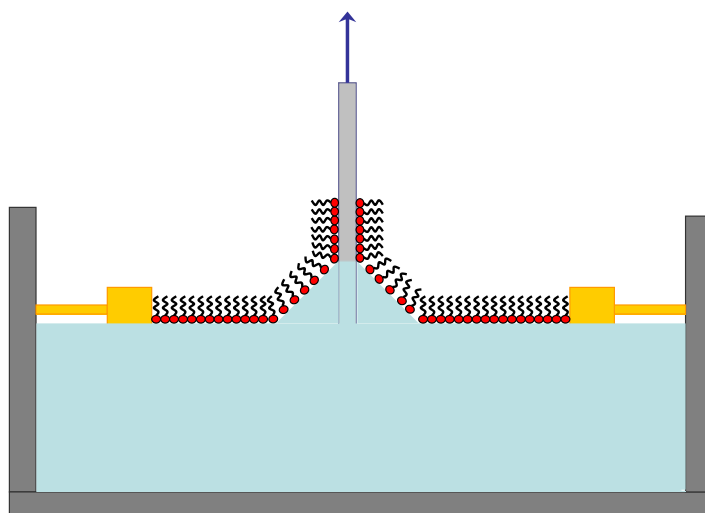
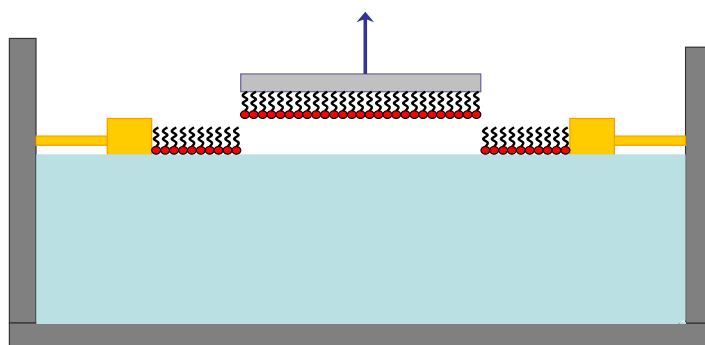Figure 2.18: Langmuir-Blodgett deposition on a substrat generally used.

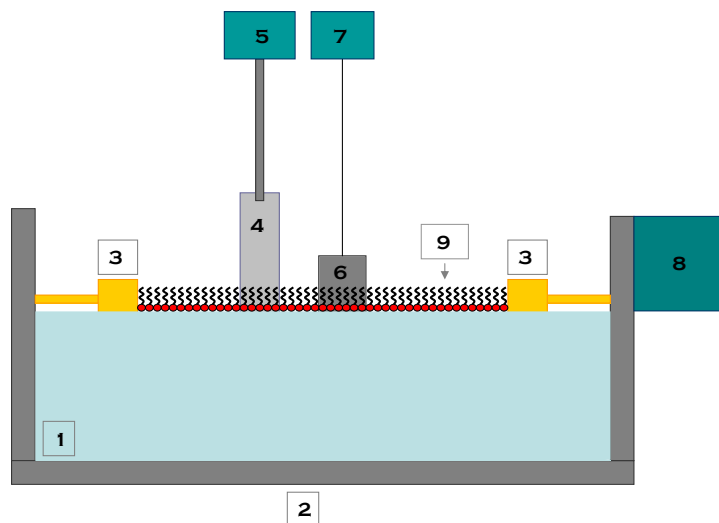Figure 2.19: Langmuir-Schaefer method, horizonal deposition of molecules.

Figure 2.20: Schematic of Langmuir-Blodgett trough. 1) Liquid subphase, 2) Langmuir-Blodgett trough, 3) Barriers, 4) Solid substrate, 5) Dipping mechanism, 6) Wilhelmy plate, 7) Microbalance, 8) Barrier mechanism, 9) Amphiphilic monolayer.

pand the monolayers throughout the development of the LB trough. Langmuir and Blodgett used in their first experiments flexible silk threads rubbed with wax to enclose and compress the molecules. Currently, the most common barriers used are the movable Teflon barrier blocks.

c)   Microbalance: The *surface pressure vs. molecular area* isotherm is one of the important indicators of monolayer properties. Something to take in account is the importance to maintain constant surface pressure during deposition in order to obtain uniform LB films. As explained in subsection 2.2.2, the tool charge to measure the surface pressure is the Wilhelmy plate or Langmuir Balance. The plate detects the downward force exerted by the liquid meniscus which wets the plate. The surface tension can then be calculated by the following equation:

[Force on Plate] = [Weight of plate] + [Surface Tension Force] [Buoyant Force]

$$F = (m_p g) + 2(t_p + w_p)\gamma_{LV} cos(\theta) - \rho_l V_p G \qquad (2.16)$$

Where, m_p corresponds to the *mass of plate*, g is the *gravitational acceleration*, t_p is the *thickness of plate*, w_p is the *width of plate*, γ_{VL} is the *surface tension of liquid*, θ is the *contact angle*, ρ_l is the *density of liquid* and V_p is the *volume of the proportion of plate immersed in liquid*.

The effect of *Bouyancy* can be removed by extrapolating the force back to the zero depth of immersion. Then the remaining component force is only the wetting force. Assuming that perfect wetting of the plate occurs ($\theta = 0$, cos (θ) =1), the surface tension can be calculated (*Erbil, HY; 2006*). Then, the surface pressure is the change in surface tension due to the addition of the monolayer (*Chechel, OV; 1991*).

2.2.4 Consideration of Langmuir-Blodgett Trough

In order to obtain the best Langmuir-Blodgett Films, some things should be into account. The maximal cleanliness and purity of components is required. The water used must be purified to remove organics and dionized to a resistivity not less than 1.8 GΩm^{-1}. If there are some impurities as small as 1 ppm, its can radically change the behaviour of a monolayer. It is important to maintain the laboratory apparatus isolated to other apparatus to prevent possible external contamination, and also eliminate the pollution of the air. For this reason, it is better that LB apparatus remains inside of a clean box, as shown in figure 2.23. And last but not least, an exact calibration of the microbalance ensures the best LB formation films.

The trough and barriers should be thoroughly cleaned by a solvent such as ethanol to remove any residual organics. Often it is necessary to aspirate the surface of the liquid with a hose in order to remove any last remaining impurities. The molecules dissolved in the suitable solvent are slowly dropped
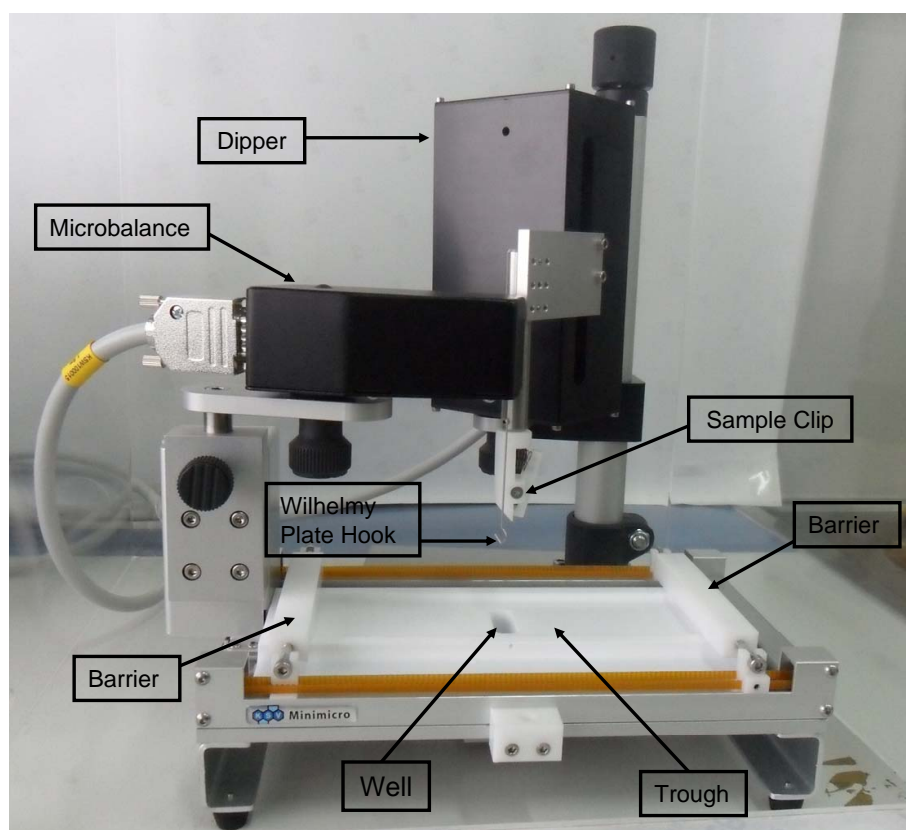
Figure 2.21: Picture with the main parts of the LB-trough used in this work.

onto the liquid surface using a clean microsyringe. The Wilhelmy plate must be absolutely clean as well, using a solvent and heated by a flame.

2.2.5 Technical data about the Langmuir-Blodgett apparatus used.

Trough	Devices	Available experiments
Flat with well	Balance and dipper	Multilayer LB-films on solid substrate and Langmuir film balance

Figure 2.22: Table of characteristics of our Langmuir-Blodgett apparatus.

The trough has a surface area of 100 mm^2, (L195 x W51 x D4 mm^3) a dipping well (L10 x W28 x D28 mm^3) and a subphase volume of 48 mL.

Mechanics

- The computer should be a PC running Windows 2000/XP/Vista. A 1GHz processor and 512MB RAM memory are recommended.

- The barrier position is controlled by a micro step driven stepping motor. The motor moves the barrier holder using a tooth belt. The holder itself is attached to a linear motion system, which is equipped with ball bearings. The barrier driving system is equipped with adjustable safety switches which stop the barrier immediately when the barrier holder hits the switches.

- The surface pressure is measured by using the Wilhelmy plate method. The force acting on the plate depends on surface pressure. This force

is measured using the electro-balance. The total measurement range of the balance is +/- 2000 mg. The width of the platinum Wilhelmy plate has been chosen so that 1 mN/m corresponds to 4 mg.

- The speed range of the dipping arm is 0.1 to 85 mm/min and maximum stroke is about 75 mm.

- The troughs are made of a solid piece of PTFE. The trough is glued onto an aluminium base plate, in which there are water channels for the thermostation of the subphase. The temperature is adjusted with a water bath circulator, which is connected to the trough with special connectors. These connectors include valves in both parts, so the connection can be opened without any leakage. The maximum temperature allowed is 60°C. The barriers are made out of hydrophilic material, which ensures that the film does not escape the barrier. The barrier material is polyacetal (Delrin) and it should be noted that Delrin is not resistant to acids or chloroform, so do not use these as cleaning agents.
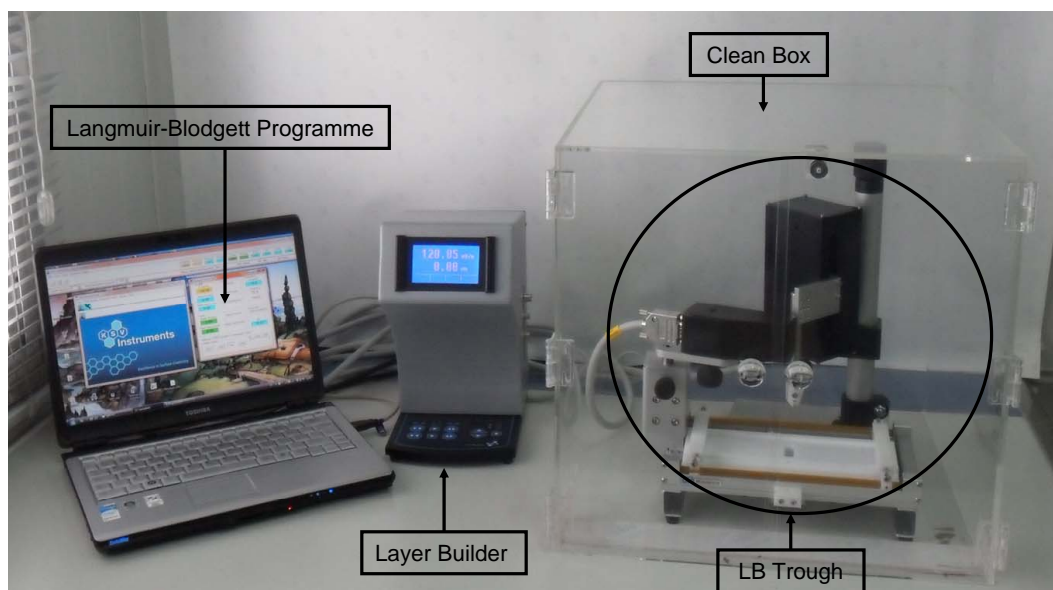
Figure 2.23: Picture with the main parts of a LB-trough.

Technical Specifications

Deposition Speed	0.1 to 85 mm/min
Speed adjust	Increment 0.1 mm
Optional speed range	0.2 to 170 mm/min
Deposition cycles	1 to unlimited
Dwell times	0 to unlimited seconds
Deposition arm	75 mm max. stroke
Max. size of substrate	25 x 25 mm
Type of motor	Servo controlled DC motor
Measuring principle	Wilhelmy plate
Dynamic range	0 to 250 mN/m
Resolution	4 µN/m
Barrier speed	0.01 mm to 400 mm/min
Accuracy	Greater than 99%
Dimensions	L195 x W51 x D4 mm^3
Volume	48 mL
Trough material	Teflon
Barrier material	Hydrophilic Delrin (polyacetal)
Temperature range	0 to + 60ºC

Figure 2.24: Table of technical specification of our Langmuir-Blodgett trough.

Chapter 3

The alkaliearth fluorides BaF$_2$ and CaF$_2$

3.1 Introduction

Among the different studies of water adsorption on surfaces, those with structures similar to the basal plane of hexagonal ice (I$_h$), the form of all natural snow and ice on Earth, have received a special interest. Bernard Vonnegut (*Vonnegut, B; 1947*) formulated the idea that such surfaces with a similar lattice parameter close to I$_h$ would be specially efficient in catalizing the formation of ice. However, not satisfying much condition that show good ice nucleation properties. Some examples are testosterone (*Head, RB; 1961*), some bacterial species (*Schnell, RC; 1974*) (it exists a bacteria that is used nowadays to create artificial snow at temperatures $\sim$2°C (*Snomax snow induce: http://www.snomax.com/products/snomax/*)), or pulverized leaves (*Schnell, RC; 1982*). The nucleation effect of these substrates has been related to thermodynamic arguments, the alignment of protons on the surface as a consequence of bonding (results in an increase or decrease of entropy that drives a favourable growth of the thin film on surface), or defects, steps, vacancies,

etc. on the surface will make it better nucleator respect others (*Fletcher, NH; 1958, 1959, 1960 and 1969*).

From the list of materials that show a surface lattice parameter close to I_h, the mostly studied compound has been the wurtzite-type polymorph of AgI (β-phase, space group *P63mc*), in the form of a smoke of crystallites, whose basal plane shows a lattice mismatch of less than 2% with respect to I_h ice. However, according to Monte Carlo simulations, a monolayer of water in registry with the surface builds with a distribution of hydrogen atoms that does not favour the layer-by-layer (2D) growth of hexagonal ice (*Shevkunov, SV; 2007*). Despite of these findings, aerosols and nanoparticles of β-AgI are good ice nucleators, as proved in dedicated environmental chambers (*Heneghan, AF; 2002 and Finnegan, WG; 2003*), and have been extensively used for rain seeding with no clear evidence of its efficiency to induce rain (*Vonnegut, B; 1947 - Edwards, GR; 1967 - Birstein, SJ; 1955 - Vonnegut, B; 1949*).

Another material exhibiting good ice nucleating efficiency is kaolinite (*Salam, A; 2006*). The (001) surfaces of this alumino-silicate, which crystallizes in the *C1* space group, have two terminations: tetrahedra-terminated SiO_4, and octahedra-terminated AlO_6. The latter has a quasihexagonal arrangement of hydroxyl groups with a lattice mismatch of about 14%. According to Density Functional Theory (DFT) calculations (*Hu, XL; 2008*), water builds a stable monolayer due to the flexibility and amphoteric character of surface hydroxyl groups where each water molecule is fully coordinated with four hydrogen bonds (H-bonds), thus leading to a passivated surface with little proclivity to accept more water.

These findings in kaolinite and AgI suggest that probably defects of the surface play a key role in the nucleating efficiency of these materials.

The surfaces of kaolinite have been rarely explored experimentally in part due to the difficulty in handling the naturally grown small crystals, which

exhibit dimensions typically below 1 μm. Despite its evident interest, this surface has not been explored experimentally, to our knowledge, at the fundamental level (see appendix A).

Another potential candidate is the alkali earth fluoride BaF$_2$ (*Fm3m space group*) (*Zink, JC; 1992*), in particular its (111) face. This surface consists on a hexagonal array of barium and fluorine ions, distributed in trilayers (F-Ba-F) with a surface lattice constant of 4,38 Å, resulting in a $\sim$ 3% lattice mismatch with respect to ice (see Fig. 3.1) easy to cleave on its (111) face. Several spectroscopy studies have been made on BaF$_2$. Sadtchenko et. al. 2002, studied water adsorption on the (111) surface of BaF$_2$ at ambient temperatures by FTIR (Fourier Transform InfraRed) spectroscopy. In their work, they measured the absorption spectra of water adsorbed layers on the surface of BaF$_2$ at 25°C at different pressures. The spectra revealed significant differences as shown in figure 3.2. At low pressures, equivalent to low humidity, a doublet was observed. Two possibilities can explain the doublet spectroscopic signature: either water molecules are adsorbed to distinct sites at the surface (Ba^{2+} and F$^-$) or they reside in two different states (liquidlike and solidlike H$_2$O). At high pressures, more water molecules adsorb on the surface and may result in disordering of the first and ordered adlayer, and consequently is driven to the formation of a liquidlike phase. For this reason a wide peak centered at 3400 cm^{-1}, close to the bulk water spectrum was observed (*Downing, HD; 1975*). Using a modified Beers law expression (*Foster, MC; 2000*), they can calculate the number of layers adsorbed on the surface (θ) (Fig. 3.2). The doublet was found to exist for $\theta < \mu$L and it was interpreted as a icelike bilayer even at ambient temperatures. According to early simulations they found that the structure of BaF$_2$ was compatible with the basal hexagonal ice face (I$_h$) (*Wassermann, B; 1994*), and the bilayer formed can be seen as a lattice of buckled six-membered rings of H$_2$O
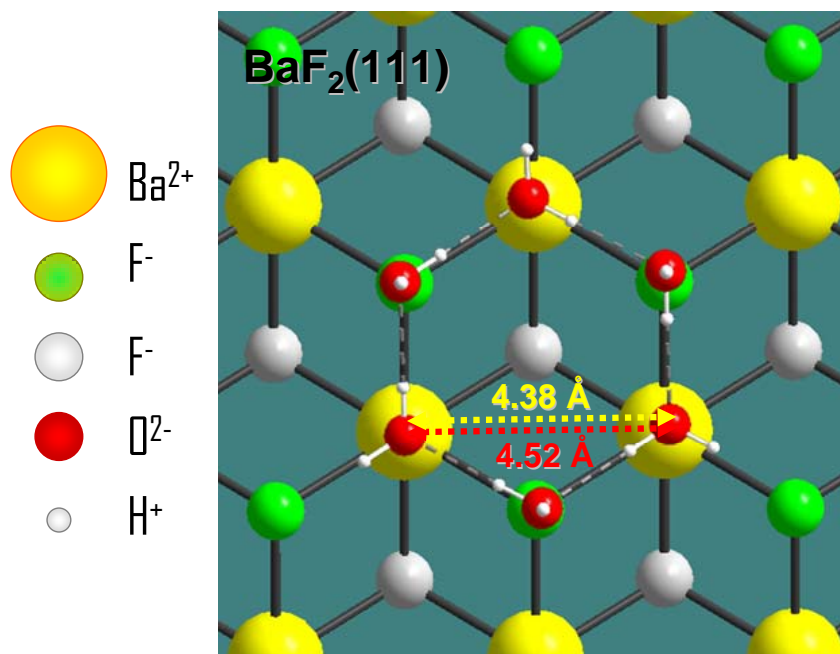
molecules interconnected by hydrogen bonds.

Figure 3.1: Scheme of an idealized I$_h$ bilayer hexamer on a (111) BaF$_2$. Barium, upper fluoride, lower fluoride, oxygen, and hydrogen are represented by yellow, green, white (biggest), red, and white (smallest) balls, respectively.

The I$_h$ bilayer lattice would be formed by rings of six water molecules bonded between them through hydrogen bonds. Molecules in the lower half of the bilayer are fourfold coordinated (designated as *S-4* by Devlin and Buch (*Devlin, JP; 1995*)) with one of the oxygen lone pairs directed to the Ba^{2+} surface ions. Molecules in the upper half of the bilayer are threefold coordinated. Water molecules at the upper layer can expose either dangling (d) H or dangling (d) O directed upward.

The enthalpy and entropy of H$_2$O adsorption on the BaF$_2$(111) surface can be described from the isotherms using the following expression (*Foster, MC; 2000*):
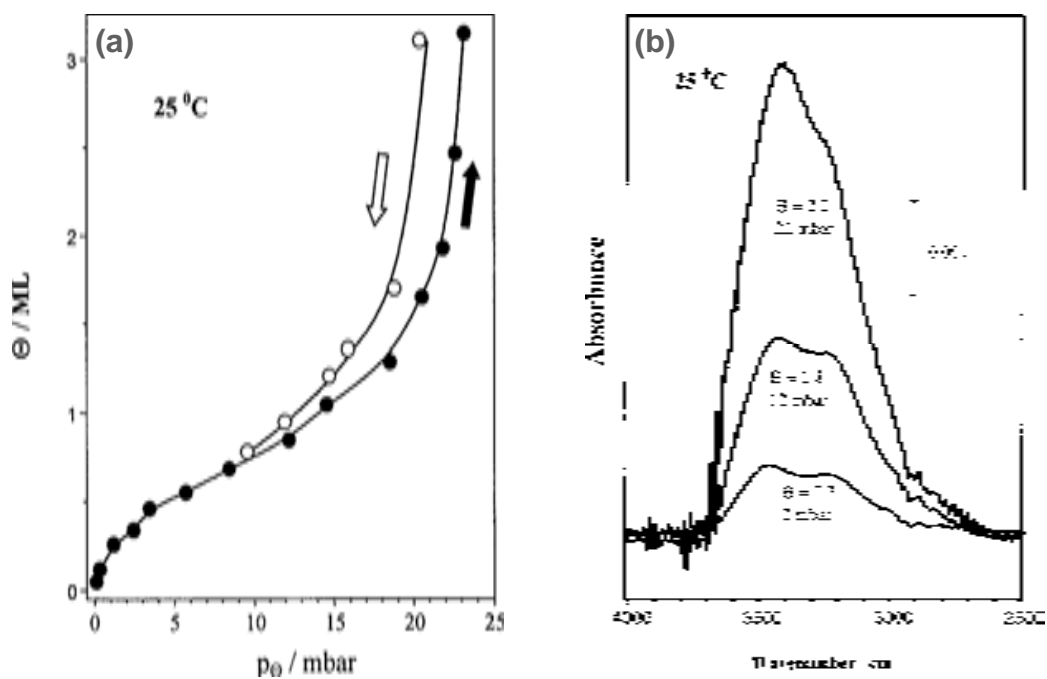
Figure 3.2: (a) Absorbances of thin water films on BaF$_2$ (111) at 25°C for several coverages. (b) Isotherms of thin water films on BaF$_2$ (111) at 25°C. Reprinted from (*Sadtchenko, V; 2002*).
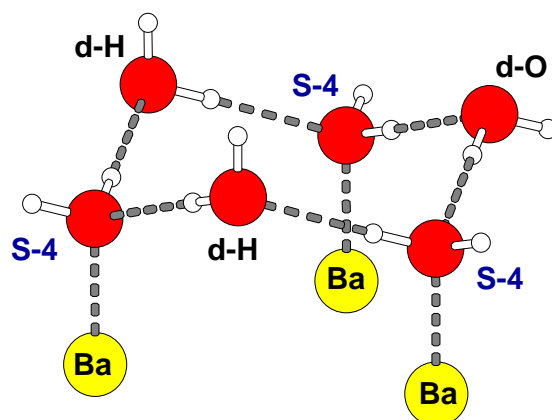

Figure 3.3: Scheme of a I$_h$ bilayer on an idealized (111) BaF$_2$ surface showing only the Ba ions.

$$ln\left(\frac{p_w}{p_\Theta}\right) = \frac{\Delta H_w - \Delta H_\Theta}{RT} - \frac{S_w - S_\Theta}{R},$$ (3.1)

where ΔH_w is the enthalpy of adsorption of bulk liquid water, ΔH_Θ is the enthalpy of adsorption on the BaF$_2$(111) surface, S_w is the entropy of bulk liquid water, and S_Θ is the entropy of a H$_2$O adlayer on BaF$_2$(111) surface and R is the ideal, or universal, gas constant, equal to 8.314 J·K^{-1}·mol^{-1}.

In terms of thermodinamics, Sadtchenko et al. concluded that at low coverages (θ=0.75$\pm$0.25 ML), the adsorption enthalpy is lower than the ice condensation enthalpy, suggesting a strong water interaction with the substrate. The enthalpy of adsorption measured at coverages close to 1 ML supports the conclusion that H$_2$O adsorption on BaF$_2$(111) leads to the formation of an ordered layer "nailed" to the substrat. This agrees with the formation of an anchored layer. However, the enthalpy measured by higher coverages ($>$1 ML) decreases and approaches the value of liquid water. This is the reason why the layer begins to be disordered and seems as a liquidlike in the FITR spectra. In terms of entropy the behavior is equivalent. At low coverages, entropy is actually higher than the entropy of bulk water. When coverage increases, then the entropy decreases rapidly, and ordered layers result to unfavorable process.

Later, Conrad et al. (*Conrad, P; 2005*) continued the study of Sadtchenko by introducing the immersion mode technique for BaF$_2$. As shown in figure 3.3, a single crystal of BaF$_2$, freshly cleaved along (111), was placed at the bottom of a vial. At t=0.04 s, the onset of nucleation at -15°C on the top of the surface can be observed. With the progress of time, ice becomes more visible spreading horizontally along the surface and growing verticaly as well. At t=0.14s, the ice covers the entire bottom part of the vial. They found that the presence of BaF$_2$ does not significantly raise the nucleation threshold of water but the freezing of water was always initiated on the surface of the
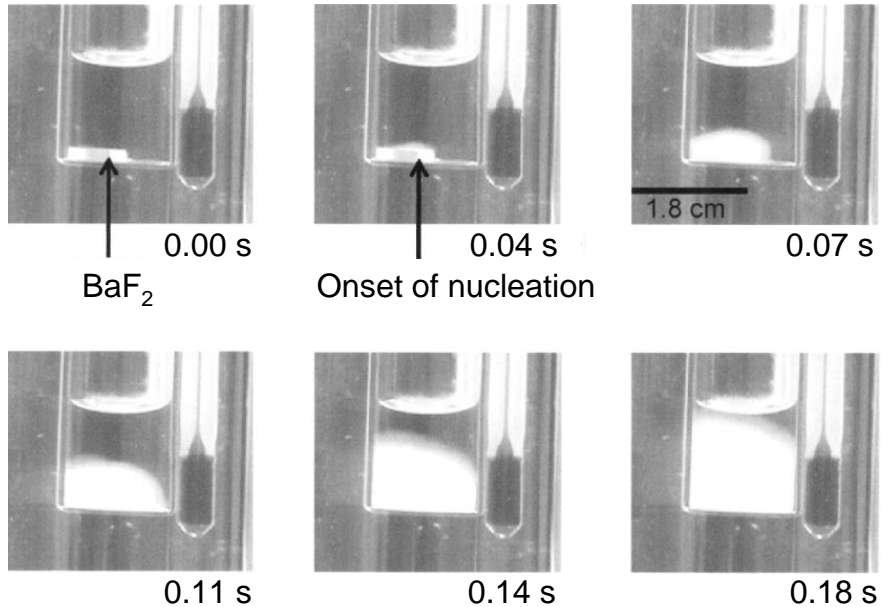
barium fluoride.

Figure 3.4: Images showing the succession of spontaneous freezing of water on a BaF$_2$ crystal in the immersion mode. Reprinted from (*Conrad, P; et.al.; 2005*).

The authors also found that the BaF$_2$ surface suffers changes after immersion. With a simple calculation, Conrad *et. al.*; 2005, could calculate that 10 μm of its surface is removed in the dissolution process. The dissolution process makes the surface slightly different than the initial one, pits appear, and steps, corners, and kinks of atomic dimensions were eroded away. Using BaF$_2$ previously pitted by water immersion they found that ice cristals were much more stable. That suggested that deffects on the surface facilitates the growing of stable hexagonal ice better than a perfect flat surface.

As mentioned above, first simulations seemed to conclude that the first water bilayer on Ba^{2+} was a perfect ice bilayer. However, Nutt and Stone (*Nutt, DR; 2002*) calculated the interaction energy between a water molecule and the barium fluoride surface and they determined the stabilities of various low coverage structures. They interpret a monolayer as a molecule of water

per BaF$_2$ surface unit. At low coverages of θ=0.5 ML (2 molecules of Ba^{2+} $\times$ 1 molecule of H$_2$O) each water molecule is in a position with no interaction with other molecules in a almost flat configuration. In this case, Nutt *et.al.*;2002, found energies that range from to 46.5 to 40.7 kJ/mol. At coverages of θ=1, the structure consists of dimers and isolated molecules (see Fig. 3.5, (a)) and the associated binding energy is 51.4 kJ/mol. When the coverage is increased, at θ=2 and θ>2 a distorted and cross-linked chain structure (see Fig. 3.5, (b)) appear, with a binding energy of 53.9 kJ/mol. The structure is almost completely lost at higher coverages (Fig. 3.5, (c)). If water molecules are forced into an icelike structure in a perfect bilayer, the associated binding energy is 38.9 kJ/mol, much less than the previous described structures. The flat configuration of the first adsorbed water molecules hinders the formation of energetically favorable I$_h$ bilayers leading to the formation of the cross-linked chain structure.

After briefly explaining the main studies previous to this work about water on barium fluoride, I'm going to describe the objective of this work and the questions that I'll try to answer.

Objectives

Our main objectives are divided in three points of interest:

1. *Why BaF$_2$ is a better nucleation agent when it has defects on the surface?* Conrad's *et.al.* research about immersed BaF$_2$ surfaces suggests that a BaF$_2$ surface rich in defects is a better nucleation agent than a perfect BaF$_2$ surface. What is the role of surface defects on the wetting of BaF$_2$? Taking advantadge of nanometric lateral resolution of SPM techniques, we will try to determine this role. This part has been published in *Cardellach, M; Verdaguer, A; Santiso, J; Fraxedas, J*; "Two-dimensional wetting: The role of atomic steps on the nucleation of thin
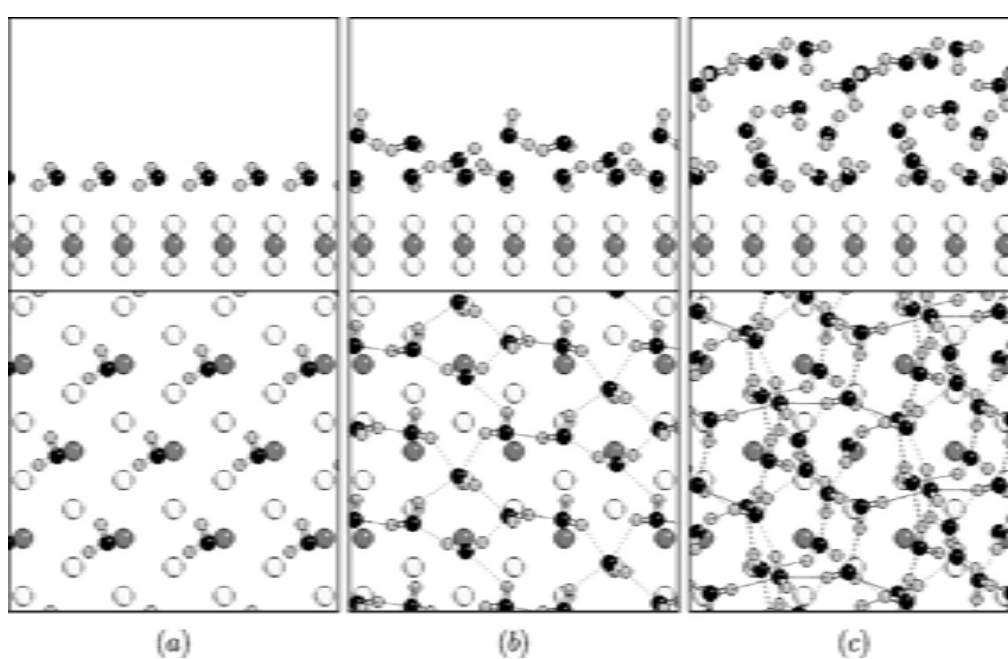
Figure 3.5: (a) Side and orthogonal views of a calculated structure for $\theta=1$ with a binding energy of 51.4 kJ/mol, (b) a cross-linked chain bilayer structure, and a typical disordered structure for $\theta=4$. Reprinted from *Nutt, DR. and Stone, AJ; 2002.*

water films on BaF$_2$(111) at ambient conditions", *Journal of Chemical Physics.* **132**, 234708 (2010).

2. *Is I$_h$ the real ice structure formed on the BaF$_2$ surface?* With Scanning Polarization Force Microscopy (SPFM) (*Hu, J; 1995*) simultaneously with Kelvin Probe Force Microscopy (KPFM), we will directly monitor the evolution of the structures of water on BaF$_2$ (111) as a function of RH (i.e. coverage) to try to answer this question. This part has been published in *Verdaguer, A; Cardellach, M; Fraxedas, J*; "Thin water films grown at ambient conditions on BaF$_2$(111) studied by scanning polarization force microscopy", *Journal of Chemical Physics.* **129**, 174705 (2008).

3. *Which is the role of the surface lattice constant?* Here we will present an investigation of the adsorption of water on (111) surfaces of BaF$_2$ and of its isostructural partner CaF$_2$. CaF$_2$ has a lower surface lattice constant, which translates into a mismatch of about 15%. So that by comparing water structures on both surfaces the influence of the lattice mismatch can be determined. Again SPM techniques are the perfect tools for such studies. This part has been published in *Cardellach, M; Verdaguer, A; and Fraxedas, J; 2011.*

3.2   Experimental details

BaF$_2$ and CaF$_2$ single crystals (Crystal GmbH, Berlin, Germany) were cleaved parallel to the (111) plane either at ambient conditions (T=22±2°C, RH∼50%) or inside the AFM globe box at low humidity (T=22±2°C, RH<10%) to obtain new fresh surfaces. Commercial Si tapping cantilevers (PPP-NCHR, Nanosensors, Neuchâtel, Switzerland), with resonance frequencies of ∼300 kHz and force constants of ∼50 Nm^{-1}, were used for amplitude modula-

tion AFM (tapping mode) and soft Pt coated cantilevers (PPP-CONTPt, Nanosensors) were used in the SPFM and contact experiments. Pt coated cantilevers had a nominal spring constant of $\sim$0.5 Nm^{-1}. SPFM and KPFM experiments were performed at a frequency of 4 kHz, well below the cantilever resonance ($\sim$13 kHz). Optical images were obtained using and optical microscope at $10\times$ magnification and at ambient conditions with controled temperature using a Peltier cooling system.

In order to control the humidity inside of the glove box, it was necessary to install a dry N_2 circuit. Once injected N_2 into the glove box, we can lower the humidity until $<5\%$. When you want the opposite effect (increasing the humidity) we need to change the N_2 flow route and then N_2 is bubbled through Milli-Q water. N_2 adsorbs water molecules and is injected into the glove box, and relative humidity is increased. So, varying the N_2 flow and the introduction of water molecules into the glove box, we can control. The humidit, was monitored with a Digitron hygrometer installed inside of the box. The RH uncertainly is $\pm5\%$.

Crystallographic directions on the surface of the BaF$_2$ crystals were determined by x-ray diffraction (Bruker D8 Advance, with a four-cicle goniometer). The azimuth ϕ angles of the (200) reflections [threefold symmetry for the (111) BaF$_2$ oriented cut] were measured for each crystal. The projections of each [100] direction at the same ϕ angles onto the crystal surface correspond to [$2\bar{1}\bar{1}$], [$\bar{1}2\bar{1}$] and [$\bar{1}\bar{1}2$] directions. Relevant [$11\bar{2}$] and [$\bar{1}10$] surface directions are readily derived from them.

The as-received bars of BaF$_2$ were cut in such a way that the exposed rectangular faces corresponded to orthogonal $\{\bar{1}10\}$ and $\{11\bar{2}\}$ family planes, respectively, as verified by x-ray diffraction. We arbitrarily assume that the relevant directions correspond to the [$\bar{1}10$] and [$11\bar{2}$] directions, respectively as shown in figure 3.6, (a) and (b), due to the cubic structure ($Fm\bar{3}m$ space
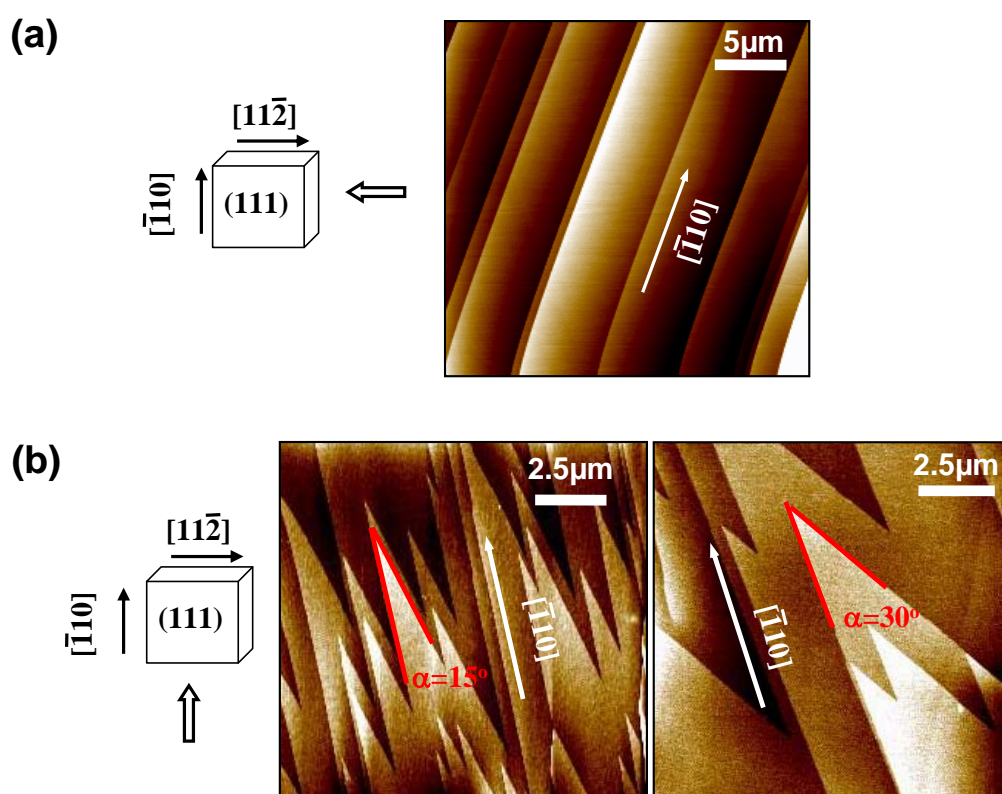
Figure 3.6: Topographic AFM images obtained in acoustic (tapping) mode of BaF$_2$(111) surfaces obtained by cleavage along the [11$\bar{2}$] (a) and [$\bar{1}$10] (b) directions. All images were taken at 21°C and RH<10%.

group) of BaF_2. (111) surfaces were generated by cleavage using a blade as shown in figure 3.7.

Figure 3.7: A bar of BaF_2 before cleaving it with razor blade.

Stepped surfaces with micron-sized terraces were obtained as observed by AFM [Figs. 3.6 (a) and (b)]. The measured step heights were ~0.4 nm, corresponding to the distance between adjacent trilayer planes (0.36 nm according to the known crystallographic structure). Higher steps were also observed, but always corresponding to integer multiples of 0.36 nm. It is important to note that different step shapes were obtained depending on the direction of cleavage. Surface generated by cleavage along the $[11\bar{2}]$ direction exhibit most of the times terraces limited by parallel straight steps in the $[\bar{1}10]$ direction [Fig. 3.6 (a)] while cleavage along the $[\bar{1}10]$ directions show lightning- or V-shaped steps [see Fig. 3.6 (b)] as already reported on isostructural $CaF_2(111)$ surfaces (*Engelhardt, JB; 2000*), as shown in figure 3.8 (left).

The direction of the tips of the triangular steps approximately corresponds to the direction of the crack propagation. Similar step distributions have also been reported for (100) cleavage planes of monoclinic L-arginine phosphate monohydrate crystals, although their origin has not been discussed in detail
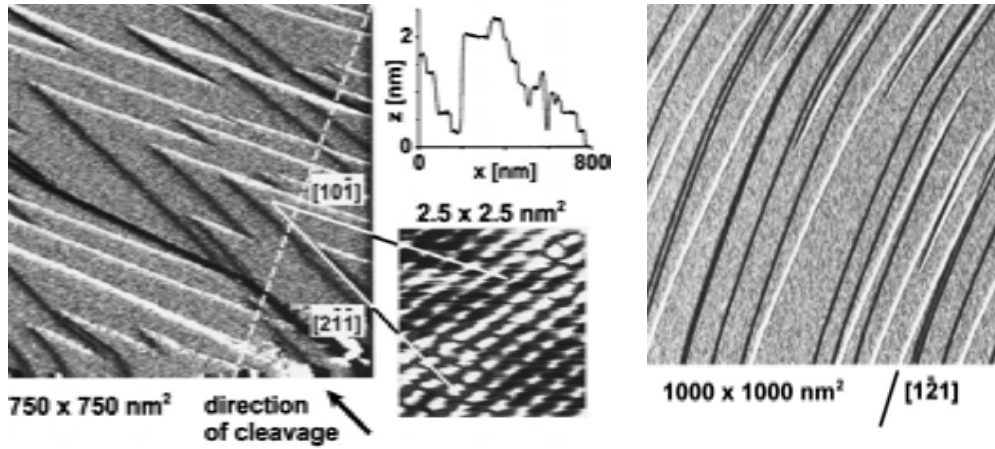
Figure 3.8: Reprinted from (*Engelhardt, JB; 2000*). Lightning-shaped step arrangements and high-resolution images with step's heights of ∼0.32 nm or integer multiples thereof, and parallel steps of (111) cleavage face of CaF$_2$.

(*Geng, YL; 2005*). One of the two main directions of the lightning-shaped steps corresponds to the $[\bar{1}10]$ direction [Fig. 3.6 (b)] while the other direction is cleavage dependent. A histogram of the distribution of the acute angles (α) between both directions measured over many different samples is shown in figure 3.9 (a). Two well differentiated groups of angles are observed, the most common one centered at $\alpha =30°$ and the other group centered in the 14°-19° range. Angles of 60°, 30°, and 19° have been reported on cleaved CaF$_2$ (111) surfaces, however, accurate measurements of angles on AFM images can be difficult due to drift during scanning which sometimes has lead to error in the analysis of the results (*Engelhardt, JB; 2002*) (see Fig.3.8 (right)). Steps at 30° from the $[\bar{1}10]$ directions correspond to steps along the $[2\bar{1}\bar{1}]$ direction, as determined from the crystallographic structure [see Fig. 3.9 (b) right]. Steps observed in the 14°-19° range do not run along well defined crystallographic directions suggesting that they consist of arrays of small $[\bar{1}10]$ and $[11\bar{2}]$ segments forming steps rich of kink sites [see Fig. 3.9 (b) left].
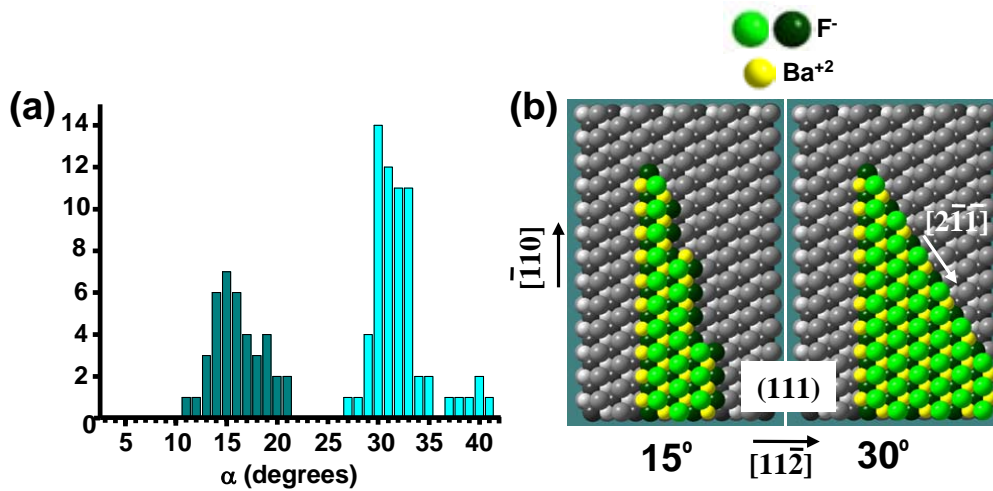
Figure 3.9: (a) Histogram of the distribution of angles between $[\bar{1}10]$ and other step directions for surfaces cleaved along the $[\bar{1}10]$ direction. (b) Representation of triangular steps on a $BaF_2(111)$ surface forming angle of $15°$ (left) and $30°$ (right), respectively. Fluorine and barium ions are represented by green and yellow balls, respectively, while the surface is represented by gray balls.

3.3 Why BaF_2 is a better nucleation agent when it has defects on the surface?

In this section we have focused our attention on the role of atomic steps on the structure of the water films, which play a key role in the stabilization of water bilayers. An important outcome of this work is that steps running along different crystallographic directions show different wettability confined to two dimensions defined by the step edges and terraces. The most hydrophilic steps correspond to $[\bar{1}10]$ directions, the main directions found on the surface after water immersion. We will show that a high density of kinks along steps does not forcibly guarantee higher wettability.

Figure 3.10 shows topographic (left) and phase (right) AFM images taken in AM-AFM (explained in detail in section 2.1.4) of water films grown on $BaF_2(111)$ at ambient conditions (T=21°C and RH∼45%). The difference

in the tip-surface interaction when scanning over a dry terrace (no hint of adsorbed water) or over terraces partially covered with water induces a large contrast in the phase shift images (right side of the figure), making them ideal to visualize the water structures on the surface (as already shown in section 3.4). In the phase images water appears in dark colour representing larger interaction with the cantilever tip (*Fraxedas, J; 2005*).

The terraces are decorated with islands [see Fig. 3.10 (a)], which exhibit an apparent height of ∼0.5 nm that has been considered compatible with an ice I$_h$ bilayer (*Miura, K; 1999*). Water films are also observed along straight steps, along [$\bar{1}$10] directions as well as along the other step directions. In general water adsorbs preferentially at the lower terrace of the steps (lower trilayered atomic plane), although in some cases water accumulates on the higher terrace (the step belonging to this atomic plane). This can be clearly observed in figure 3.10 (a). More interesting structures appear when the V-shaped steps are present at the surface [see, i.e., Fig. 3.10 (b) and (c)]. Water becomes confined in the acute angles formed by steps of the same terrace. When water accumulates in the lower terrace of the steps, it exhibits curved shapes resembling menisci wetting the steps. This is the 2D case of the 3D menisci formed between surfaces (think of water partially filling a glass cylinder).

Examples can be also found in figure 3.11. Similar structures can be observed on the upper part of the tips of steps (upper terraces). In order to address this important issue we show in figure 3.11 the time evolution of the water films while scanning over the same area. The comparison of the images, (1-3), readily evidences the perturbation induced by the tip. Note the formation of islands on the terraces, which were absent in the first image. Note also that some steps decorated in their lower terraces become undecorated and the menisci become better defined after successive scans. Finally, we observe in
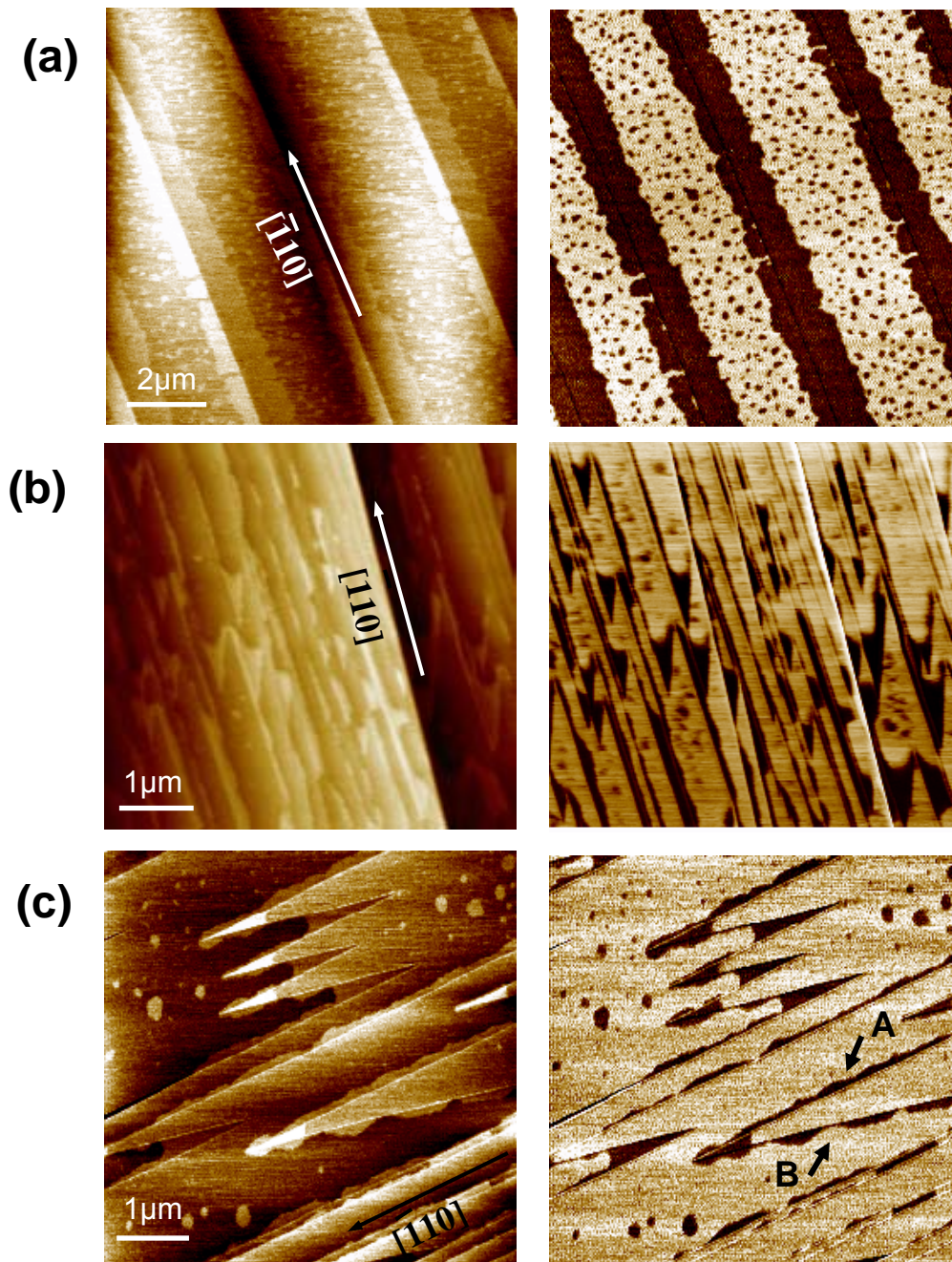
Figure 3.10: Topographic (left) and phase (right) AFM images taken at ambient conditions (T=21°C and RH∼45%) in acoustinc (tapping) mode of a BaF$_2$(111) surface obtained by cleavage along: (a) the [11$\bar{2}$] direction and (b) and (c) the [$\bar{1}$10] direction. In (c) steps running along [$\bar{1}$10] and [11$\bar{2}$] are indicated by A and B, respectively, highlighting different wettability behavior.

the left side of the first image, roughly in its equator, a 2D droplet arising from a meniscus. The shape of this droplet changes until the droplet detaches and slips toward a close-lying step and the meniscus reservoir becomes emptied. A more evident example of how the tip can empty a reservoir is shown in the lower right part of the images (large meniscus in the central image).

Figure 3.12 shows SPFM and KPFM images of a BaF$_2$(111) surface. The left image shows the combined contribution from topography and dielectric response. In this case it is difficult to distinguish among step and water film edges because they show similar apparent heights. However, the KPFM image taken simultaneously (right image) shows a clear contrast between the water films (white colour) and the dry BaF$_2$(111) surface (dark colour). The contrast between both regions (about + 60 meV contact potential) in the KPFM images is induced by the averaged orientation of the water molecule dipoles pointing up from the surface at ambient conditions (21°C, RH$\sim$50%). Since in SPFM the perturbation induced by the tip is negligible, the presence of menisci results from an intrinsic process. No significant difference in the CPD (contact potential difference) was observed between water islands on the terraces and the water films at the triangular steps indicating that the dipole distribution on both films should be similar and suggesting a comparable bilayer structure in water films limited by sites and water films growing on terraces. In addition, the KPFM images show a homogeneous contact potential distribution over the water films again indicating a similar dipole orientation of the water molecules that are close to the steps and in the center of the film thus suggesting a similar structure within the lateral resolution of the images ($\sim$20 nm).

It is also remarkable that stable neighbouring menisci sharing a common step exist [see Fig. 3.11 (4)], suggesting that flow of water molecules between both terraces is strongly reduced. This effect may be understood within the
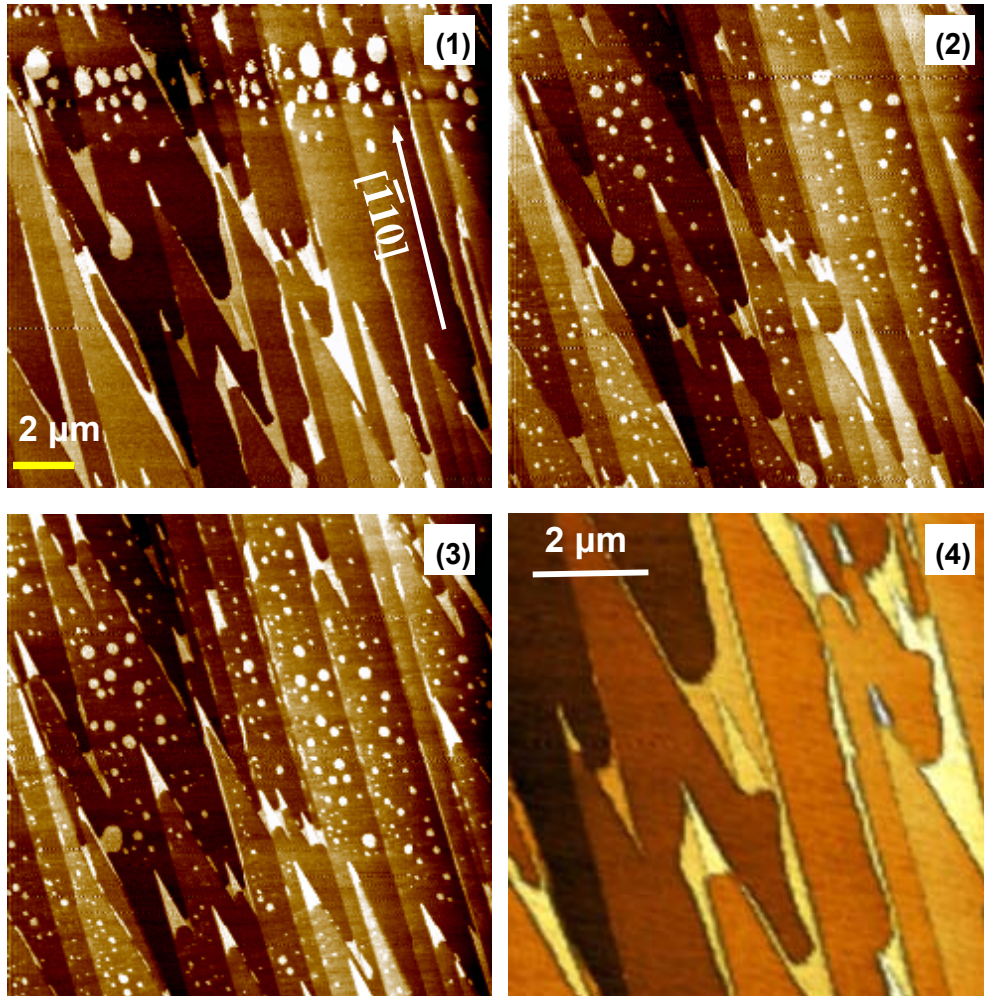
Figure 3.11: Topographic AFM images obtained in acoustic (tapping) mode of BaF$_2$ surfaces obtained by cleavage along the [$\bar{1}$10] directions. The images, (1)-(3), show the evolution after sequential scanning on the same region. The acquisition time per image is 170 s. Image (4) corresponds to a zoom of the central region of (1). The perturbation induced by the scanning tip can be observed in the formation of the different structures.

framework of the Ehrlich-Schwoebel model with efficient energy barriers at the step edges although no quantitative estimations of such barriers for this particular system are available (*Ehrlich, G; 1966 and Schwoebel, RL; 1966*).
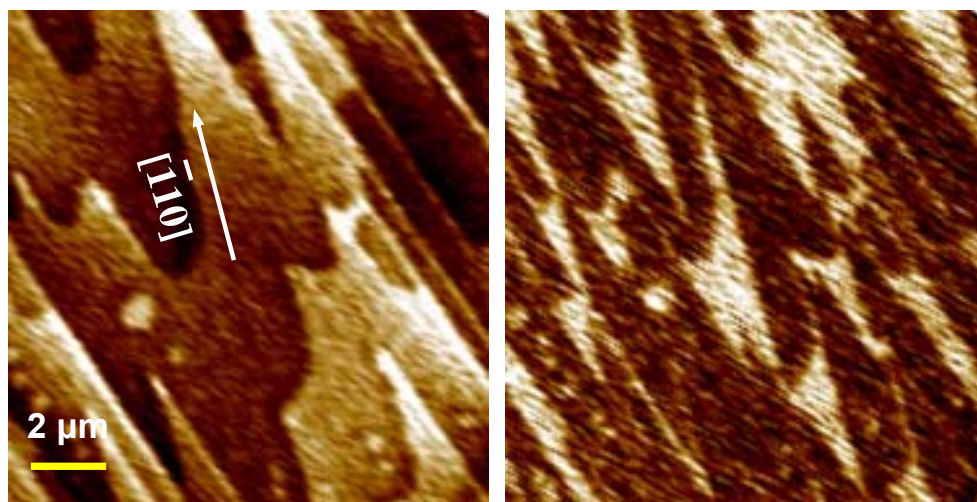

Figure 3.12: SPFM (left) and KPFM (right) images taken on a BaF$_2$(111) surface. All images were taken at 22°C and RH~50%

An alternative way of showing the intrinsic accumulation of water at steps is by using an optical microscope in an independent setup. In figure 3.13 a series of images of a freshly cleaved BaF$_2$(111) surface taken at RH ~55% for decreasing sample temperatures is shown. Note that the steps are clearly observed even at the moderate magnification used (10×). Darker areas corresponding to the adsorbed water layers on BaF$_2$(111) are observed to grow on the surface as the temperature of the sample is decreased (i.e., RH of the air close to the surface is increased). These dark areas show triangular structures very similar to what is observed by AFM. At some point water films are thick enough to show the well known interference pattern and overpass the step limitations inducing droplet coalescence. Although the observation of very thin water films with optical microscopy (Fig. 3.13) might be sur-

prising, just mention that recent examples of the observation of monoatomic graphene layers on SiO_2 have been reported (*Blake, P; 2007*).

3.3.1 Water-steps interaction

The accumulation of water at step edges, both on lower and higher lying terraces, as shown in Figs. 3.10 and 3.11, is an evidence of the high diffusion of water on the $BaF_2(111)$ surface at RT. In a recent work, Shluger and co-workers computed using density functional theory the diffusion barriers for water on $BaF_2(111)$ at RT to be 0.2 eV in the ideal case (water diffusing on defect free surfaces) and below 1 eV when different kinds of vacancies are considered, concluding that molecular water should be extremely mobile on this surface at RT, as well as on the (111) surfaces of CaF_2 and SrF_2 (*Foster, AS; 2009*). These calculations are in line with the here presented results, although they consider individual water molecules on both ideal and defective surfaces in a vacuum (no interaction with other water molecules) but in apparent contradiction with previous contact angle measurements (*Sadtchenko, V; 2002*) and with our own measurements, where the observed contact angles lie well below 15°, indicating almost perfect wetting.

We thus have 2D structures, islands (most probably due to the nucleation of water around defects, i.e., fluorine vacancies, a nucleation that may imply water dissociation) (*Wu, Y; 1994*) and water adhered to steps, in equilibrium with the water vapour pressure. At the RH achieved in the present work, the estimated coverage is below 1 ML, by direct comparison with isotherms of thin films of water on BaF_2 (111) at 25°C as determined by FTIR spectroscopy (*Sadtchenko, V; 2002*) (see Fig. 3.2). In this low coverage region it has been claimed that water is distributed as a 2D gas (absorption/desorption) and 2D bilayer structures, in agreement with our observations. According to the mentioned FTIR results, the highest adsorption enthalpy is $\sim$0.58 eV at
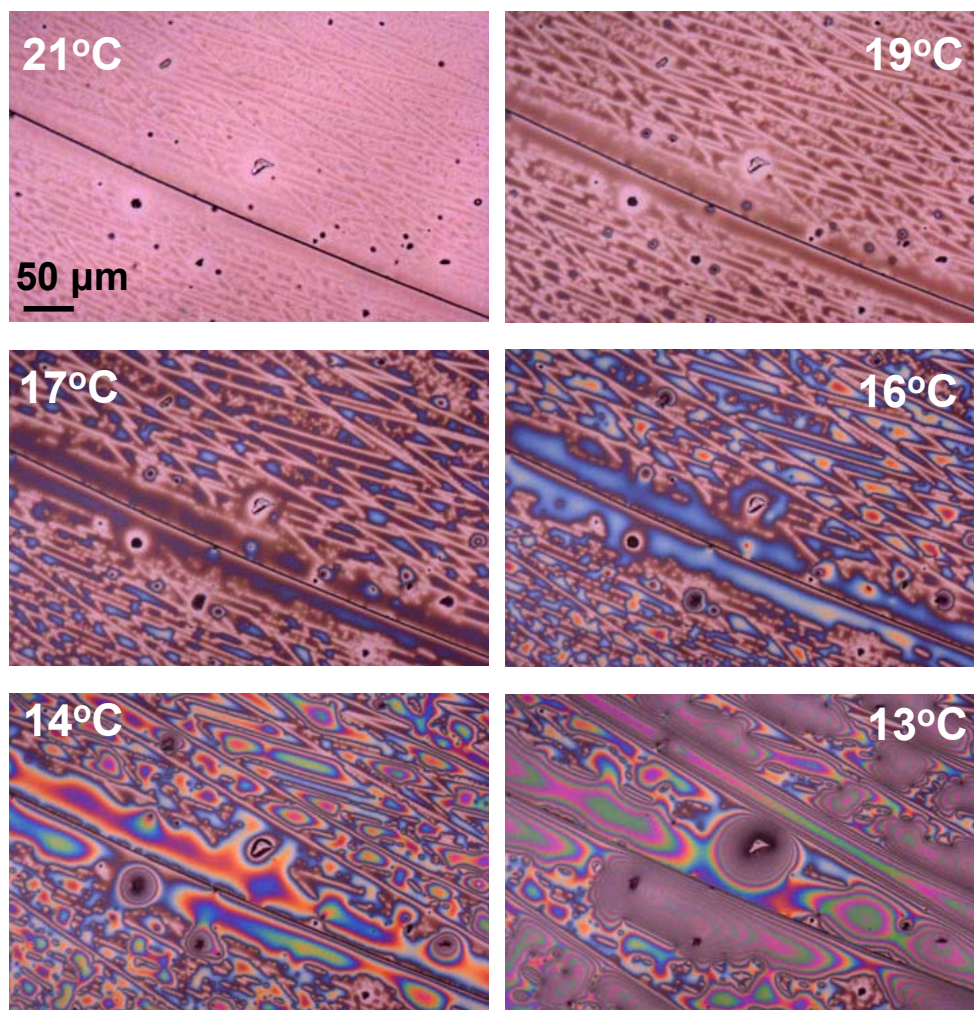
Figure 3.13: Optical microscopy images of a BaF$_2$(111) surface obtained by cleavage along the [$\bar{1}$10] direction. Images were taken at constant ambient RH~55% and variable sample temperatures, indicated in the figure. As temperature decreases the RH close to the surface increases and water adsorbs on the surface forming patterns very similar to the patterns formed by water bilayer patches observed using AFM.

$\sim$0.75 ML in good agreement with the most stable bilayer structure (distorted and cross-linked chain) found by ab initio calculations (0.54 eV) (*Nutt, DR; 2002*). At lower coverages, $\sim$0.2 ML corresponding to $\sim$5% RH, the measured adsorption enthalpy is $\sim$0.38 eV, which is very close to calculated binding energies of monomers of water on top Ba^{2+} ions from *ab initio* calculations (0.4 eV)(*Foster, AS; 2009 and Nutt, DR; 2002*). Such low energies suggest a scenario where water molecules readily diffuse as a 2D gas on the BaF_2(111) surface.

Assuming equilibrium conditions, we can consider the 2D gas/2D bilayer system analog to water droplets in contact with a solid surface in equilibrium with water vapor but reduced to two dimensions. The wetting of the water films at the step edges will then be determined by the interplay of different interfaces, namely, vapor-substrate, vapor-water film, water film-substrate, vapor-step, water film edge-step, and vapor-water film edge. The steps should exhibit different interfacial energies or line tensions since they correspond to different crystallographic directions (see Fig. 3.6), so that we will label the corresponding line tension according to the angle that the step direction forms with respect to the [$\bar{1}$10] direction: $\alpha = 0°$ ([$\bar{1}$10] itself), $\alpha = 15°$, and $\alpha = 30°$, respectively. The measured contact angles (θ) obtained from different images corresponding to different steps and different samples give $\theta = 15 \pm 5°$, $\theta = 50 \pm 10°$, and $\theta = 35 \pm 5°$ for $\alpha = 0°$, $\alpha = 15°$, and $\alpha = 30°$, respectively. Figure 3.14 shows the $\alpha = 15°$ case. Note that water preferentially wets along the [$\bar{1}$10] steps (more hydrophilic) and that the less hydrophilic step corresponds to $\alpha = 15°$. This is at first sight surprising since one would expect a higher degree of water attachment for the direction corresponding to $\alpha = 15°$, given the larger density of kinks relying on the ideal structure.

Defects at steps are known to play a key role as water nucleation sites. Hydroxide groups formed by water dissociation are known to be good nucle-
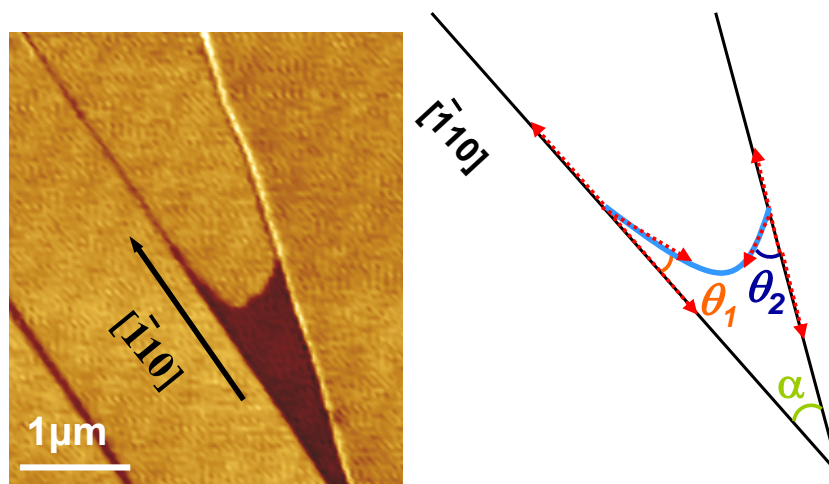
Figure 3.14: (a) Phase AFM image obtained in acoustic (tapping) mode of a BaF$_2$(111) surface obtained by cleavage along the [$\bar{1}$10) direction. The image shows a detail of a water meniscus between two steps forming an angle of 15° evidencing two different contact angles. At the step along the [$\bar{1}$10] crystallographic direction the contact angle is lower (more hydrophilic) than at the step at 15° from this direction. A scheme indicating the relevant angles and directions is shown in (b).

ation sites, as discussed above for terraces. In addition, the formation of BaO at step edges has been considered a better nucleation site for water than regular defect sites (*Wu, Y; 1994*). In our case, since our experiments provide no chemical information, we cannot be more explicit on this point. However, we do observe that the steps with presumably larger defect density turn out to be the less hydrophilic.

Contact angle values obtained along straight steps are not reliable due to pinning effects, thus information on wetting has to be extracted using a different approach. An example is shown in Fig. 3.10 (c). The step running along the [$\bar{1}$10] direction (A) is fully covered with water as it would be expected for a hydrophilic interface. However, the adjacent step (B) is covered with 2D droplets, thus exhibiting a less hydrophilic character. The additional modulation in shape is due to thermal fluctuations, where molecules

flow along the steps (periphery diffusion), move from steps to terraces and then reattach to the step at different sites (terrace diffusion), and move between the steps and terraces with no correlation between motion at different sites (attachment-detachment) (*Jeong, HC; 1999*).

According to Marmur, θ does not depend on the geometry of the system (in this case triangular) if the motion of the contact line is not constrained (*Marmur, A; 1996*). In this case the measured contact angles correspond to their intrinsic values. The fact that for $[\bar{1}10]$ steps θ exhibits the same values for both the α=15° and α=30° geometries strongly suggests that the measured θ values correspond to intrinsic values, given that the defect density is higher for the α=15° case, which should induce a higher probability of pinning.

An analysis based on the heterogeneous growth model of Chernov, where the Gibbs free energy of the system involving all interfaces is considered, does not lead to any quantitative conclusion since the concerned energies are unknown. On the other hand one should be cautious when comparing calculated interfacial energies with experiments performed in ambient conditions since, to our knowledge, all such energies have been computed in ideal conditions, that is, involving solid-vacuum interfaces instead of solid-vapor interfaces (*Puchin, VE; 2001*). In fact one would expect solid-vapor interfacial energies to be smaller than their solid-vacuum counterparts, based on experimental evidences (*Bailey, AI; 1967*). We believe that the involved interfacial energies should be of the order of 0.073 Nm^{-1}, the well-known value for vapor-liquid interfaces for pure water and at RT (surface tension), and well below the surface energy value of the (111) surface of BaF$_2$, estimated to be 0.33 Nm^{-1} according to *ab initio* calculations (*Shi, H; 2006*). As an illustration example, just mention the case of the liquid water-ice interfacial energy, which has been experimentally determined as 0.03 Nm^{-1} (*Luo, SN; 2005*). We should add that the reduction of the water bilayers down to

nanometric dimensions should increase the interfacial energies, as suggested by experimental evidence by grazing-incidence x-ray scattering (*Fradin, C; 2000*) and AFM measurements (*Fraxedas, J; 2005*).

The apparent contradiction of a weak water-surface interaction, as theoretically predicted and experimentally verified, which leads to a high surface diffusion and the observed macroscopic high degree of wettability, can be thus explained by the accumulation of water at steps, where those along the $[\bar{1}10]$ directions significantly contribute due to their hydrophilic character.

3.3.2   Water-induced surface pitting

As mentioned above, Conrad *et al.* showed experimentally that the pitting of a submerged BaF$_2$(111) surface dramatically improves its ice nucleating ability (*Conrad, P; 2005*). In that study AFM images of BaF$_2$(111) surfaces were shown after immersion in water. The topography evidenced rough surfaces with pit patterns with height of 20-40 nm. We decided to do a more complete examination of the modifications of the BaF$_2$(111) surfaces induced by water dissolution. Freshly cleaved BaF$_2$(111) crystals were immersed in Milli-Q water for a controlled amount of time and then dried with nitrogen and immediately imaged with AFM. In Fig. 3.15 we show images of the surface for different immersion times. For short times a homogeneous roughness of the surface is observed and the triangular structures start to become visible. For immersion times larger than 15 seconds, triangular etching pits can be clearly observed on the surface. A close look at the pits reveals a stepped structure that forms equilateral triangles over the entire surface. The directions of the steps forming those triangles correspond to $[\bar{1}10]$ directions, which are hydrophilic as discussed above. For larger times structures with steps forming angles of 60° and 120° can be observed on the surface, again all of them belonging to the $[\bar{1}10]$ family. Such structures are very similar
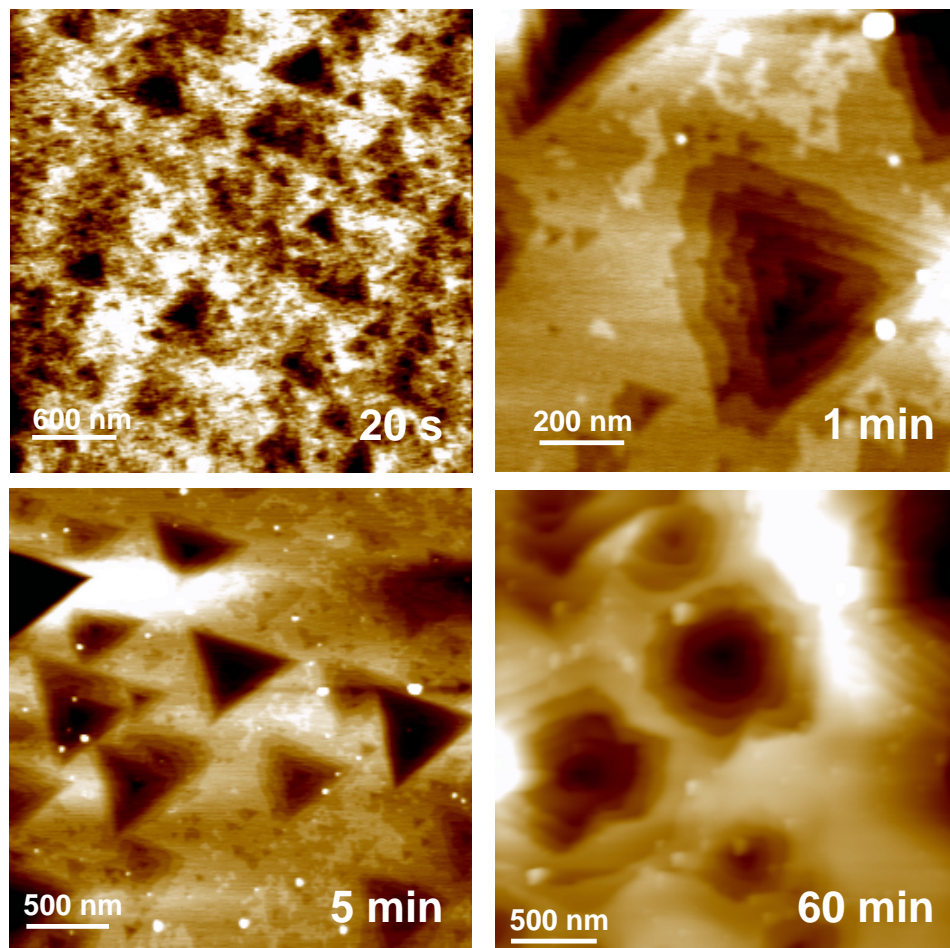
Figure 3.15: Topographic AFM images obtained in acoustic (tapping) mode of BaF_2(111) surfaces obtained by cleavage and then immersed in water for different times: 20 s, 1 min, 5 min, and 60 min. For immersion times higher than 15 s triangular pits produced by water etching can be observed. The directions of the triangles correspond to $[\bar{1}10]$ crystallographic directions. For large immersion times triangular as well as hexagonal step structures can be observed. All images were taken at RT and RH<10%.

to those formed by etching of different substances on CaF$_2$(111) (*Motzer, C; 2009*). A surface rich on such steps would induce a network of water bilayers stabilized by the sites and would enhance multilayer ice growing in a more efficient way as compared to cleaved BaF$_2$(111) surfaces.

3.4 Is I$_h$ the ice structure formed on BaF$_2$ surfaces?

Figure 3.16 shows a tapping mode AFM image of a BaF$_2$(111) surface cleaved in air and taken at RH$\sim$50%. The left and right images correspond to topographical and phase images, respectively. The topographical image shows two atomically flat terraces covered by $\sim$1 nm high islands and separated by a $\sim$0.4 nm step (the step that crosses the image from top to bottom). The step height corresponds to the distance between two adjacent trilayers (0.36 nm). The phase image exhibits clearly differentiated regions, where topographically higher regions exhibit negative phase contrast. Note that the islands are not completely compact, showing some pits that are clearly seen in the phase image. The images resemble AFM images previously obtained in noncontact mode by Miura (*Miura, K; 1995*). In that work, the islands were interpreted as water droplets grown on a continuous water film. It has to be pointed out that the images were taken in tapping mode and certainly no attempt to work in a noncontact regime was ever tried at this point. In fact, liquid water on surfaces can be only imaged by AFM when working in noncontact regimes and in special cases as droplets confined in nanostructures (*Luna, M; 1999. Fraxedas, J; 2005. Santos, S; 2011*). The fact that the $\sim$1 nm high islands can be imaged in tapping mode without particular experimental conditions points toward a solidlike nature. Phase contrast probably arises from the capillary interaction between the islands and the water layer

covering the tip. In some experiments it was possible to image the islands even in contact mode as shown in figure 3.17. In this mode, the liquid water on the bare $BaF_2(111)$ surface would be dragged by the contact with the tip so only a solidlike nature of the islands can explain such images.
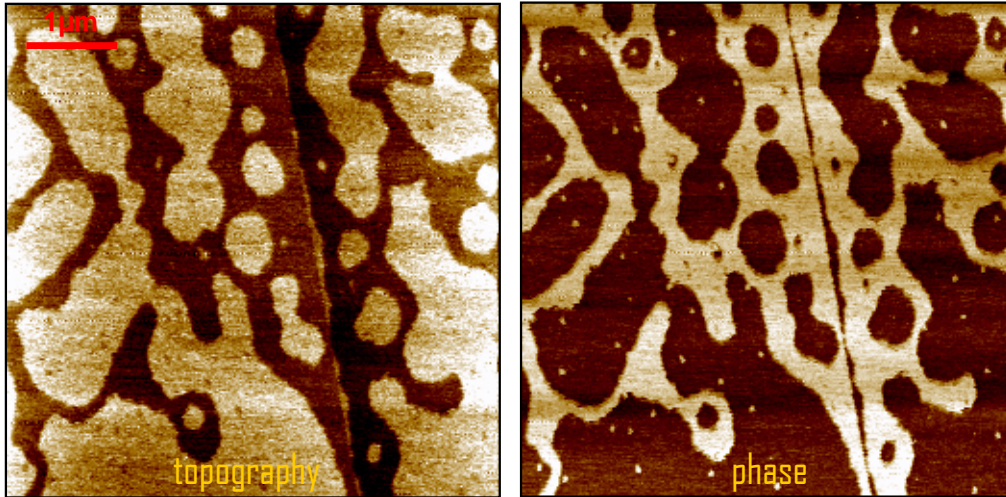

Figure 3.16: The left and right images correspond to topographical and phase images, respectively, of adsorbed water on BaF_2 surface. Bright islands can be observed on two flat terraces separated by step corresponding to adsorbed water films. In the phase image, a dark contrast can be observed at the islands. The conditions of this image are: 44% RH, T=8°C and area=5x5μm^2.

Miura found that the small droplets grew with time, and after approximately 20 nim at 70% RH, a complete film was formed on the surface. The same behaviour was observed with a similar time scale, as illustrated in Figs. 3.18 (a)-(c). However, an inspection of a larger image of the measured zone [Fig. 3.6 (d)] reveals that water adsorption is in fact induced by the tip due to water neck formation between the tip and the sample (*Sacha, G; 2006*). Unscanned regions remain unmodified, exhibiting the same overall aspect as the beginning of the experiment [compare Fig. 3.18 (d) and (a)]. It can be percibed that the behavior is the same for surfaces with V-shape steps that flat surfaces (or parallel steps) as shown in figure 3.19.

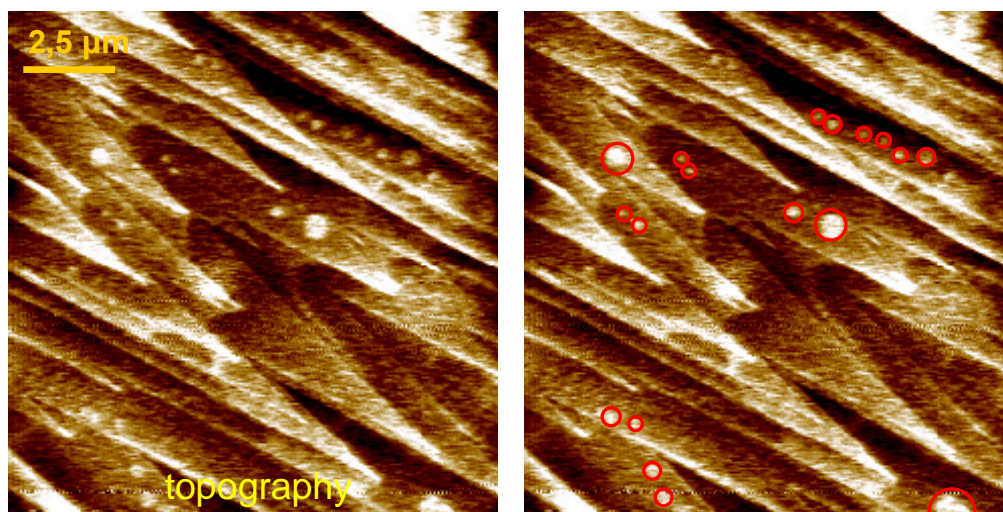Once the influence of the tip was identified, in order to minimize it and

Figure 3.17: The left and right images correspond to the same topographical image in contact mode. It shows some dots on the surface. Knowing that in contact mode liquid water is destroyed by the tip, the observed dots correspond to solid structures, then these represent ice islands.

avoid water neck formation, was performed SPFM measurements. In Fig. 3.20, we observe SPFM (left) and KPFM (right) images taken simultaneously on a BaF$_2$(111) surface at ambient conditions. In Fig. 3.20, (a), we can observe an irregular and discontinuous film partially covering two terraces. The simultaneous KPM image, Fig. 3.20, (b), shows that the areas covered by the film (we will qualify them as wet areas as opposed to the uncovered dry areas) show a bright contrast. Figures 3.20 (c) and (d) show SPFM and KPM images, respectively, of a stepped surface where terraces become almost completely covered by the film. In the corresponding KPM images, a clear voltage contrast between the dry and the wet regions is observed, exhibiting the wet regions more positive SPD (Surface Potential Difference) values, above 30 mV and with typical upper values of 60 mV, depending on the experiment. Positive SPD values imply a net dipolar contribution in the wet areas with dipoles pointing outside the surface (111) plane. From the SPFM images, the apparent water layer thickness results to be in the 0.6-1
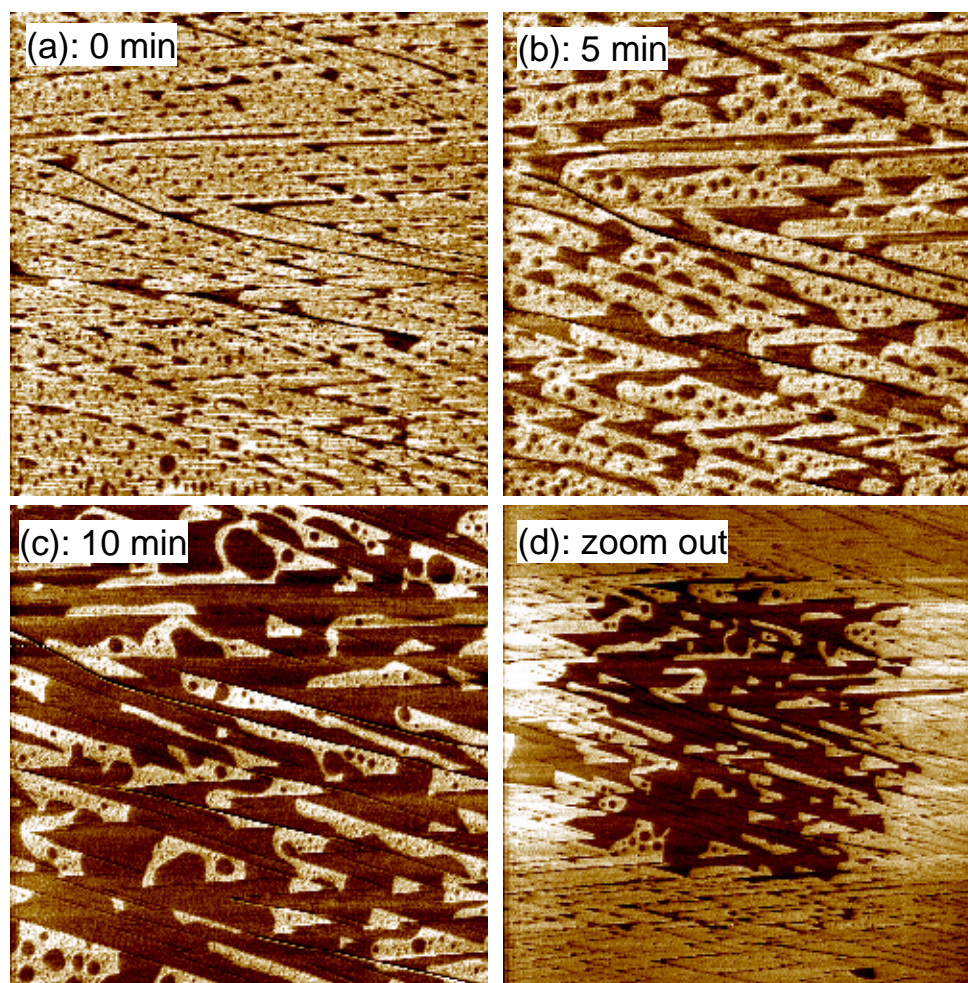
Figure 3.18: Four phase images of a wet surface (darker areas in the image) grows with time as more water molecules adsorb on the surface. If a larger image is taken (zoom out), only the region that has been perturbed by the tip shows a significant grow of the wet area. 9x9 μm^2.
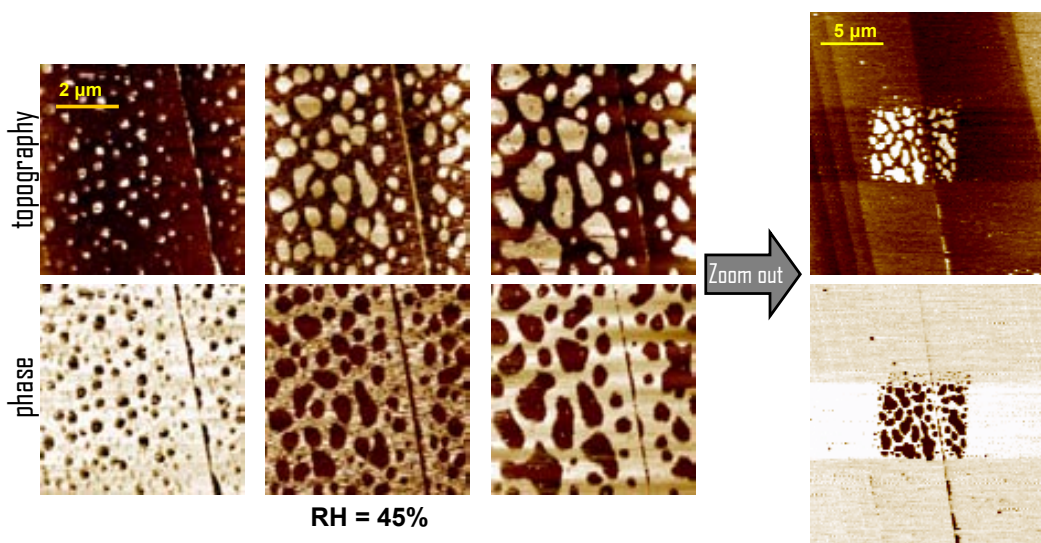
Figure 3.19: Top and bottom images correspond to topographical and phase images respectively. This is another exemple of perturbation by the tip on the surface. The time between the first image and the zoom out picture is 25 min.

nm range at ambient conditions. This value is in coincidence with the height as determined in tapping mode (*Santos, S; 2011*).

Figure 3.21 shows the time evolution of water adsorption on BaF$_2$(111) as a function of RH. In this case, BaF$_2$ single crystals were cleaved inside the glove box at low humidity ($\sim$ 10%) in oder to keep the surface clean and dry. After cleavage, the crystal surfaces were found to be always positively charged. The contact potential measured a few minutes after cleavage often exceeded 10 V, our instrumental upper limit for V_{dc}, the strong electrostatic interaction between the tip and the sample thus preventing useful measurements under such conditions. The fact that the charging was found to be always positive suggests that cleavage expels fluorine ions, leaving an excess of barium ions (Ba^{2+}) on the surface. This large initial contact potential decreases slowly with time but faster when RH is slightly increased. At already 20% RH, the contact potential turns out to be low enough ($<$5 V) allowing the performance
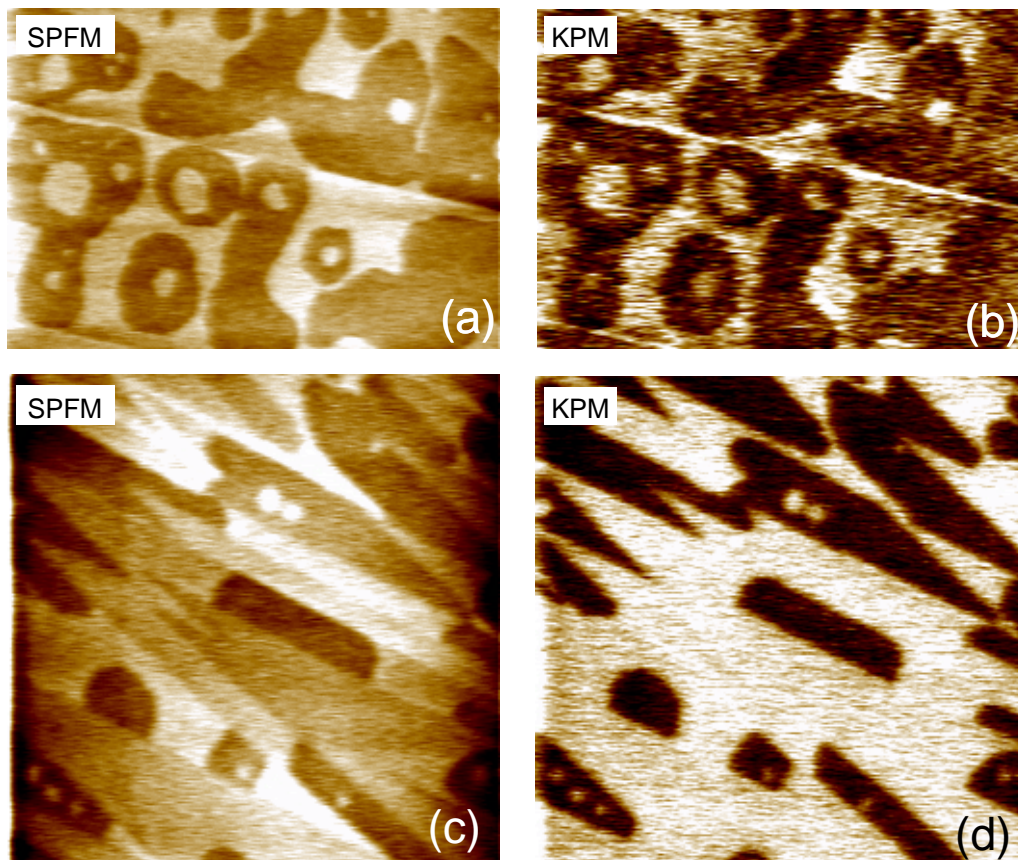
Figure 3.20: Two examples of SPFM and KPFM images taken on a BaF$_2$ (111) surface at ambient conditions (RH$\sim$50%). (a) SPFM image (12x8 μm^2) showing an irregular and discontinuous film partially covering two terraces. The simultaneous KPFM image (b) shows a bright contrast corresponding to wet areas covered by the film. (c) and (d) show SPFM and KPFM images, respectively, of a stepped surface where terraces become almost completely covered by the film. In the corresponding KPFM images, the contrast between the dry and the wet regions is rather large. SPDs of 30 to 60 mV can be measured from the KPFM images. The apparent thickness of the water film has been measured to be between 0.6 and 1 nm.

of SPFM measurements. The electrostatic compensation of the surface charge of the crystal is probably due to OH adsorption through water dissociation on the free sites left by fluorine ions, as previously suggested from x-ray photoelectron spectroscopy experiments (*Wu, Y; 1994*). SPFM and KPM images were taken in the 10%-70% RH range, and in figure 3.21 a sequence of SPFM and KPM images for selected values of RH is shown. At low RHs (<30%, top left corner in figure 3.21), some islands can be seen on the surface as well as some terraces completely covered by a water film.

KPM images show a contrast between the wet and the dry regions but with an opposite sign as compared to those observed at ambient conditions (we can compare with figure 3.20), with wet regions being darker (in other words, it has a more negative surface potential). Between 30% and 60% RH, a transition in the KPM images can be observed and in a dynamical process that typically takes between 20 to 40 min, the sign of the contrast between dry and wet regions continuously reverse recovering what was found at ambient conditions (compare images labeled 1 and 4 in the 30%>RH>60% region). If RH is lowered during the transition was found to be irreversible (see Fig. 3.25). Once the transition was completed, a decrease of RH reduced the SPD but the wet areas always kept a more positive surface potential value than the dry surfaces (Fig. 3.25). At RH~60% (bottom left corner in figure 3.21), the surface potential contrast tends to disappear. This corresponds to a full coverage of the surface by a water film. The time evolution of the SPD is summarized in figure 3.22.

3.4.1 Island heights

As mentioned above in section 3.2, in SPFM images, output signals correspond to topography and sample polarizability, and in the image both contributions are mixed. When imaging thin films on a substrate exhibiting
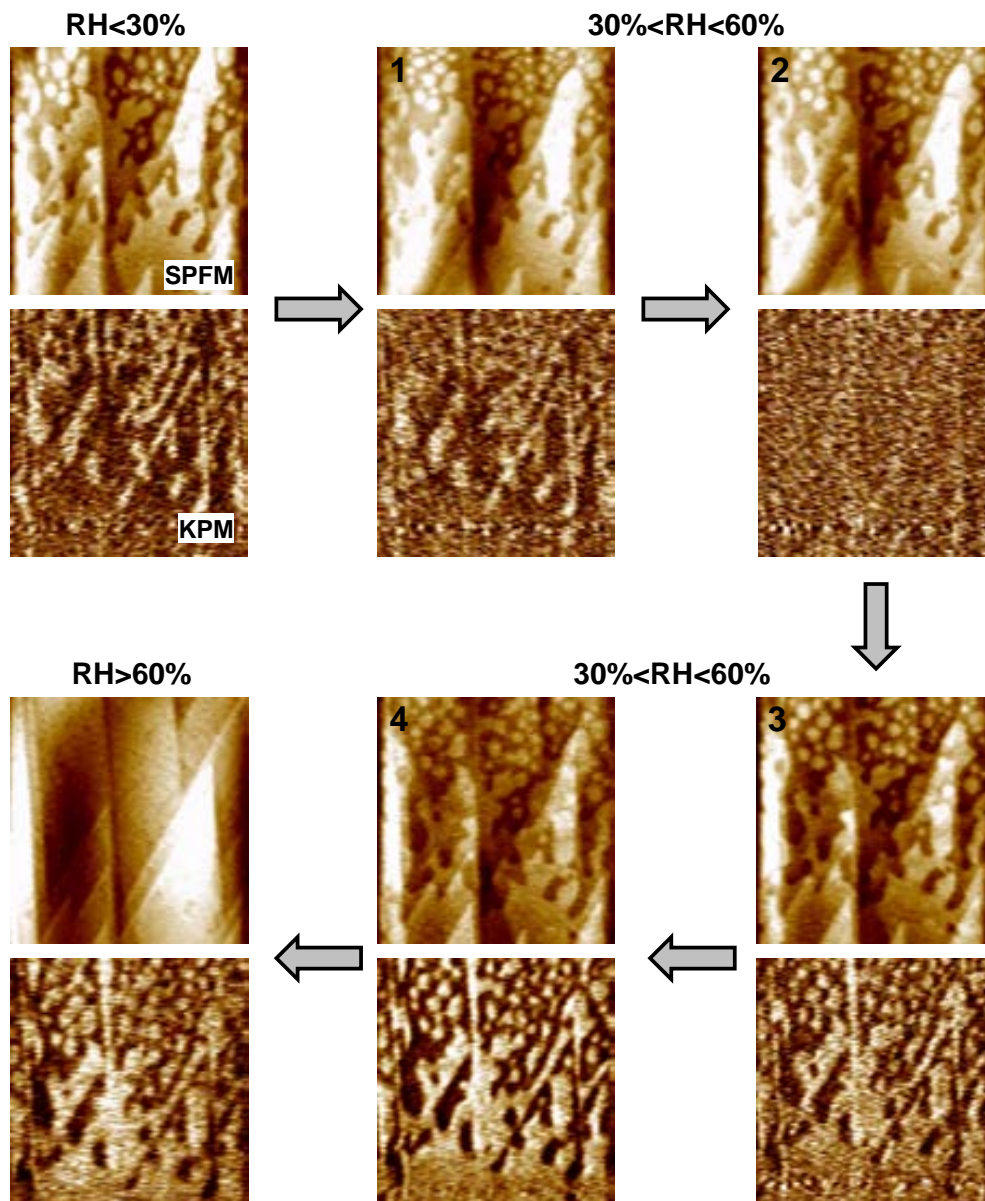
Figure 3.21: Evolution of water adsorption on $BaF_2(111)$ as a function of RH. 20x20 μm^2 SPFM and KPM images are shown for selected values of RH. At low RHs (<30%), some islands on the surface and some terraces completely covered by a water film can be observed. KPM images show a contrast between the wet and the dry regions but with an opposite sign as compared to those observed at ambient conditions (compare with the previous figure), with wet regions being darker (i.e., having a more negative surface potential). In the 30%>RH>60% region, the sign of the contrast between dry and wet regions continuously reverse recovering what was found at ambient conditions. For RH>60%, the surface potential contrast tends to disappear. This corresponds to a full coverage of the surface by a water film so that dry and wet regions can no longer be distinguished in the SPFM images.
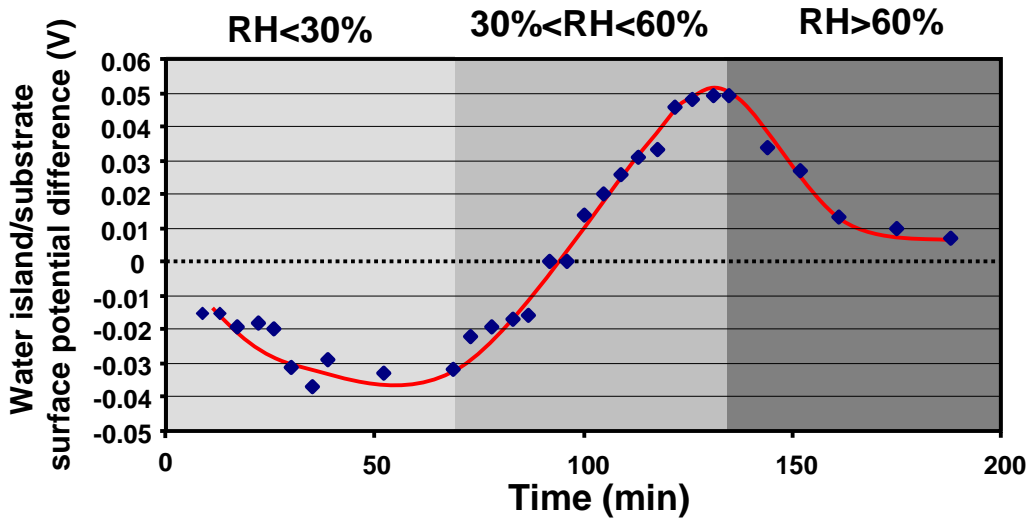
Figure 3.22: Time evolution of the SPD between wet and dry regions from KPM images of the previous figure. Notice the sign crossover at the 30%>RH>60% region from -30 to +50 mV. For RH>60%, the contrast disappears with time. Solid red line is just a guideline for the eye.

very different dielectric constants (ε), the apparent height of the films measured by SPFM could be very different from the real value (*Hu, J; 1995*) (we will see an example in chapter 4). As a general rule, the apparent thickness will be smaller than the real one if $\varepsilon_{film} < \varepsilon_{substrate}$, and is larger when $\varepsilon_{film} > \varepsilon_{substrate}$. The dielectric constant of BaF$_2$ ($\varepsilon_{BaF_2} = 7.3$) is considerably smaller than the dielectric constant of water or ice ($\varepsilon_{water(25°C)} \sim 80$), so that the apparent thickness in our images should be larger than the real one. From SPFM images, the real height can be estimated from a simple model approximating the tip as a point charge and using the image charge method to find the force applied to the tip (*Hu, J; 1995*). The observed apparent heights in ambient conditions span from 0.6 to 1 nm (see Fig.3.23), depending on the experiment, and the estimated real height using the mentioned model results between 0.3 an 0.5 nm. In the case of hexagonal I_h ice, the distance between two adjacent bilayers is $c/2 = 0.37$ nm and both planes of a bilayer are separated by ~ 0.1 nm (see Fig. 3.3). Adding an estimated bilayer-surface

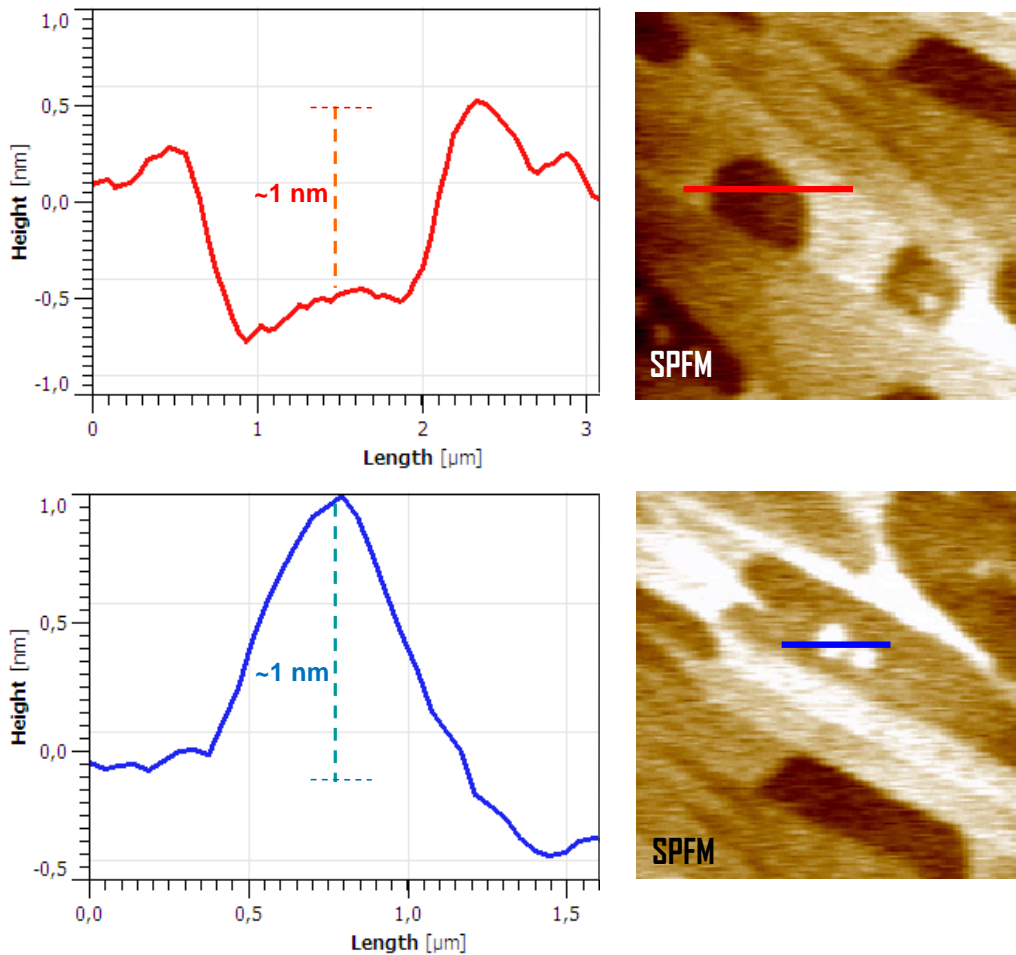distance of 0.2-0.3 nm, we obtain about 0.3-0.4 nm for a bilayer height, close to the estimated value.

Figure 3.23: SPFM images of BaF$_2$ with its profiles. The first one profiles a hole (water free) with a thickness of ~1 nm. The bottom one, profiles a water droplet of ~1 nm.

More elaborated methods (*Gómez-Moñivas, S; 2001*) can be used to model the tip but they lead to similar results, given the experimental uncertainty. The apparent height is approximately constant up to 55% RH, and then it strongly drops with increasing RH down to approximately 0.2 nm at 65% (see Fig. 3.24). This is due to the fact that at higher humidities, the surface becomes completely covered (see Fig. 3.21, RH>60%). The decrease

of the apparent height is due to the adsorption of water molecules on the dry areas, thus reducing the dielectric constant contrast. At 65%, we have a surface fully covered by water molecules but with different thickness on different regions. The measured height of the higher regions becomes then not influenced by variations on ε, and we measure distances close to real thicknesses. The islands height thus corresponds to two atomic layers (single bilayer). Miura *et al.* found estimated real heights of $\sim$0.5 nm from their 1 nm films due to ε contribution although they were using a different SPM noncontact operation mode (*Miura, K; 1999*).
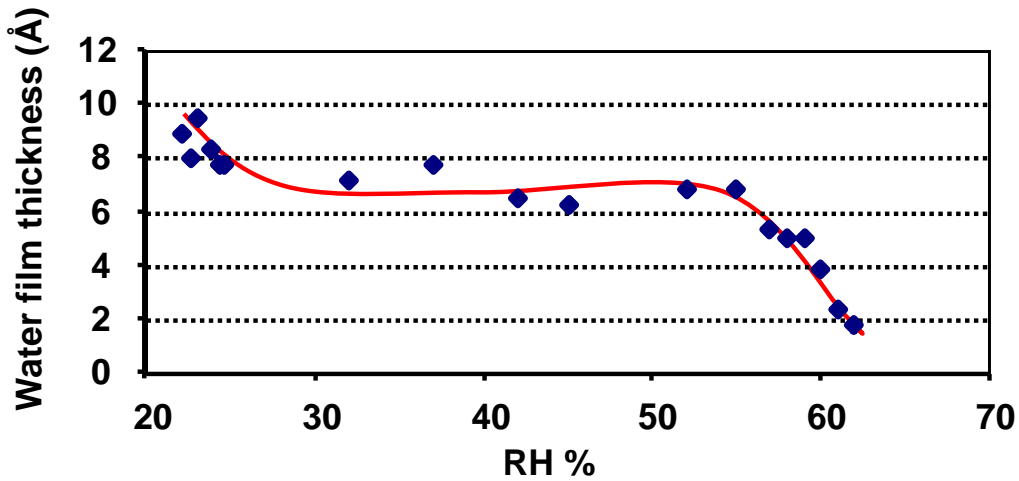

Figure 3.24: Evolution of the apparent height of the water islands with RH. It ranges from 0.6 to 1 nm until high humidity conditions are reached (RH>60%). The apparent height is overestimated due to the contribution in the SPFM image of the important difference between the dielectric constant of water ($\epsilon_{water(25°C)} \sim 80$) and of the BaF$_2$ ($\epsilon_{BaF_2} = 7.3$) substrate. At high humidity, the apparent height drops and differences as low as 0.2 nm can be measured due to the wetting of the entire surface. The red solid line is just a guideline for the eye.

3.4.2 SPD sign crossover

From adsorption isotherms of water on BaF$_2$(111) obtained from combined IR experiments (*Sadtchenko, V; 2002*) and MD calculations (*Wassermann,*

B; 1994), a model was proposed for the evolution of water structures as a function of humidity. At low coverages (RH<20%), an equilibrium between a 2D gas of isolated water molecules adsorbed on Ba ions and 2D icelike islands was suggested. These islands would consist of single ice I_h bilayers with probably a few molecules adsorbed on top. At coverages between 1 and 2 ML (1 ML=1 water molecules adsorbed per surface barium ion), the bilayer would not yet be complete and the water film would still be formed by islands. At high humidity regimes (RH∼70%), the icelike structure would be completely disordered and the adsorbed water film would be liquidlike (*Nutt, DR; 2002*).

The here presented SPM experiments are in line with much results, although with some differences. As discussed above, the actual island heights would correspond to a single bilayer. We indeed observe 2D islands at RHs as low as 20% (see Fig. 3.21, RH<30%) as well as the coalescence of islands and the formation of a uniform film at high RHs (see Fig. 3.21, RH>60%). In the high humidity regime, the SPD observed in the KPM images tends to disappear indicating the loss of any dipolar preferential orientation. This transition was observed at constant RH (65%) with a time scale of 20 min, which most probably corresponds to the disordering of the water film due to massive adsorption of water molecules on top of the icelike bilayers.

Let's explore the SPD sign crossover encountered at intermediate RHs (Fig. 3.21, 30%<RH<60%). This change, from negative to positive, takes about 40 min at constant 30% RH and becomes faster if the RH is increased during the experiment. Hence, the RH value, at which the transition is complete, strongly depends on how fast RH is varied. RH∼30% was found to be the minimum value upon which the transition was observed. For samples cleaved at ambient conditions (∼50% RH), only positive SPD values were observed. Sadtchenko *et. al.* found that for coverages above 1ML (RH>40%)

adsorption isotherms are irreversible. Hysteresis in the isotherms suggests that relevant changes in the water structure should be at hand when the film reaches a critical thickness between 1 and 2 ML (*Sadtchenko, V; 2002*). A transition from a highly ordered hexagonal icelike structure to a liquidlike disordered structure was proposed for coverages above 1 ML to explain the observed hysteresis. This process was considered to be a kinetic process that would be completed on a time scale of 10-20 min. According to their results, 1ML coverage should be at $\sim$40% RH. This humidity value is close to the RH where the surface potential transition is observed. However, there are some indications suggesting that the observed transition is not related to the transition from an icelike to a liquidlike structure but to a solidlike-solidlike transition. First of all, we are able to image water islands at 50% RH, once the transition is already completed, using tapping or contact mode. This would be hardly achievable with a liquidlike layer. Second, the contact potential measurements indicate that the dipoles of the water molecules forming 2D islands have to be in average oriented with a component normal to the surface. A transition from negative to a strong positive SPD indicates that water molecules, once the transition is complete, should be in average oriented with their dipoles normal to the surface, pointing the H-atoms perpendicularly to it. This is in contradiction with a disordered liquidlike layer scenario, where the water molecules would have no preferential orientation.

3.4.3 Structure of the water bilayer

Now the KPFM results are analyzed within the hexagonal I$_h$ model. The surface potential film of a monolayer film on a substrate can be expressed by (*Wu, Y; 2003*):

$$V_{film} = -\frac{(\phi_{subst} - \phi_{tip})}{e} + \frac{\mu}{A_{film}\varepsilon_{film}\varepsilon_0}, \qquad (3.2)$$
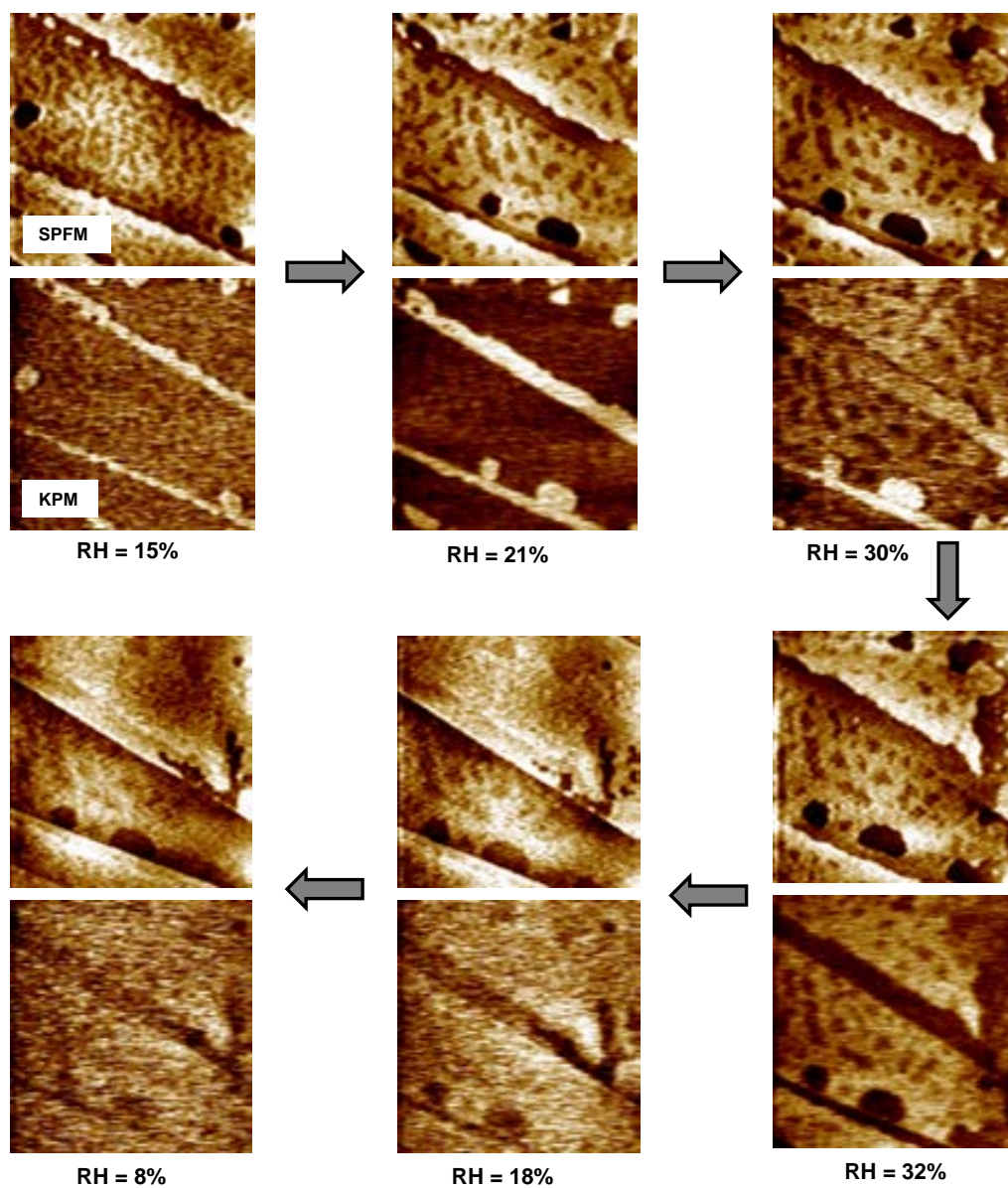
Figure 3.25: Evolution of water adsorption on $BaF_2(111)$ as a function of RH. SPFM and KPM images are shown for selected values of RH. At low RHs (below 30%), we can observe some islands on the surface and some terraces covered by a water film. KPM images show a contrast between the wet and the dry regions. From 30% RH, the sign of the contrast between dry and wet regions continuously reverse recovering what was found at ambient conditions. After the SPD crossover, we tried to retorn to the initial point with the decrease of humidity and no reversible process is given.

where ϕ_{subst} and ϕ_{tip} represent the work functions of the substrate and the tip, respectively, e the electric charge, μ the net dipole of the molecules forming the monolayer normal to the substrate, A_{film}, the area occupied by each molecule with nonzero dipole, and ε_{film} and ε_0 the permittivities of the film and of free space, respectively. The first term in Eq. (3.2), $\phi_{subst} - \phi_{tip}/e$ represents the contact potential difference between the substrate and the tip, and the second term, $\mu/A_{film}\varepsilon_{film}\varepsilon_0$ the contribution to the surface potential from the dipole moment of the molecules forming the monolayers as derived from the Helmholtz equation. The SPD between a region covered by the monolayer and a region with bare substrate can be then written as

$$\Delta V = V_{film} - V_{subst} = \frac{\mu}{A_{film}\varepsilon_{film}\varepsilon_0}, \qquad (3.3)$$

where only the term related to the dipole moments of the film remains. It is important to notice that this difference is independent of the tip. Equation (3.3) can be easily extrapolated to our particular case of a bilayer on a BaF$_2$ substrate, leading to the expression

$$\Delta V = V_{bilayer} - V_{BaF_2} = \frac{\mu_{lower}}{A_{lower}\varepsilon_{film}\varepsilon_0} + \frac{\mu_{upper}}{A_{upper}\varepsilon_{film}\varepsilon_0} \qquad (3.4)$$

where μ_{lower} and μ_{upper} stand for the net dipole normal to the surface of the water molecules located at the lower or upper half of the bilayer (see figure 3.3 which refers to bilayer scheme of water on BaF$_2$), respectively, and A_{lower} and A_{upper} represent the areas occupied by molecules located at the lower or upper half of the bilayer, respectively. In the case of a I_h bilayer $A_{lower} = A_{upper} \sim 7$ molecules nm^{-2}, so that Eq. (3.3) can be used with $\mu = \mu_{lower} +$

μ_{upper} and $\varepsilon_{film}=\varepsilon_{bilayer}=\varepsilon_{ice(0_C^\circ)}\sim90$.

Then the contribution from each individual layer can be estimated. It seems reasonable to assume that water molecules of the lower half of the bilayer will be the most stable in the structure of the ice bilayer given that they are fully coordinated and structured by the Ba sublattice. It can be considered that they ideally from a uniform and rigid film with all the dipoles pointing in the same orientation with respect to the surface. In the ideal ordered I_h structure (ice XI; the most stable configuration of ice I_h), the water dipole of a molecule of the lower half has $\alpha\approx80°$ inclination with respect to the surface normal (c-axis) (see Fig. 3.26). Using basic trigonometry, we can calculate that the projection of the dipole on the normal direction is ~1 D, 0.34 times the total water dipole (2.95 D for liquid water and 3.09 D for ice). Using this value, together with $A_{lower}\sim7$ molecules nm^{-2} and ε_{film}, in the first term of Eq. (3.4), we obtain $\Delta V_{lower}\sim30$ mV, where Δ_{lower} represents the contribution of the lower half to the SPD between BaF$_2$ and the lower half of the bilayer.
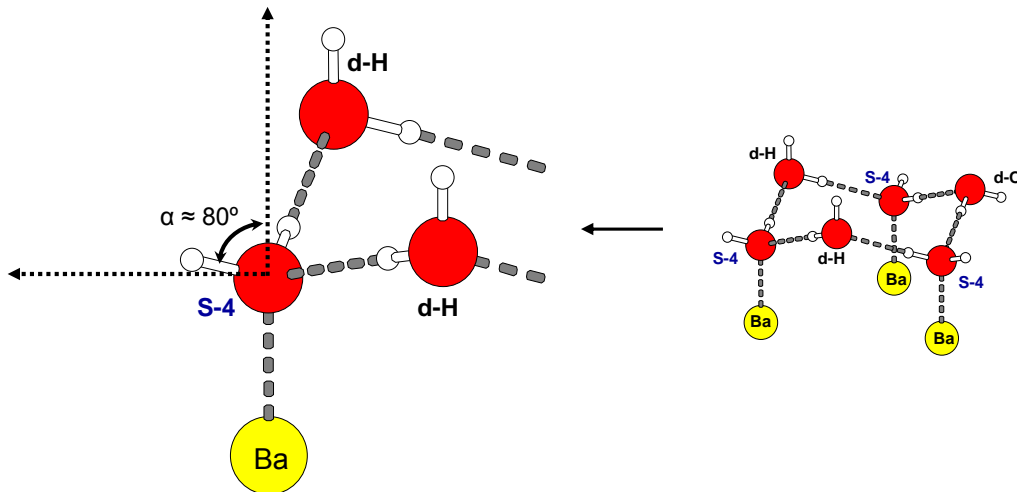

Figure 3.26: Angle inclination with respect to the surface normal of a ideal ordered I_h water molecule.

A similar calculation can be used for the upper part of the bilayer. Again, in an ideal ordered I$_h$ structure, all molecules at the upper bilayer would have H-bonds aligned along the c-direction. In this case, the dipole of the water molecules in the normal direction is ∼2D, resulting in ΔV_{upper}∼60 mV, which added to ΔV_{lower} would give a total of ΔV∼90 mV. This value is noticeably larger than the experimentally observed SPD value (ΔV≤60 mV). Highly ordered structures such as ice XI should be discarded since they can only be achieved at cryogenic temperatures (*Fukazawa, H; 1998*). A I$_h$ basal plane formed by cleavage of an ice crystal is expected to have half of the molecules in the d-H configuration and half of them in the d-O configuration according to the Bernal-Fowler rules, thus giving μ_{upper}=0 (*Devlin, JP; 1995*). This surface structure corresponds to a high energy configuration and it relaxes in the presence of sufficient thermal energy (80-200 K). Thus, we would expect the upper half of the bilayer to be disordered with a negligible contribution to the SPD. However, since the experimentally observed SPD is significantly larger than ΔV_{lower}, it can be concluded that the I$_h$ scenario is not the most appropriate in line with the combined experimental-theoretical work claiming the instability of the I$_h$ bilayers on BaF$_2$ (*Sadtchenko, V; 2002*).

In solidlike water bilayers, as in the present case, the substrate and the small thickness play a key role providing stability and orientation of the molecules in the layer. The actual configuration should be regarded as dynamic, with the water vapor/solidlike layer in equilibrium, with adsorption of water molecules involving continuous changes in structuring due to relaxation of H-bonds and molecular orientations.

The negative SPD value at low RHs can be tentatively explained if the substrate plays even a more dominant role in the presence of a less dense water vapor. In this case, fluorine atoms may attract hydrogen atoms reversing the sign of the dipoles (*Sadtchenko, V; 2002*). In this case, one could tentatively

propose a dominant d-O orientation of the upper half molecules in order to make them coincide with the experimentally observed value (-30 mV). However, in some experiments negative SPD values as low as -80 mV have been observed, which can hardly be explained with a I_h bilayer structure. At this point, one important consideration has to be taken into account concerning the stability of this distribution. It was mentioned that SPD envolves from negative to positive with time and, when decreasing RH, the negative values are not restored. This means that the positive SPD values correspond to a more stable phase and that the structure corresponding to negative SPD values is metastable, probably a kinetic phase.

The KPFM results clearly demonstrate a relevant net dipolar distribution of the bilayer films, so that molecular models should take into account this experimental fact. A potential candidate structure, a distorted cross-linked chain structure, was proposed by Nutt and Stone as the most likely structure instead of the perfect water bilayer (*Nutt, DR; 2002*). In this configuration, many molecules situated at the upper part of the bilayer show H dangling bonds, suggesting a positive dipole normal from the surface. However, the present knowledge of the bilayer structure is far from being well established, calling for more experimental and theoretical investigations.

3.5 Which is the role of the surface lattice constant?

This section presents a comparation the water adsorption behavior between $BaF_2(111)$ and its isostructural partner $CaF_2(111)$. CaF_2 has a lower surface lattice constant, 3.845 Å, which translates into a mismatch of about 15% (see Fig.3.27). High-quality (111) surfaces of both materials can be obtained by cleavage and turn out to be ideal for fundamental studies on the importance

of lattice parameters matching with ice.

Both of freshly cleaved surfaces exhibit micronsized flat terraces separated by steps. Depending on the cleavage direction the step structure can be formed either by long parallel steps along $[\bar{1}10]$ directions or by triangular (V-shaped) structures involving both $[\bar{1}10]$ and higher Miller index directions (i.e. $[11\bar{2}]$) (*Engelhardt, JB; 2000 and Hirth, S; 2006*). In our experiments the angle formed by both directions ranges from 10° to 45°, being the most common 15° and 30° as explained above. The isostructural character of both BaF$_2$ (111) and CaF$_2$ (111) translate into identical surface morphologies, so that it is impossible to distinguish them directly from the images, unless and accurate determination of the step heights is done (3.6 and 3.2 Å for BaF$_2$(111) and CaF$_2$(111), respectively).
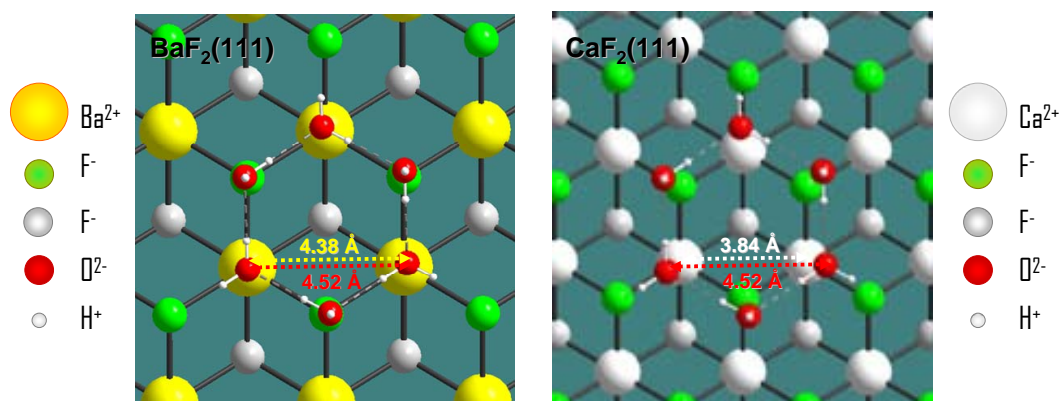

Figure 3.27: Scheme of an idealized I$_h$ bilayer hexamer on a (111) BaF$_2$ (a) and CaF$_2$ (b) surface. Barium, calcium, upper fluorine, lower fluorine, oxygen and hydrogen atoms are represented by yellow, cyan, light gray, gray red and white balls, respectively. The distances between the three water molecules forming the lower part of the bilayer structure almost match the distances between Ba ions in BaF$_2$ enabling pseudoheteroepitaxy. However, on CaF$_2$ the difference is too large to accommodate a hexamer on the surface.

Figure 3.28 shows AM-AFM phase images of cleaved BaF$_2$(111) (a,b) and CaF$_2$(111) (c,d) surfaces taken at ambient conditions. The interaction of the

tip with the sample is different on the dry and the wet areas of the surface. The different interaction induces a large phase contrast in the phase images that changes from negative values on wet regions to positive on dry regions, if set to $0°$ at free oscillation far from the surface. On $BaF_2(111)$ water patches fill the vertexes of the triangular steps, specially for lower terraces forming asymmetric menisci [see Fig. 3.28, (a) and (b)]. The asymmetry arises from the different wetting properties of the steps forming the triangular structure as discussed in *Cardellach, M; 2010*. However, on $CaF_2(111)$ the presence of menisci under the same experimental conditions is not observed [see Fig. 3.28, (c) and (d)]. Thus, water decorates the steps but menisci are exclusively observed on $BaF_2(111)$.

Figure 3.29 shows topography (left) and phase (right) images of a $CaF_2(111)$ surface taken at ambient conditions scanning over the same area (the elapsed time between two consecutive images is 15 min). Water adsorption starts at the terraces forming small rounded islands and narrow ribbons following the step edges. As more water is adsorbed on the surface the rounded islands grow and coalesce while the films decorating the steps become wider. However, no filling of the triangular steps vertexes is observed even at high coverages (compare with figures 3.5 and 3.11).

The differences in water adsorption scale but have a profound effect on the way the surface wets on a macroscopic level. Using an optical microscope with a modest magnification we already reported that wetting of a $BaF_2(111)$ surface follows the step structure at the surface (*Cardellach, M; 2010*). This effect can be observed in figure 3.30 (left), where we show optical microscopy images with a $10\times$ magnification taken on a freshly cleaved BaF_2 (111) surface for decreasing sample temperature, similar to what was shown in figure 3.13. Note that the V-shaped steps are readily observable with the optical microscope, due to the contrast induced by the adsorbed water (steps are not

BaF$_2$(111)
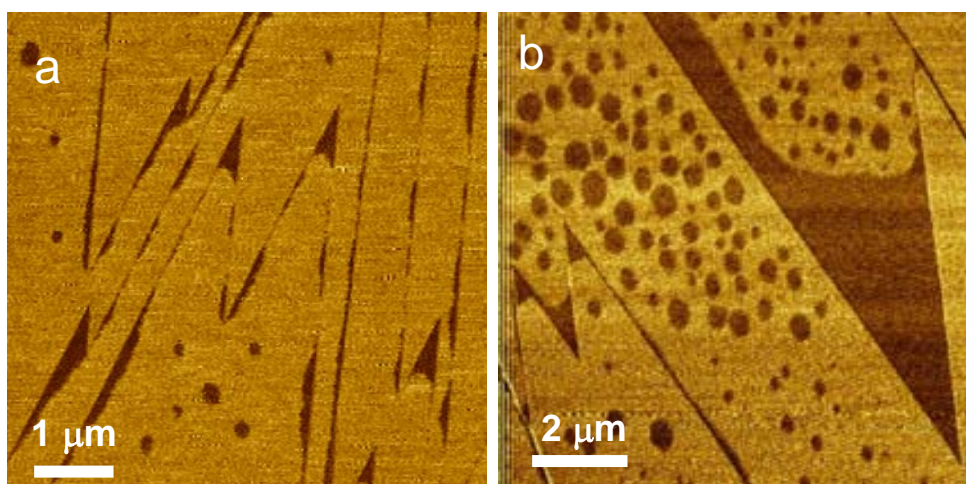
CaF$_2$(111)
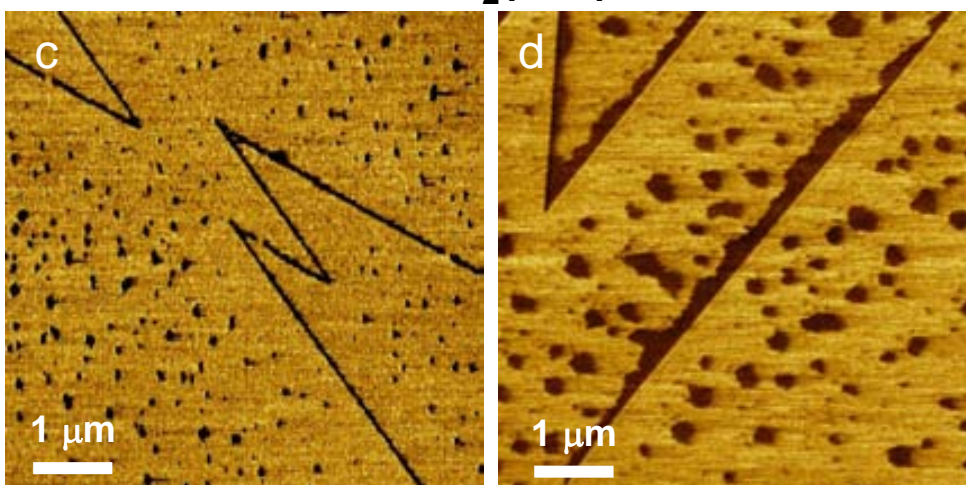

Figure 3.28: Phase contrast images taken at ambient conditions of water patches (darker in the images) absorbed on BaF$_2$(111) (a, b) and CaF$_2$(111) (c,d). The V-shape step structure of the surface induces the formation of meniscii on BaF$_2$(111) but not on CaF$_2$(111)
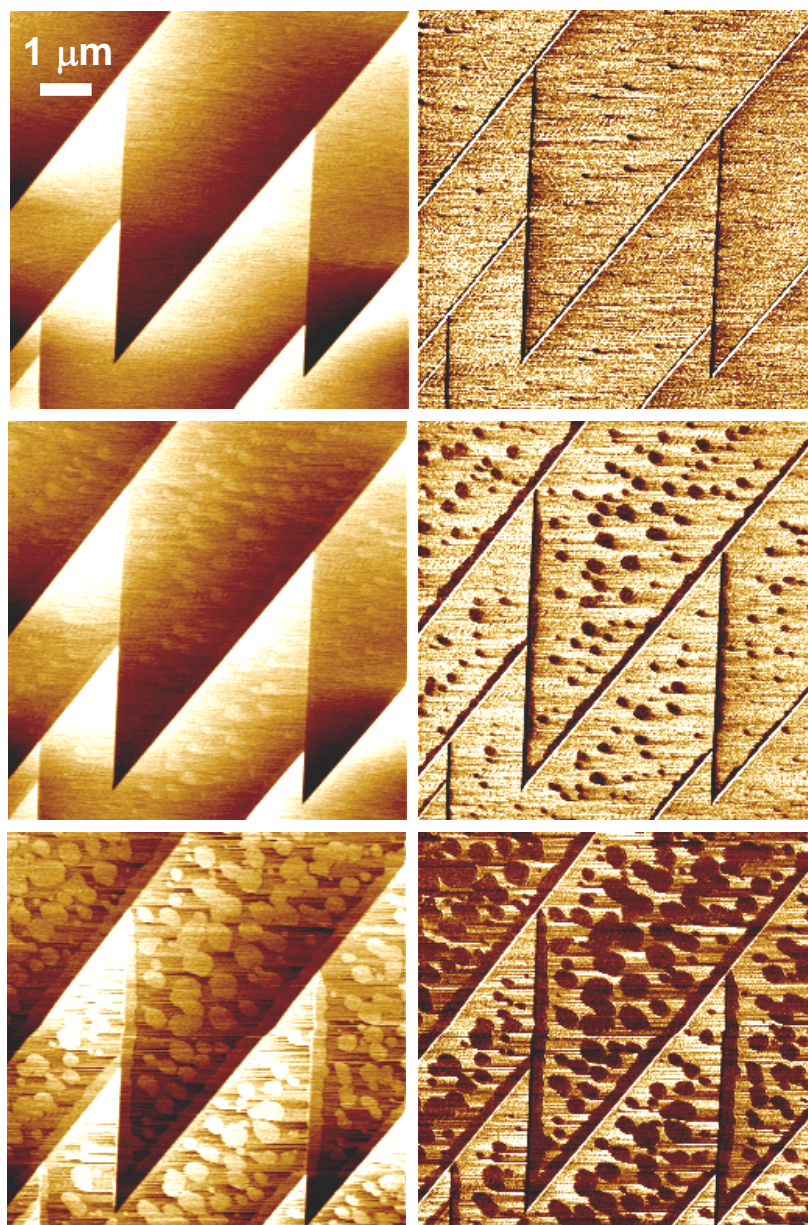
CaF$_2$(111)

Figure 3.29: SFM topography (left) and phase (right) images of water on CaF$_2$(111). Repeatedly scanning over the same area induces water adsorption. Even at high coverages the filling of the step vertexes is not observed. The elaspsed time between two consecutive images is 15 min.

observed in dry conditions). However, on CaF$_2$(111) [Fig. 3.30 right] water patches are not strongly affected by the steps and when observed through the optical microscope they show small rounded shapes that do not reveal any step structure. On CaF$_2$(111) the only observed influence of the step structure on the water patches is the presence of a higher concentration of rounded patches along large cracks of the surface that were already observed at dry conditions. On BaF$_2$(111) as coverage increases the poliedric water patches grow and interconnect between them forming a complex net of patches that minimizes the presence of dry spots. On the other hand on CaF$_2$(111) the rounded patches connect between them forming a labyrinth structure full of dry spots.

CaF$_2$(111) was also investigated using SPFM and KPFM in order to obtain more information on the water dipole distribution [see Fig. 3.31 and compare to previous results on BaF$_2$ (111) in section 3.3]. Accurate KPFM measurements on BaF$_2$(111) at low humidity, already reported in a previous study, have shown a negative CPD on water films as compared to dry areas. This contrast was interpreted as a negative dipole induced by a preferential orientation of the water molecules with the hydrogen atoms pointing towards the sample. As humidity increases there is a sign crossover of the contact potential contrast and the water film showed a maximum positive contrast of about 50 mV at 50% RH (see section 3.4.2). This sign crossover suggest a dipole flipping of the water molecules to an orientation with the hydrogen pointing up as more water molecules adsorb on the surface. In figure 3.31 we show typical SPFM and KPFM images of a BaF$_2$(111) surface at ambient conditions where the triangular shape water structures can be clearly observed as well as rounded features with the same contact potential. Contact potential differences between dry and wet areas on CaF$_2$(111) are not so well defined and they do not show any homogeneous distribution over the
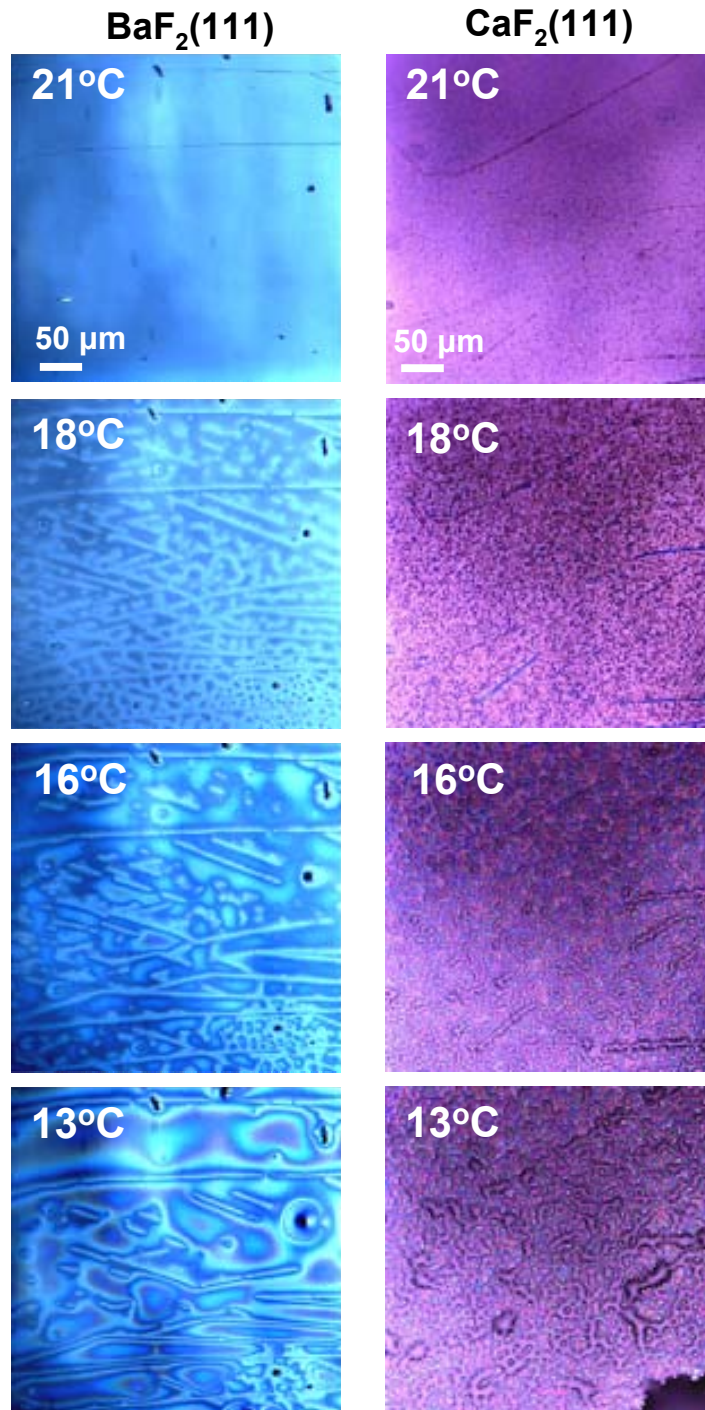
Figure 3.30: Water adsorption on $BaF_2(111)$ (left) and $CaF_2(111)$ (right) as observed by optical microscopy with a magnification of $10\times$. As the sample temperature is decreased the relative humidity in the vicinity of the sample increases and more water adsorbs on the surface. Water films on BaF_2 show poliedric edges revealing the surface step structure. On CaF_2 water small rounded droplets are formed that coalesce with increasing coverage.

water film indicating a more random orientational distribution of the water molecules forming the film. For all the measurements performed on CaF$_2$ (in the 5% to 60% RH range) water films always show a positive contrast. This contrast is maximum at low humidities (40 mV) and it reduces as RH is increased disappearing at around 60% RH. A negative contrast is never observed for water films on CaF$_2$(111).

3.5.1   Comparison between BaF$_2$ and CaF$_2$

DFT calculations have shown that at RT water monomers adsorbed on both BaF$_2$(111) and CaF$_2$(111) surfaces are extremely mobile even when adsorbed in defects and that they are only strongly bound at neutral vacancies (*Foster, AS; 2009*). Water monomers adsorb weakly on BaF$_2$ and CaF$_2$(111) surfaces but stronger than on most closed-packed transition metal surfaces: 0.51 eV for Ca, 0.49 eV Ca as compared with $\leq$0.4 eV for Ru, Rh, Pt, Pd, Cu, Ag and Au (*Michaelides, A; 2003 and Carrasco, J; 2009*). Migration barriers for BaF$_2$ were found to be smaller although the difference (0.3 eV for CaF$_2$ and 0.2 eV BaF$_2$) is not dramatic and similar mobility is expected at RT. Non contact AFM images of CaF$_2$(111) exposed to residual vacuum gases have shown features that have been assumed to be water monomers adsorbed on defects at the surfaces (*Hirth, S; 2006*). Such features were found to be stable at RT suggesting that molecules are trapped and cannot diffuse. Taking into account DFT and non contact AFM experiments it can be assumed that water molecules on both CaF$_2$ and BaF$_2$ are extremely mobile except when trapped at vacancies of the terraces and indeed at steps. According to that one would expect that water patches on the surfaces would form as an accumulation of water molecules surrounding water molecules trapped in defective sites at terraces and accumulation of water steps.

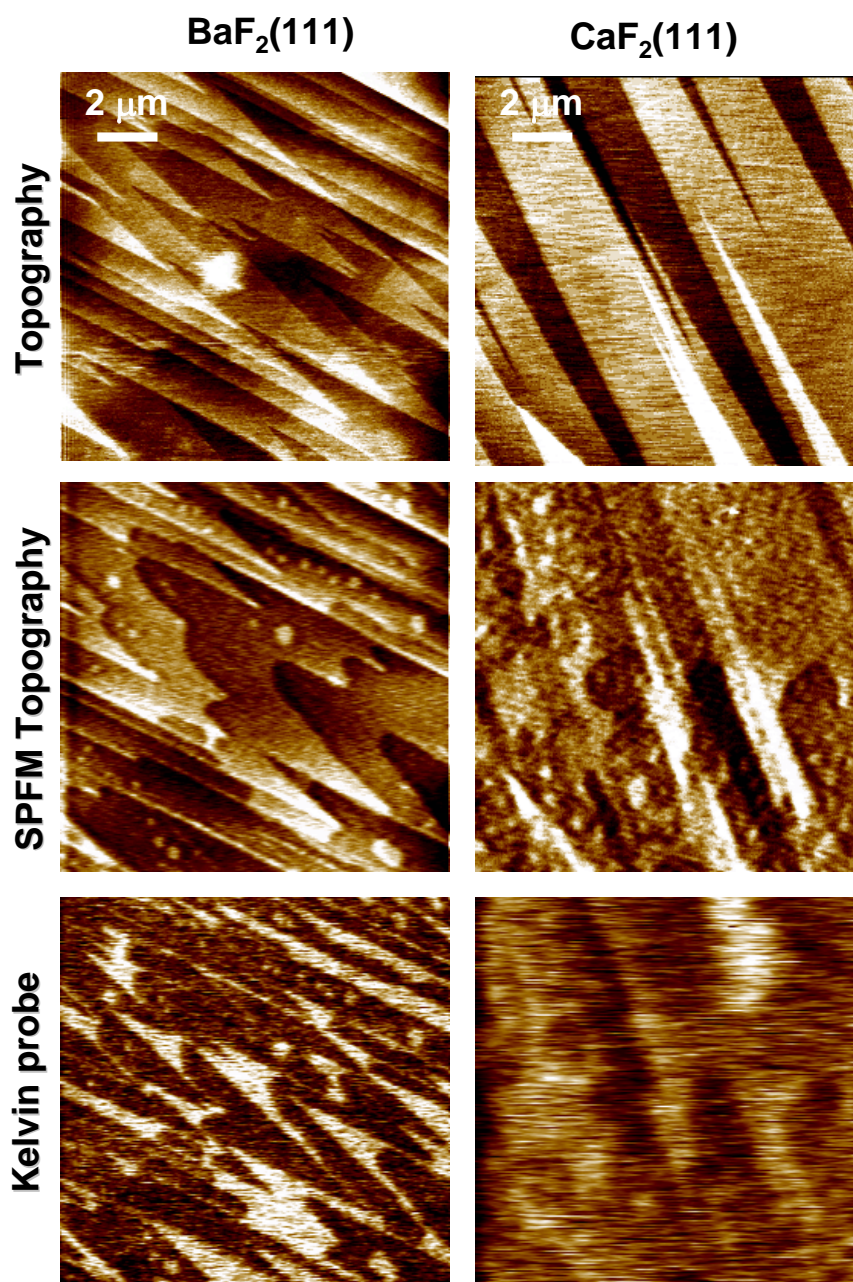A water hexamer on a BaF$_2$(111) surface shows a buckled structure formed

BaF₂(111)   **CaF₂(111)**

Figure 3.31: Contact SFM, SPFM and KPFM images of $BaF_2(111)$ and $CaF_2(111)$ surfaces at ambient conditions. In contact images only the step structure is observed. By subtracting the contact image from the SPFM image the regions covered by the water film can be identified. In KPFM wet areas show a bright contrast due to the average dipole orientation of the water molecules. The KPFM contrast is homogeneous with a well defined edges on $BaF_2(111)$ and more diffuse on $CaF_2(111)$ indicating a major structuration of the water molecules forming the films on $BaF_2(111)$.

by three water molecules on low lying positions acting as H donors adsorbed on the Ba atoms and three water molecules in an up lying position that would be adsorbed approximately on the F sites (*Nutt, DR; 2002*). The interaction of the water molecules at the F sites is very weak, due to a large height difference between both planes of water molecules. However, water monomers on BaF$_2$ and CaF$_2$ (111) surfaces absorb with a tilt due to H-bonding with a neighboring fluorine atom and thus with an unfavorable configuration to act as H-donor for other water molecules. This adsorption configuration affects the formation of the water hexamers and bilayers and the most stable bilayer structure was predicted to be a cross-linked chain structure as already explained above (section 3.1). This is corroborated from KPFM measurements on water layers on BaF$_2$(111) at low humidity that indicates a negative average water dipole orientation not compatible with an I$_h$ bilayer structure. On CaF$_2$(111) the distance between Ca atoms is smaller than for Ba atoms on BaF$_2$(111). This facilitates the formation of water clusters and hinders the formation of hexagonal bilayers.

KPFM images suggest that water patches on BaF$_2$(111) are more structured than water patches on CaF$_2$(111) with a pseudo-ferroelectric character as shown for water films grown on Pt(111) (*Su, X; 1998*). On both images taken at ambient conditions a positive contrast on the wet regions is observed. However, while on BaF$_2$(111) the contrast edge is well defined and homogeneous over the patches, for CaF$_2$(111) the images show heterogeneous contrast although of the same order as for BaF$_2$(111), thus indicating that the noise in the image is not instrumental but that it corresponds to the variation of the dipole orientation of water molecules inside the water films. No clear relationship between the topography and different Kelvin probe contrast are obtained as can be seen from the bright feature observed in the KPFM image (top right) not related to any special topographic feature. The maximum

contrast is obtained at low humidity indicating a more ordered structure for lower coverage. As more water molecules adsorb on the water films they tend to randomize the dipole orientation. The measurements suggest that although the water molecules of the patches observed on $BaF_2(111)$ are not forming a perfect I_h bilayer, the structure that water molecules form through H-bonds accommodate very easily on the surface because of lattice matching. That would favour the growth of larger water structures on $BaF_2(111)$ as compared to $CaF_2(111)$.

The growth process can be summarized as following. Water molecules get trapped on defects at the terraces and steps and form the initial nucleus other molecules H-bond to the trapped molecules and patches grow with rounded edges, truncated by steps. On vertexes the patches that grow on the two steps forming the vertexes contact to each other easily. On $BaF_2(111)$ the structure of the two patches growing from each step matches the substrate and probably the edges of both structures fit to each other when they contact, i.e. it is easy for a water molecule diffusing and arriving at the limit of the two patches to find a configuration that favors both H-bonding to water molecules of the patches and adsorption at the substrate. On $CaF_2(111)$ this seems not to be the case because of the mismatch between H-bond distances and the substrate structure. On $CaF_2(111)$ it is easy to observe patches grown on two different steps very close to each other but without coalescence.

3.6 Tip influence: contact or non-contact?

As explained in section 3.4, the tip in AM-AFM exercise a perturbation on the surface that causes a variation in the wetting phenomena (see figures 3.18 and 3.19). Then, the real height and the wetting process of the water layers on the sample is distorted and we needed to perform SPFM to avoid water

films to be perturbed. However, AM-AFM has a better resolution than SPFM and can provide different information on wetting. Therefore there was a need to find a way to optimize the system in order to perform real non-contact at ambient conditions (as worked until now in the previously experiments) with a better topographical resolution than SPFM. This will allow that the surface and the water layers formed will be undistorted by the tip during the scanning *(Santos, S; 2011)*. BaF$_2$ was used as an example, given the accumulated experience.

Working in AM-AFM, the tip oscillates near the surface, and sometimes it contacts intermittently against the surface (or something adsorbed on). Depending on the surface-tip distance arise four types of different forces become dominant (*van der Waals, capillarity, adhesion and repulsion*) that influence in the water layers height measurement *(Weisenhorn, A.L; 1989, Hansma, PK; 1994, Albrecht, TR; 1991)*.

We know that the SiO$_2$ tip is always covered by a thin water film (except when the tip is treated to be hydrophobic). When the thin water film on the tip contacts with the surface, different interaction forces can distort the topographic images. To avoid this, the tip has to be in real non-contact with the surface (i.e. water on the tip and water on the sample can not directly interact). The surface can be hydrophilic (wet) or hydrophobic (dry) and therefore give rise to different situations. In each case, explained below, the measured height is different.

1. **The surface is hydrophobic** (as shown in Fig. 3.32, a). The figure is divided in three parts. The first one (left) shows the tip, covered by a thin water film, with no mechanical contact with the surface. We define this system as *Wnc* (Water non-contact). In this mode, neither the tip nor the surface (and water layers) are perturbed. If the surface is scanned in this mode, the topographic information will be real. In the

middle of the figure is shown how the thin water film is contacting with the surface, defining Wc as Water contact. It last part of the picture (right), the tip contacts directly with the surface (mecanichal contact ($Rep.$), generating repulsion between these bodies.
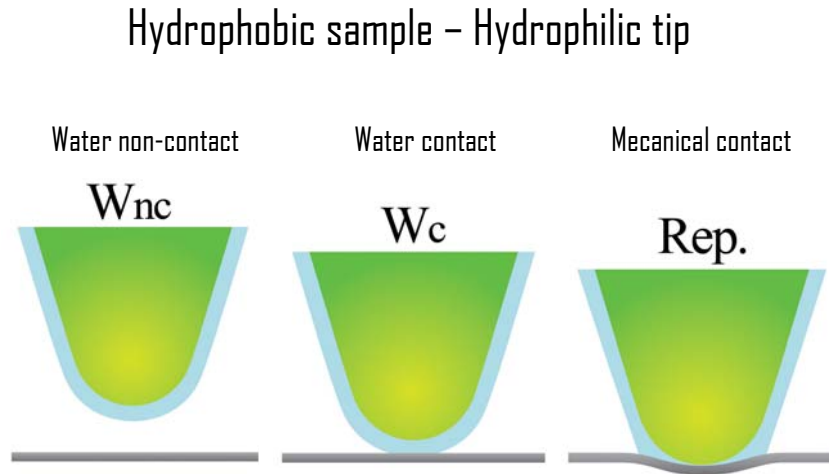
Hydrophobic sample – Hydrophilic tip

Figure 3.32: From *Santos, S; 2011.* (a) shows the three different positions of the (hydrophilic) tip respect to the (hydrophobic) sample. In the first one, called Wnc, the tip does not touch the surface. In the middle, called Wc, the thin film water formed around the tip is in contact with the surface; while the last part of the figure, called $Rep.$, the tip is in real contact with the hydrophobic sample (mecanical contact). (b) shows the three different positions of the (hydrophilic) tip respect to the (hydrophilic) sample. In the first one, called Wnc, the tip does not touch the surface. In the middle, called Wc, the thin film water formed around the tip is in contact with the thin film water adsorbed on the surface, and this contact creates a water neck between the two bodies. The last part of the figure, called $Rep.$, the tip is in real contact with the hydrophobic sample (mecanical contact).

2. **The surface is hydrophilic** (as shown in Fig. 3.32, b). The hydrophilic surfaces have a thin film water adsorbed on them. This figure is divided in three parts as the previous one. In the left part, the tip covered by a thin film water does not interact with the surface (covered by a thin film water as well), named Wnc as in the previous case. In this case, the result is a real image of topography with a real height measurements. In the middle of this figure, the thin water film from the tip creates a water neck with the thin water film from the surface. In the

last case (right), the tip and the surface are in real contact (mechanical contact (*Rep.*)).

In order to understand the differences between each case, figure 3.33 is introduced where the four types of forces that are involved in the tip-sample interaction are shown:

- *Van der Waals long-range interactions = F_{vdW} (Hamaker, HJ; 1937)*

- *Capillary forces (bridge formation) = F_{CAP} (Yaminsky, VV; 1999)*

- *Adhesion forces = F_{AD} (Derjaguin, BV; 1975)*

- *Repulsive force (mechanical contact) = F_{Rep} or F_{DMT} (modeled here with the Derjaguin-Muller-Toporov (DMT) model of contact mechanics) (Derjaguin, BV; 1975)*

All the forces can be included in Eq. (3.5), which corresponds to the dimmed spring *(Garcia, R; 1999)*.

$$m\frac{d^2z}{dt^2} + \frac{m\omega_0}{Q}\frac{dz}{dt} + kz = F_{ts} + F_0 cos\omega t, \qquad (3.5)$$

where the effective mass of the tip is defined as $m = k/(\omega_0)^2$ (where the cantilever spring constant is k and ω_0 is the resonance frequency), $F_0 cos\omega t$ is the drive force, and F_{ts} is the force between the tip and the sample, defined as:

$$F_{ts}(d) = F_{VdW} + F_{CAP} + F_{AD} + F_{DMT} \qquad (3.6)$$

In figure 3.33, the parameter d is introduced to define the distance between the tip and the sample. In fact, the effective interaction distance between the tip and the sample is the distance that considers the water layers adsorbed on the surfaces, named d^* *(Santos, S; 2011)*. If the surface is hydrophobic
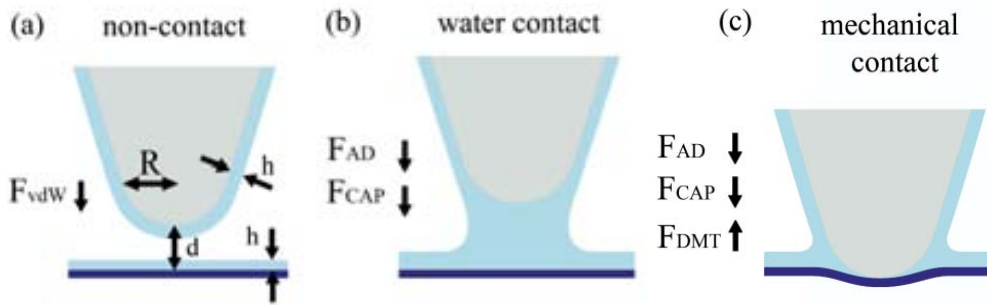
Figure 3.33: The forces involved between the tip and the sample in the three different tip positions (see Fig. 3.32 and Fig. ??). a) Water non-contact. Van der Waals force (F_{VdW}) is emerged, generating an attractive interaction. b) Water contact (water neck between the bodies). Adhesion and capilary forces (F_{AD}, F_{CAP}) arise from this water contact. c) Mecanical contact (tip-sample real contact). Adhesion and capilary forces (F_{AD}, F_{CAP}) are involed in the attractive forces while a repulsive force (F_{DMT}) is generated as well.

(see Fig. 3.32), the effective distance is $d^*=d\text{-}h$ (where h is the thickness of the thin film water adsorbed on). If the surface is hydrophilic (see Fig. ??), then the effective distance $d^*=d\text{-}2h$ (considering the two film water formed on the tip and sample). Solutions of this equation were obtained by the M. Chiesa's group from Laboratory of Energy and Nanosciences, Masdar Institute of Science and Technology, Abu Dhabi, and different solutions for different conditions were obtained.

Experimental measurements are performed, to compare with the simulation results, on a $BaF_2(111)$ sample displaying both wet and dry regions on the surface (see Fig.3.34 and 3.35). As shown in this chapter, BaF_2 is ideal to compare interactions between the tip and wet regions where water patches are formed and dry regions where water patches are not present due to its high surface diffusion. At experimental level, it is necessary to find the appropriate conditions to establish the tip in the *Wnc* case, in order to obtain real topographical images of the surface. To perform this, the amplitude setpoint and the free amplitude (A_0) is varied. It has observed that we can pass from a mode to another one (for example from attractive mode (*Wnc*)

to repulsive mode (*Wc* or *Rep.*)). To obtain real non-contact topographical images (*Wnc mode*) we need to stay in attractive regime, and remain there, where real images and real heights are measured (see Fig. 3.34).
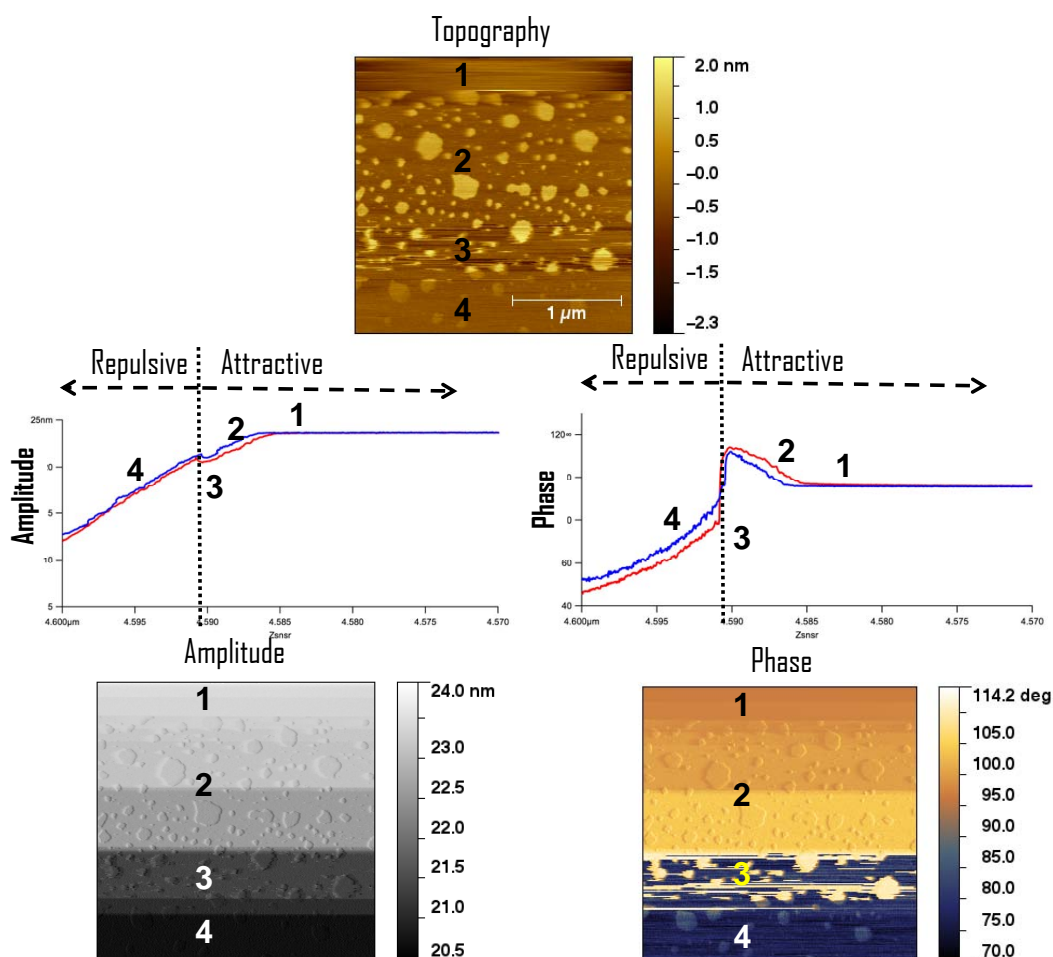

Figure 3.34: Graphics of amplitude (left) and phase (right) about the interaction experienced by the tip on the surface. At large distaces, neither topographic nor amplitud or phase images show anything *(1)*. When the tip is approached to the sample, it experiences an attraction to the sample *(2)*. Before moving from one regime (attractive) to other (repulsive), the tip is in *(3)*. After this point, the tip experiences a repulsion to the sample *(4)* and starts in real contact with the sample. In order to obtain real images without *Wc* or *Rep.* interactions, is required to place the tip in *(3)*

In figure 3.35 the *simulation values* of the water patches height are shown with outlined markers and the *experimental values*, with the respective error

bars, with squares. The true water height h in the simulations is considered h=0.6 nm, what represents in fact $\approx$ a water bilayer. The experimental and simulated values in figure 3.35, correspond to A_{sp}/A_0=0.8-0.9 nm. For the small value of free amplitude of $A_0\sim3$ nm we obtain an experimental value of apparent height of h=0.6 $\pm$ 0.1 nm (filled squares in figure 3.35 where A_0=3 nm). Then increasing the free amplitude to $A_0\sim10$ nm, leads to the Wc/Wnc scenario according to simulations. The prediction was that h slightly increases in this case, and is matched by experimentation as shown in the figure. The results shown h=0.85±0.15 nm in the experimental case and h=0.9 nm in the simulations. Further increasing the free amplitude to A_0=30 nm leads to the Wc/Wc and the $Rep./Wc$ cases. At this point the apparent height of water should increase to a maximum according to predictions. Particularly in the $Rep./Wc$ case it should be approximately four times higher than that in the Wnc/Wnc case. The experimental values are in fact h=1.3±0.1 and 1.9±0.51 nm, respectively, and the simulation values are h=1.2 and 2.3 nm. The smallest values of h are experimentally obtained in the $Rep./Rep.$ case for which h=0.3±0.05 nm (experimental) and h=0 nm (simulation). This is observed when A_0=60 nm. Water layers on $BaF_2(111)$ are known to have a solid-like nature even at room temperature (*Verdaguer, A; 2008*) so even at repulsive regime the water layers are probably not totally displaced by the tip and a thickness is measured even for this case. In addition it was experimentally proven that only when images where performed in the Wnc/Wnc case the shape of the water films remained constant. On all other cases perturbation of the sample is observed through repeatedly scanning over the same area due to water adsorption induced by the tip (*Verdaguer, A; 2008*).
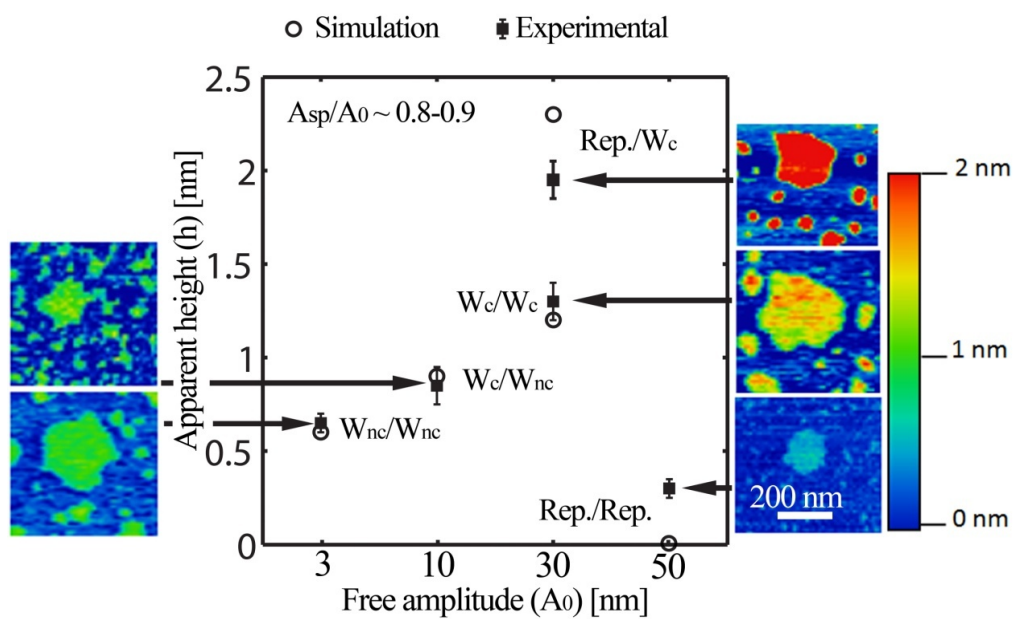
Figure 3.35: Experimental versus simulation values for the apparent height h of water patches on a BaF$_2$(111) sample displaying both wet and dry regions. The y-axis shows the values of apparent height in nm and in the x-axis the four types of interactions described above are shown by working at free amplitudes of 3, 10, 30 and 60 nm respectively.

3.7 Summary

We have studied the role of steps in the interaction of water with freshly cleaved (111) surfaces of BaF_2 in ambient conditions using different SPM imaging methods and optical microscopy, and the main conclusions are:

- Steps provide a stabilizing effect for the growth of the two-dimensional water patches.

- Water patches are preferentially observed on terraces limited by triangular steps (induced by cleavage).

- These patches are larger for lower terraces and show an asymmetric meniscuslike shape that can be related to the different wettability of the steps.

- Steps running along the $[\bar{1}10]$ directions are by far the most hydrophilic ones.

- In general, our results prove that morphological defects such as steps can be crucial for improving monolayer wetting and stabilization of multilayer grown on surfaces that show a good lattice mismatch relationship with water molecules forming ice.

We have applied different AFM imaging methods to study the interaction of water with freshly cleaved $BaF_2(111)$ at ambient conditions. Our main conclusions about the present work are:

- We have evidenced the strong perturbation of the water adsorption on the surface due to water neck formation when using AM-AFM.

- SPFM has allowed to image the evolution of water structures as a function of RH.

- At RH<20% metastable water structures in the form of islands partially cover the surface.

- The islands observed have a non-liquid structure as have been imaged with tapping and contact modes as well.

- A sign crossover from negative to positive could be observed at RH>30%. This is a consequence of the energetic balance between the competing water vapor/solidlike and solidlike/substrate interfaces.

- Our results point toward a configuration other than I$_h$.

- At RH>30%, the surface starts to be covered with an uniform film leading to a homogeneous surface potential distribution.

It has been compared water adsorption on BaF$_2$(111) and CaF$_2$(111) at ambient conditions. Since water adsorption energies and water diffusion barriers on both surfaces are similar the main conclusions are:

- SPM and optical microscope images show that the step structure formed by cleavage determines the wetting properties of BaF$_2$(111) both at nanometric and macroscopic level.

- On CaF$_2$(111) the step structure plays a minor role and wetting is determined by other defects.

- What determines the different water structures formed on both surfaces is the difference in the mismatch between lattice parameters of the surface and I$_h$ hexagonal ice.

- The difference in lattice parameters modifies the interplay between adsorption energies and H-bond energies of water molecules at the surface.

Chapter 4

SPFM/KPFM - Graphene

Graphene is a two-dimensional crystal consisting of a single layer of carbon atoms arranged hexagonally, with very appealing electronic for a complete new development of a generation of nanometric devices. Graphite, nothing but the surperposition of graphene layers bound through van der Waals interactions, is hydrophobic. Many potential applications based on graphene might be hindered by the presence of water, so that it is necessary to know in detail the interaction between water and graphene, which can be very different than with graphite.

4.1   A brief introduction to graphene

Carbon is probably the most studied chemical element in nature. In fact, carbon is fundamental in large number of biological processes and is involved in many energy aspects of life and it can build a wide variety of very complex compounds. It is known for centuries that pure carbon at ambient conditions could only exist in two different types of material:

- Graphite (used commonly in pencils)

- Diamond (slightly less stable than graphite)

Graphene is the basis of the other graphitic forms. In the 1970s, inter-leaved graphite compounds (thin sheets of graphite between layers of other materials) were studied. After that, it triggered a series of studies about large chains formed by carbon named polyynes (see figure 4.1). Later, in the eighties (1985), a compound called fullerene, a molecule of 60 carbons (C_{60}) with a soccer-ball shape, was discovered by the chemists Robert Curl, Richard E. Smalley and Harry Kroto. Fullerenes currently have important applications in drug delivery. A few years later, the Japanese physicist Sumio Iijama was able to identify a cylindrical carbon structure nowadays known as carbon nanotubes. Carbon nanotubes can be understood as very thin sheets of graphite (graphene) wrapped around theirselves, which can acquire exceptional chemical, electronic, mechanical and optical properties that give rise to a wide variety of applications.

With the advent of the new century, it became possible to isolate and manipulate the first sheets of graphite only one molecule thick. This material was named graphene and it is known as an allotropic form of carbon composed of layers of carbon (sp^2 bonded) organized in honeycombs. In 1947 P.R. Wallace discussed its structure for the first time. Now graphene could be produced relatively easily by mechanical exfoliation or by heating SiC, and it was possible to calculate unequivocally the thickness of one sheet (3.4Å).

Since its discovery, graphene has been object of intense study. André K. Geim and Philip Kim demonstrated that layers of graphene can be easily obtained and they characterized samples with different thickness (*Geim, A.K and Kim, P; 2008*). Graphene is the most two-dimensional known material, made with only a one-atom-thick sheet of carbon. This means that graphene has some unusual electronic properties and that it is a surface material.

There are two properties that make graphene a unique material. First of all, graphene exhibits a high quality and arrangement in its lattice. This
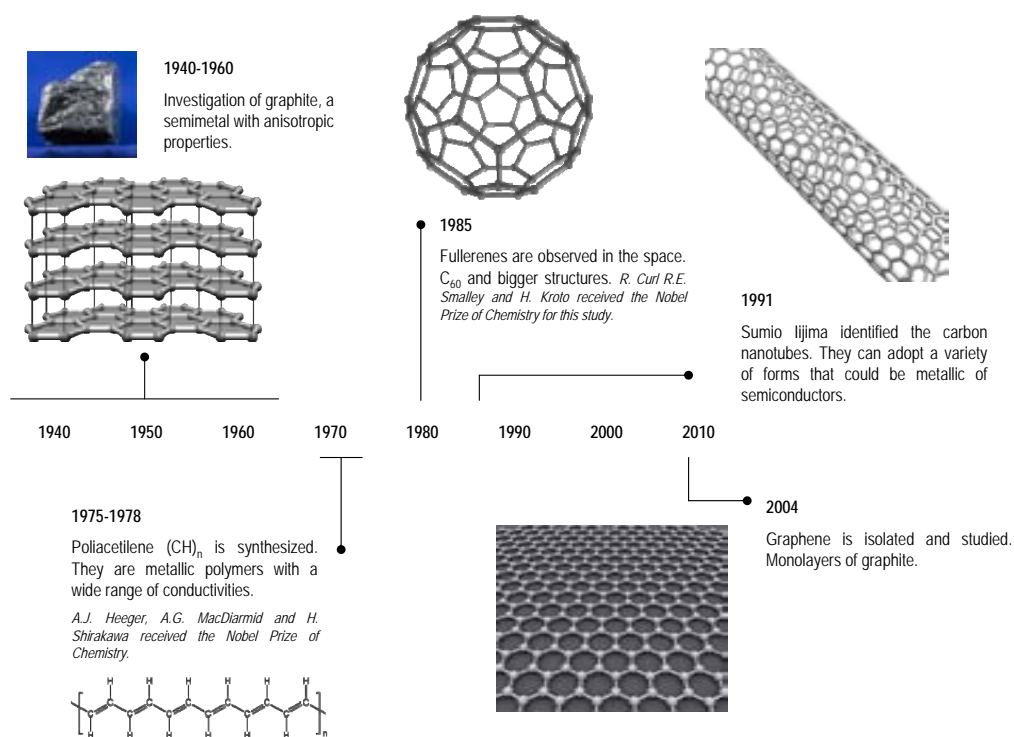
1940-1960

Investigation of graphite, a semimetal with anisotropic properties.

1985

Fullerenes are observed in the space. C_{60} and bigger structures. *R. Curl R.E. Smalley and H. Kroto received the Nobel Prize of Chemistry for this study.*

1991

Sumio Iijima identified the carbon nanotubes. They can adopt a variety of forms that could be metallic of semiconductors.

1940   1950   1960   1970   1980   1990   2000   2010

1975-1978

Poliacetilene $(CH)_n$ is synthesized. They are metallic polymers with a wide range of conductivities.

A.J. Heeger, A.G. MacDiarmid and H. Shirakawa received the Nobel Prize of Chemistry.

2004

Graphene is isolated and studied. Monolayers of graphite.

Figure 4.1: Schedule of the investigation of different carbon allotropes over time

gives it a great flexibility and resistance, and it can deform by 10% without losing its properties. The second characteristic that makes graphene special is its high electric conductivity, because its electrons can move through the lattice with no impediment.
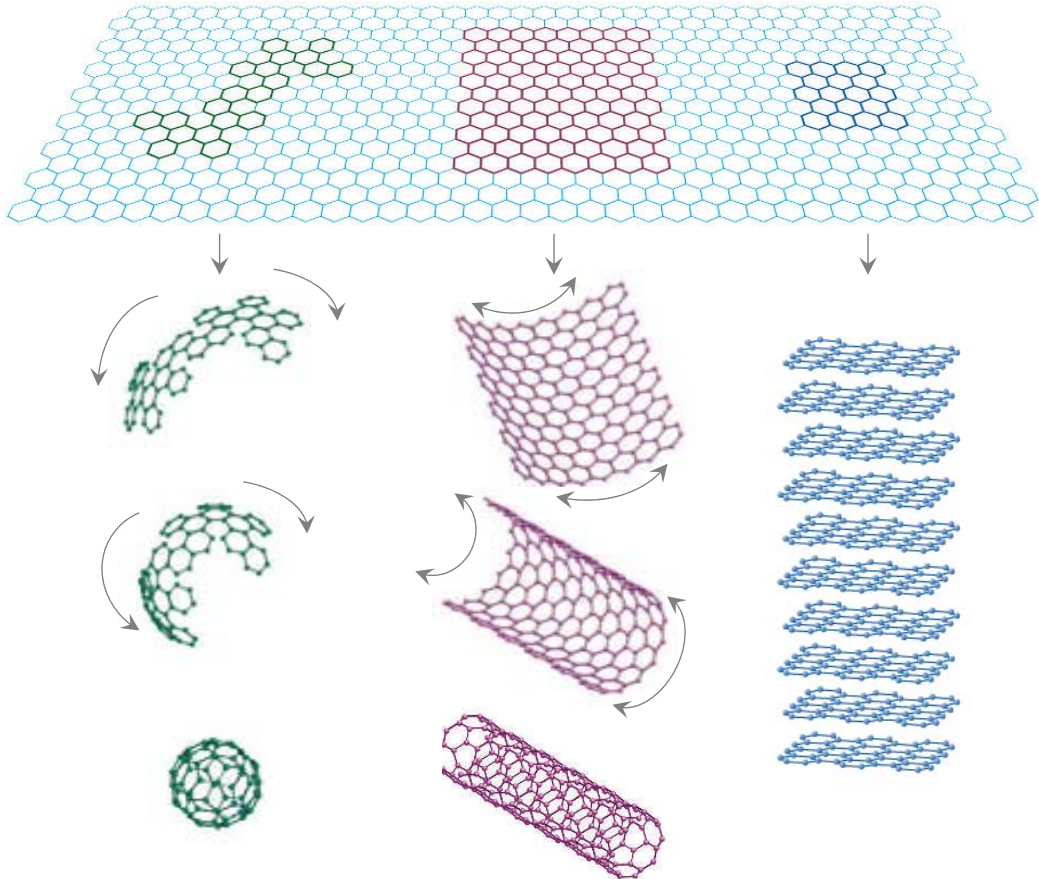

Figure 4.2: Mother of all graphitic forms. Graphene is a 2D building material for carbon materials of all other dimensionalities. It can be wrapped up into 0D buckyballs (fullerenes), rolled into 1D nanotubes or stacked into 3D graphite (from *Geim, AK; 2007*)

4.1.1   Band structures of solids

Before talking about the electronic properties of graphene, it is important to briefly mention the main band structures of solids. Solids are classified as

metals, semiconductors, insulators and semi-metals. The properties of these solids are given by the Fermi level position (E_f). Fermi level corresponds to the highest occupied energetic level. The lowest unoccupied energetic levels make the conduction band, and the highest occupied energetic levels constituted the valence band.

In metals, the conduction and valence bands overlap and create a non-zero density of states in the Fermi level, therefore there is no gap. This makes the material a good conductor. Electrons that are below the Fermi level can jump to the closest unoccupied high levels and create electric current with no necessity of excitation. The type of charge carrier is electrons.

In semiconductors, the conduction and valence band are separated by an energetic gap that hinders the passage of electrons from the valence to conduction band and therefore the electrons have to be excited. Doping the semiconductor will shift the Fermi level either towards the valence band or towards the conduction band, making the semiconductor p-type or n-type, respectively. In a p-type semiconductor holes are the majority carriers and electrons the minority carriers, whereas in a n-type semiconductor it is vice-versa.
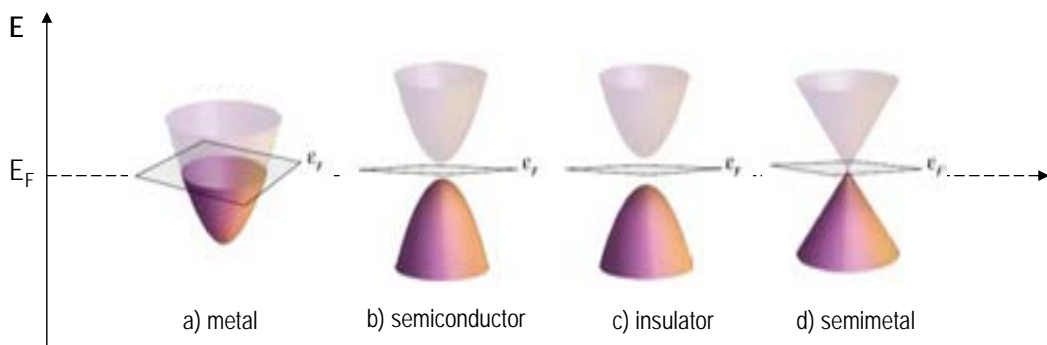

Figure 4.3: Exemples of the band structes of a (a) metal, where the Fermi level (E_f) lies within the conduction band (b) semiconductor, with a band gap energy (E_g) between valence and conduction bands, (c) insulator, (d) semi-metal, where the valence and conduction bands touch at a point-the Fermi point.

When the electronic bands become too large, the excitation of electrons to the conduction band is then unlikely. This is an insulator solid.

There is a type of solid that is between the metals and semiconductors. It is called a semi-metal and is characterized by having no gap between bands, there is no overlapping and the bands touch at only one point (the Fermi point or k-point). Then, electrons can easily jump from the lower cone to the upper cone (see figure 4.3). Semi-metals have two types of charge carriers: electrons and holes.

4.1.2   Graphene properties

Grephene is a semimetal, thus it participates in the best of both worlds: with metals shares a zero-band-gap that facilitates the electron pass from the valence band to the conductive band; with semiconductors shares the fact of having two types of carriers (electrons and holes).

Electronic properties

Electrons move through the lattice of graphene and interact with the electrostatic field of the crystalline net. Then, electrons are drive up and down on the surface in a complex way. The result of this movement is a different electron mass with respect to the usual and established electron mass (called effective mass).

In 1947 P.R. Wallace (*Wallace, P. R.; 1947*) established a lineal relationship between E and k for low energies near to the six corners of the two dimensional hexagonal Brillouin zone (see figure 4.4). Due to this linear dispersion, electrons and holes near these six points behave like relativistic particles and electrons and holes are called Dirac fermions (*Novoselov, KS; 2005* and *Zhang, Y; 2005*), and the six corners of the Brillouin zone are called the Dirac points (*Semenoff, G. W.; 1984*). This dispersion is described by:

$$E = \hbar\nu_F\sqrt{k_x^2 + k_y^2} \tag{4.1}$$

where Fermi velocity $\nu_F \sim 10^6$ m/s (*Avouris, P; 2007*).

Graphene shows a high electronic mobility at room temperature. Furthermore was experimentally observed that electrons and holes have practically the same mobility (*Charlier, J.-C; 2008*), and its resistivity would be 10^{-6} Ωcm, less than the resistivity of silver, the substance with lowest resistivity known at room temperature.
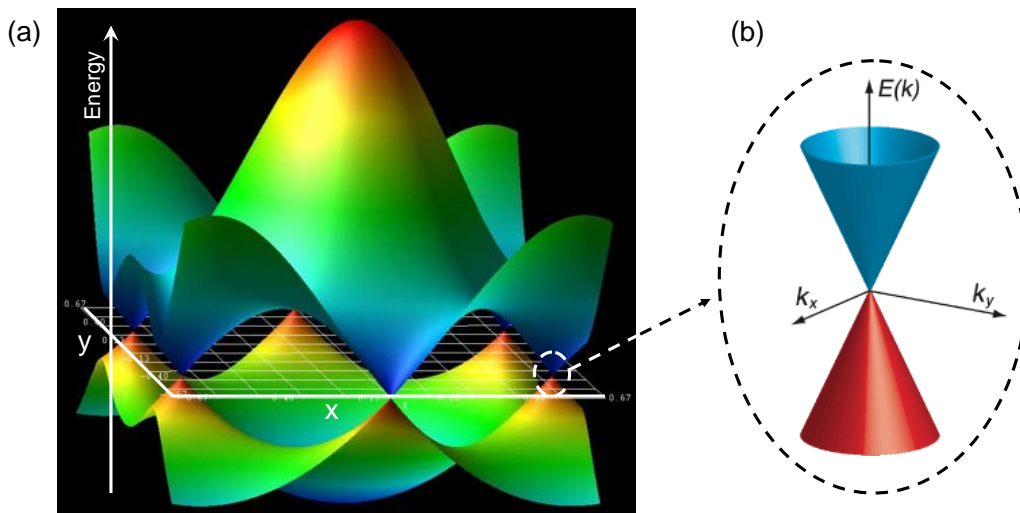

Figure 4.4: (a) The valence band (top) and the conduction band (bottom) touch at six points that lie at the Fermi energy. At these Dirac points, the density-of-states is zero, so graphene can be considered as a zero-gap semiconductor. At low energies the dispersion is linear. (b) Cone structure of the energy dispersion relation at low energies at the six Brillouin zone corners.

Mechanical properties and potential applications

Since 2009, graphene appears to be one of the strongest materials ever tested. Measurements have shown that graphene has a breaking strength 200 times greater than steel (*Lee, C.; 2008*). However, the process of separating it from graphite will require some easy and economical technological development to

be used in industrial processes. Graphene paper is one example of recently
developed material which has a lighter, stronger, harder and more flexibility
than steel, a recyclable and sustainably manufacturable product. Then easily
one thinks that a material with these intrinsic properties could be used to
develop new tools and devices.

Graphene is a material with a wide potential application. Some applications of graphene are:

- Graphene nanoribbons: single layers of graphene that are cut in a particular pattern to give it certain electrical properties. They can be in a zigzag or armchair configuration. If the zigzag is the configuration of edges, is predicted that the behavior of the sheet will be metallic while armchair is the configuration, the behavior of the graphene layer will be semiconducting. Graphene nanoribbons are a possible alternative to copper for integrated circuit interconnects.

- Graphene transitors: due to its high electronic quality, and its response to perpendicular external electric field, allowing one to build FETs (Field-Effect Transitors) (*Avouris, P; 2007 - McEuen, PL; 1998*).

- Graphene optical modulators (*Liu, M; 2011*).

- Integrated circuits: it has the ideal properties to be an excellent component of integrated circuits. In 2008, the smallest transitor so far, one atom thick, 10 atoms wide was made of graphene (*Ponomarenko, L. A; 2008*).

A lot of more applications like electrochromic devices (*Ekiz, O.O; 2011*), transparent conducting electrodes (*Wu, J.B; 2010*), solar cells, ultracapacitors, or anti-bacterial (*Mohanty, N; 2008*) made the graphene an extraordinary compound.

4.2 Why graphene is of our interest?

Our interest for graphene became before that water adsorption was measured by Novoselov. Novoselov *et.al.* calculated the resistance R of a relatively thick multilayer of graphene during its exposure to various gases. A short time of gas exposure (few seconds) was required to observe that the surface was covered by different species. One of these species was water. As shown in figure 4.5. there are three peaks corresponding to water molecules adsorbed on graphene. If the sample is removed to a vacuum system, water is easily removed (see figure 4.5, top left). This was the first evidence that water molecules can be adsorbed onto graphene surfaces and interact at ambient conditions (*Novoselov, KS; 2004*).

Later, *J. Moser* and *A. Verdaguer* published a paper about the environment of graphene probed by electrostatic force microscopy, where they checked that water molecules are adsorbed on the thin sheets of graphene. It is well known that graphite is highly hydrophobic (*Chakarov, DV; 1995*). Therefore the thin layers of graphite (graphene) where expected to be hydrophobic as well. But in this work they could measure how a dipole layer (coming from water molecules) was formed (*Moser, J; 2008*).

Moser, J. *et. al.* used Electrostatic Force Microscopy (EFM), similar to KPFM, to study the distribution of dipoles on surfaces (*Zerweck, U; 2005*), in order to probe the electrostatic environment of graphene sheets. They found that water molecules form a dipole layer on top of graphene that can generate an electric field as large as $\sim 10^9$ Vm^{-1}. Thin graphene sheets were optically located, imaged by AFM, and occasionally examined by Raman spectroscopy to identify single layer specimens.

Topography images were obtained in AM-AFM mode (Fig. 4.6 (a) and (b)) and then the AFM tip was lifted by a given amount, and a bias V_{dc} was applied to the Si backgate and a potential $V_{ac}\cos(\omega t)$ was applied to the tip.
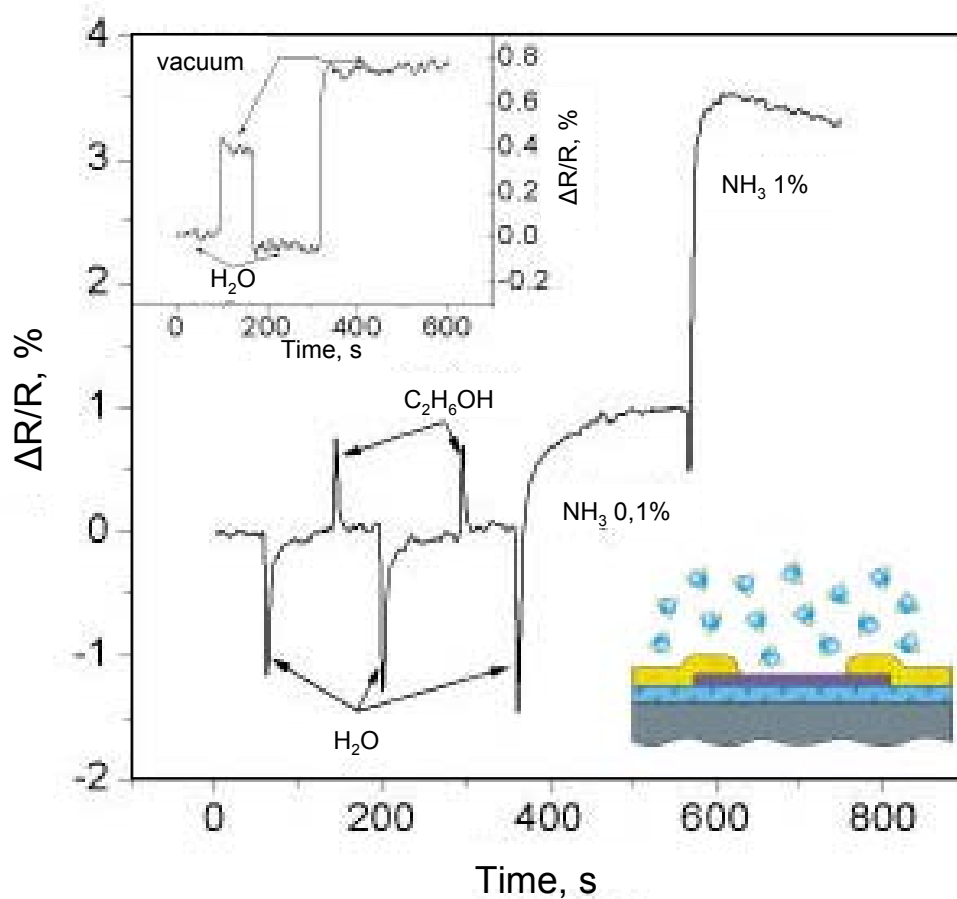
Figure 4.5: Species adsorbed on a graphene device. When the device is exposed to a gas flow, some species can be observed on the surface such as water. When the experiment is carried out at vacuum conditions, there is no water evidence (top left). *From Novoselov; KS; 2004.*

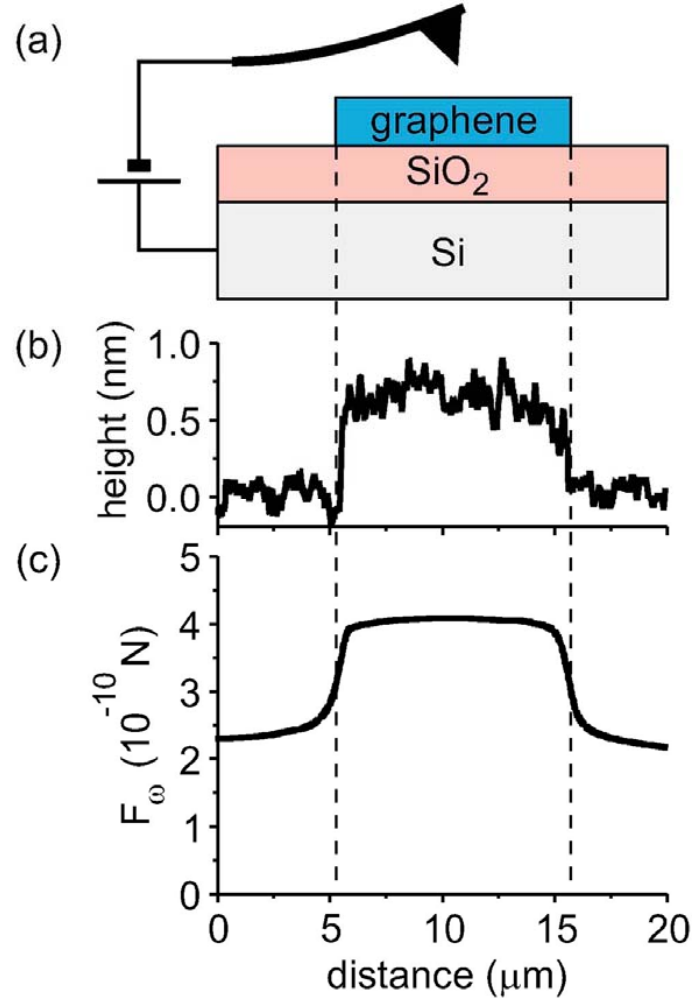The tip experienced a force whose term at the frequency ω (see Fig. 4.6 (c)).

Figure 4.6: (a) Schematic of the EFM setup. (b) In a first pass, the topography of the graphene sheet is recorded. (c) In a second pass, a dc voltage V_{ac}=1 mV is applied to the tip at a frequency set to the resonance frequency of the cantilever. The sample is scanned at a constant height of about 50 nm and the oscillating force is measured (*Figure from J.Moser and A.Verdaguer, 2008*).

Figure 4.7 compares measurements of the electrostatic force sensed by the tip in EFM on a single graphene layer. The measurements was first performed in dry N_2 with a relative humidity of less than 3%, thus corresponding to a submonolayer water coverage on clean SiO_2 (*Verdaguer, A; 2007*). Without taking it out of the dry environment, the sample was heated to 160°C for 1h

and measured again (see Fig. 4.7 (b)). Eventually, moist N_2 was introduced until RH≈50% (∼3 water monolayers on clean SiO_2 (*Albert, A; 2007*) (Fig. 4.7 (c)). Therefore, graphene appears to be sensitive to water and water molecules adsorb and desorb onto the graphene sheets. It is surprising because graphite is highly hydrophobic as explained before (*Luna, M; 1999*).

The conclusion from those results are that was water molecules form a dipole layer on top of graphene generating a large electric field. It is expected that water can have a strong influence on the transport properties of graphene devices depending on the ambient conditions.

The objectives

Our main objectives referring to graphene and its properties are:

1. *The influence of the tip shape in SPFM measurements.* Graphene is an ideal flat and stable material that can be used as a model surface to study the contribution of the dielectric response to the SPFM signal.

2. *How water is adsorbed on graphene sheets?* Here I present an experimental procedure to charge individual few layer graphene (FLG) films deposited on a SiO_2/Si wafer using SPM techniques. Once charged the FLG films are characterized using SPFM and KPM. FLG films are found to discharge into the Si substrate through the water film adsorbed on the SiO_2 surface.

4.3   Experimental details

All the experiments shown here were carried out at room temperature and in the same conditions explained in the previous chapter for BaF_2 and CaF_2. All experiments where performed under low humidity conditions (RH<10%).
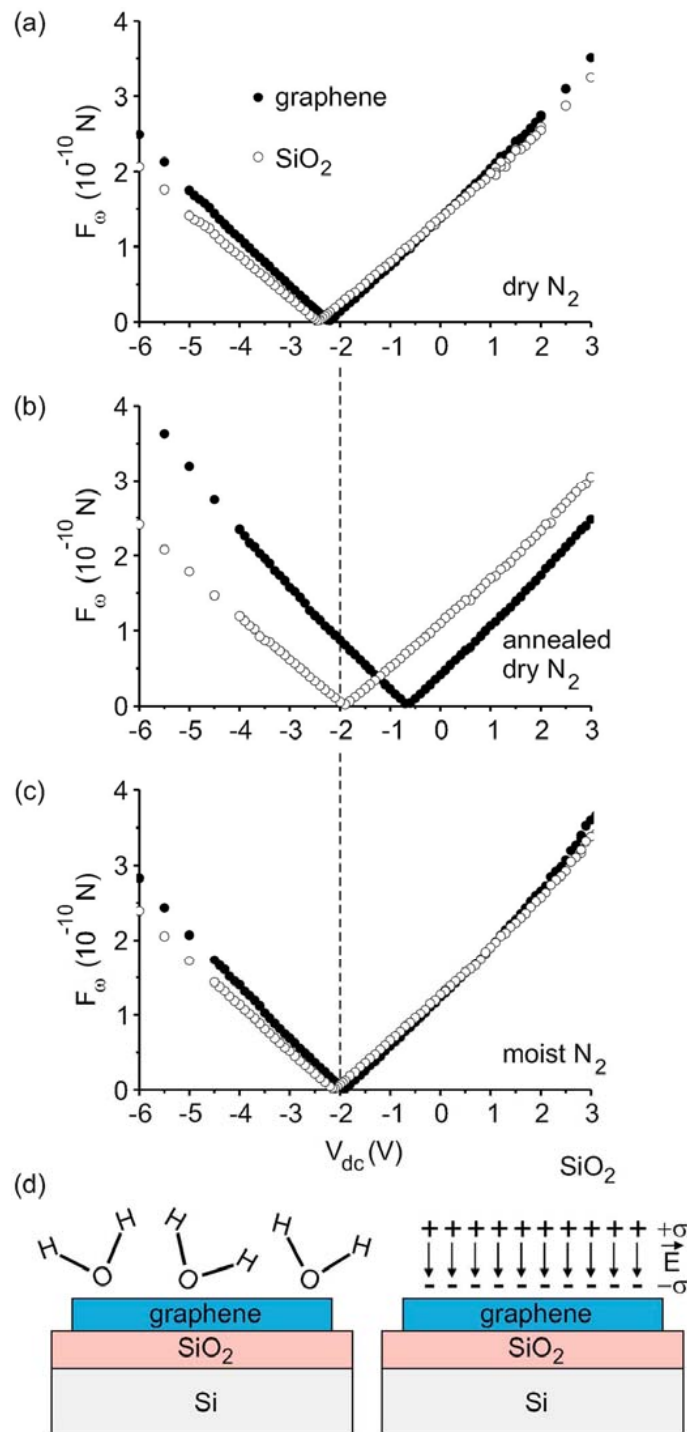
Figure 4.7: Force term F_ω experienced by the AFM tip as a function of V_{dc} in a (a) dry N_2; (b) dry N_2 after heating the sample to $160°C$ for 1 h in dry N_2; (c) moist N_2. (d) Water molecules adsorb on average with the oxygen atom pointing towards the graphene sheet, and form a dipole layer with an effective surface charge σ (schematic not on scale) (*Reproduced from J.Moser and A.Verdaguer, 2008*).

Working in a low humidity, the environment is crucial since it is known that the electrostatic properties of the SiO_2 surface (*Verdaguer, A; 2008*) and the graphene films (*Moser, J; 2008*) are very sensitive to RH. In addition, the measurements can become strongly unstable by the formation of a water neck meniscus between the tip and the sample, especially when electric fields are present (*Sacha, GM; 2006*).

Few-Layer Graphene (FLG) films on silicon wafers were prepared using the conventional micromechanical exfoliation technique (*Schedin, F; 2007*), where a flake of bulk Kish graphite is repeatedly cleaved with an adhesive tape and pressed down onto a silicon wafer coated with a 280 nm thermally grown silicon oxide. Graphene sheets were localized by optical microscope as shown in Fig. 4.8.
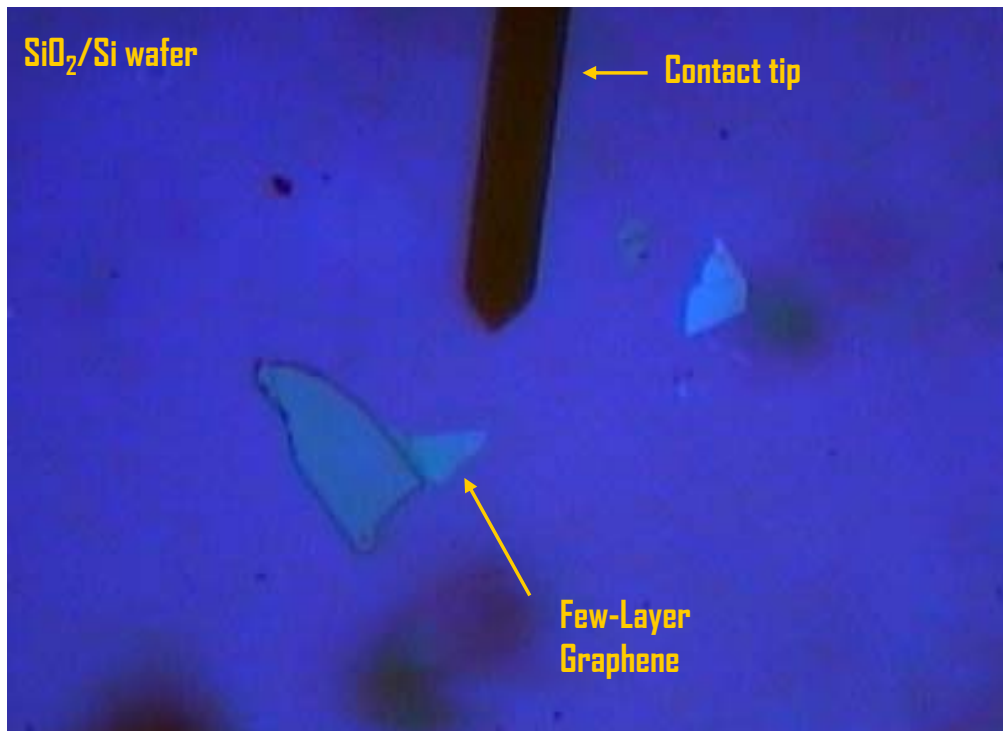
Figure 4.8: Graphene sheets on SiO_2/Si and a platinum-coated cantilevers as observed with the optical microscope from the Agilent 5500 AFM.

Charge injection is performed as follows. The silicon substrate is connected to ground during the experiment. An image in contact mode of the FLG film is taken with the tip grounded (see Fig. 4.9, top left). Then, the tip is placed above the FLG film, brought into contact with it and a bias (V_{inj}) is applied to the tip within the -10 to 10 V range (Fig. 4.9, top right). After a few minutes the tip is retracted to about 200 nm from the surface, keeping the tip biased (Fig. 4.9, lower left). With this procedure the FLG film becomes charged acquiring an initial electric potential V_0, different from V_{inj}, which envolves with time as discussed below. Once the tip is retracted from the surface, V_{inj} on the tip is switched off and a dual SPFM + KPM image is taken (Fig. 4.9, lower right). Using this method non-contact conditions can be guaranteed throughout the experiment on the FLG film thus avoiding the formation of a water neck between the tip and the sample (*Sacha, GM; 2006*) that would perturb the discharge process. An image in contact mode with the tip grounded can be performed to discharge the FLG, as can be seen by comparing KPM images before charging and after discharging.

4.4 The influence of the tip shape in SPFM measurements.

Figure 4.10 shows contact (top), SPFM (middle) and KPM (bottom) images of a few microns wide few-layer graphene (FLG) sample. Several protrusions due to 3D folding of the FLG can be observed. From contact measurements of flat areas the FLG thickness H was estimated to be $H = 1.6 \pm 0.4$ nm. Assuming a graphite basal plane separation of $\sim$0.3-0.4 nm, this leads to an FLG formed of $\sim$5 layers. However, it has been reported that a single graphene layer can also exhibit 1.6 nm step heights due to the uncertain FLG-SiO$_2$ interfacial contribution (most probably due to water), since such
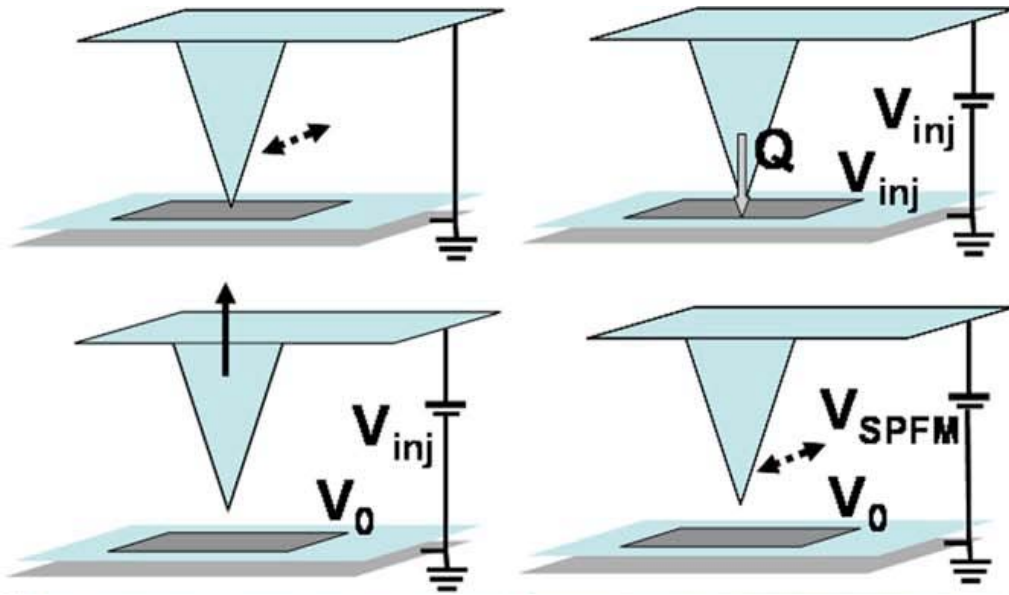
Figure 4.9: Scheme of the experimental charging and measurement procedure used.

samples are prepared in air *(Schedin, F; 2007)*. Therefore, our sample could also consist of a single monolayer. No Raman experiments were attempted. The KPM image taken simultaneously with the SPFM image (figure 4.10 bottom) shows a contact difference potential slightly less positive in the FLG region as compared to the SiO_2 substrate, as has been already reported in the literature (*Datta, S; 2009*).

The SPFM image is an amplified replica of the topography of the FLG film obtained from the contact image (see profiles in Fig. 4.11). We are even able to distinguish some of the larger protrusions observed in the contact image. This fact indicates that the loss of resolution due to the higher tip-sample distance (*Góomez-Moñivas, S; 2001*) in SPFM, evaluated in the 10-20 nm range, has a minor effect for images of this size. Note the large difference in the height between contact (1.6 nm) and SPFM (50 nm) images. This difference in the measured height is due to the fact that in SPFM differences in

$F(2\omega)(\partial\,C/\partial z)$ term in equation 4.2 (*explained into the experimental chapter*) include the contribution from both the topography and the dielectric constant of the sample. The different dielectric constant between the FLG ($\epsilon \sim \infty$) and SiO$_2$ ($\epsilon = 3.9$) becomes the main contribution to the measured thickness contrary to what was described for water on BaF$_2$(111) (see section 3.4.1) where the contribution is less important. We point out the importance of using homogeneous planar surfaces such as graphene in order to correctly characterize the actual topographic height.

$$F_{2\omega} = \frac{1}{4}\frac{\partial C}{\partial z}[(V_{ac}^2 cos(2\omega t)] \tag{4.2}$$

The macroscopic shape of the tip

To quantify the large difference between the SPFM signal and real topography of a graphene sheet, *GM. Sacha* (member of the Biological Neurocomputation Group of Universidad Autónoma de Madrid) simulated the electrostatic interaction with the generalized image charge method (GICM) (*Sacha, GM; 2006*). The GICM is based on the replacement of the tip by a set of point charges and segments that are adjusted in order to keep the electrostatic potential constant over the tip surface. The electrostatic force (and force gradient) can be obtained directly from the interaction of the charges inside the tip with their images from the derivative of the capacitance C with respect to the tip-sample distance since $F \propto \partial C/\partial z$. One of the main advantages of this method is that macroscopic elements such as the sample or the cantilever can be included in the simulation by a series of image charges (*Sacha, GM; 2006*). The GICM is able to deal with distances between a few nanometers for the tip-sample distance D and several microns for the tip length L (*Gomez-Moñivas, S; 2001*). This characteristic can be used to analyze the influence of the macroscopic shape of the tip in the SPFM signal. To simulate the tip,
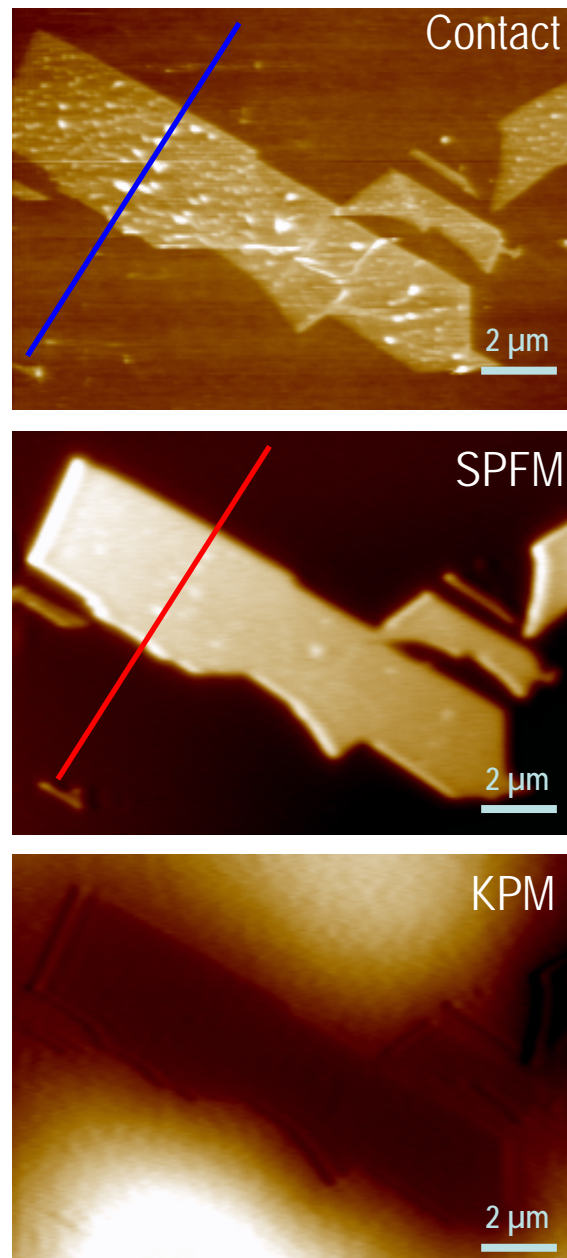
Figure 4.10: Contact (top), SPFM (middle) and KPM (bottom) images taken for an FLG film transferred onto a SiO_2 surface.

he considered a generic tip with a half-angle $\theta=10°$, $L = 12.5$ μm, tip radius R between 50 and 200 nm and an applied voltage $V= 7.5$ V (see Fig. 4.12).
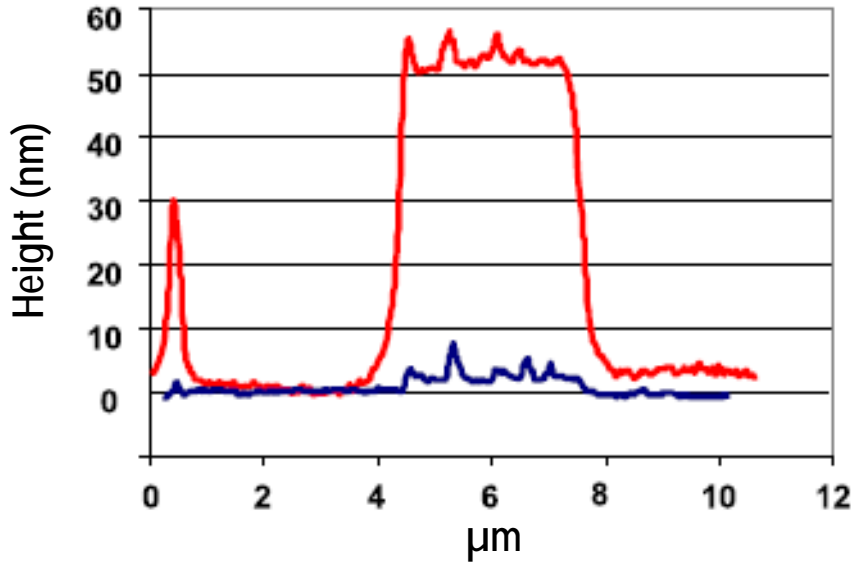

Figure 4.11: Measured height for both contact (blue, upper in figure 4.10) and SPFM (red, lower in figure 4.10)

In Fig. 4.13 is shown the electrostatic force F as a function of D for both FLG and SiO_2. Following the asymptotic potential approach (*Sacha, GM; 2004*) and taking into account that the thickness of SiO_2 is almost an order of magnitude smaller than the tip length, FLG is approximated for simplicity by a semi-infinite metallic sample. In this case, the voltage on the graphene is nearly the same as the one on the Si backgate, which is grounded during the experiment. Moreover, its large size compared to the tip prevents the electric field from penetrating in SiO_2, which is located below. SiO_2 was included in the simulation as a semi-infinite dielectric sample with $\epsilon=3.9$. To estimate the SPFM displacement (D_{SPFM}) we focus on a fixed D for SiO_2 and calculate the distance that would give the same force over the FLG. For clarity, we have explicitly shown this process in figure 2.5 for $D=20$ nm.
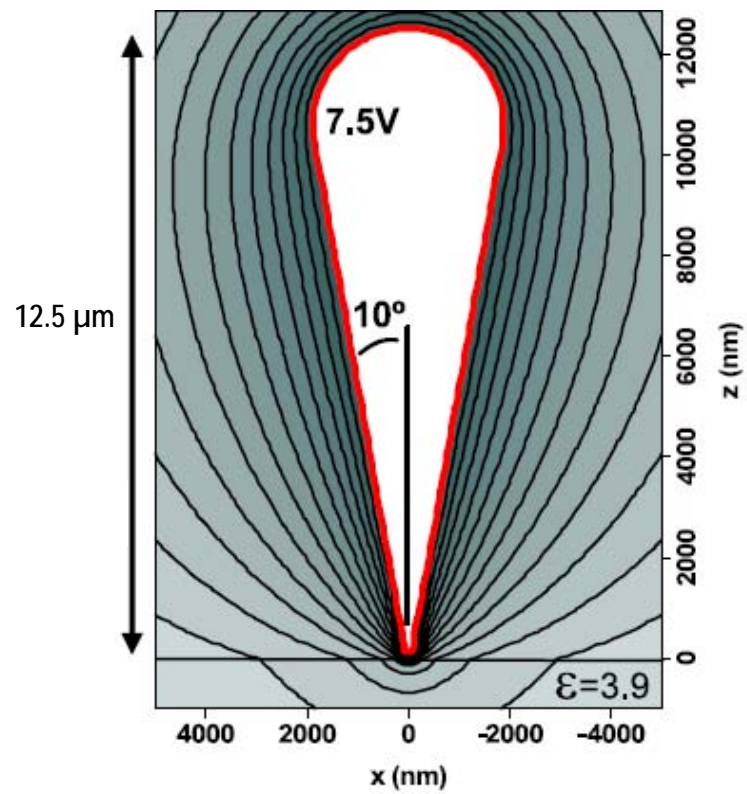
Figure 4.12: Generalized image charge method simulation shape of the tip: R=50 nm, V=7.5 V, θ=10° and L=12500 nm.

As depicted from Fig. 4.13 (a), D_{SPFM} for a spherical tip lies below 10 nm. However, Fig. 4.13 (b) shows that the contrast for a macroscopic tip with the same R can be increased up to 60 nm, in good agreement with the experimental values shown in Fig. 4.10. This large difference is due to the slower convergence that the F versus D curve suffers for a macroscopic tip over a metallic sample when D increases. Due to the long-range nature of the electrostatic force, the very high mutual polarization between the FLG (metal) and the macroscopic shape of the tip is felt at distances as large as D=100 nm. Focusing on the differences in the contrast values between the spherical and macroscopic tip, we conclude that the main contribution to the SPFM contrast is essentially due to the macroscopic shape of the tip and to a limited extent to the shape of tip apex.

Figure 4.14 shows calculated D_{SPFM} values for R=50, 100, 150 and 200 nm compared to measured D_{SPFM} values as a function of D. Below 12 nm tip-sample distance the operation in the SPFM mode becomes unstable, even at low humidity, with the risk of snapping to contact. Although the GICM is optimized for including differences of several orders of magnitude in the simulations, it cannot accurately simulate tip radii below 50 nm due to the large difference with the tip length (12,500 nm). Although direct comparison cannot be made between theory and experiments it can be observed that the experimental values are placed in the lower limit of the curves, which correspond to the lowest values of the tip radii (SEM images gave R=25±5 nm for the tips of the batch used in the experiments).

On the other hand, the difference between theory and experiments for large values of D is the result of the increasing contribution of the conducting cantilever to the SPFM signal, which becomes more important at larger distances due to the decreasing contribution from the tip. The large dimension of the cantilever (30 μm wide) compared with the graphene means that at any
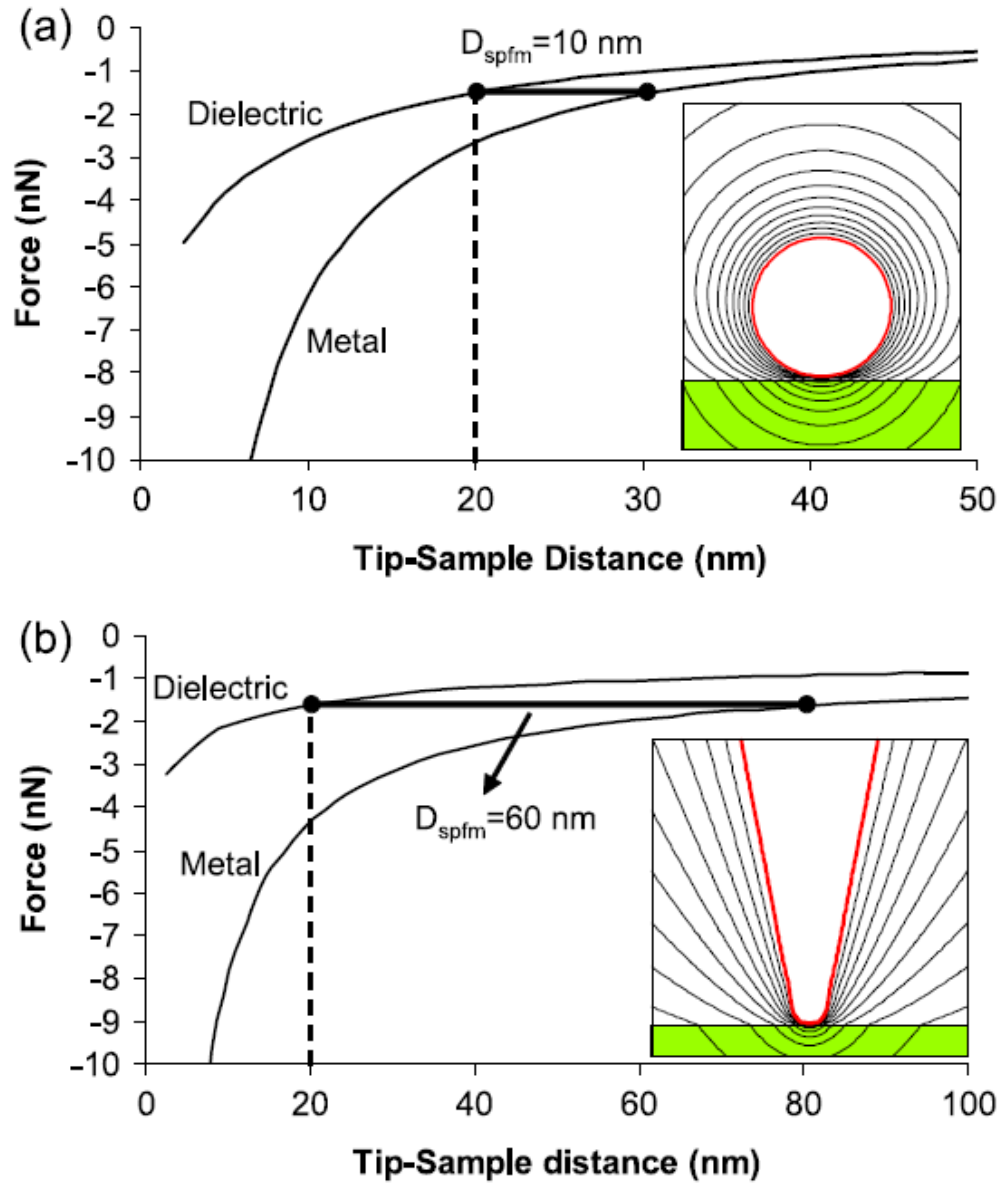
Figure 4.13: Simulations of the electrostatic force for both a metallic (ϵ=3.9) sample for a spherical (R=50 nm) (a) and a macroscopic (R=50 nm, θ=10° and L=12500 nm) tip (b). The SPFM displacement for D=20 nm is shown in both figures. In both cases V=7.5 V.

time during the measurements part of the cantilever is on top of the grapheme and part of it is on top of the SiO$_2$ substrate, and thus the contribution of the cantilever to the image is a convolution of both interactions. This effect might be reduced by reducing the dielectric constant of the cantilever side exposed to the sample while preserving the metallic conductivity of the tip and cantilever (i.e. metallic coating on the detector side), having in mind the need for using low force constant cantilevers, ideally <1 Nm^{-1}, in order to enhance the force sensitivity.
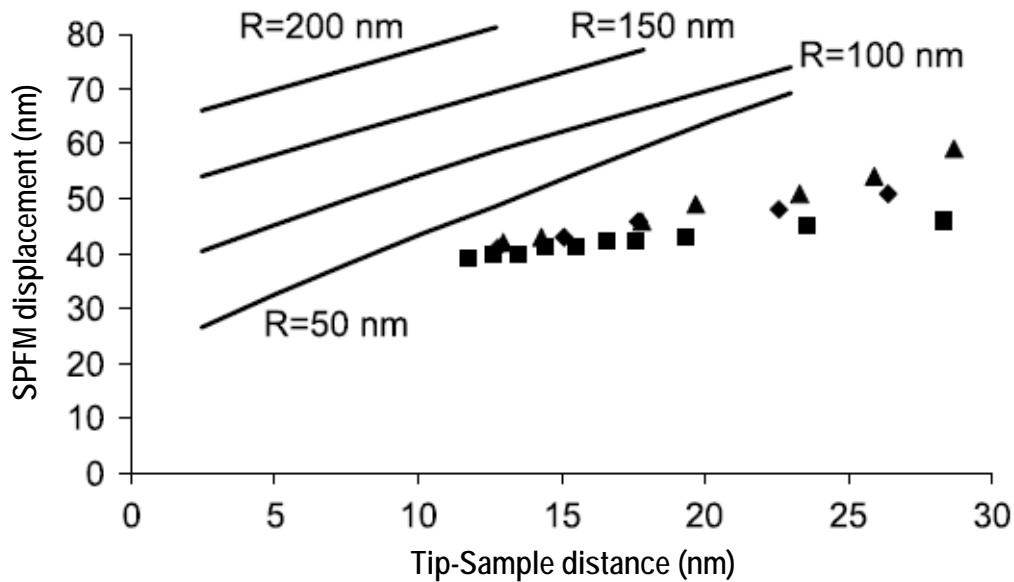
Figure 4.14: Simulated SPFM displacements compared with experimentally determined displacements as a function of the tip-sample distance. The experimental points correspond to three different measurements made in different sessions. Scanning electron microscopy images of the brand new tips gave a tip radius of R=25±5 nm.

As it can be seen in Fig. 4.14, D_{SPFM} is an almost linear function of D for all the tip radii. A good knowledge of D could be used to estimate the effective electrostatic tip radius (*Sacha, GM; 2005*). The relevance of the tip radius and shape shown in Figs. 4.13 and 4.14 is in good agreement with previous works (*Gómez-Moñivas,S; 2001, Zerweck, U; 2005, Sadewasser, S;*

2004, Sacha, GM; 2008) where the electrostatic signal in different setups (EFM, KPFM, non-contact AFM, SCM, etc.) has been analyzed. Although the electrostatic force always depends on the tip geometry when the sample is dielectric, its influence in the final image strongly depends on the microscope setup (*Sadewasser, S; 2004*). Using the results shown in Figs. 4.13 and 4.14, we can quantitatively compare the influence of the macroscopic shape of the tip and the tip apex in SPFM. As we show in Fig. 4.13, the macroscopic shape of the tip makes the SPFM contrast six times bigger than that of a spherical tip with the same radius. If Fig. 4.14, however, the numerical simulations show that changes in the tip radius have a much smaller effect. For example, focusing on the smallest tip-sample distance in Fig. 4.14 (2.5 nm), the SPFM contrast takes values between 27 and 67 nm for tip radii between 50 and 200 nm. A four times bigger tip radius only doubles the contrast. This effect is much smaller than the one shown in Fig. 4.13 (six times bigger) due to the macroscopic shape of the tip.

4.5   How water is adsorbed on graphene sheets?

Figure 4.15 shows SPFM (top left) and KPM (top right) images of a few microns FLG sample. In the SPFM images the FLG films show a high contrast (apparent height) due to the huge difference in the dielectric constant between SiO_2 and the FLG films, as discussed in the previous section. The KPFM image, taken simultaneously with the SPFM image, shows a CPD slightly less positive in the FLG region compared to the SiO_2 substrate, in agreement with recent results (*Datta, SS; 2009*). In KPFM images of the FLG film after charging it at RH<5% with -8V (down left) and +8V (lower right), respectively are also shown in Fig. 4.15. In the KPM images the FLG film charged with +8V (-8V) show a bright (dark) CPD contrast.
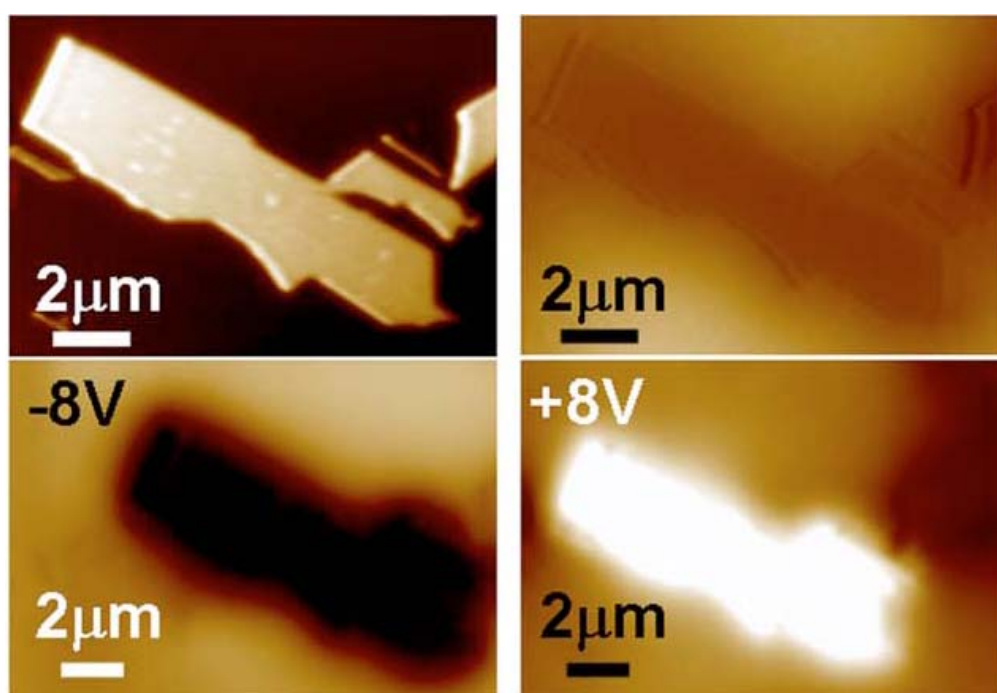
Figure 4.15: SPFM (top left) and KPM (top right) images of a FLG film before charging at low RH. Bottom: KPM images of the same film after charging to (left) -8V and (right) +8V.
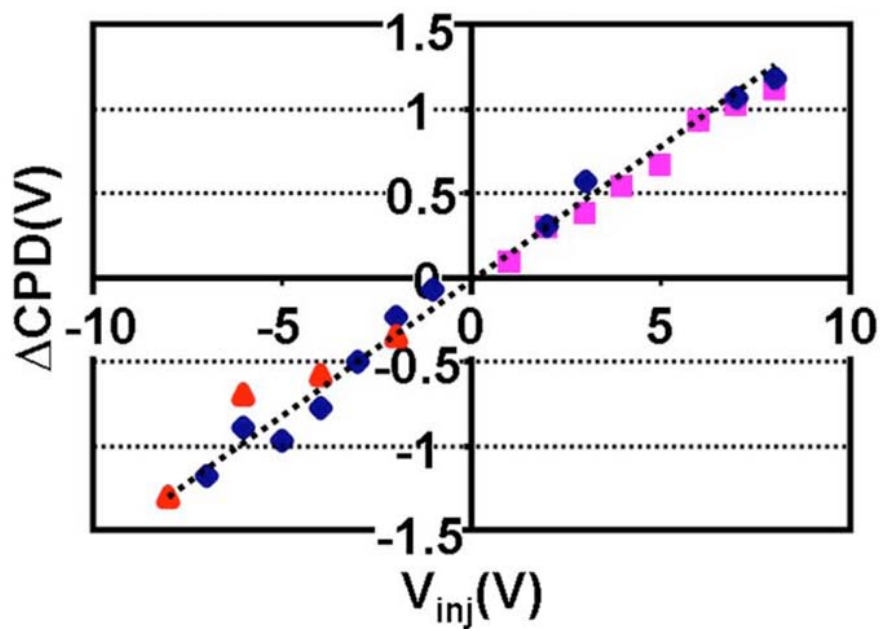
Figure 4.16: ΔCPD after charge injection-CPD discharged vs voltage applied to the tip during the charging process (V_{inj}) measured from KPM taken after charge injection. ΔCPD appears to be proportional to V_{inj}. Different symbols denote different experiments with different tips and different samples. All experiments were performed at RH<5%.

Charge and discharge of graphene

In the following part of the section, I will describe the investigations on charge and discharge of FLG films by measuring the CPD between the FLG film and the tip. First of all is characterized our experimental setup by measuring the dependence of CPD on V_{inj}. Then is studied the influence of humidity in the environment, which brings us to consider various discharge mechanisms. In Fig. 4.16 is plotted the difference between CPD (ΔCPD) measured on three different FLG films before and after charging them as a function of V_{inj} at RH<5%, showing a linear behavior with a slope s∼0.1 (ΔCPD≈s·V_{inj}). After each charge injection and measurement of ΔCPD graphene is brought back to its initial state (by discharging) in order to avoid any charge accumulation effect. Different contributions can influence the charging process and the subsequent ΔCPD measurements:

1. A poor tip-FLG contact

2. The geometry of the tip-FLG system

3. The discharging of the FLG film into the environment

4. The loss of some of the injected charge during the retraction of the tip

In order to check the tip-FLG contact, the contact time between the tip and the FLG film was increased up to 30 min (the usual contact time was ∼1-3 min). Additionally, the increase in the load applied to the tip during the charging process was verified. Both parameters had no effect on the measured ΔCPD. This indicates that the electrical contact betweeen the FLG film and the tip was good enough. In addition, the high reproducibility of the obtained slope over several independent experiments rules out an uncontrolled loss of charge during injection.

The slope s strongly depends on the geometry of the system represented by the tip and the FLG film. It has been measured $s\sim 1$ for FLG films with areas ranging from 6 to 30 μm^2. Measurements performed on much larger FLG films (in the order of the tip dimensions, 200-400 μm^2) still show a linear behavior but with $s\sim 0.3$. Thus, to control quantitatively the charging process, one should take into account the influence of the full cantilever-tip-graphene geometry.

CPD on a charged FLG film is not constant with time and FLG films discharge with a decay rate that strongly depends on the RH of the environment. In Fig. 4.17 (a) is shown the time evolution of KPM images of a FLG film charged at 8V and at 30% RH. The images show how the positive charge spreads over the silicon substrate while the initially confined FLG film discharges. The evolution of a cross section is shown in Fig. 4.17 (b). The CPD on the FLG film decreases and CPD values on the SiO_2 surrounding the film increase due to positive charges that are moving away from the FLG film and toward the substrate. It is well known that a clean SiO_2 surface rich in OH superficial groups is a very hydrophilic surface and a few monolayers of water molecules are expected to be adsorbed on the surface for a wide RH range (*Verdaguer, A; 2007*). Thus, the main discharge process would be through water molecules adsorbed on the FLG film itself (*Moser, J; 2008*) and the water film on the SiO_2 substrate. At t=28 min in Fig. 4.17 the CPD on the FLG and the substrate area films surrounding it level at the same value. From this time on the entire CPD profile lowers with time with minimal changes in its shape. This behavior clearly suggests that the slower discharge of the water film surrounding the FLG film is limiting the faster migration of charges from the FLG film to the water film.

The time evolution of the mean CPD measured on the FLG film at different RH conditions exhibits an exponential-like decai [Fig. 4.18 (a)]. Only
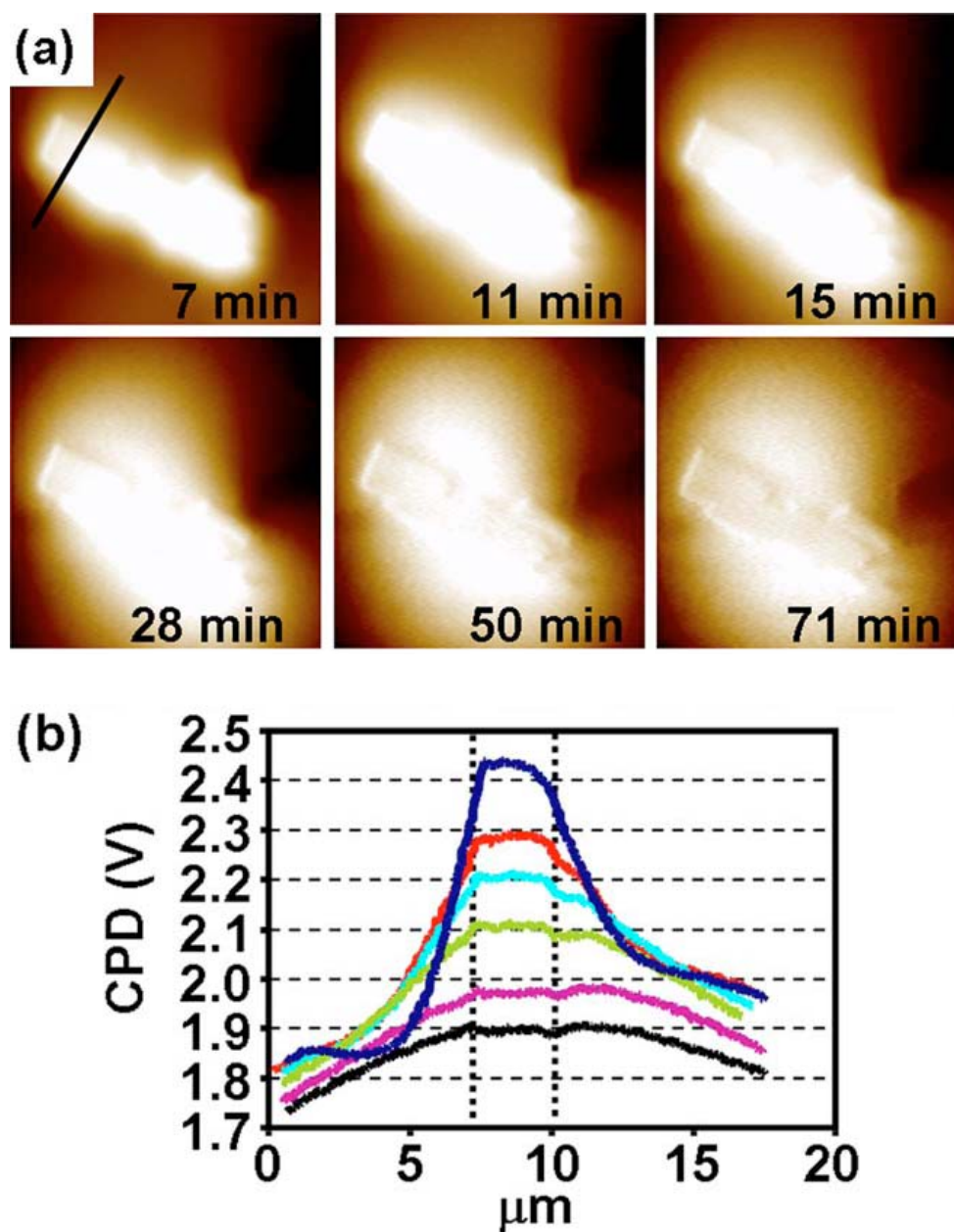
Figure 4.17: (a) Time evolution of KPM images of a FLG film charged at +8V and at 30% RH. (b) Cross section profiles of the same images.
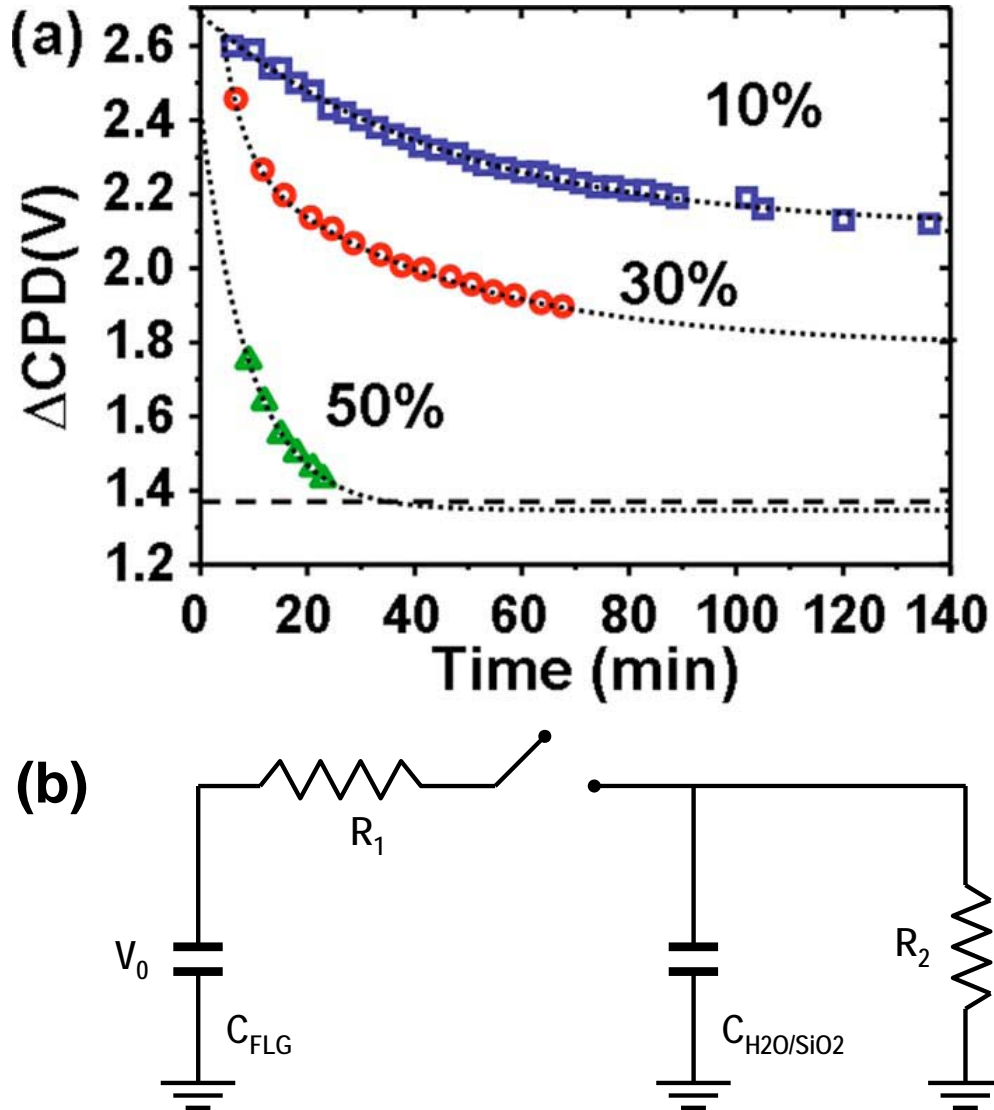
Figure 4.18: (a) Equivalent RC circuit modeling the discharge of the FLG film. Some of the components of the circuit can be neglected at low humidity (R_2) and at high humidity (C_{H_2O/SiO_2}). (b) Evolution with time of the FLG film CPD value after charging it at +8V for 10%, 30%, and 50% RH. Exponential decays used to fit the data (Eqs. 4.3 and 4.4) are shown and the CPD value of the discharged FLG film is marked ($\sim$1.4 V).

the data taken at 50% RH decays to the CPD value of the FLG film before charge injection (∼1.4 V for that particular sample) for the times measured. Very similar decays were obtained for both positive and negative voltages.

In order to explain our results is modelled our system as an equivalent circuit formed by capacitors and resistances [Fig. 4.18 (b)]. One capacitor (D_{FLG}) is formed by the FLG film and the SiO_2/Si substrate while the other (C_{H_2O/SiO_2}) is formed by the water film adsorbed on the SiO_2 and the SiO_2/Si substrates (the Si substrate is grounded). R_1 represents the resistance that limits the flow of charges on the FLG film to the water film. R_2 models the discharge of the water film mainly through the diffusion of the water molecules on the SiO_2 surface. The solution of the differential equations of the circuit is in the form:

$$V_{FLG}(t) = A_1 e^{m_1 t} + A_2 e^{m_2 t} \tag{4.3}$$

where,

$$m_{1,2} = -\frac{1}{2}\left[\frac{1}{C_1 R_1} + \frac{1}{C_2 R_1} + \frac{1}{C_2 R_2}\right] \pm \frac{1}{2}\sqrt{\left[\frac{1}{C_1 R_1} + \frac{1}{C_2 R_1} + \frac{1}{C_2 R_2}\right]^2 - 4\frac{1}{C_1 C_2 R_1 R_2}}$$
$$\tag{4.4}$$

and $V_{FLG}(0) = A_1 + A_2 \equiv V_0$. At 10% RH we can simplify the model by considering that $R_2 \to \infty$ and can thus be ignored. We obtain that

$$V_{FLG}(t) = \frac{C_T V_0}{C_{H_2O/SiO_2}} + \frac{C_T V_0}{C_{FLG}} e^{-t/R_1 C_T}, \tag{4.5}$$

where C_T stands fot the total capacitance ($1/C_T = 1/C_{FLG} + 1/C_{H_2O/SiO_2}$) and V_0 is the initial voltage at the C_{FLG} capacitor. Equation 4.3 shows the voltage decay for the FLG film going from V_0 to $V_F = C_T V_0/C_{H_2O/SiO_2}$ with a time constant R_1 and C_T depend on RH. The increase in water molecules on the SiO_2 surface in contact with the FLG film will increase the ratio of charge

transfer between the FLG and the water film, thereby lowering the resitance in the model. The amount of water adsorbed on SiO_2 would clearly affect C_{H_2O/SiO_2} and water adsorbed on or below the FLG film could also modigy C_{FLG}. The experimental data fitted with this model is shown in Fig. 4.18 (a) with a time constant of $\sim$50 min. At high humidity there is a high diffusion of charges on the surface and it can be considered that R_2 is so small that no charge is accumulated in C_{H_2O/SiO_2}. The equivalent RC circuit is thus simplified by a circuit composed of a capacitor C_{FLG} that discharges through a resistance R_1. The CPD value decays exponentially to its precharging value (1.4 V for RH=50% with a time constant of $\sim$10 min, in Fig. 4.18, (a)). At intermediate humidity the discharge of the FLG film depends strongly on the charge accumulated in the water surrounding it and how fast these charges diffuse away from the FLG film. In the model that means that none of the processes are dominating the discharging and both R_1 and R_2 must be taken in account. Data taken at 30% RH [Fig. 4.18 (a)] can only be fitted then using the two exponential decays shown in Eqs. 4.3 and 4.4.

4.6   Summary

- Is found a large contrast in SPFM images of FLG transferred onto a SiO_2 surface due to the differences in dielectric response ($\epsilon_{graphene} \sim \infty$, and ϵ_{SiO_2}=3.9). Using GICM, it has shown that the macroscopic shape of the tip must be included in the simulations to quantitatively reproduce the experimental SPFM images. The main contribution to the SPFM comes from the macroscopic shape of the tip rather than the tip radius.

- CPD measured on the FLG film using KPM shows a linear relationship with the voltage applied to the tip during the charge injection for both negative and positive voltages ranging from -10 to +10V.

- CPD follows RH dependent exponential decays with time. FLG films discharge mainly through the water layer adsorbed on the SiO_2

Chapter 5

Aliphatic alcohol Langmuir-Blodgett films on graphite

5.1 Introduction of my work

Molecular self-assembly is the spontaneous association of molecules under equilibrium conditions into stable, structurally well-defined aggregates joined by noncovalent bonds. It is a great strategy to form nanostructures and nanoparticles. One of the most known and studied self assembly structure is the monolayer. The most frequently investigated SAM system is alkanethiols on gold. The thiol head group acts as an anchor group which is covalently bond to the gold. The carbon chain is referred as the backbone which is assumed to stabilize the SAM due to Van der Waals interactions (*Schmidt, E; et.al.; 1993*) (see Fig. 5.1). Langmuir-Blodgett technique allows to produce thin films on a liquid-gas interface through the help of barriers that compress the molecules to organize them as a homogeneous monolayer. Then the monolayer can be transferred to a substrate by immersion through the
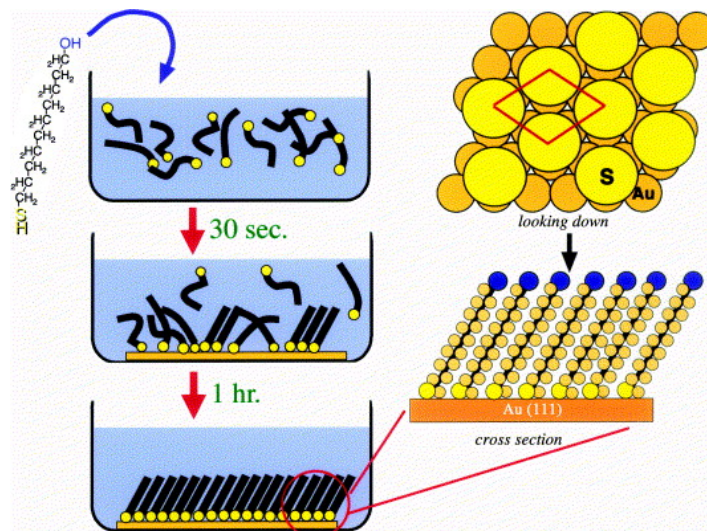
179

monolayer (see section 2.2).

Figure 5.1: The self-assembly process. An n-alkane thiol is added to an ethanol solution (0.001 M). A gold(111) surface is immersed in the solution and the self-assembled structure rapidly evolves (taken from *Castner, DG; and Ratner, BD; 2002*).

Our goal in this chapter is to use this technique in order to form an aliphatic alcohol film anchored on a graphite surface through van der Waals interactions. The idea comes from another study made in Israel by Dr. *M. Lahav* and Dr. *L. Leiserowitz*, who observed how aliphatic alcohol SAMs can be used to catalyze the freezing of water at high temperatures.

Their studies showed that the deposition of alcohols (*n*-1-alkanols and *w*-*n*-alkanediols) at the surface of small droplets of pure water increase ice nucleation from -15°C to -2°C (*Popovitz-Biro, R; 1996 and Gavish, M; 1990*). They found that the alcohol molecules form two-dimensional crystalline domains at the air-water interface, with a unit cell close to that of the hexagonal form of ice (I_h).

The structure of these alcohol films is in essence the same as that of their respective three-dimensional crystals and depends on the number of carbon

atoms in the molecular chain and whether this number is odd or even. Lahav, M. *et.al.* tested different pure alkanols (hydroxyl head group with an alkane tail), different pure alkanediols (alkane tail between to hydroxyl head groups), a mixture of alkanols with alkanes, and a mixture of alkanediols with alkanes as well. The reason for that was to prove the ability to induce ice nucleation. It is known that alkanes have a surface lattice distances different to alkanols and alkanediols, therefore they should show different matching with hexagonal ice (I_h) (*Arbel-Haddad, M; 1998*), and therefore the nuclation ability is expected to be different. In Fig.5.2 is shown the freezing temperatures observed for alkanols and alkanediols mixted with alkane solution. The active component represents alkanol and alkanediol. Is proved that when more active component is present in a alkanol-alkane mixture, the freezing temperature is higher, while in the case of alkanediol-alkane mixture the freezing temperature remains constant when the rate of active component arrives to 20%. This means that alkanols are better nucleators than alkanediols.

In each experiment they prepared 10-15 water drops of 10 μL, and they were placed on a microscope cover glass slide (treated with octadecyltrichlorosilane in order to obtain a hydrophobic surface). Then they put 1 μL of alcoholic solution in $CHCl_3$ (concentration of 0.2 mM) onto each water drop, which were organized as a monolayer (film) of aliphatic alcohol.

M. Lehav *et.al.* observed that the freezing temperature of water drops covered by a monolayer film of the alcohols depends on chain length of the molecule. The decrease in the chain length causes an increase of molecular motion and finally it leads to a worse mismatch between the crystalline monolayer film and ice. In addition, they found that the temperature of ice nucleation decrease with increasing alkane content in the film for a mixed film of alkanols and alkanediols . As explained above, the alkanes are inactive components which disturb the lattice of hydroxyl groups (OH) at the
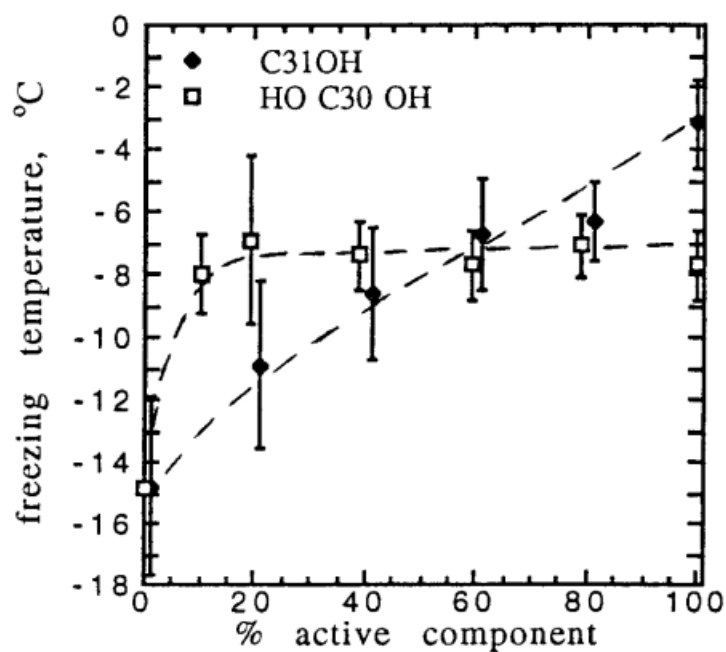
Figure 5.2: Induced ice nucleation temperatures under mixed films composed of an ice nucleating alcohol, either $C_{31}H_{63}OH$ (rhombs) or $HO(CH_2)_{30}OH$ (squares), with the alkane $C_{32}H_{66}$ mixture (taken from *J. Phys. Chem. B, Vol. 102, No. 9, 1998*).

interface, reducing the coherence of nucleation sites for ice. For this reason, is expected that if more alkane is introduced into the solution, the T° of ice formed decreases.

The freezing point curve for the *n=odd* series increases with chain length as shown in firgure 5.3.
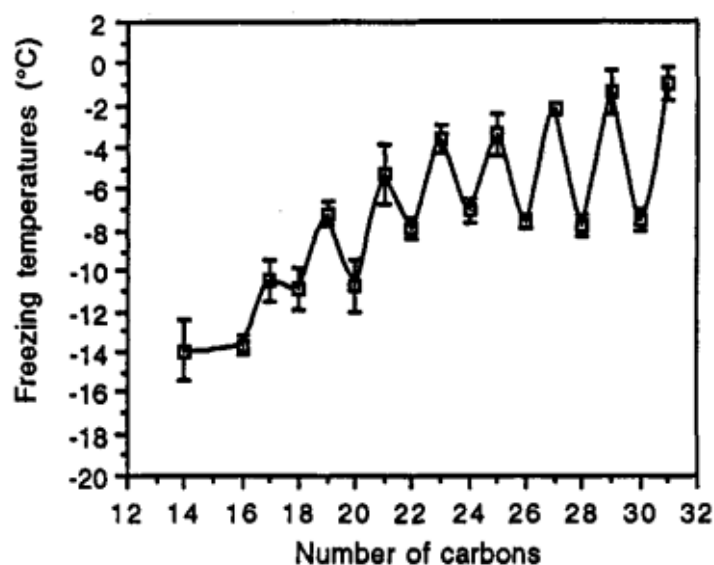
Figure 5.3: Freezing temperatures of supercooled water drops covered by monolayers of aliphatic alcohols $C_nH_{2n+1}OH$ vs the number of carbon atoms in the chain.

This trend suggested to them that the orientation of the OH groups in the odd and even analogs are not the same, the odd ones have a better structural match with ice (*Popovitz-Biro; 1994*).

This was the starting point of our interest in aliphatic alcohol films. The intention is to transfer LB films formed on the water-air interface as in the droplet surfaces in the Popovitz-Biro experiments to graphite (graphit has been used as a hydrophobic model surface) in order to obtain a homogeneous film with hydroxyl groups pointing up to study the adsorption of water and the ice nucleation on the film formed. In short, we want to observe the same

behaviour explained by Lehav *et.al.* but starting from a solid sample. Two important points make this work interesting and innovative:

1. LB films are very well stablished on hydrophilic substrates (eg. mica), but the use of hydrophilic substrates is not interesting for our objective because OH groups will pointing down, bonded with the substrate. We need the OH groups pointing up to create our hydrophilic surface. Therefore, will be necessary to use a hydrophobic substrate in order to obtain the mentioned orientation, and the chosen substrat this purpose is graphite.

2. LB films on hydrophobic substrates have never been tryied to our knowledge, mainly because the formation of monolayers is not so natural as in hydrophilic case (see Fig. 5.10), and the bonds between the substrate and the molecules will be only van der Waals, much weaker than SAMs on hydrophilic substrates (see Fig. 2.18).

5.2 Experimental

All SPM experiments were carried out at RT with the same Agilent 5500 atomic force microscope (AFM) as in the previous chapters of BaF_2/CaF_2 and graphene. The AFM was operated in the acoustic (AM-AFM) mode and in the noncontact electrostatic mode SPFM. The microscope was enclosed in a glove box that allows the environment control . Humidity control was achieved by circulating dry N_2 to decrease RH or by bubbling N_2 through Milli-Q water to increase it as in previous experiments.

The graphite used was *H*ighly *O*riented *P*yrolytic *G*raphite (HOPG, NT-MDT, Zelenograd, Russia). In order to have a fresh face, graphite was cleaved using a conventional tape at ambient conditions (T=22±2°C, RH∼50%).

When a fresh face is obtained, the substrate is ready to prepare a Langmuir-Blodgett film on.

Three aliphatic alcohols were selected with an even carbon number: hexadecanol, tetracosanol and octacosanol (16, 24 and 28 carbons, respectively), and three aliphatic alcohols with an odd carbon number: heptadecanol, tricosanol and heptacosanol (17, 23 and 27 carbons, respectively). These alcohols were also chosen because of their lengths (hexadecanol and heptadecanol less than 20 carbons, tricosanol and tetracosanol near to 25 carbons, and heptacosanol and octacosanol near to 30 carbons), because, as I said previously, the chain length influences the compaction of the layer formed (i.e., when the chain contains more carbons, more van der Waals bonds are involved, then the interaction is stronger and the layer formed is more robust.

5.2.1 Alcohol solutions

We selected three aliphatic alcohols with an odd number of carbons and three aliphatic alcohols with an even number of carbons to try to observe the difference explained by Lahav, M. *et.al.* In Fig. 5.4 is shown the characteristics of alcohols selected.
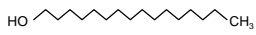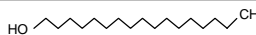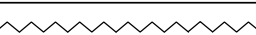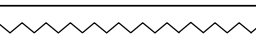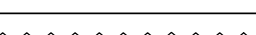
Alcohol name	Number of Carbons	Molecular weight	Molecular structure
Hexadecanol	16	242.44 g/mol	HO〜〜〜〜CH₃
Heptadecanol	17	256.5 g/mol	HO〜〜〜〜CH₃
Tricosanol	23	340.63 g/mol	HO〜〜〜〜CH₃
Tetracosanol	24	354.6 g/mol	HO〜〜〜〜CH₃
Heptacosanol	27	396.73 g/mol	HO〜〜〜〜CH₃
Octacosanol	28	410.7 g/mol	HO〜〜〜〜CH₃

Figure 5.4: Table with the names of the aliphatic alcohols chosen, the number of carbons and the molecular weight of each one.

For a proper distribution of the alcohol molecules on water trough is necessary to prepare alcohol solutions with a soluble and volatile solvent with an appropriate concentration. Then, the suitable concentrations calculated for our Langmuir-Blodgett apparatus are explained below (see Fig. 5.5).

Alcohol name	Number of Carbons	Concentration	Volume deposited
Hexadecanol	16	0.12 mg/mL	50 µL
Heptadecanol	17	0.123 mg/mL	50 µL
Tricosanol	23	0.17 mg/mL	50 µL
Tetracosanol	24	0.18 mg/mL	50 µL
Heptacosanol	27	0.20 mg/mL	50 µL
Octacosanol	28	0.21 mg/mL	50 µL

Figure 5.5: The table shows the concentration calculated for a number of molecules of $3x10^{17}$. The aim is getting the same number of molecules in every alcohol solution.

5.2.2 Alcohol solution deposition and dipping preparation

The principal steps to prepare the Langmuir-Blodgett films on graphite are:

1. Cleaning the trough (section 2.2.4).

2. Cleaning the microbalance.

3. Fill the trough with Milli-Q water.

4. Substrate placement in the clamp.

5. Place the barrier, dipper and balance values to zero.

6. Lowering the substrate and immersing it.

7. Deposit the alcohol solution on the water.

8. Wait between 15 to 20 minuts while the molecules of the alcohol are dispersed on the water surface and chloroform is evaporated.

9. Closure of the barriers until the complete formation of the monolayer.

10. Rise the sample.

In the graphic 5.6 one can see the formation of a monolayer. Region A in the graphic represents when alcohol molecules are dispersed on the liquid (water) with no preferential organization. When the barriers are close enough (region B), alcohol molecules begin to organize themselves in order to form a monolayer. Region C is the critical point when the monolayer is just completed and it is broken to form a bilayer. Then, it's necessary to stop the barriers before region C but near to it (to ensure the formation of the monolayer).

To control the formation of the monolayer, the surface pressure ("target") must be fixed and controlled, because it is the limit where we want to stop the barriers before rising the sample. This parameter varies depending of the alcohol solution, and it has been studied for each one. In Fig. 5.7 is shown the values of "target" for each alcohol solution.

In this process there are some critical parameters that must to be controlled carefully. First of all, it is important to control the maximum pressure in the closure of the barriers. If much pressure is excerced, then the monolayer break and multilayers are formed on the water surface.

Another important step is dipping process and the rise of the sample. The molecular deposition depends on the velocity of the sample rise. In general, when the process is slower, the molecule distribution on graphite is better.
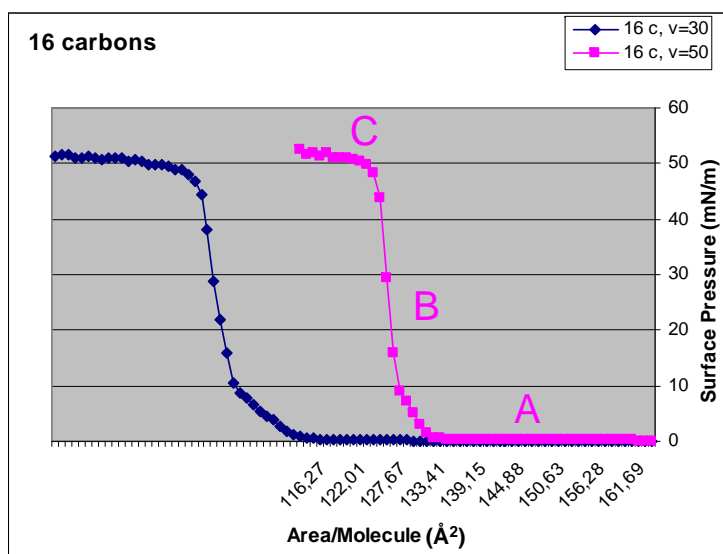
Figure 5.6: Typical isotherms of aliphatic alcohols. In this case it represents the hexadecanol isotherm at different closure speed of barriers (v=30 mm/min in blue, v=50 mm/min in pink). The layer compaction is worse if the speed of the barriers is high because molecules have no time to organize properly. For this reason when the v=30 mm/min the molecules take longer to organize themselves and the occupied surface (area) is less than the v=50 mm/min case. In order to obtain the best monolayers on graphite, all the following experiments have been made at v=30 mm/min.

Alcohol name	Number of Carbons	Target parameter mN/m
Hexadecanol	16	40
Heptadecanol	17	45
Tricosanol	23	35
Tetracosanol	24	25
Heptacosanol	27	25
Octacosanol	28	20

Figure 5.7: The table shows the target parameter (pressure limit) for each alcohol. The values must be respected because the increase of the value implies the breaking of the monolayer.

5.2.3 Monolayer's height

The first studied parameter is the influence of the molecule length in the mormation of the monolayer. It is known that the aliphatic alcohols are vertically placed on the surfaces interacting between them trough van der Waals interaction. The literature shows that the structure of alkanethiols on surfaces is not exactly vertical but they are placed making an angle between 0° to 30° respect the substrate (see figure 5.9) (*Popovitz-Biro, R; et.al; 1993*), and here is assumed the same behavior. Therefore, knowing that the C-C bond has a length of 1.54 Å, the C-O bond is the order of 1.43 Å, O-H bond is ~0.96 Å and C-H bond is ~1.07 Å, and applying the law of sines and cosines can be calculated the theoretical height of an alcoholic chain on graphite substrate when the deviation is nonexistent (0°) and when the deviation is of the order of ~30° as shown in figure 5.8. Then, is assumed that the experimental length calculed will be between these two values (theoretical vertical length (0°) and theoretical ~30° length).

Alcohol name	Number of Carbons	Theoretical length at 0º	Theoretical length at 30º
Hexadecanol	16	26.56 Å	23 Å
Heptadecanol	17	28.1 Å	24 Å
Tricosanol	23	37.34 Å	32 Å
Tetracosanol	24	38.88 Å	34 Å
Heptacosanol	27	43.5 Å	38 Å
Octacosanol	28	45.04 Å	39 Å

Figure 5.8: In this table is calculed the theoretical vertical height of every chain, and the theoretical real height considering an angle of 30° respect to the sample (see figure 5.9).
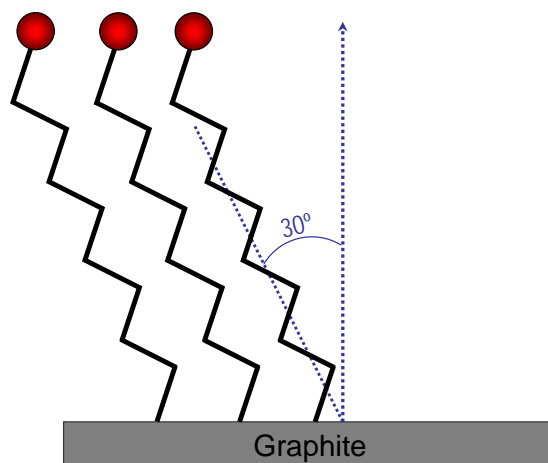
Figure 5.9: The expected placement of the monolayers respecto to the substrate can range from 0° to 30°. Here is shown the maximum deviation possible.

5.3   Results

As explained before, in the first part of this work it was decided to do Langmuir-Blodgett samples (i.e. vertical dipping), despite the difficulty of handling and formation of layers in hydrophobic substrates. The results of these experiments were not so satisfactory. But it allows to take an idea about which alcohols tend to get together in monolayer easily and which alcohols have difficulty to do it. In figure 5.10 is shown how will be the theoretical alcohol deposition on hydrophobic surface as graphite through Langmuir-Blodgett technique. The results obtained by AFM and SPFM of the different alcohols deposited on graphite are explained below.

5.3.1   A hydrophilic substrat to start: mica

As explained until now, mica is a hydrophilic substrate and suitable for LB technique. The easy and simple handling of mica, makes it a excellent sample in order to compare with the hydrophobic ones. As shown in Fig. 5.11, the
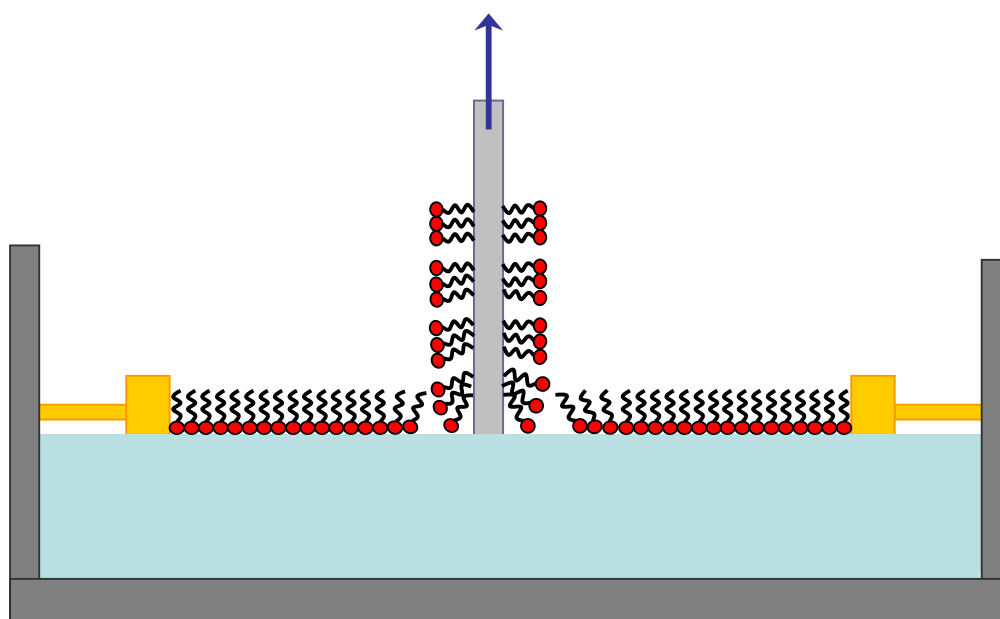
Figure 5.10: A schematic view of the formation of our LB films on graphite. The transfer of the molecules is clearly more difficult than the transfer of a monolayer on a hydrophilic substrate (see figure 2.18).

formation of aliphatic alcohol monolayer on mica is pretty good, with almost no holes and layer overlapping (i.e. multilayers).
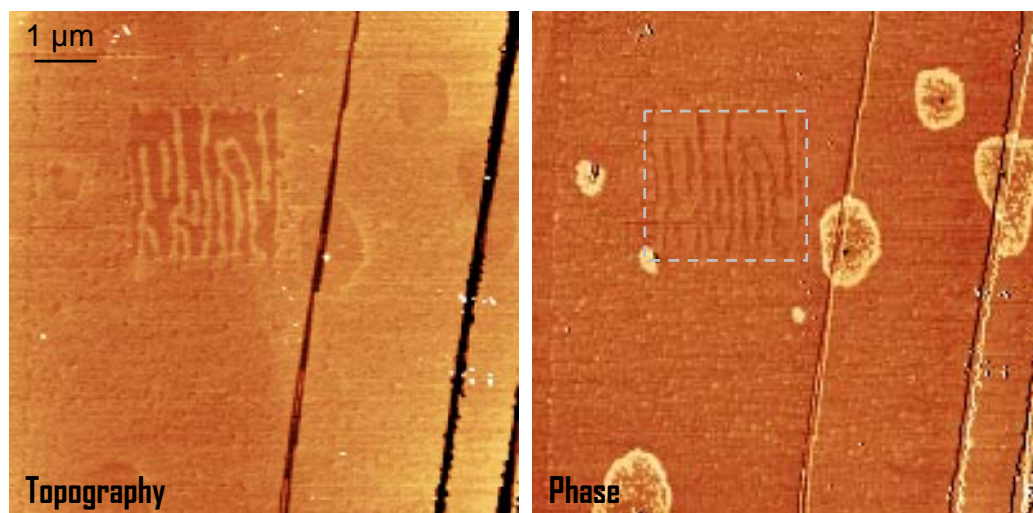

Figure 5.11: Topographic (left) and phase (right) of hexadecanol layer on mica in AM-AFM mode. This image is the result of a zoom out as seen on the dotted grey box in the phase image. The quality and homogeneity of the monolayer on mica is easily seen.

5.3.2   Hydrophobic substrat: graphite.   Comparation of odd and even

Popovitz-Biro, B; et.al. observed that there exist structural differences in monolayers deppending on the number of chain carbons of aliphatic alcohols. They showed that molecules with an odd number of carbon atoms have a better structural match with I_h ice, and molecules with an even number of carbon atoms are less effective. This is extrapolated to the present case and is assumed that the films with chains of an odd number of carbons will form easily the monolayers respect to even ones (see Fig. 5.12).

Depending on the number of carbons that contains the chain, the monolayer adopts a more or less stable conformation. As shown on the left side

in Fig. 5.12, there is a monolayer formed by aliphatic alcohols with an even carbon chain. The hydroxyl heads of the chains, pointing upwards, create steric hinderance between them, in other words, are nuisance, for this reason is more complicated that monolayer formation takes place. If one focuses to the right side of the Fig. 5.12, a monolayer of an odd carbon chain is shown. Can easily be seen how the formation of monolayers on graphite are more harmonious, hydroxyl heads have more space and one should think that in this conformation the molecules are felt more comfortable.
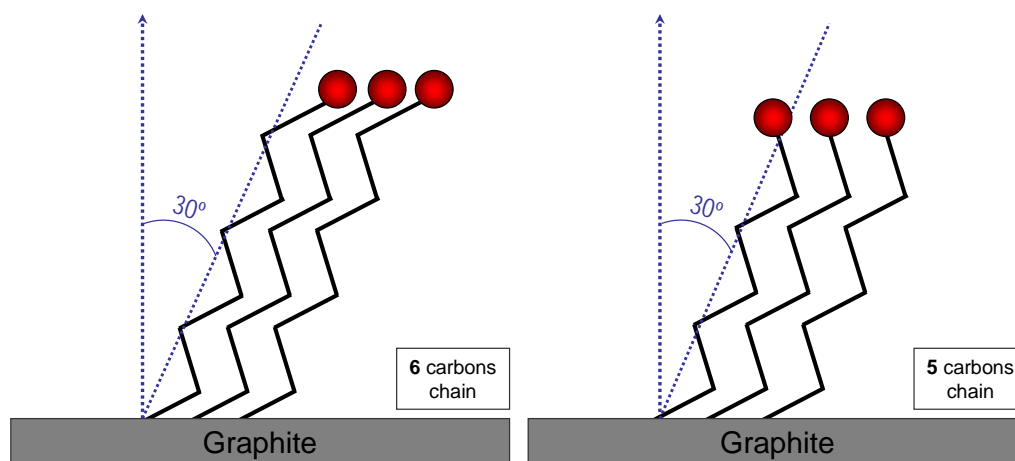

Figure 5.12: Left: monolayer of an aliphatic alcohol with an even number of carbon atoms on graphite with a deviation angle of 30° respecto to the vertical axis. Right: monolayer of an aliphatic alcohol with an odd number of carbon atoms on graphite with the same deviation angle of 30°.

Odd carbon chains on graphite

17-C (heptadecanol), 23-C (tricosanol) and 27-C (heptacosanol) were prepared. As shown in Fig. 5.12, aliphatic alcohols with and even carbon chain have a chain orientation less natural than aliphatic alcohols with and odd carbon chain. Heads of odd chains are more separated resulting a lower steric hindrance, which indicates a simpler and easier formation. This is what is observed in the proposed case. The formation of aliphatic alcohol monolayers

with an odd carbon number is frequently observed, but as will be explained below, multilayers are often observed as well. In Figs. 5.13, 5.14 and 5.15 are shown monolayers of 17, 23 and 27 C respectively with their profiles.
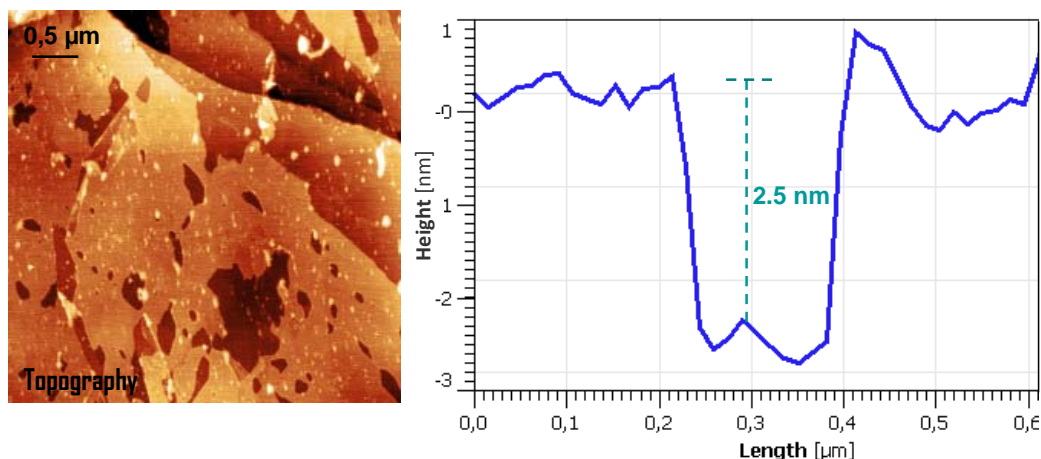

Figure 5.13: Topographic (top-left) and phase (top-right) AFM images in AM-AFM mode of heptadecanol layers on graphite. A monolayer is formed on graphite as is shown in the profile image (below) about 25 Å (near to theoretical value of 24 Å).

Even carbon chains on graphite

16-C (hexadecanol), 24-C (tetracosanol) and 28-C (octacosanol) samples were prepared. Monolayers of these aliphatic alcohols were not observed. Only in exceptional cases monolayers have been observed with hexadecanol. Multilayers are the most common conformation with aliphatic alcohols with even carbon number. In Figs. 5.17 and 5.18 are shown small crowds with different heighs that corroborate the fact that its hardly placed to make monolayers. Rarely is observed the formation of complete monolayer of hexadecanol as shown in Fig. 5.16, where only patches of monolayers are observed. Often is shown molecules adsorbed on the surface, but the height of these layers is less than theoretical height calculated, indicating a non-vertical deposition, perhaps because the molecules are more comfortable in other conformations.
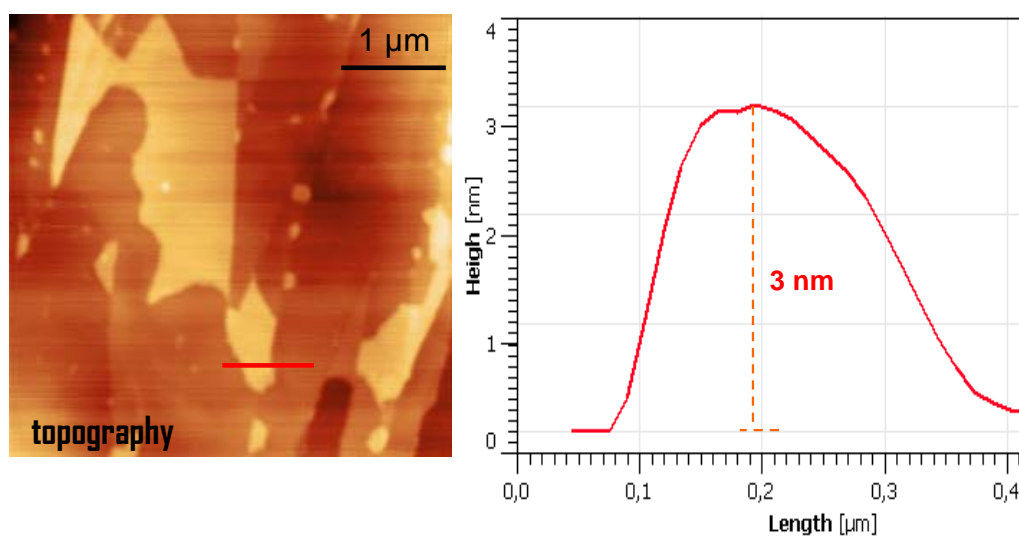
Figure 5.14: Topographic (top-left) and phase (top-right) AFM images in AM-AFM mode of tricosanol layers on graphite. A monolayer is formed on graphite as is shown in the profile image (below) about 30 Å (near to theoretical value of 32 Å).
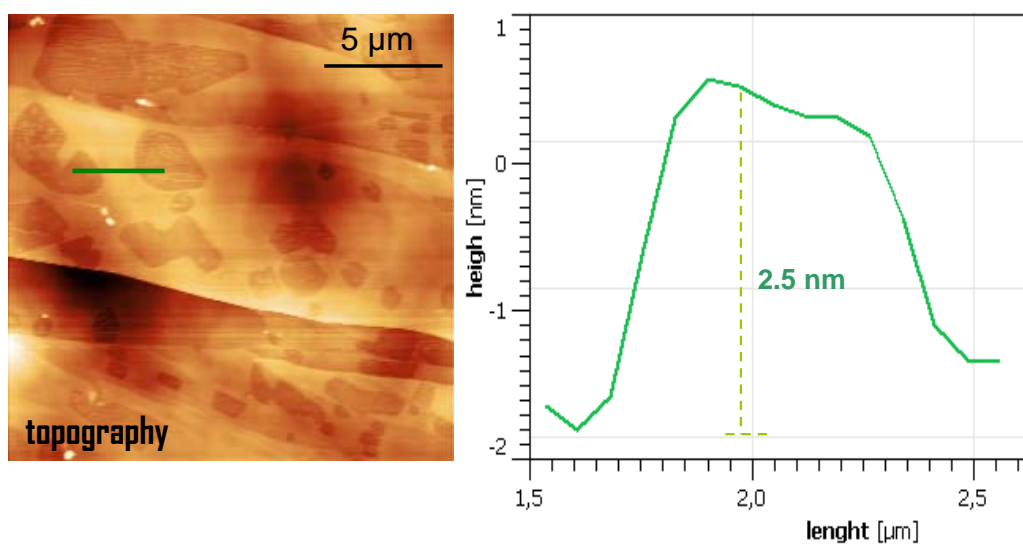

Figure 5.15: Topographic (top-left) and phase (top-right) AFM images in AM-AFM mode of hepta-cosanol layers on graphite. A monolayer is formed on graphite as is shown in the profile image (below) about 25 Å (near to theoretical value of 38 Å).
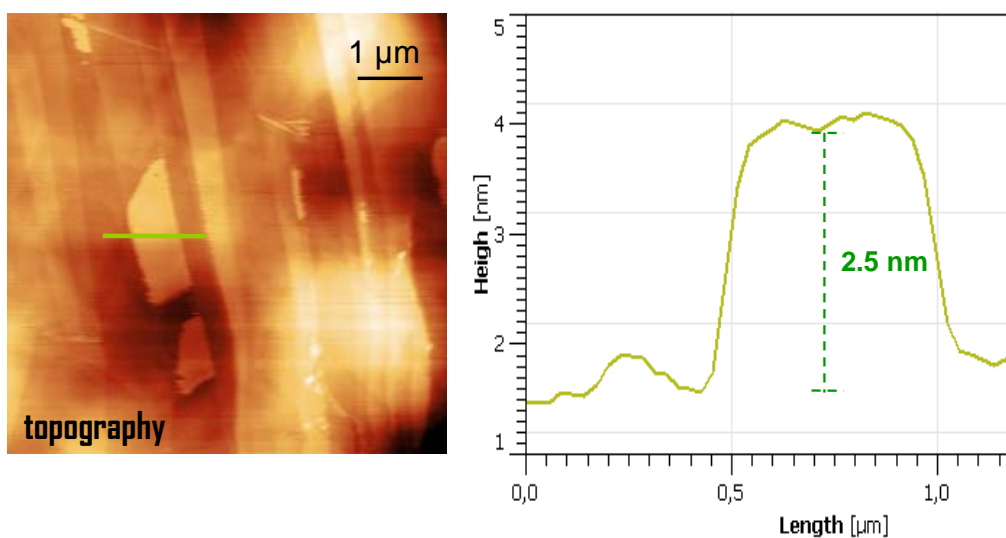
Figure 5.16: Topographic (top-left) and phase (top-right) AFM images in AM-AFM mode of hexadecanol layers on graphite. In this case, a monolayer is formed on graphite as is shown in the profile image (below) about 25 Å (near to theoretical value of 23 Å).

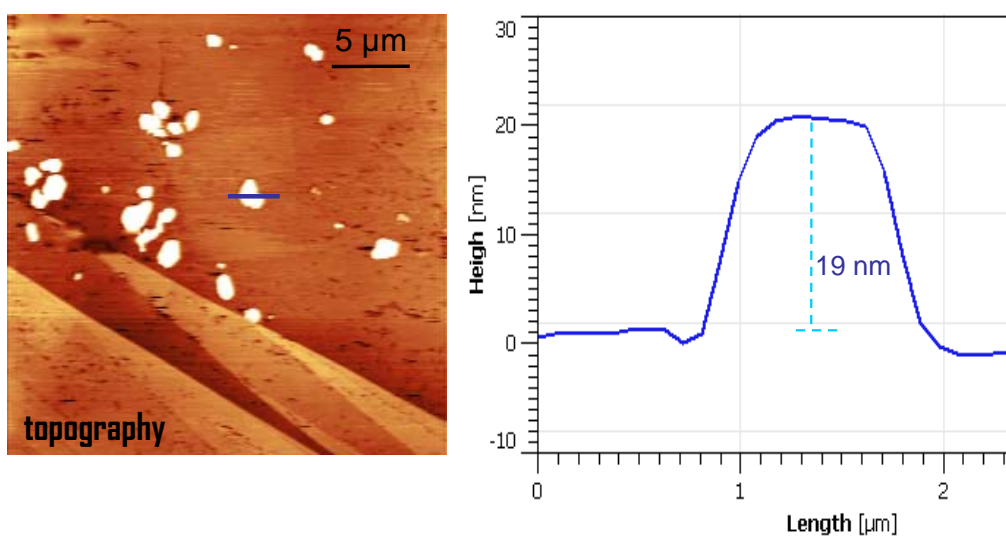

Figure 5.17: Topographic (top-left) and phase (top-right) AFM images in AM-AFM mode of tetracosanol layers on graphite. Multilayers are shown on graphite as is shown in the profile image (below) about 190 Å (so far to theoretical value of 34 Å).
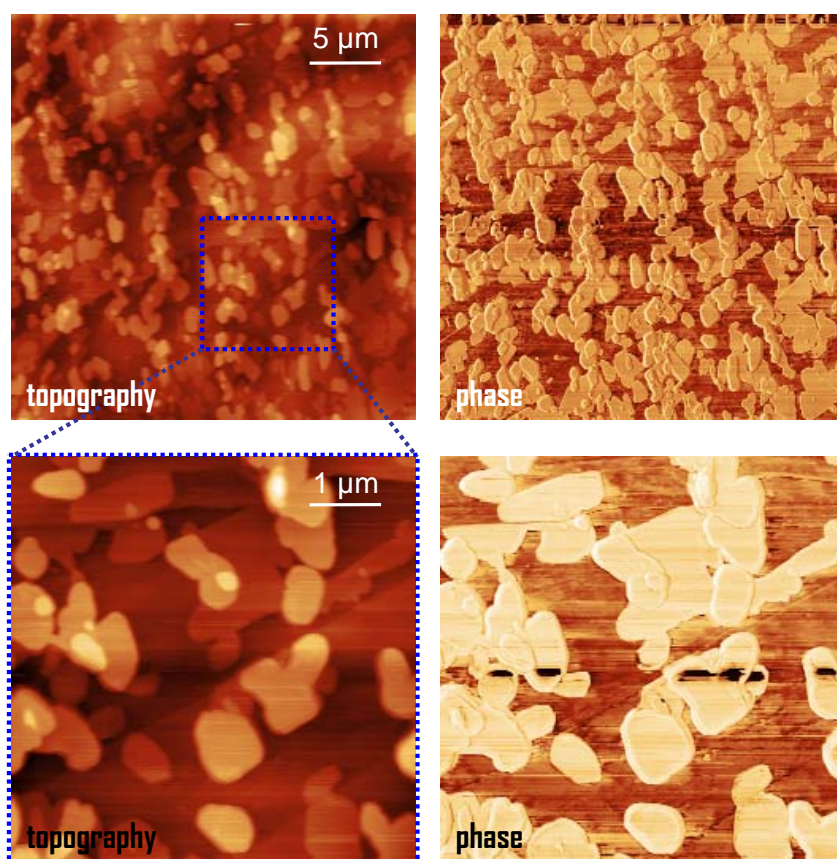
Figure 5.18: Topographic (top-left) and phase (top-right) AFM images in AM-AFM mode of tetra-cosanol layers on graphite. Multilayers of different heights are shown on graphite.

5.3.3   Length comparison

A key focus of this investigation is the length of aliphatic alcohols as Lehav, et.al postulated. In the present case is also extrapolated their results to the present work. They observed that if the chain is long, monolayer is easily formed on water droplet principally due to the large amount of van der Waals interactions involved, which stabilized and strengthens the system. Here apply the same principle, it is that longest chains will form monolayers easily and more stable than the shortest ones.

The largest aliphatic alcohol used is octacosanol (28C), but as explained in the previous subsection is very difficult to obtain monolayers from this compound, therefore it is necessary to focus our attention to odd carbon number alcohols: heptadecanol, tricosanol and heptacosanol (17C, 23C and 27C respectively), and in particular the largest and shortest ones (heptadecanol and heptacosanol). It is true that both compounds form monolayers on graphite relatively easily, but it is also true that is easier to see monolayers when the aliphatic alcohol chain is larger. If one compares the formation of monolayers on graphite between tricosanol (23C) and heptacosanol (27C), is difficult to appreciate changes in formation behaviour, but if one compares between heptadecanol (17C) and heptacosanol (27C) the results are more critical. While the formation, localization and AFM scan of heptacosanol can be found between 70 to 80% of cases, heptadecanol only can be found between 40 to 50% of the cases, indicating a lower stability respect to the largest one.

5.3.4   Multilayers and aggregations

As I have been emphasizing over the last sections, the formation of multilayers on graphite is often observed, especially with alcohols with an even carbon atoms, but in general some multilayers can not be avoided for any aliphatic alcohol used here. The fact to work with graphite causes a non-natural dipping

comparing with hydrophilic substrates like mica, and it makes that monolayers can be easily deformed, crowded together in multilayers or even disperse through the graphite surface (see Fig. 5.19). In Fig. 5.20 is shown how multilayers are arranged as bilayers or multiple bilayer (with well defined structures). Formation of bilayers on this system is specially favored because will form through H-bonds interactions between OH terminal groups of the molecules (see Fig. 5.22).
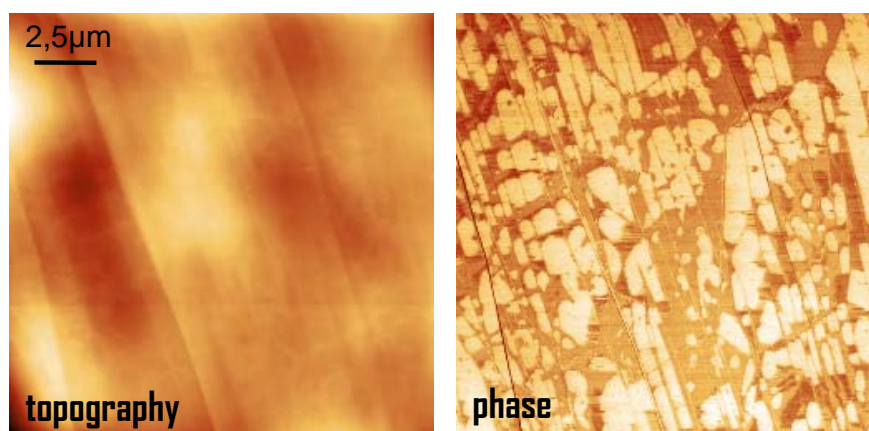

Figure 5.19: Tophography and phase images of a hexadecanol sample. The topography information is quite poor, and it would seem that nothing is adsorbed on. But phase image allows us corroborate the presence of alcohols on graphite although the distribution is not an homogeneous film.
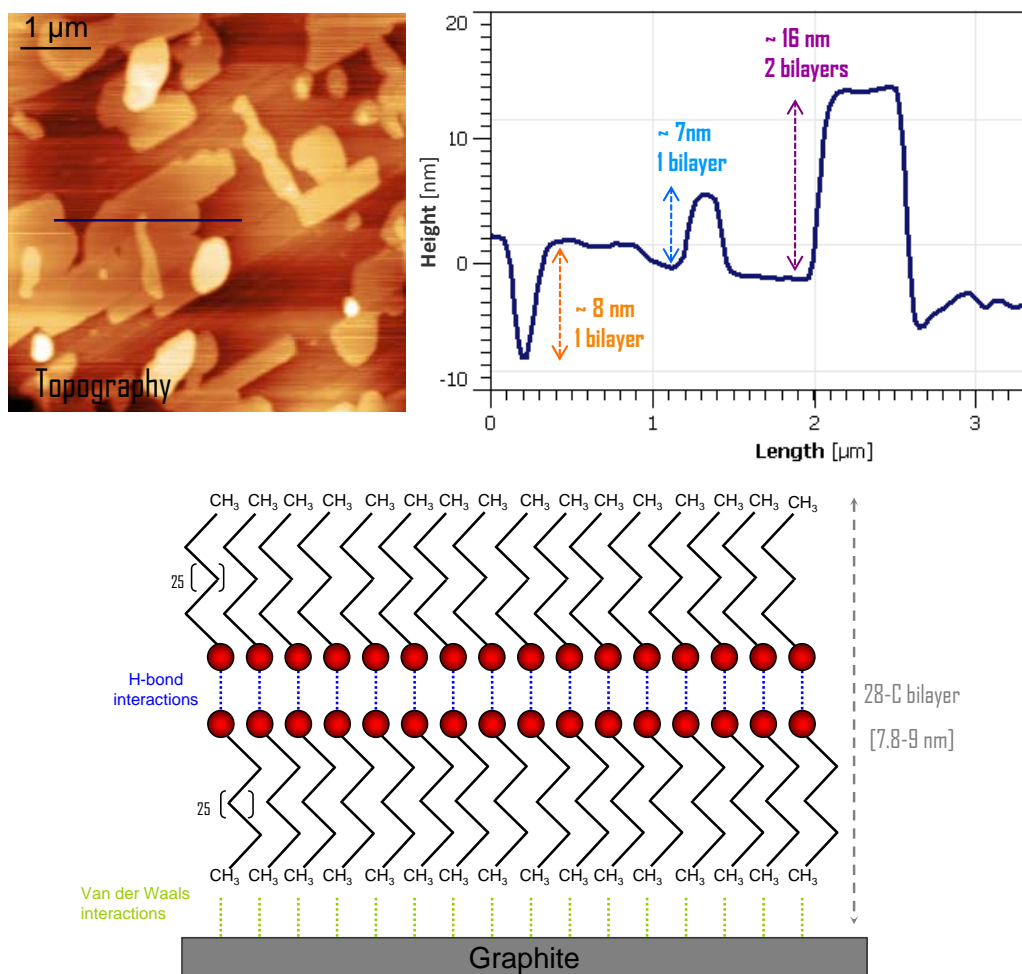
Figure 5.20: Multilayers are the protagonist in many samples. Bilayers and multiple bilayers appear often and hardly ever desapear by the tip effect. They are stronger than monolayers by far. At bottom is shown a schematic bilayer of an aliphatic alcohol showing the van der Waals interactions between graphite and metyl groups, and H-bond interactions between OH groups of both chains.

5.3.5 Easily deformation of layers

Despite the quality of monolayer on mica shown in Fig. 5.11, the action of the AFM tip is dramatic. Over time, the monolayers set on mica start to move, dragged by the tip, and the modification of the monolayer is observed (see Fig. 5.21). But not only film degradation occurs on mica, as it is also observed the sub-monolayer formation due to the tip movement (i.e, the tip moves the alcohol molecules getting a film deposited on mica). It is shown in Fig. 5.22.

On graphite, the molecule-substrate interaction is weaker than mica, so possible perturbation at the monolayer due to tip-sample interactions must be carefully taken into account. As shown in the sequence of images in figure 5.23, the layer formed on graphite (in this case it is less than a monolayer) is progressively degraded with time. This shows us that the interaction between the CH_3 group and graphite surface is quite weak and, once more, the tip has the ability to interact with the layers causing a movement. With regard to multilayers, they remain undisturbed during the scanning, probably due to the compaction and the strong interaction between molecules.

The degradation of the monolayer due to the tip perturbation were already observed on monolayers on mica, where the monolayer-sample interaction is stronger. Then, it is expected that for monolayers on graphite to have this phenomena even enhanced. However monolayers on graphite can be seen, its are even not stable with time and after 24h. the monolayers desapear on the sample.
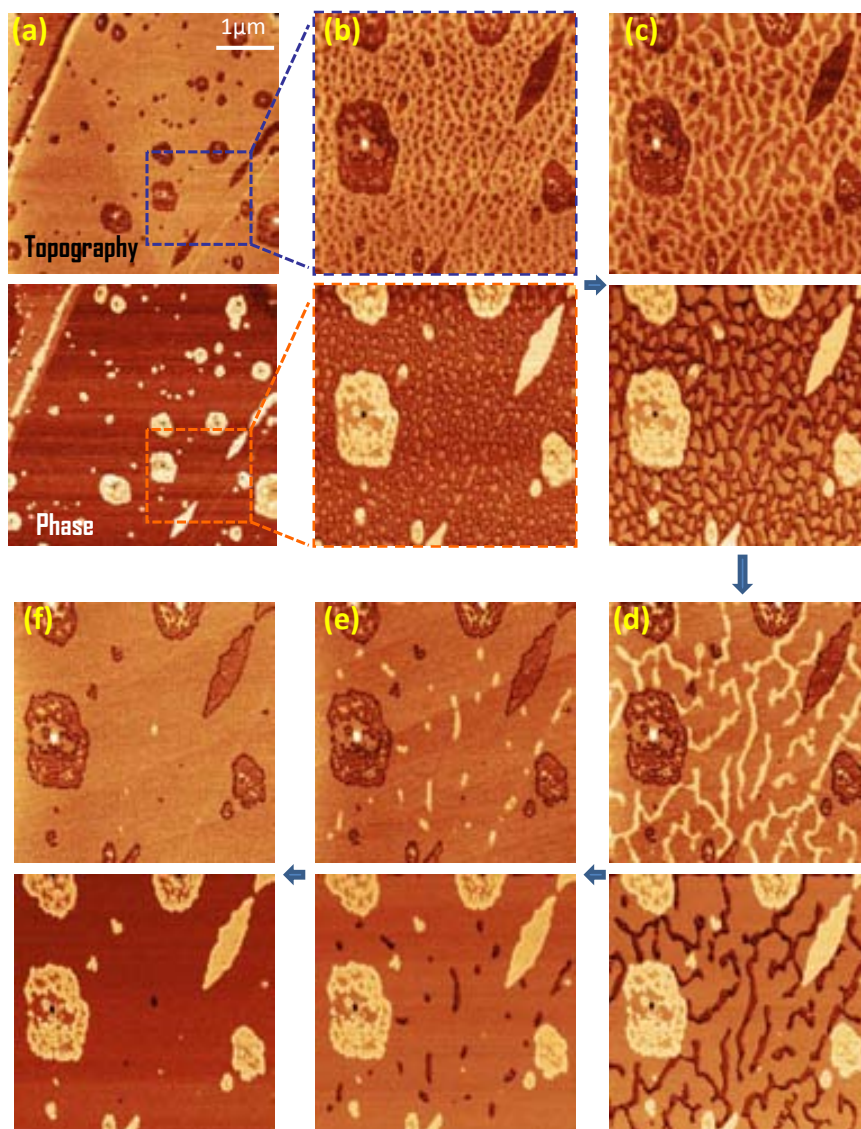
Figure 5.21: Mica images sequence in AM-AFM mode shows how tip perturbes the sample spreading the alcohol molecules showing a film degradation.
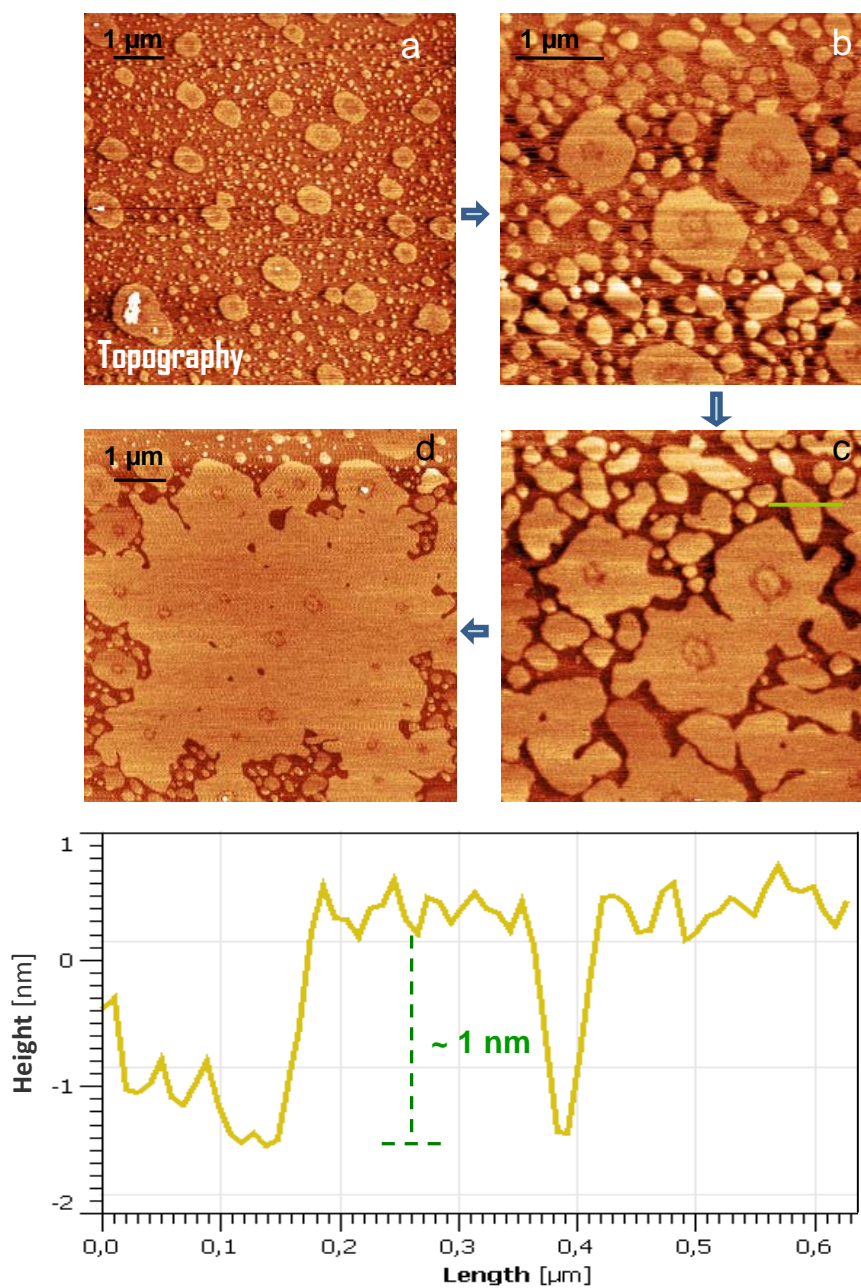
Figure 5.22: The formation of a new layer of hexadecanol on mica (less than a monolayer as seen in the profile) is induced by the tip, that moves alcohol molecules during the scan time. When a zoom out is done (d) is seen the sub-monolayer created.

Figure 5.23: Heptadecanol (16C) sub-monolayer transferred on graphit. The phase images allows to view how the tip perturbes the sample in a short time. The last image shows the surface almost covered by hexadecanol molecules.

5.3.6 SPFM and KPFM images of films

An attempt of SPFM and KPFM was also made with the thin films on mica and graphite. The present work provides information about hexadecanol (16C) on mica and graphite, and heptacosanol (27C) on graphite.

Hexadecanol on mica and graphite
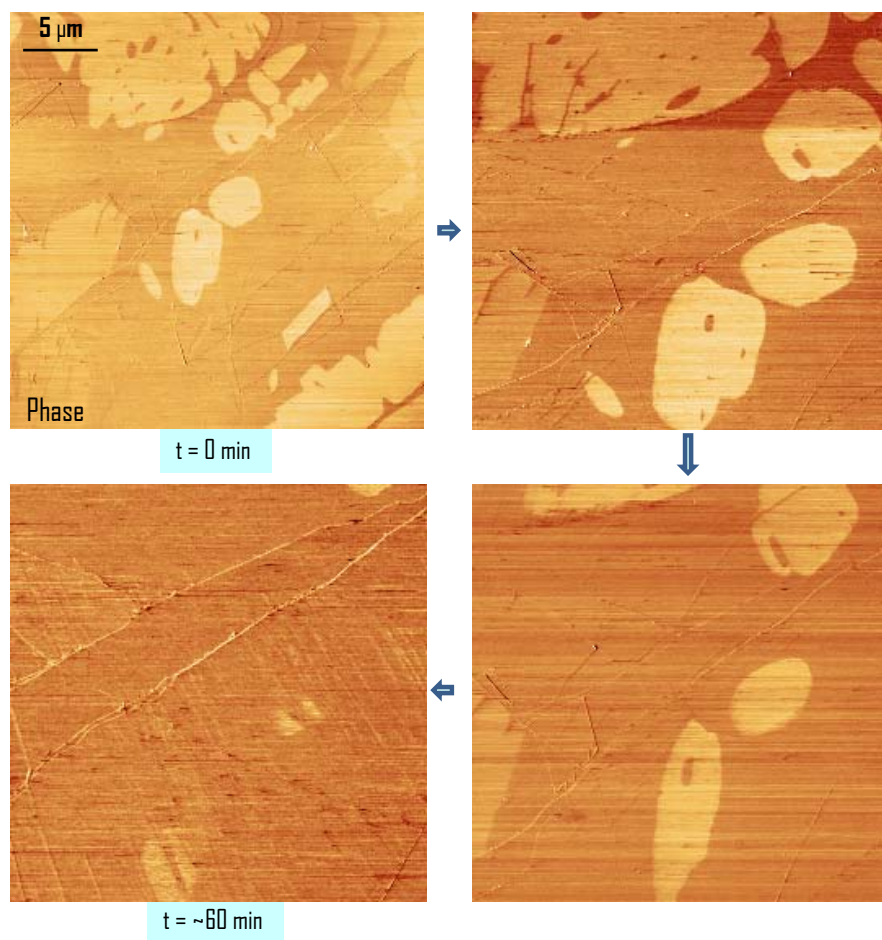
The most common situation in AM-AFM mode refering to hexadecanol is the incomplete monolayer formation, in other words, rarely a monolayer is observed, as shown in Fig.5.12 (a, b and c) and Fig.**??**. Using SPFM one can figure out the placement of the chains on graphite. In Fig. 5.12 (d) can be seen the scarce information of SPFM, similar to that shown in Fig.5.12 (a). It is reasonable because the chains are not placed vertically. Instead, the Kelvin image in Fig.5.12 (e) gives us information because a contrast between graphite and alcohol chains is seen. Graphite is depicted by dark colors and alcohol chains by light colors. So that means that hydroxyl groups are oriented to upwards but at the same time the placement of the chains is semi horizontal preventing the proper formation of the monolayer (probably due to the steric hindrance, explained in section 5.3.2).

When hexadecanol is transferred on mica, is known that if a monolayer is formed OH groups are pointed downwards, and CH_3 groups are pointing upwards. This means that in kelvin images will shown a negative contrast respect to mica substrate. In Fig.5.25 is shown this behavior although the height of the layer is less than a monolayer (see profile in Fig.5.25). When a zoom out is done, is shown how a layer is formed by the tip effect as explained before (see 5.3.5), and CPD of mica is clearly positive and hexadecanol layer is clearly negative corroborating a placement of OH downward.
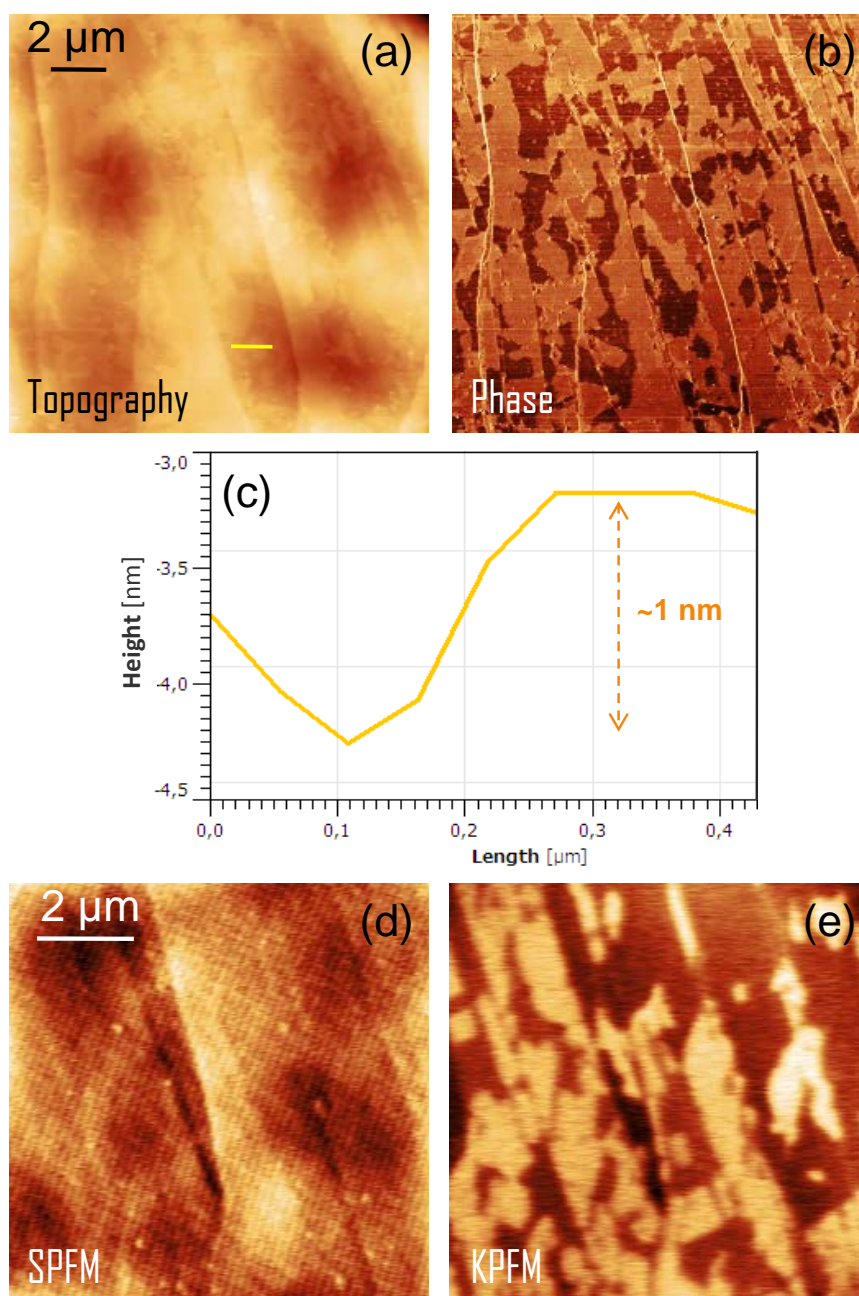
Figure 5.24: (a) Topographic image of hexadecanol. (b) Phase image. (c) Profile of a layer island on graphite. As shown, the heigh of the island is about 1 nm, less than the estimated above in Fig. 5.8, where a hexadecanol monolayer will have a length between 2.656 and 2.3 nm. (d) SPFM image of the same area. (e) KPFM image. The contrast shown here indicates a preferential orientation of the alcohol where the hydroxyl groups are pointing upwards.
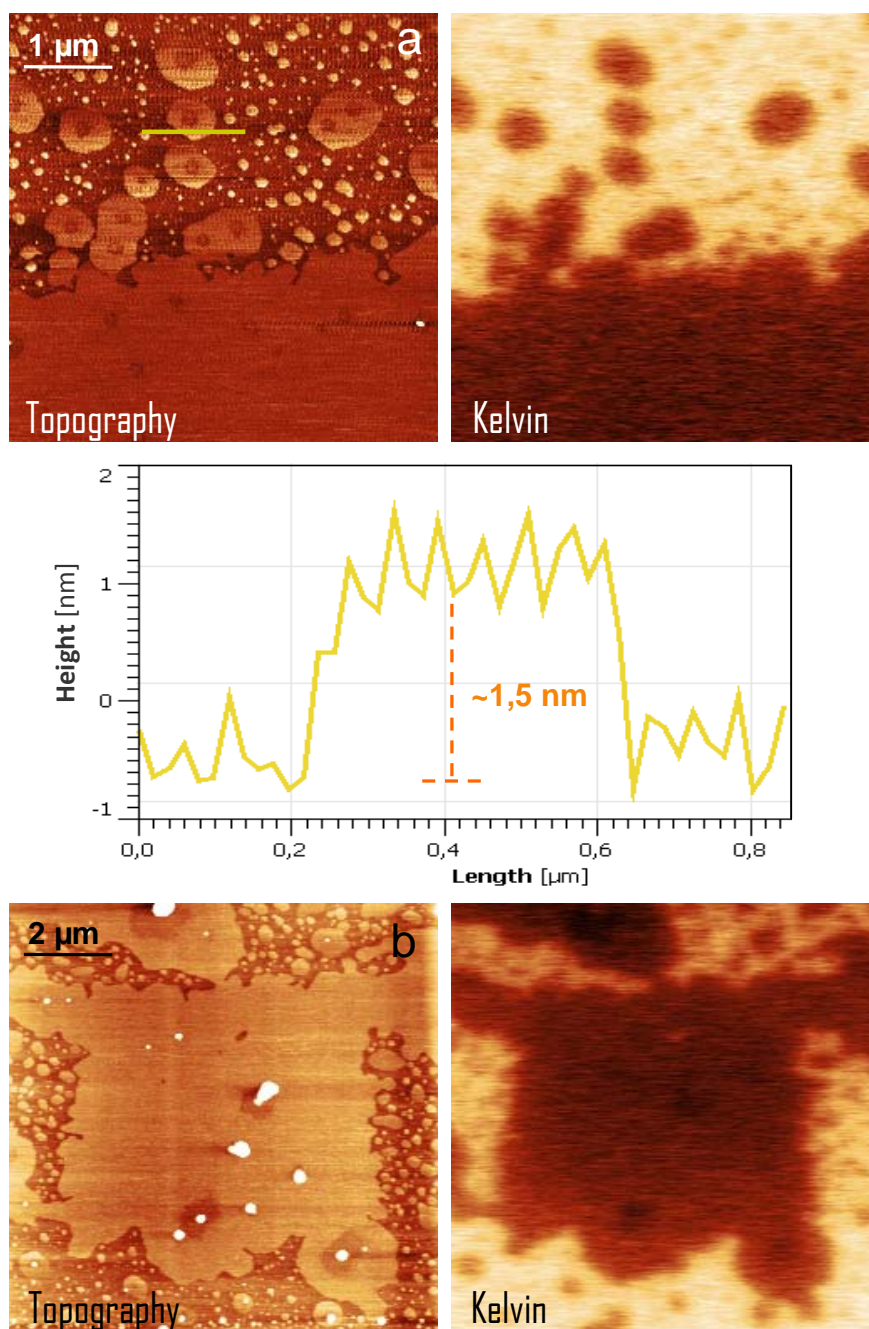
Figure 5.25: (a) Topography, Kelvin and profile of hexadecanols transferred on mica. Profile indicates a sub-monolayer is formed. The contrast shown here indicates a preferential oriention of the alcohol where the hydroxyl groups are pointing downwards. (b) Zoom out done in this area shows the covering induced by the tip.

Heptacosanol on graphite

This section is interesting because have been taken images of monolayers and multilayers. In Fig.5.26 a heptacosanol monolayer is shown. The contact potential in Kelvin image is clearly white for monolayers transferred on graphite, but some dark dots appear as well, proving that other conformations are adopted on surface probably being bilayers or aggregations.
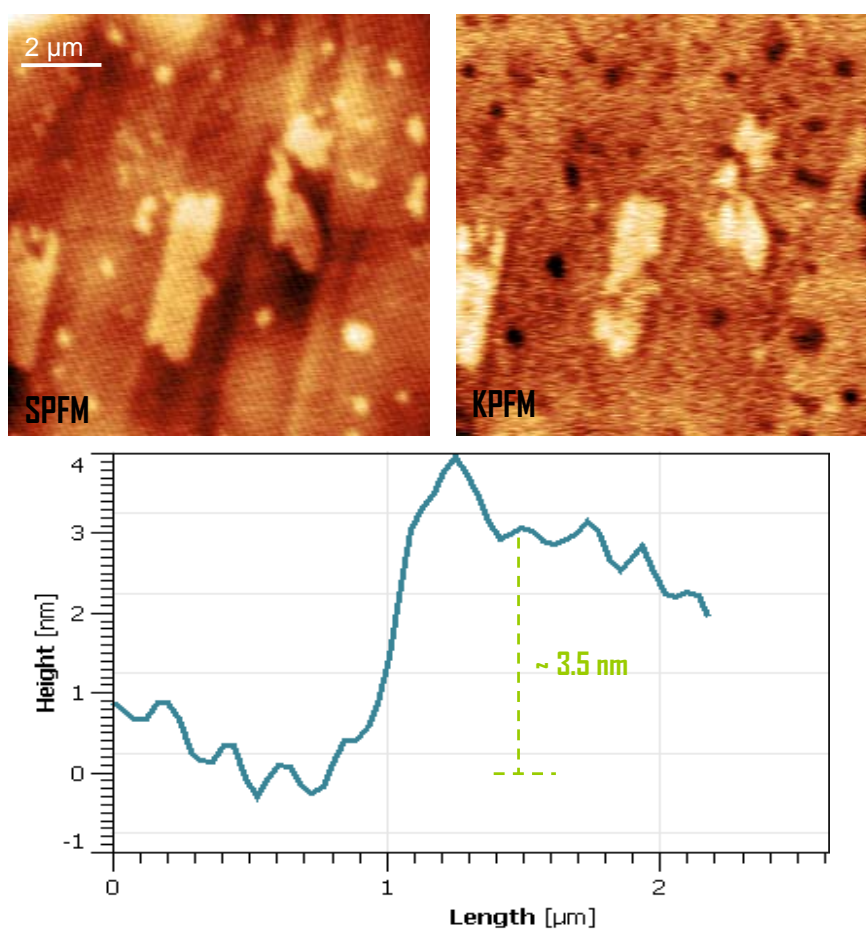
Figure 5.26:

Contact potential is an interesting issue when bilayers or multiple bilayers come on the scene. If a bilayer is formed on graphite, CH_3 groups will point

upward, then the difference in contact potential between graphite and layers will be near. As shown in KPFM image in Fig.5.27, the difference in contact potential is more positive for bilayers of heptadecanol than graphite. But if Fig.5.28 is shown, KPFM image shows multilayers of heptadecanol with a negative contact potential, just the opposite of the last figure.
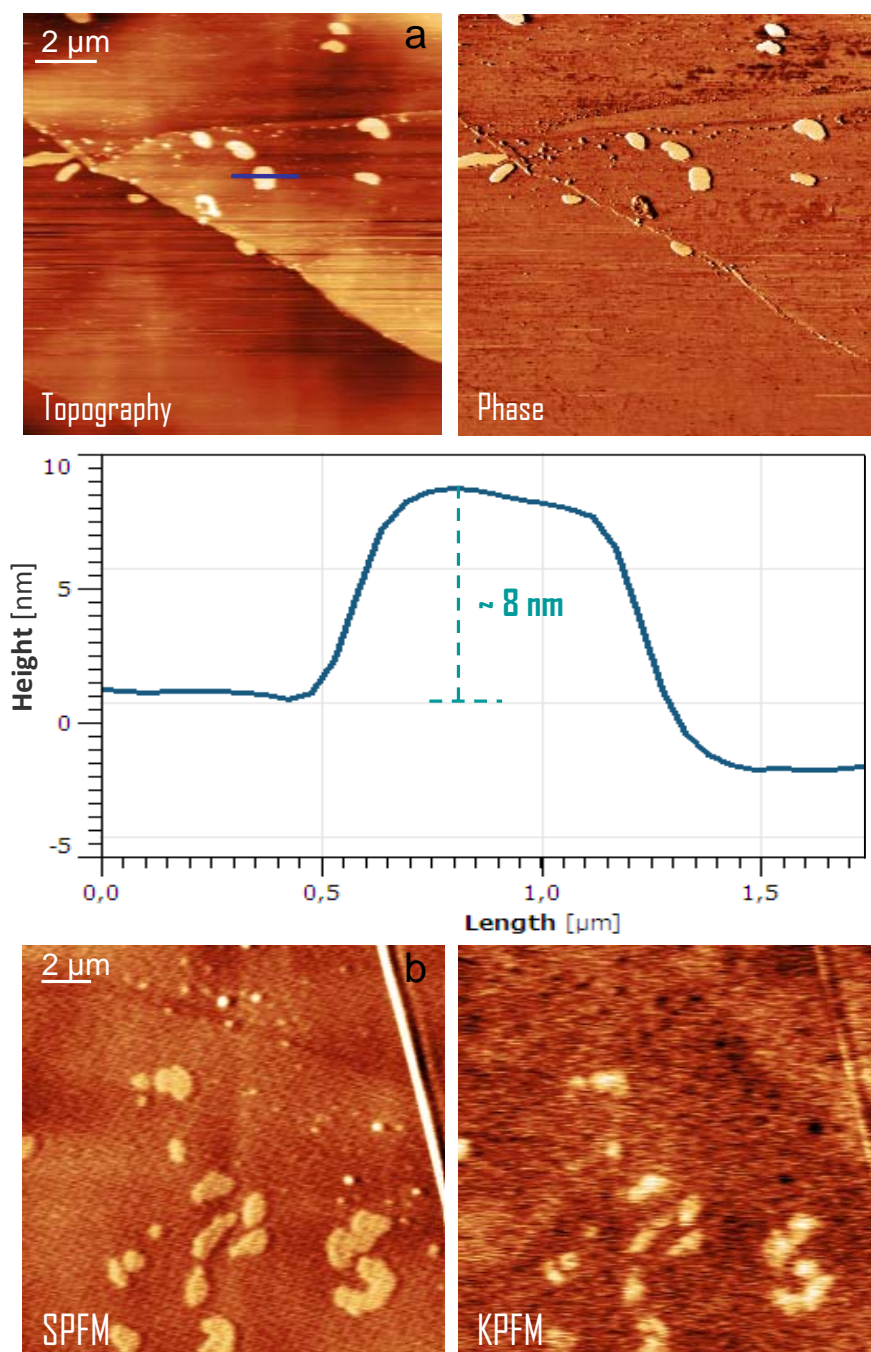
Figure 5.27: (a) Topography and phase images of heptacosanol on graphite. The height of one of these bilayers is shown in the profile. According to Fig.reffig.LB4 the values of a heptacosanol monolayer are 38-43.5 Å, and the values for a bilayer will be between 76 and 87 Å. (b) SPFM and KPFM images. Bilayers show a positive contact potential about 11 mV.

Figure 5.28: a) Topography and phase images of heptacosanol on graphite. The height of one of these bilayers is shown in the profile. (b) SPFM and KPFM images. Bilayers show a negative contact potential about -18 mV.

5.3.7   Optical microscope images
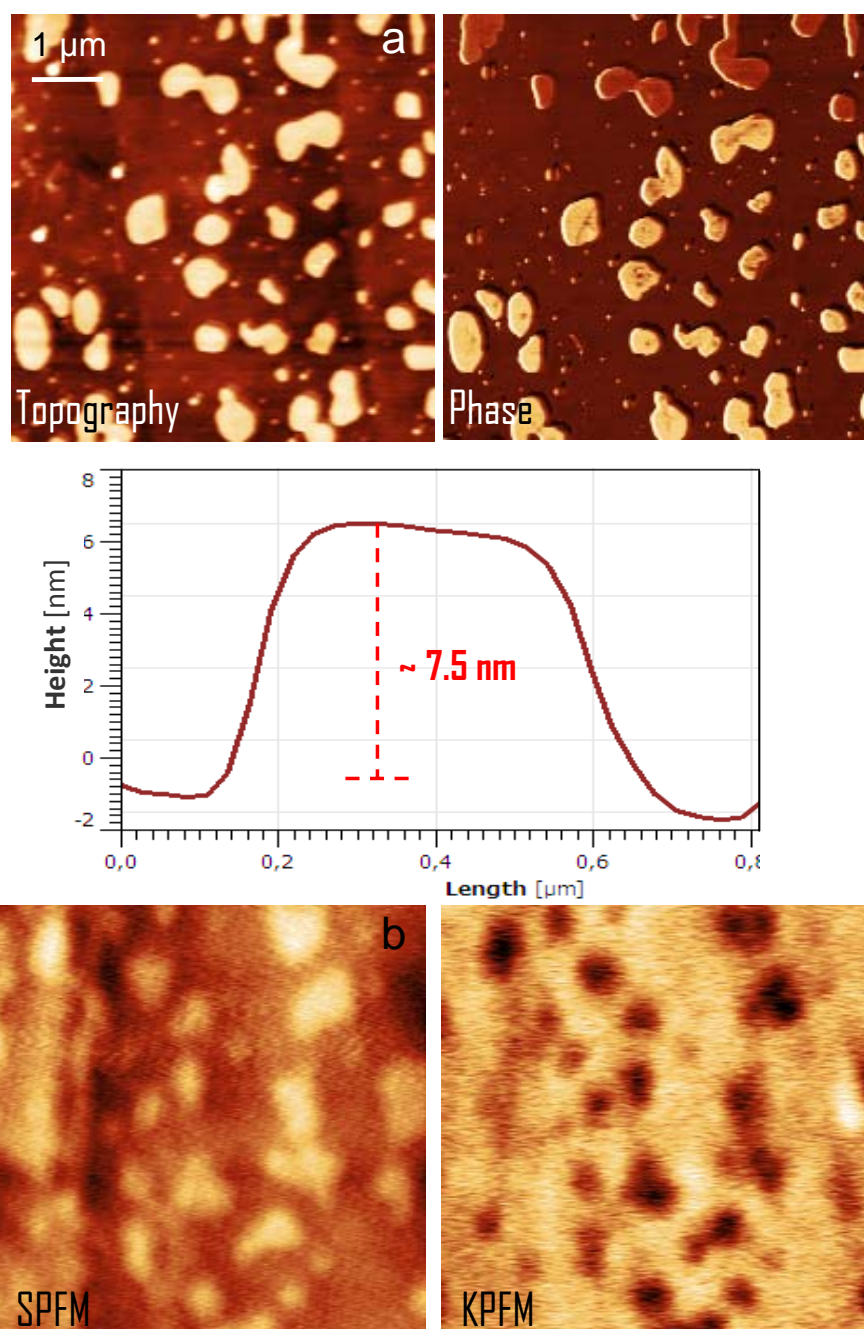
With an optical microscope, as done for BaF_2 and CaF_2 (see section 3.5.1), I tried to see how water condenses on a hexadecanol and heptacosanol samples. This process is carried out applying a voltage on the sample, causing a decrease of temperature that causes a water condensation on the surface. Both experiments are done at the lowest magnification of microscope (10×), and the differences observed between the samples are less than in AFM. However, some notable observations are done:

- When a voltage is applied water is condensed on both samples .

- The threshold voltage, where water starts to condense, is similar for hexadecanol and heptacosanol and proves that there are alcohols deposited on the surfaces in both cases. If there were no alcohols on one of the samples, more difference would seen between them because one of them will show hydrophobic character and the other one hydrophilic character.

- Droplets deposited on surface are slightly bigger for heptacosanol than for hexadecanol (compare Fig. 5.29 and 5.30).

- The critic voltage, where the change of state from liquid to solid starts, is so similar, but probably will be different if it could be measured in more detail.
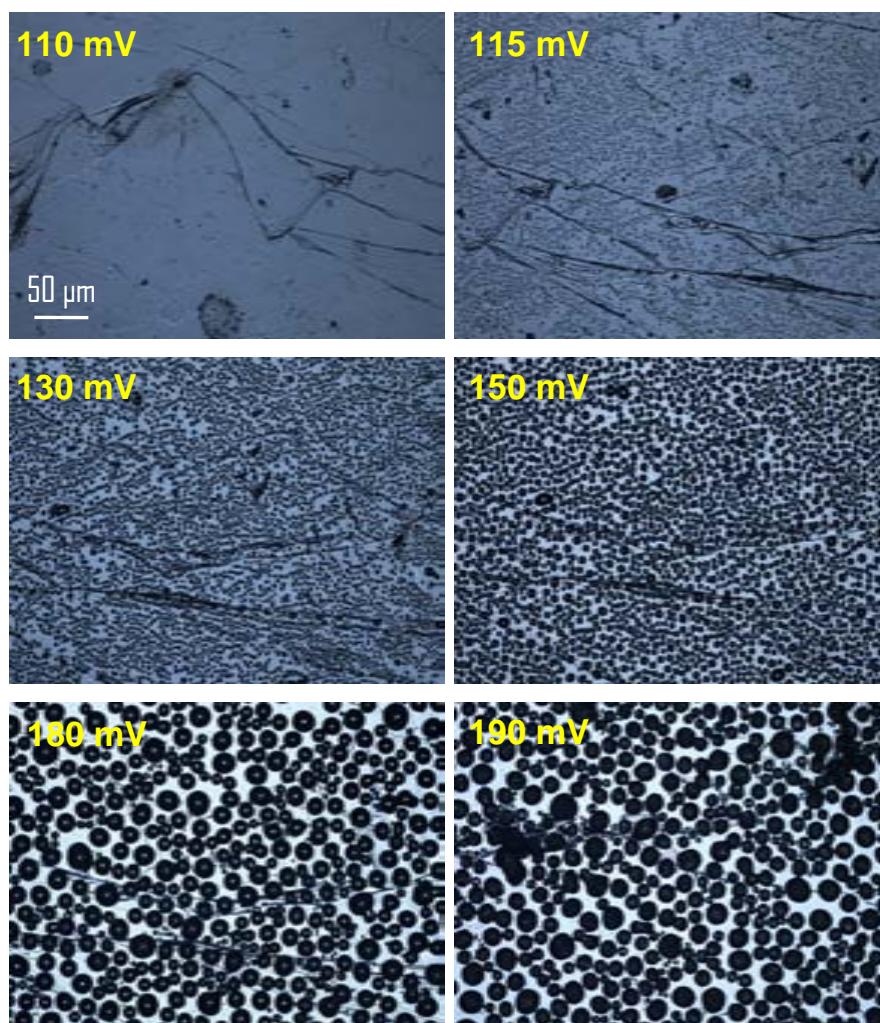
Figure 5.29: Optical image sequence of hexadecanol (16C). The water condensation starts at 115 mV and state change takes place at ∼190 mV.
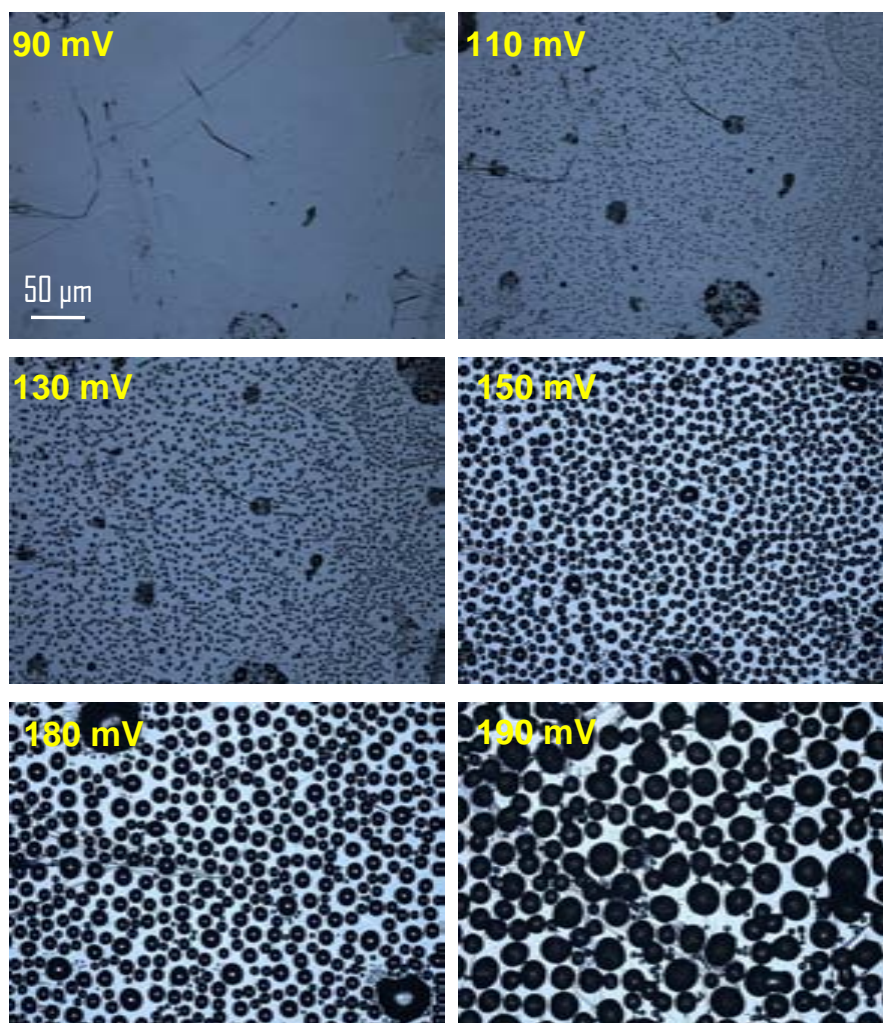
Figure 5.30: Optical image sequence Heptacosanol (27C). The water condensation starts at 110 mV and state change takes place at ∼190 mV.

Chapter 6

Conclusions

The present thesis was aimed the study of water interaction with different surfaces, each exposed at ambient conditions of temperature and humidity. The main conclusions drawn from this work are:

1. Morphological defects such as steps can be crucial for improving mono-layer wetting and stabilization of multilayers on surfaces like BaF_2, which shows a good lattice mismatch relationship with water molecules forming ice. Steps in BaF_2 causes a stabilization effect with regard to the growth of the two-dimensional water patches.

2. It has been shown that the height of BaF_2 islands lies in the 0.3-0.5 nm range, so close to a bilayer thickness. With the help of KPFM a sign crossover of SPD was possible to see, as a consequence of the energetic balance between the competing water vapor/solidlike and solid-like/substrate, and it demonstrates a net dipolar distribution of the bilayer films thus implying a significant degree of orientation below and above the transition. This points toward a configuration other than I_h.

3. Comparing the two isostructural compounds BaF_2 and CaF_2, it has been demonstrated that the mismatch between lattice parameters of

the structure and the I_h hexagonal ice is the most important parameter to consider.

4. It has been shown that the macroscopic shape of the tip is a very important parameter to consider in SPFM simulations. The main contribution to the SPFM comes from the macroscopic shape instead of from the tip apex.

5. It is demostrated that FLG films are discharged mainly through the water layer adsorbed on the SiO_2 surface, giving a non-completely hydrophobic character to the graphene shits.

6. It is demostrated that the formation of hydrophilic monolayers and bilayers on a hydrophobic substrate (graphite) is possible.

Chapter 7

Bibliography

- Abraham, FF; "Monte-Carlo simulation of physical clusters of water molecules", *Journal of Chemical Physics.* **61**, 3 (1974)

- Albrecht, TR; Quate, CF; "Atomic resolution with the Atomic Force Microscope on conductors and nonconductors", *Journal of Vacuum Science and Technology A-Vacuum Surfaces and Films.* **6**, 2 (1988)

- Albrecht, TR; Grutter, P; Horne, D; Rugar, D; "Frequency-Modulation detection using High-Q cantilevers for Enhanced Force Microscope sensitivity", *Journal of Applied Physics.* **69**, 2 (1991)

- Avouris, P; Chen, Z; Perebeinos, V; "Carbon-based electronics", *Nature Nanotechnology.* **2**, 10 (2007)

- Bailey, AI; Kay, SM; "A direct measurement of influence of vapour of liquid and of oriented monolayers on interfacial energy of mica", *Proc. R. Soc. London, Ser. A.* **301**, 47 (1967)

- Bardon, S; Ober, R; Valignat, MP; Vandenbrouck, F; Cazabat, AM; Daillant, J; "Organization of cyanobiphenyl liquid crystal molecules

in prewetting films spreading on silicon wafers", *Physics Review E.* 59:6808-6818 (1999)

- Bennig, G; Gerber, C; Stroll, E; Albrecht, TR; Quate, CF; "Atomic resolution with Atomic Force Microscope" *Surface Science.* **198**, 1-6 (1987)

- Binnig, G; Rohrer, H; "Scanning Tunneling Microscopy", *Helvetica Physica Acta.* **55**, 6 (1982)

- Binnig, G; Quate, CF; Gerber, C; "Atomic Force Microsopy", *Physical Review Letters.* **56**, 9 (1986)

- Birstein, SJ; "The role of adsorption in heterogeneous nucleation. 1. Adsorption of water vapor on silver iodide and lead iodide", *Journal of meteorology.* **12**, 4 (1955)

- Blake, P; Hill, EW; Castro Neto, AH; Novoselov, KS; Jiang, D; Yang, R; Booth, TJ; and Geim, AK; "Making graphene visible"', *Applied Physics Letters.* **91**, 063124 (2007)

- Blodgett, KB; "Films built by depositing successive monomolecular layers on a solid surface"', *Journal of the American Chemical Society.* **57**, 1 (1935)

- Bruch, LW; Glebov, A; Toennies, JP; Weiss, H; "A Helium atom scattering study of water-adsorption on the NaCl (100) single-crystal surface", *Journal of Chemical Physics.* **103**, 12 (1995)

- Cantrell, W and Heymsfield, A; "Production of ice in tropospheric clouds - A review", *Bulletin of the American Meteorological Society.* **86**, 795 (2005)

- Cardellach, M; Verdaguer, A; Santiso, J; Fraxedas, J; "Two-dimensional wetting: The role of atomic steps on the nucleation of thin water films on BaF2(111) at ambient conditions", *Journal of Chemical Physics*. **132**, 234708 (2010)

- Carrasco, J; Michaelides, A; Scheffler, M; "Insight from first principles into the nature of the bonding between water molecules and 4d metal surfaces", *Journal of Chemical Physics*. **130**, 184707 (2009)

- Chakarov, DV; Osterlund, L; Kasemo, B; "Water-adsorption on graphite (0001)", *Vacuum*. **46**, 8-10 (1995)

- Chang, TM; Dang, LX; "Molecular dynamics simulations of CCl_4-H_2O liquid-liquid interface with polarizable potential models", *Journal of Chemical Physics*. **104**, 17 (1996)

- Charlier, JC; Eklund, PC; Zhu, J; Ferrari, AC; "Electron and phonon properties of graphene: Their relationship with carbon nanotubes", *Carbon Nanotubes*. **111**, 673-709 (2008)

- Chechel, OV; Nikolaev, EN; "Devices for production of Langmuir-Blodget-Films", *Instruments and Experimental Techniques*. **34**, 4 (1991)

- Conrad, P; Ewing, GE; Karlinsey, RL; Sadtchenko, V; "Ice nucleation on $BaF_2(111)$", *Journal of Chemical Physics*. **122**, 6 (2005)

- Datta, SS; Strachan, DR; Mele, EJ; Charlie Johanson, AT; "Surface Potentials and Layer Charge Distributions in Few-Layer Graphene Films", *NanoLetters*. **9**, 7 (2009)

- Derjaguin, BV; Muller, VM; Toporov, YP; "Effect of contact deformations on adhesion of particles", *Journal of Colloid and Interface Science*. **53**, 2 (1975)

- Devlin, JP; Buch, V; "Surface of ice as viewed from combined spectroscopic and computer modeling studies", *Journal of Physical Chemistry.* **99**, 45 (1995)

- Descartes, R; *Les Météores* (1637)

- Dorsey, NE; "Water at -72 degrees C", *Science.* **108**, 2798 (1948)

- Downing, HD; Williams, D; "Optical-constants of water in ifrared", *Journal of Geophysical Research.* **80**, 12 (1975)

- Edwards, GR; Evans, LF; Hamann, SD; "Nucleation of ice by mechanical shock", *Nature.* **223**, 5204

- Ehrlich, G; Hudda, FG; "Atomic view of surface self-diffusion - Tungsten on Tungsten", *Journal of Chemical Physics.* **44**, 1039 (1966)

- Ekiz, OO; Urel, M; Guner, H; Mizrak, AK; Dana, A; "Reversible Electrical Reduction and Oxidation of Graphene Oxide", *ACS Nano.* **5**, 4 (2011)

- Engelhardt, J; Dabringhaus, H; and Wandelt, K; "Atomic force microscopy study of the CaF2(111) surface: from cleavage via island to evaporation topographies", *Surface Science.* **448**, 187 (2000)

- Engelhardt, J; Dabringhaus, H; and Wandelt, K; "Atomic force microscopy study of the CaF2(111) surface: from cleavage via island to evaporation topographies", *Surface Science.* **516**, 216 (2002)

- Erbil, HY; McHale, G; Rowan, SM; Newton, MI; "Determination of the receding contact angle of sessile drops on polymer surfaces by evaporation", *Langmuir.* **15**, 21 (1999)

- Eustathopoulos, N; Nicholas, MG; Drevet, B; "*Wettability at High Temperatures*", Pergamon (1999)

- Ewing, GE; "Thin film water", *Journal of Physical Chemistry B.* **108**, 41 (2004)

- Ewing, GE; "Ambient thin film water on insulator surfaces", *Chemical Review (Washington, D.C.).* **106**, 1511 (2006) and references therein.

- Finnegan, WG; Chai, SK; "A new hypothesis for the mechanism of ice nucleation on wetted AgI and AgI center dot AgCl particulate aerosols", *Journal of the Atmospheric Sciences.* **60**, 14 (2003)

- Fletcher, NH; "Size effect in heterogeneous nucleation", *Journal of Chemical Physics.* **29**, 3 (1958)

- Fletcher, NH; "Entropy effect in ice crystal nucleation", *Jounal of Chemical Physics.* **30**, 6 (1959)

- Fletcher, NH; "Ice crystal nucleation by aerosol particles", *Discussions of the Faraday Society.* **30**, 39-45 (1960)

- Fletcher, NH; "Active sites and ice crystal nucleation", *Journal of the Atmospheric Sciences.* **26**, 6 (1969)

- Foster, MC; Ewing, GE; "Adsorption of water on the NaCl(001) surface. II. An infrared study at ambient temperatures", *Journal of Chemical Physics.* **112**, 15 (2000)

- Foster, AS; Trevethan, T; and Shluger, AL; "Structure and diffusion of intrinsic defects, adsorbed hydrogen, and water molecules at the surface of alkali-earth fluorides calculated using density functional theory", *Physics Review B.* **80**, 115421 (2009)

- Fox, HW; Zisman; WA; "The spreading of liquids on low energy surface. 1. Polytetrafluoroethylene", *Journal of Colloid Science.* **5**, 6 (1950)

- Fradin, C; Braslau, A; Luzet, D; Smilgies, D; Alba, M; Boudet, N; Mecke, K; and Daillant, J; "Reduction in the surface energy of liquid interfaces at short length scales", *Nature (London).* **403**, 871 (2000)

- Frank, FC; "Snow crystals", *Contemporary Physics.* **23**, 1 (1982)

- Franklin, B; "Of the stilling of Waves by means of Oil" (Letter to William Brownrigg and the Reverend Mr. Farish). London, November 7, (1773)

- Frantz, P; Agrait, N; Salmeron, M; "Use of capacitance to measure surface forces .1. Measuring distance of separation with enhanced spatial and time resolution", *Langmuir.* **12**, 13 (1996)

- Fraxedas, J; Verdaguer, A; Sanz, F; Baudron and Batail, P; "Water nanodroplets confined in molecular nanobeakers", *Surface Science.* **588**, 41 (2005)

- Fukazawa, H; Ikeda, S; Mae, S; "Incoherent inelastic neutron scattering measurements on ice XI; the proton-ordered phase of ice I-h doped with KOH", *Chemical Physics Letters.* **282**, 2 (1998)

- Geim, KA; Novoselov, KS; "The rise of graphene", *Nature Materials.* **6**, 183 (2007)

- Geim, KA; Kim, P; "Carbon wonderland", *Scientific American.* **298**, 4 (2008)

- Geng, YL; Xu, D; Wang, XQ; Yu, GW; Zhang, GH; Zhang, HB; "AFM study of surface morphology of 100 cleavage planes of L-arginine acetate crystals", *Journal of Crystal Growth.* **282**, 208 (2005)

- Gennes, PG; Brochard-Wyart, F; Quéré; D; "*Capillarity and wetting phenomena*", Springer (2002)

- Girifalco, LA; Good, RJ; "A theory for the estimation of surface and interfacial energies. 1. Derivation and application to interfacial tension", *Journal of Physical Chemistry.* **61**, 7 (1957)

- Gómez-Moñivas, S; Froufe, LS; Carminati, R; Greffet, JJ; and Sáenz, JJ; "Tip-shape effects on electrostatic force microscopy resolution", *Nanotechnology.* **12**, 496 (2001)

- Hansma, PK; Cleveland, JP; Radmacher, M; Walters, DA; Hillner, PE; Bezanilla, M; Fritz, M; Vie, D; Hansma, HG; Prater, CB; Massie, J; Fukunaga, L; Gurley, J; Elings, V; "Tapping mode Atomic Force Microscopy in liquids", *Applied Physics Letters.* **64**, 13 (1994)

- Head, RB; "Steroids as ice nucleators", *Nature.* **191**, 479 (1961)

- Heneghan, AF; Wilson, PW; Haymet, ADJ; "Heterogeneous nucleation of supercooled water, and the effect of an added catalyst", *Proceedings of the National Academy of Sciences of the United States of America.* **99**, 15 (2002)

- Henderson, MA; "The interaction of water with solid surfaces: fundamental aspects revisited", *Surface Science Reports.* **46**, 1 (2002)

- Hirth, S; Ostendorf, F; Reichling, M; "Lateral manipulation of atomic size defects on the $CaF_2(111)$ surface", *Nanotechnology.* **17**, 7 (2006)

- Hohenberg, PC; Halperin, BI; "Theory of dynamic critical phenomena", *Reviews of modern physics.* **49**, 3 (1977)

- Hu, J; Xiao, XD; Salmeron, M; "Scanning Polarization Force Microscopy - A technique for imaging liquids and weakly adsorbed layers", *Applied Physics Letters.* **67**:476-478 (1995)

- Hu, XL and Michaelides, A; "Water on the hydroxylated (001) surface of kaolinite: From monomer adsorption to a flat 2D wetting layer", *Surface Science.* **602**, 4 (2008)

- Isaacs, ED; Shukla, A; Platzman, OM; Hamann, DR; Barbiellini, B; Tulk, CA; "Compton scattering evidence for covalency of the hydrogen bond in ice", *Journal of Physics and Chemistry of Solids.* **61**, 3 (2000)

- Israelachvili, JN; Adams, GE; "Direct measurement of long-range forces between 2 mica surfaces in aqueous KNO_3 solutions", *Nature.* **262**:774-776 (1976)

- Israelachili, JN; "*Intermolecular and Surface Forces*", Academic Press (1992)

- Jeong, HC and Williams, ED; "Steps on surfaces: experiment and theory", *Surface Science Reports.* **34**, 171 (1999)

- Kashchiev, D and Sato, K; "Kinetics of crystallization preceded by metastable-phase formation", *Journal of Chemical Physics.* **109**, 19 (1998)

- Knight, C; Singer, SJ; Kuo, JL; Hirsch, TK; Ojamae, L; Klein, ML; "Hydrogen bond topology and the ice VII/VIII and Ih/XI proton ordering phase transitions", *Physical Review E.* **73**, 5 (2006)

- Langmuir, I; "The adsorption of gases on plane surfaces of glass, mica and platinum", *Journal of the Americal Chemical Society.* **40** (1918)

- Langmuir, I; "Control of precipitation from cumulus clouds by various seeding techniques", *Science.* **112**, 2989 (1950)

- Lee, C; Wei, XD; Kysar, JW; Hone, J; "Measurement of the elastic properties and intrinsic strength of monolayer graphene", *Science.* **321**, 5887 (2008)

- Libbrecht, KG; "The formation of snow crystals - Subtle molecular processes govern the growth of a remarkable variety of elaborate ice structures", *American Scientist.* **95**, 1 (2007)

- Liu, M; Yin, XB; Ulin-Avila, E; Geng, BS; Zentgraf, T; Ju, L; Wang, F; Zhang, X; "A graphene-based broadband optical modulator", *Nature.* **474**, 7349 (2011)

- Luna, M; Colchero. J; Bar, AM; "Study of water droplets and films on graphite by noncontact scanning force microscopy", *Journal of Physical Chemistry B.* **103**, 9576 (1999)

- Luo, SN; Strachan, A; and Swift, DC; "Deducing solid-liquid interfacial energy from superheating or supercooling: application to H2O at high pressures", *Modell. Simul. Mater. Sci. Eng.* **13**, 321 (2005)

- Maksyutenko, P; Rizzo, TR; Boyarkin, OV; "A direct measurement of the dissociation energy of water", *Journal of Chemical Physics.* **125**, 18 (2006)

- Marcus, Y; Bennaim, A; *Journal of Chemical Physics.* "A study of the structure of water and its dependence on solutes, based on the isotope effects on solvation thermodynamics in water", **83**, 9 (1985)

- Marmur, A; "The lotus effect: Superhydrophobicity and metastability", *Langmuir.* **20**, 9 (2004)

- Mate, CM; McClelland, GM; Erlandsson, R; Chiang, S; "Atomic-scale friction of a tungsten tip on a graphite surface" *Physical Review Letters.* **59**, 17 (1987)

- McEuen, PL; "Nanotechnology - Carbon-based electronics", *Nature.* **393**, 6680 (1998)

- Mélin, T; Deresmes, D; Stiévenard, D; " Charge injection in individual silicon nanoparticles deposited on a conductive substrate", *Applied Physics Letters.* **81**, 5054 (2002)

- Meyer, G; Amer, NM; "Simultaneous measurement of lateral and normal forces with an optical-beam-deflection Atomic Force Microscope", *Applied Physics Letters.* **57**, 20 (1990)

- Michaelides, A; Ranea, VA; de Andres, PL; King, DA; "General model for water monomer adsorption on close-packed transition and noble metal surfaces", *Physics Review Letters.* **90**, 216102 (2003)

- Mittal, KL; "*Contact Angle Wettability and Adhesion*", Vol.**5**. VSP/Brill, Leiden (1964)

- Miura, K; *Physics Review B.* "Water-adsorption on a BaF_2 (111) surface in air observed with Force Microscopy", **52**, 7872 (1995)

- Miura, K; Yamada, T; Ishikawa, M; and Okita, S; "Apparent contrast of molecularly thin films of water at ionic crystal surfaces", *Applied Surface Science.* **140**, 415 (1999)

- Mohanty, N; Berry, V; "Graphene-Based Single-Bacterium Resolution Biodevice and DNA Transistor: Interfacing Graphene Derivatives with Nanoscale and Microscale Biocomponents", *NanoLetters.* **8**, 12 (2008)

- Moser, J; Verdaguer, A; Jimnez, D; Barreiro, A and Bachtold, A; "The environment of graphene probed by electrostatic force microscopy", *Langmuir.* **23**, 9699 (2008)

- Motzer, Ch; Reichling, M; "High resolution study of etch figures on CaF(2) (111)", *Journal of Applied Physics.* **105**, 064309 (2009)

- Nakaya, U; Matsumoto, A; "Simple experiment showing the existence of liquid water film on the ice surface", *Journal of Colloid Science.* **9**, 1 (1954)

- Nonnenmacher, M; O'Boyle, MP; Wickramasinghe, HK; "Kelvin Probe Force Microscopy", *Applied Physics, Letters.* **76**, 2921 (1991)

- Novoselov, KS; Geim, AK; Morozov, SV; Jiang, D; Zhang, Y; Dubonos, SV; Grigorieva, IV; and Firsov, AA; "Electric field effect in atomically thin carbon films", *Science.* **306**, 666 (2004)

- Novoselov, KS; Geim, AK; Morosoz, SV; Jiang, D; Katsnelson, MI; Grigorieva, IV; Dubonos, SV; Firsov, AA; "Two-dimensional gas of massless Dirac fermions in graphene", *Nature.* **438**, 7065 (2005)

- Nutt, DR and Stone, AJ; "Adsorption of water on the $BaF_2(111)$ surface", *Journal of Chemical Physics.* **117**, 800 (2002)

- Pauling, L; "The nature of the chemical bond. II. The one-electron bond and the three-electron bond", *Journal of the American Chemical Society.* **53**, 3225-3237 (1931)

- Pérez, M; "Gibbs-Thomson effects in phase transformations", *Scripta Materialia.* **52**, 8 (2005)

- Pockels, A; "Surface Tension", *Nature.* **43**, 437 (1891)

- Pockels, A; "On the relative contamination of the water surface by equal quantities of different substances", *Nature.* **47**, 418 (1892)

- Ponomarenko, LA; Schedin, F; Katsnelson, MI; Yang, R; Hill, EW; Novoselov, KS; Geim, AK; "Chaotic dirac billiard in graphene quantum dots", *Science.* **320**, 5874 (2008)

- Pruppacher, HR; Microphysics of Clouds and Precipitation (1997)

- Puchin, VE; Puchina, AV; Husinga, M; and Reichling, M; "Theoretical modelling of steps on the $CaF_2(111)$ surface", *Journal of Physics: Condens. Matter.* **13**, 2081 (2001)

- Rayleigh, FRS; "Measurements of the amount of oil necessary in order to check the motions of camphor upon water", *Proc. R. Soc. London.* **47**, 364-367 (1890)

- Roco, MC; *Journal of Nanoparticle Research.* "Nanoparticles and nanotechnology research", **1**, 1 (1999)

- Rodgers, P; Nanoscience and Technology, 2009 (llibre)

- Sacha, GM; and Sáenz, JJ; "Cantilever effects on electrostatic force gradient microscopy", *Applied Physics Letters.* **85**, 2610 (2004)

- Sacha, GM; Verdaguer, A and Salmeron, M; "Induced water condensation and bridge formation by electric fields in atomic force microscopy", *Journal of Physical Chemistry B.* **110**, 14870 (2006)

- Sacha, GM; Gómez-Navarro, C; Sáenz, JJ; *Applied Physics.* **101**, 024310 (2007)

- Sadewasser, S; Carl, P; Glatzel, T; Lux-Steiner, MC; "Influence of uncompensated electrostatic force on height measurements in non-contact atomic force microscopy", *Nanotechnology.* **15**, S14 (2004)

- Sadtchenko, V; Conrad, P; Ewing, GE; "H_2O adsorption on $BaF_2(111)$ at ambient temperatures", *Journal Chemical Physics.* **116**, 4293 (2002)

- Salam, A; Lohmann, U; Crenna, B; Lesins, G; Klages, P; Rogers, D; Irani, R; MacGillivray; Coffin, M; "Ice nucleation studies of mineral dust particles with a new continuous flow diffusion chamber", *Aerosol Science and Technology.* **40**, 2 (2006)

- Salmeron, M; Xu, L; Hu, J; Dai, Q; "High-resolution imaging of liquid structures: Wetting and capillary phenomena at the nanometer scale", *MRS bulletin.* **22**, 8 (1997)

- Salmeron, M; "Scanning polarization force microscopy - A technique for studies of wetting phenomena at the nanometer scale", *Oil and gas science and technology.* **56**, 1 (2000)

- Santos, S; Verdaguer, A; Souier, T; Thomson, NH; Chiesa,M; "Measuring the true height of water films on surfaces", *Nanothecnology.* **22**, 46 (2011)

- Schedin, F; Geim, AK; Morozov, SV, Hill, EW; Blake, P; Katnelson, MI; Novoselov, KS; "Detection of individual gas molecules adsorbed on graphene"*Nature Materials.* **6**, 652 (2007)

- Schnell, RC; "Biogenic sources or atmospheric ice nuclei", *Bulletin of the american meteorological society.* **55**, 6 (1974)

- Schonenberger, C; Alvarado, SF; "Observation of single charge-carriers by Force Microscopy", *Physical Review Letters.* **65**, 25 (1990)

- Schwoebel, RL; Shipsey, EJ; "Step motion on crystal surfaces", *Journal of Applied Physics.* **37**, 3682 (1966)

- Semenoff, GW; "Condensed-Matter simulation of a 3-dimensional anomaly", *Physical Review Letters.* **53**, 26 (1984)

- Shafrin, EG; Zisman, WA; "Constitutive relations in the wetting of low energy surfaces and the theory of the retraction method of preparing monolayers", *Journal of Physical Chemistry.* **64**, 5 (1960)

- Shaw, RA; Durant, AJ; Mi, Y; "Heterogeneous surface crystallization observed in undercooled water", *Journal of Physical Chemistry B.* **109**, 20 (2005)

- Shevkunov, SV; "Nucleation of water vapor in microcracks on the surface of beta-AgI aerosol particles: 1. The structure of nuclei", *Colloid Journal.* **69**, 3 (2007)

- Shi, H; Eglitis, RI; and Borstel, G; "Ab initio calculations of the BaF_2 bulk and surface F centres", *Journal of Physics-Condensed Matter.* **18**, 8367 (2006)

- Stix, G; "Nanotechnology is all the rage. But will it meet its ambitious goals? And what the heck is it?", *Scientific American.* **285**, 3 (2001)

- Su, XC; Lianos, L; Shen, YR; Somorjai, G; "Surface-induced ferroelectric ice on Pt(111)", *Physics Review Letters.* **80**, 1533 (1998)

- Ugural, AC; Fenster, SK; "*Advanced Strength and Applied Elasticity*" 4th ed. (2003)

- Verdaguer, A; Weis, C; Oncins, G; Ketteler, G; Bluhm, H; and Salmeron, M; "Growth and structure of water on SiO_2 films on Si investigated by Kelvin probe microscopy and in situ x-ray spectroscopies", *Langmuir.* **23**, 9699 (2007)

- Verdaguer, A; Cardellach, M; Fraxedas, J; "Thin water films grown at ambient conditions on $BaF_2(111)$ studied by scanning polarization force microscopy", *Journal of Chemical Physics.* **129**, 174705 (2008)

- Verwey, EJW; "The charge distribution in the water molecule and the calculation of the intermolecular forces", *Recueil des Travaux Chimiques des Pays-Bas.* **60**, 887-896 (1941)

- Vonnegut, B; "The nucleation of ice formation by silver iodide", *Journal of Applied Physics.* **19**, 593 (1947)

- Vonnegut, B; "Nucleation of supercooled water clouds by silver iodide smokes", *Chemical Reviews.* **44**, 2 (1949)

- Wallace, PR; "The band theory of graphite", *Physical Review.* **72**, 11 (1947)

- Wassermann, B; Reif, J; and Matthias, E; "Different modes of water aggregation on (111)surfaces of fluorite structures", *Physics Review B.* **50**, 2593 (1994)

- Weisenhorn, AL; Hasma, PK; Albrecht, TR; Quate, CF; "Forces in Atomic Force Microscopy in air and water", *Applied Physics Letters.* **54**, 26 (1989)

- Wu, YT; Mayer, JT; Garfunkel, E; and Madey, TE; "X-ray photo-electron spectroscopic study of water-adsorption on $BaF_2(111)$ and $CaF_2(111)$ surfaces", *Langmuir.* **10**, 1482 (1994)

- Wu, YT; Hayashi, K; Saito, N; Sugimura, H; and Takai, O; "Imaging micropatterned organosilane self-assembled monolayers on silicon by means of scanning electron microscopy and Kelvin probe force microscopy", *Surface and Interface Analysis.* **35**, 1 (2003)

- Wu, JB; Agrawal, M; Becerril, HA; Bao, ZN; Liu, ZF; Chen, YS; Peumans, P; "Organic Light-Emitting Diodes on Solution-Processed Graphene Transparent Electrodes", *ACS Nano.* **4**, 1 (2010)

- Yoreo, JJ and Vekilov, PG; "Principles of crystal nucleation and growth", *Biomineralization.* **54** (2003)

- Zhang, YB; Tan, YW; Stormer, HL; Kim, P; "Experimental observation of the quantum Hall effect and Berry's phase in graphene", *Nature.* **438**, 201 (2005)

- Zerweck, U; Loppacher, C; Otto, T; Grafstorm, S; Eng, LM; "Accuracy and resolution limits of Kelvin probe force microscopy", *Physical Review B.* **71**, 12 (2005)

- Zheligovskaya, EA; Malenkov, GG; "Crystalline water ices", *Uspeckhi Khimii.* **75**, 1 (2006)

- Zink, JC; Reif, J and Matthias, E; "Water-adsorption on (111) surfaces of BaF_2 and CaF_2", *Physics Review Letters.* **68**, 3595 (1992)

- Zdrojek, M; Mélin, T; Diesinger, H; Stiévenard, D; Gebicki, W; Adamowicz, L; "Charging and discharging processes of carbon nanotubes probed by electrostatic force microscopy", *Journal of Applied Physics.* **100**, 114326 (2006)

Appendix A

During the present thesis, there were some topics that were interesting for us but there was no time to develop properly. An example is the study of kaolinite. Once finished the studies of BaF_2 and CaF_2, the attention was focused in this compost. Kaolinite is a clay mineral with a quasihexagonal arrangement of hydroxyl groups as explained in section 3.1. The intension was to show if kaolinite leads the ice nucleation due to its lattice mismatch as BaF_2.
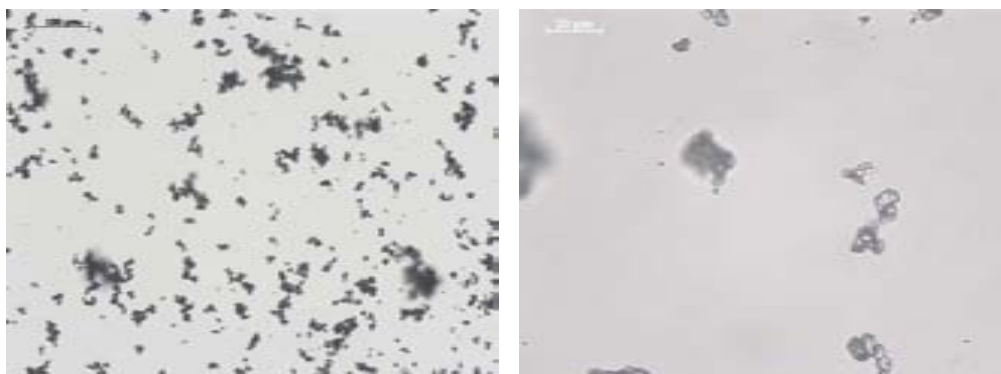

Figure 7.1: Two images of kaolinite taken with an optical microscope of 100 μm (left) and 20 μm (right).

The first step was to get images with an optical microscopy, the easiest option to preview the surface of kaolinite. As shown in figure 7.1, the obtained images do not give us relevant information about the geometry of kaolinite

due to the resolution limit of the microscopy. Therefore SEM (Scanning Electron Microscope) was selected. SEM offers three-dimensional images with a better resolution. In figure 7.2 one can see how kaolinite is built by small hexagonal pieces and clusters composed by these hexagonal pieces. The next step was trying to view the kaolinite geometry with AFM. However, some difficulties arose because kaolinite is a mineral powder, and the handling is really difficult. In AM-AFM mode, the probe is often in contact with the substrate and interact (sometimes drags the sample) or damage it, and the sample can damage easily the tip as well. In figure 7.3 is shown an AFM image of kaolinite.
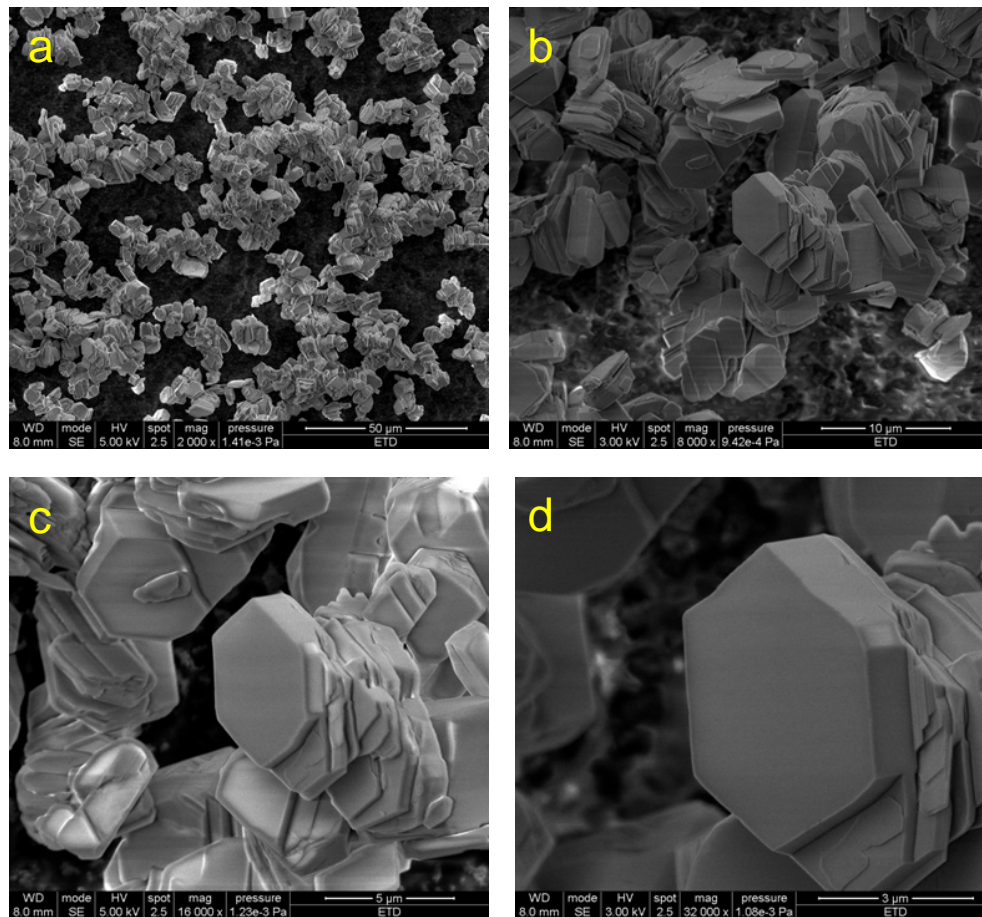
Figure 7.2: SEM images of kaolinite. At top left (*a*), an overview of a kaolinite sample (powder), is impossible distinguish the hexagonal geometry. In images *b, c* and *d* one can observe some hexagonal pieces and kaolinite clusters.
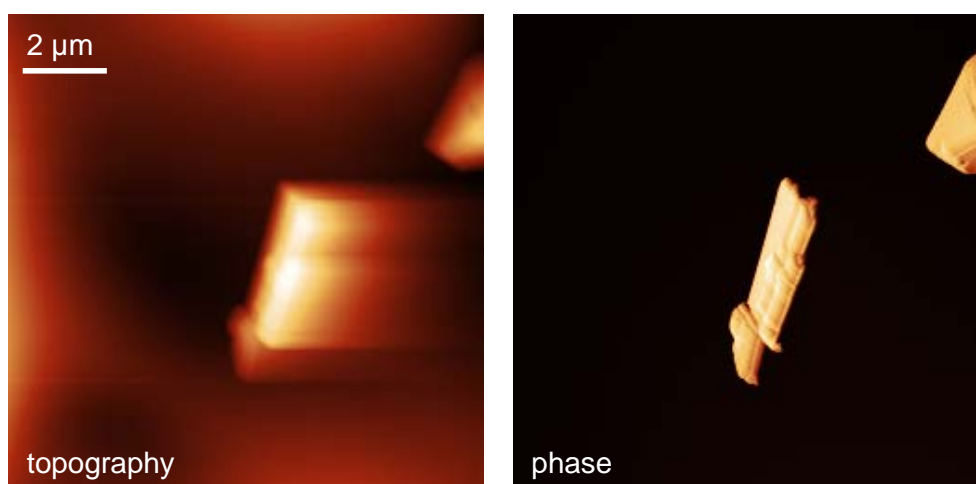
Figure 7.3: Topographic (left) and phase (right) AFM images taken at ambient conditions (T=21°C and RH~45%) in acoustic (AM-AFM) mode of kaolinite disposed on mica.

Glossary

- AC - Alternating Current

- AFM - Atomic Force Microscopy

- AM-AFM - Amplitude Modulation Atomic Force Microscopy

- CIN2 - Centre d'Investigació en Nanociència i Nanotecnologia

- CMC - Critical Micellar Concentration

- CPD - Contact Potential Difference

- CSIC - Consejo Superior de Investigaciones Científicas

- DC - Discontinuous Current

- DMT - Derjaguin-Muller-Toporov (model)

- DNA - DesoxyriboNucleic Acid

- DFT - Density Functional Theory

- EFM - Electrical Force Microscopy

- FLG - Few Layer Graphene

- FTIR - Fourier Transform InfraRed

- IBM - International Business Machines

- ICN - Institut Català de Nanotecnologia

- IR - InfraRed

- KPFM - Kelvin Probe Force Microscopy

- LB - Langmuir-Blodgett

- LFM - Lateral Force Microscopy

- LS - Langmuir-Schaefer

- PTFE - PolyTetraFluoroEthylene

- RH - Relative Humidity

- RT - Room Temperature

- SAM - Self Assembled Monolayer

- SEM - Scanning Electron Microscope

- SFA - Surface Forces Apparatus

- SPD - Surface Potential Difference

- SPFM - Scanning Polarization Force Microscopy

- SPM - Scanning Probe Microscopy

- STM - Scanning Tunneling Microscopy

- UHV - Ultra High Vacuum